The effect of the gas phase chemistry on the catalytic oxidation of ammonia over platinum

Vom Fachbereich Chemie
der Technischen Universität Darmstadt

Zur Erlangung des Grades
Doktor – Ingenieurs (Dr. –Ing.)

Dissertation
von Pablo Ignacio Hernández Arango
aus Medellín, Kolumbien

Erstgutachter: Prof. Dr. – Ing. Herbert Vogel
Zweitgutachter: Prof. Dr. Martin Votsmeier

Darmstadt 2021

Pablo Ignacio, Hernández Arango: The effect of the gas phase chemistry on the catalytic oxidation of ammonia over platinum.
Darmstadt, Technische Universität Darmstadt.
Jahr der Veröffentlichung der Dissertation auf TUPrints: 2022
Tag der Einreichung: 28.09.2021
Tag der mündlichen Prüfung: 06.12.2021

06. Dezember 2021

Erklärungen laut Promotionsordnung

§8 Abs. 1 lit. c PromO

Ich versichere hiermit, dass die elektronische Version meiner Dissertation mit der schriftlichen Version übereinstimmt und für die Durchführung des Promotionsverfahrens vorliegt.

§8 Abs. 1 lit. d PromO

Ich versichere hiermit, dass zu einem vorherigen Zeitpunkt noch keine Promotion versucht wurde und zu keinem früheren Zeitpunkt an einer in- oder ausländischen Hochschule eingereicht wurde.

§8 Abs. 1 PromO

Ich versichere hiermit, dass die vorliegende Dissertation selbstständig und nur unter Verwendung der angegebenen Quelle verfasst wurde.

§8 Abs. 2 PromO

Die Arbeit hat bisher noch nicht zu Prüfungszwecken gedient.

Pablo Ignacio Hernández Arango
Mattstraße 3
63743 Aschaffenburg

Abstract

Catalytic oxidation of ammonia (NH_3) by the Ostwald process for obtaining nitric oxide (NO) and the subsequent production of nitric acid, has been widely studied and implemented. This process is carried out over Platinum (Pt), in which the formation of NO is favored. However, it is remarkable the need to identify possible gas phase reactions that may occur by means of which is increased or inhibited the NO formation.

Chemical processes in the gas phase, who implies the species included in the Ostwald process, for instance the homogeneous oxidation of NH_3 or the selective non – catalytic reduction of nitrogen oxides (NO_X) by NH_3, have been reported and implemented. One of the key features of these homogeneous schemes is its reliance on the characteristics of each process variables. Therefore, it is of interest, determining the occurrence of such reactions in the gas phase of Ostwald process for NH_3 oxidation.

Due to the complexity of the chemical mechanisms of the processes in the gas phase, reduction, and eventual implementation through computational simulation tools is necessary. While catalytic reactions favor the NO formation, the gas phase reactions promote the N_2 and N_2O formation due to NO reduction. This simulation, will allow to establish the route by which these sub products are formed, reducing the process efficiency, and increasing the environmental impact of the Oswald process.

Comparison of results when the pure catalytic process and the coupled catalytic and gas phase processes are simulated, allow to define the effect of the gas phase chemistry over the overall process.

Dedication and Acknowledgments

"There is not perfection, but there are some experts in the world, who realized that the perfection only would come by the disciplinated and daiary training."

Dr. Ph. David Hormachea

The present work was developed during my scholarship as a doctoral student the Institute for Technical Chemistry and Macromolecular Chemie in the Research Group of Prof. Dr. –Ing. Herbert Vogel at the Technical University of Darmstadt.

The Government of Colombia honored me with a full scholarship to develop my studies at this institution and the people associated with this project were pleased to consider my participation as part of this wonderful working group within the framework of a research project, as challenging as fun.

I particularly appreciated the trust placed by Professors Vogel and Votsmeier and the freedom they gave me during my academic research.

The excellent atmosphere in the research group has a particular impac on the success of the work. The humanity and the excellent specialist knowledge of the colleagues contributed to this. I am especially grateful with Dr. –Ing. Artur Wiser, Dr. –Ing. Bejamin Bernhard Kühne, Michael Hass, without all these people this job would not have been possible.

My special thanks go to my parents and brothers, who conducts me through the way of knowledge and discipline. They have been always by my side even from the distance, even thought that I am usually far away from their expectations.

My fully deeply thankfulness to my beloved wife Carolina Suárez Vallejo. A powerful woman and incredible chemical engineer, who has been able to support me, leading me and inspiring me in the way of live through teha patience and mercy, even when she knows, how difficult I am. Always when I get a goal, I must recognize that she shows me every day the highly target in our lives.

I do not deserve this from you, my Lord, but you have been good with me, as always, one more time. *All this, especially my life, belongs to you*.

Contents

Symbols, abbreviations, conventions

Symbol	Description	Unit
a_{ji}	Factor of the effect of the species *j* in the reaction *i* as third body	$m^3\ kmol^{-1}$
a_{nj}	Coefficients *(n from 1 to 7)* to calculate the thermodynamic properties	(*)
A_i	Arrhenius factor for the calculation of the forward rate constant of reaction *i*	(*)
$A_{i_{j\to k}}$	Flux of element *A* from species *j* to species *k* through reaction step *i*	$kmol\ m^{-3}\ s^{-1}$
A_{nn}	Terms (*nn*) of the matrix *A* for the calculation of D_{nj}	
A_{nj}	Terms (*nj*) of the matrix *A* for the calculation of D_{nj}	
b_i	Exponent of temperature for the calculation of the forward rate constant of reaction *i*	Dimensionless
B_{nn}	Terms (*nn*) of the matrix *B* for the calculation of D_{nj}	
B_{nj}	Terms (*nj*) of the matrix *B* for the calculation of D_{nj}	
C	Molar concentration of species in the gas phase	$kmol\ m^{-3}$
c_f	Temperature dependent fall of parameter	Dimensionless
C_j	Molar concentration of species *j*	$kmol\ m^{-3}$
C_{P_j}	Heat capacity at constant pressure of species *j*	$kJ\ kmol^{-1}\ K^{-1}$
C_{P_M}	Heat capacity at constant pressure of mixture of gases	$kJ\ kmol^{-1}\ K^{-1}$
$[D]$	Matrix of the generalized coefficients of the Fick's law	$m^2\ s^{-1}$
D_{nj}	Mass diffusion coeficients	$m^2\ s^{-1}$
E	Total Energy	J
E_{A_i}	Activation energy of reaction *i*	$J\ kmol^{-1}$
$\vec{F}$	External body force vector	$kg\ m\ s^{-2}$
F	Fall off reaction parameter	(*)
F_c	Fall off reaction parameter	(*)
$F_{i_{j\to k}}$	Effect of a reaction step *i* over the transformation of one species *j* to other species *k* by means of an element *A*	Dimensionless
$\vec{g}$	Gravity vector	$m\ s^{-2}$
h_M	Sensible enthalpy of mixture of gases	J
h_j	Sensible enthalpy of component *j*	J
h_f	Heat transfer coefficient in the fluid – side	$kW\ m^{-2}\ K^{-1}$
H_j^o	Enthalpy of species *j*	$kJ\ kmol^{-1}$
ΔH_i^o	Enthalpy change of reaction *i*	$kJ\ kmol^{-1}$
$\bar{\bar{I}}$	Unity tensor	$kg\ m\ s^{-2}$
$\vec{J}_j$	Diffusion flux of species *j*	$kg\ m^{-2}\ s^{-1}$

k_j	Thermal conductivity of species *j*		W m^{-1} K^{-1}
k_M	Thermal conductivity of mixture of gases		W m^{-1} K^{-1}
k_{m_j}	Mass transfer coefficient in the fluid – side		kg m^{-2} s^{-1}
k_i	Forward rate constant of reaction *i*		(*)
k_{-i}	Bakward rate constant of reaction *i*		(*)
k_0	Low – pressure limit of the forward rate constant of reaction *i* according to Lindemann formulation		(*)
k_∞	High – pressure limit of the forward rate constant of reaction *i* according to Lindemann formulation		(*)
K_{C_i}	Equilibrium constant of reaction *i* based in concentration		Dimensionless
K_{p_i}	Equilibrium constant of reaction *i* based in pressure		Dimensionless
$\dot{m}$	Total mass flow		kg s^{-1}
$\dot{m}_j$	Mass flow of species *j*		kg s^{-1}
$\dot{M}_j^w$	Mass flux of species *j* at boundary *w*		kg m^{-3} s^{-1}
Mw_j	Molecular weight of component *j*		kg $kmol^{-1}$
$\vec{n}$	Normal vector to surface		Dimensionless
$n_{A,j}$	Number of atoms *A* in species *j*		Dimensionless
n_f	Temperature dependent fall of parameter		Dimensionless
$N_{A,i}$	Sum of number of atoms *A* on both side of reaction step *i*		Dimensionless
N_s	Number of species in reaction *i*		Dimensionless
N_R	Number of reactions in chemical mechanism		Dimensionless
P	Pressure		bar
P_r	Fall of parameter related to pressure limited parameters		kmol m^{-3}
p_0	Pressure as a boundary condition		bar
$\dot{Q}_w$	Heat flux to the wall from a fluid		kW m^{-2}
r	Overall rate of reaction		kmol m^{-3} s^{-1}
r_i	Rate of reaction *i*.		kmol m^{-3} s^{-1}
R	Universal constant of gases	8.3143	kJ $kmol^{-1}$ K^{-1}
R_j	Net reaction rate of species *j*		kmol m^{-3} s^{-1}
R_I	Ratio for kinetic parameter *I* for the same reaction between different mechanisms		Dimensionless
$\vec{S}$	Generic transported entitie (momentum, mass or energy)		(*)
$S_{C,i}$	Sensitivity coefficients of reaction *i*		Dimensionless
S_j	Selectivity to conversion of species *j*		%
S_j^o	Entrophy of species *j*		kJ $kmol^{-1}$ K^{-1}

ΔS_i^o	Entrophy change of reaction *i*	kJ kmol^{-1} K^{-1}
S_h	Energy (heat) source due to chemical reactions	kW m^{-2}
dS	Differencial of surface	m^2
t	Time	S
T	Temperature	K
T_j^*	Dimensionless temperature for calculation of transport properties	Dimensionless
T_{nj}^*	Binary dimensionless temperature for calculation of mass diffusion coefficients	Dimensionless
T_f	Bulk temperature in the fluid	K
T_{f1}	Fall off reaction parameter for temperature	K
T_{f2}	Fall off reaction parameter for temperature	K
T_{f3}	Fall off reaction parameter for temperature	K
T_{ref}	Reference temperature	298.15 K
T_w	Temperature in the wall	K
V	Scaled radial velocity	s^{-1}
V^{CS_i}	Reaction volume associated to the catalytic surface (i)	m^3
$\vec{v}$	Velocity vector	m s^{-1}
v_0	Magnitude of the velocity	m s^{-1}
v_i	Velocity component in orthogonal coordinate *i*	m s^{-1}
x_j^w	Molar fraction of species *j* at boundary *w*	Dimensionless
x_j^f	Molar fraction of species *j* in the fluid	Dimensionless
X_j	Consumption or conversion of species *j*	%
$X_{RC,i}$	The degree of rate control of reaction *i*	Dimensionless
Y_j	Mass fraction of molecule *j*	Dimensionless
α_f	Fall off reaction parameter for temperature	Dimensionless
ε_j/k_B	Lennard – Jones parameter based on the species vibration mode	K
$\left[\varepsilon/k_B\right]_{nj}$	Binary Lennard – Jones parameter based on the species vibration mode	K
μ_j	Dynamic viscosity of species *j*	Pa s
μ_M	Dynamic viscosity of mixture of gases	Pa s
ξ_{RI}	Progress of reaction RI	Dimensionless
ρ	Density	kg m^{-3}
σ_j	Lennard – Jones parameter based on the species size	Å
σ_{nj}	Binary Lennard – Jones parameter based on the species size	Å

$\bar{\bar{\tau}}$	Stress tensor	kg m s^{-2}
τ_{ij}	Stress tensor component in orthogonal coordinate	kg m s^{-2}
υ'_{ji}	Stoichiometric coefficient of species *j* as reactive in reaction *i*	Dimensionless
υ''_{ji}	Stoichiometric coefficient of species *j* as product in reaction *i*	Dimensionless
υ_{ji}	Global stoichiometric coefficient of species *j* in reaction *i*	Dimensionless
ϕ_{nj}	Interaction parameter for calculation of transport properties	Dimensionless
χ_j	Generical formula of chemical species *j*	–––
Ω_{μ_j}	Collision integral for the dynamic viscosity of species *j*	(*)
Ω_D	Collision integral for the diffusion coefficient of species *j*	(*)
$\partial\Omega$	Computational domain	–––

(*) the units are dependent on the equation in which the parameter or variable is used.

Abbreviation	Description
CatOx	Exclusiv catalytic oxidation process
CatOxGP	Catalytic oxidation process with gas phase effect
MAR	Maximum aspect ratio
MCI	Mesh convergence index
MOQ	Minimum orthogonal quality
MOS	Maximum orthogonal skewness
NCQ	Normalized cell quantity
NSR	Normalized simulation results
UHV	Ultrahigh – vacuum

1. Introduction

The catalytic oxidation of NH_3 is a key step in the high scale production of nitric acid, which, as one of the most ussefuls commodities, is spredwhile consumed in the production of fetilizers [IHS 2020] but is used as well in the production of special polymers as Nylon ® [Hey 2018].

Nitric acid is a highly demanded commodity in the chemical industry. The annual production is around more than 80 mio. tons a year with a market value of around US$ 15 billion. [Hey2018]. A continuing growth of world population requires an increase in production of food. Then, the demand in nitrogen – based fertilizers will always grow.

The Ostwald process was patented in 1902 [Ost 1902], since then it has been studied with a view to optimizing it and has been industrially established for more than 100 years. The process is globally composed of the following steps, which are consideren in the process diagram shown by Figure 1:

- The NH_3 oxidation to a nitrous oxide (NO) in a heterogeneously catalyzed reaction, in which knitted and woven gauzes made of platinum and platinum alloys are used as catalyst.
- The quenched NO oxidation to NO_2 in presence of excess O_2.
- The absorption of NO_2 in water to generate nitric acid.

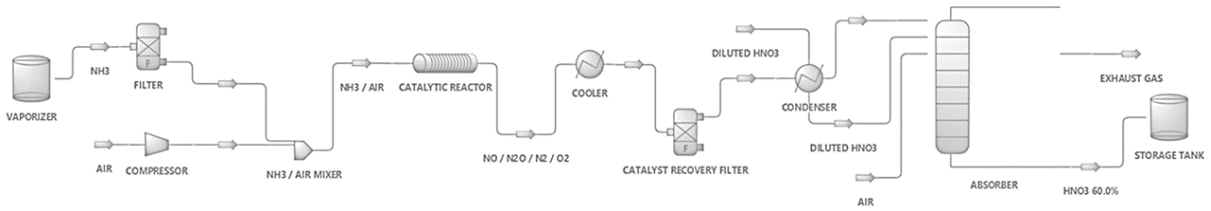

Figure 1. Process flow diagram for the Ostwald process (adapted) [CEW 202].

As precursor process of the main reagent (NO), the first step, it is the NH_3 oxidation, has a special interest from the point of view of the technologies of reaction engineering. The reaction is driven by mass and heat transfer phenomena under industrial conditions, and the knowled and understanding of those phenomena have been a mean core of research and investigation. Furthermore, the possibility of NH_3 to be oxidazed directly in the gas phase by either the combustion with O_2 or the reduction of NO, makes this gas phase process one point of interes in the optimization of this technology.

Unfortunatelythe, it is possible to note that the catalytic oxidation of NH_3 not only yields to the useful NO but produces nitrogen (N_2) and nitrous oxide (N_2O) as well. Both sub products, but specially the N_2, trends to reduce the efficiency of the process. Meanwhile the N_2O is highly undesirable since it has a high global warming potential. For this reason, efforts of the process research in this area seek to understand the conditions and phenomena that allow the selectivity maximization of the heterogeneous reaction, seeking the production of NO instead of the production of N_2 and N_2O.

Considering that the NH_3 oxidation has a good performance (yielding about 96.0 % of the desired product, NO) and that there exist technologies to destroy produced N_2O in secondary or tertiary steps of the process (e. g. SCR) (N_2O is 300 times stronger as green house gas compared to CO_2). Those technologies are expensive and require an additional catalyst, which can enable the decomposition of produced N_2O, but the reaction which leads to N_2O remains unchanged [Wis 2020].

In fact, to conduct the Ostwald process, the reaction RI is expected, but the reactions RII and RIII appear as side reactions that create the undesired species (N_2 and N_2O) with a yielding about 5.0 %.

$$4NH_3 + 5O_2 \rightarrow 4NO + 6H_2O \qquad \textbf{RI}$$

$$4NH_3 + 3O_2 \rightarrow 2N_2 + 6H_2O \qquad \textbf{RII}$$

$$2NH_3 + 2O_2 \rightarrow N_2O + 3H_2O \qquad \textbf{RIII}$$

So many studies have been conducted to describe the reaction mechanism of the chemical process which take place in the catalytic surface [Reb 2002] [Raf 2012]. Other studies have been focused on the effect of the catalyst material [Hin 2016] [Hin 2018]. Actual studies tray to explain the effect of the turbulence and catalyst shape over the behaviour of the process.

The main objective of this dissertation is to explain whether the process that occurs in the gas phase has any significant effect on the overall behaviour of the catalytic oxidation of NH_3, especially in terms of changes in the selectivity to the formation of products. If such effect is significant, some later research topics could be, among others: (i) the definition of chemical kinetic mechanisms that couple the heterogeneous and homogeneous processes, (ii) the study of process conditions or catalyst geometries that minimize adverse effects or maximize the beneficial effects from the gas phase process. Finaly, the Figure 2 summarizes the purpouse of this contribution.

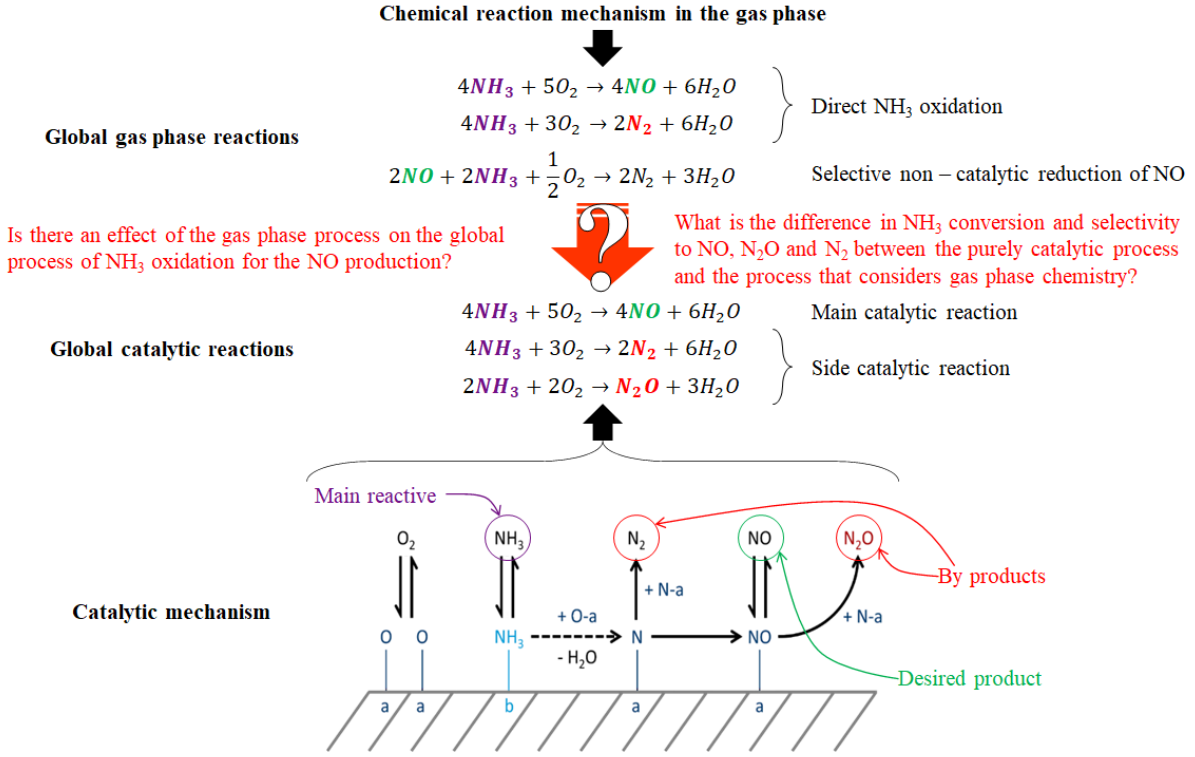

Figure 2. Graphycal summary of the proposal of this project.

2. Motivation and scope of this work

The catalytic oxidation of NH_3 by the Ostwald process for obtaining NO and the subsequent production of nitric acid, has been widely studied and implemented. This process is carried out in catalytic routes, in which the formation of NO is expected. However, it is remarkable the need to identify and to know the process conditions that contribute to the decrease in NO formation. This inefficiency in the formation of the expected product is reflected in the formation of by – products: N_2 and N_2O. The first of them as a direct indicator of the chemical inefficiency of the process. The second, N_2O, as an undesirable product since it is a highly polluting gas that favors the greenhouse effect.

One of the causes that may be attributable to the inhibition in the formation of NO may be the chemical process that may take place in the gas phase. Determining how extent is the effect of the physical−chemical phenomena existing in the gas phase, under the industrial operating conditions of the Ostwald process, by the comparison of the NH_3 conversion and selectivities to NO, N_2O and N_2 with the pure catalytic process, is the main objective of this work.

Chemical processes in the gas phase, who implies the species included in the Ostwald process, for instance the homogeneous oxidation of NH_3 or the selective non – catalytic reduction of nitrogen oxides (NO_X) by NH_3, have been reported and implemented. One of the key features of these homogeneous schemes is its reliance on the characteristics of each process variables. Therefore, it is of interest, determining the occurrence of such reactions in the gas phase of Ostwald process for NH_3 oxidation.

It has been said that the homogeneous reactions are dominant over higher temperatures, in fact, the heterogeneous process provides heat for homogeneous process. The radicals generated on the surface of catalyst would be transported into the gas phase and then react with molecular or radical species present in the gas phase. The higher the temperature, the higher the generation of those radicals and higher the net reaction rate in the gas phase. For this reason, the concept that the radicals generated by heterogeneous processes are important for the homogeneous one should be taked in account. Pressure is not a process variable to be underestimated. It has been shown that for high pressure, the gas phase process plays a strong role in combustion.

It has also been indicated that the effect of the gas phase process is highly dependent on both the type of fuel and the type of catalyst. The most important radicals are produced in the gas phase for the leanest mixtures (oxidant – fuel mixtures in which the fuel composition is lower than the stoquiometric required for combustion).

Under low temperature conditions, the gas phase combustion could be neglected, because of that the researchers put they efforts to develop catalysts able to operate at lower temperatures, although this may sacrifice conversion and therefore performance. Minimizing the possibilities of occurrence of gas phase reactions for catalytic processes has been in the sights of the development of these technologies. For this reason, alternatives have been proposed such as: minimize the volume available for homogeneous reactions by filling the reactors with inhert matterials, at least experimentally, even know that it implies an increase of the pressure drop of the reactor, which could make the results unsuitable for a process at industrial scale.

Due to the complexity of the chemical mechanisms of the processes in the gas phase, the reduction of those mechanisms, and its eventual implementation through computational simulation tools is necessary. While catalytic reactions favor the NO formation, the gas phase reactions promote the N_2 and N_2O formation due to direct NH_3 oxidatión with O_2 or by NO reduction in the presence of NH_3. This simulation, will allow to establish the route by which these sub products are formed, reducing the process efficiency, and increasing the environmental impact of the Oswald process.

Under this complex scenario of process interaction, NH_3 oxidation and the incidence of the gas phase process are a good subject to be investigated through "in – silico technics" by means of computer modeling. In computational fluid dynamics (CFD) simulations the kinetic and mass transfer effects can be modeled deciphering and understanding the interaction between the different aspects that affect the chemical process. For this, a lot of research effort has been put in and broad recommendations have been established that can favor obtaining valid results, such as:

- Considering a nonuniform grid for the discretization of the computational domain, finer near the wall and the entrance to the catalytic section should be used, because in those regions, the largest gradients for the dependent variables were expected.
- The heat transfer simulation could take an isothermal boundary condition on the wall according to experimental observations.
- Be attentive to that the increase in the total computational time due to the reaction model in the gas phase could be dramatic.
- Direct calculation of chemical source terms and found that this procedure results in a stable behaviour from the point of view of the numerical convergence. It also permits the inclusion of homogeneous chemical reactions without drastically increasing the computational time. The definition of the temperature profile plays an important role in determining the homogeneous contribution to the overall process. That inclusion of full heat transport in the wall is essential to the accurate simulation of the reactor performance.

Comparison of simulation results when the pure catalytic process and the coupled catalytic and gas phase processes are considered, allow to define the effect of the gas phase chemistry over the overall process. Thus, all the efforts of this research have been focused on solving the research questions:

Is there an effect of the gas phase process on the global process of NH_3 oxidation for the NO production?

What is the difference in NH_3 conversion and selectivity to NO, N_2O and N_2 between the purely catalytic process and the process that considers gas phase chemistry?

In any case, the answer to this question will lead to the discussion regarding the conditions in which this effect occurs and its quantification. This means that, in effect, the answer to this research question is neither unique nor unequivocal.

This work begins with a literature overwiew and the stablishment of the state of knowledge based on previous published work on: (i) effect of gas phase reactions in catalytic combustion as global process with different fuels, (ii) specific effect of gas phase reactions in catalytic oxidation of NH_3, (iii) experimental investigation and simulation about the catalytic combustion and the gas phase effects.

It should be noted that there is no previous information, sufficiently specific, clear, and focused on explaining, through process simulation, the effect of the process in the gas phase on the catalytic oxidation of NH_3.

The chemical kinetic mechanism devoted to the simulation of the catalytic oxidation of NH_3 over platinum and the chemical kinetic mechanism that could take place in the process of the gas phase are described. First, the detailed chemical mechanism for the process in the gas phase, which was selected to be used in this investigation is explained. Second, since the kinetic mechanisms in the gas phase tend to be so complex that their direct use for computational studies is impertinent, an exercise of mechanism reduction is presented that aims to reduce its complexity and facilitate its use as input information in the

simulation. Third, based on a pathway analysis, under typical conditions of the Ostwald process, the routes by which the gas phase mechanism can describe the presumed gas phase process are described. Finally, a brief comparison is presented between the gas phase mechanism, which was chosen to carry out this study, and other chemical mechanisms, reported to describe the same process. It should be noted that in this chapter, it has been considered allusions and annotations that have been confirmed by means of comparison with previous studies.

A theoretical part describes the mathematical and computational models used in this investigation, as well as some comments and characteristics of the implementation of the simulation.

After this, a brief description and analysis of reported operating conditions of the Ostwald process is presented, from which the simulation and study conditions corresponding to this work are established.

The following chapters refer to the results obtained in this research work. The order of the information presented corresponds to the types of reactors considered as the object of study. These are: (i) catalytic square mesh reactor, (ii) stagnation point reactor, and (iii) planar channel flow reactor.

The catalytic square mesh reactor is a simplification of the industrial scale meshes used for the NH_3 oxidation. The Figure 3 present schematically this simplification. The simplification to two dimensions models implies, from the point of view of th software, that the model considers that there is no significant gradients of dependent variables in the "non shown" direction, and a depth of 1.0 m is considered.

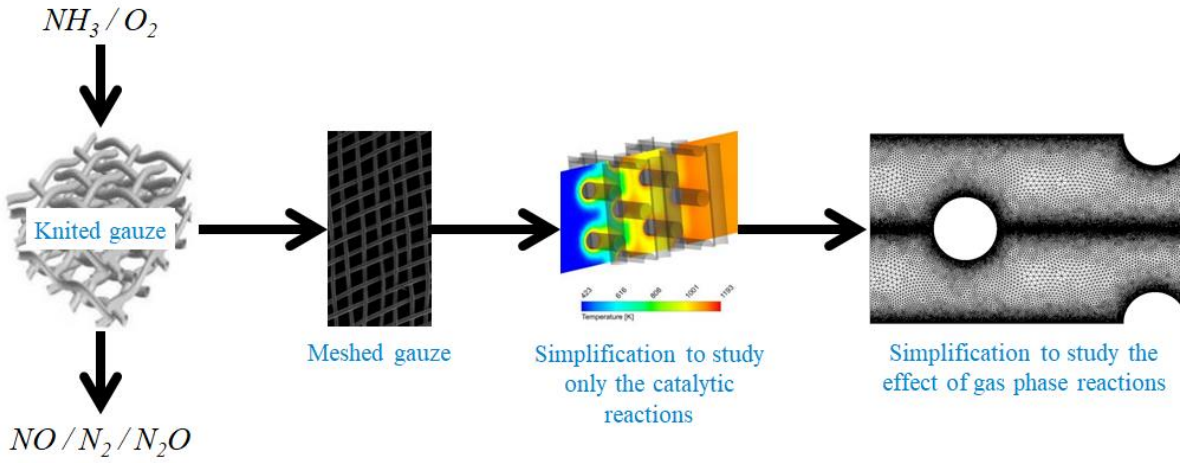

Figure 3. Simplification of the computational domain to conduct the study of the effect of gas phase reactions on the NH_3 oxidation [Hey 2018] [Wis 2020].

The stagnation point reactor is a simplification that allows to consider the simulation only in the axial direction, perpendicular to the catalytic surface, whit the assumption that radical velocities are functions of the axial coordinate only. Tin the stagnation flame model, the stagnation plane boundary conditions appear, which assumes axial convection and diffusion velocities to zero, and the stagnation plane temperature has to be specified [Bra 2016]. It is spreadly used in experimental investigacion of catalytic processes. And finaly, the planar channel reactor is a geometrical simplification that allows the simulation to be conducted avoiding the effect of curvatures in the fluid flow. In any case, the simulations conducted in this research was based on two dimensional schemes.

Within these chapters, the following information is presented: (i) specific requirements of the model, (ii) geometry and discretization of the computational domain (meshing) associated with the simulation, (iii) validation of the meshing by means of a spatial convergence analysis, (iv) boundary conditions and specific configuration of the simulation, and (v) results, discussion and analysis of the

simulations carried out for the purely catalytic process (CatOx) and the process that considers the effects in the gas phase (CatOxGP).

The last chapter draws general conclusions based on this research. It consideres some suggestions that can be taked into account for the operation of the catalytic oxidation of NH_3 in the Ostwald process and stablishes some suggestions for further works that could be conducted to better understand the effect of the gas phase process in the catalytic oxidation of NH_3. The figure 4 sumarises the scope of this project.

Having presented the structure of this document, it is useful to go back a few steps and underline two important methodological points:

1. Due to the scarcity of information from both simulation and experimentation, regarding the effect of the process in the gas phase on the catalytic oxidation of NH_3, it is of interest to carry out a purely computational study of this aspect. It has been widely demonstrated that the use of computational tools allows the initial response to scientific and technical questions to be addressed, which can later be obtained through experimental strategies. Such is the case of this study, in which, starting from a theoretical approach, it is intended to elucidate whether (or not) there is an effect of the process in the gas phase, and from there to give rise to the discussion about the relevance of implementing experimental research in this regard.

2. Due to the complexity posed using chemical kinetic mechanisms in the gas phase, in which the presence of multiple reactions and chemical species implies an increase in computational resources and makes the selection of computational tools difficult, it is necessary to facilitate the exercise by simplifying the compuational domain. This simplification has been made through the consideration of different types of reactors. Since the first aim of this document is to elucidate the effect of the process in the gas phase, the geometry or the type of reactor should not be more important than the analysis of the chemical process itself, and on the contrary, it should facilitate the use of the available computational tools.

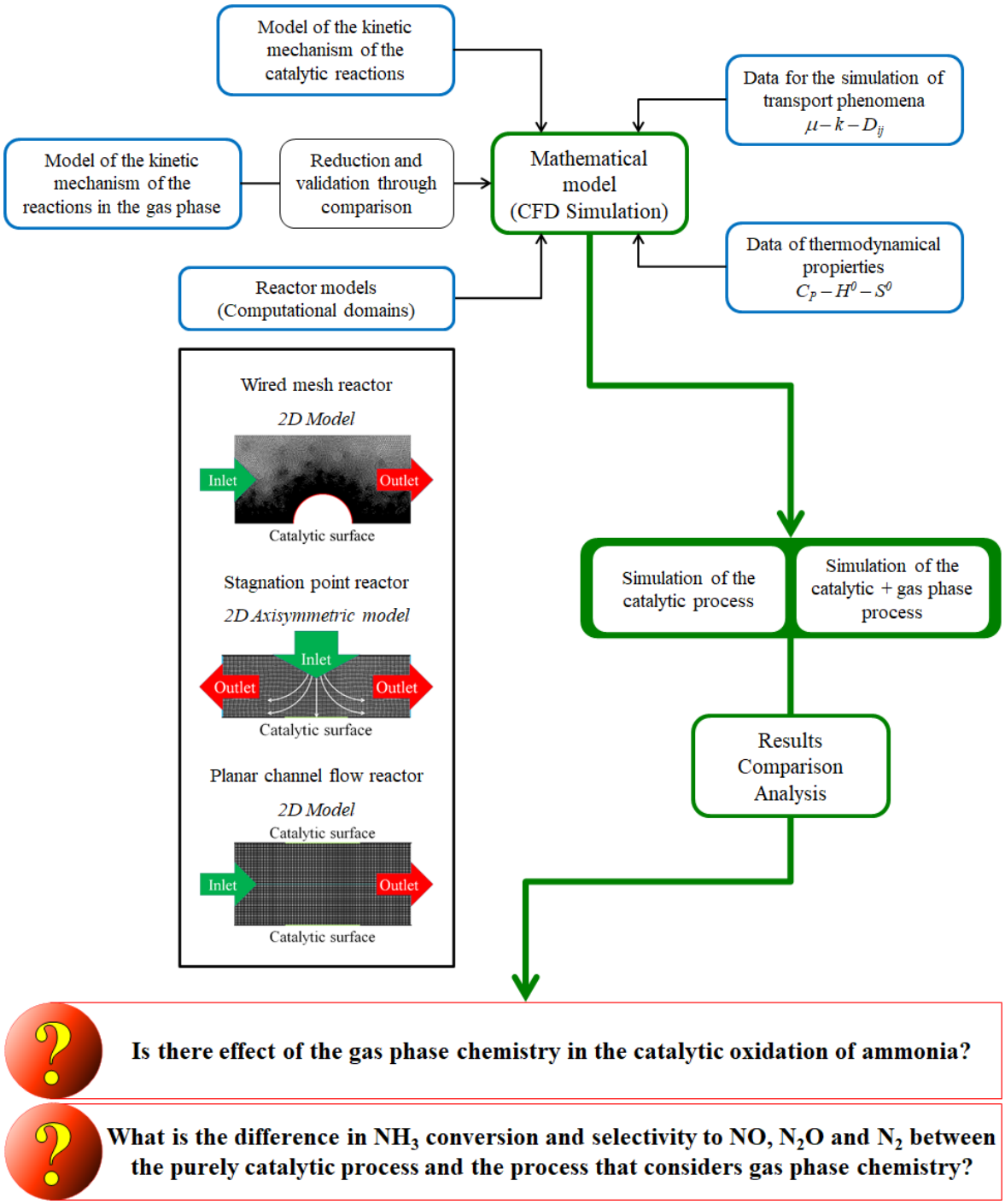

Figure 4. Graphic summary of the scope of this work

3. State of knowledge

This chapter presents a review of the scientific information reported on the effect of the gas phase process on the catalytic oxidation processes of different fuels, and, on the catalytic oxidation of NH_3. The information presented considers different experimental and computational studies. However, in the case of the effect on the catalytic oxidation of NH_3, sufficiently conclusive computational information about the effect of the process that takes place in the gas phase has not been reported. In each section, details and characteristics of these studies are noted, which were subsequently considered to carry out the work reported in this document.

The chemical mechanisms used for the simulation of the catalytic and gas phase process are presented. Those two mechanisms have been used with the parameters reported by their autors, but specially for the gas phase case, a methodology for the reduction and analysis of this information is reported.

This section presents mathematicaly the phenomenological and physico chemical background used to conduct the simulations. Finally, da report of industrial conditions to carry out the Oswald process, wich are used as simulation conditions are shown.

3.1. Experimental investigation about the effect of gas phase reactions in catalytic combustion

Experimental research on the combustion of hydrocarbons is a widely disseminated scientific field. It is known [Gri 30] that the reaction rate in the gas phase for hydrocarbons is higher than for NH_3 and much higher than for systems for the selective non – catalytic reduction of NO_X from NH_3. Therefore, the information from the state of the art regarding the oxidation of hydrocarbons in the gas phase, even more so when catalytic processes are considered, is of interest to foresee the conditions in which the processes in the gas phase may or may not influence on the oxidation of substances based on catalysis.

Morales [Mor 1989], Martin [Mar 1989], Lødeng [Lød 1999], and Burch [Bur 1999] studied ethane (C_2H_6) and propane (C_3H_8) oxidative dehydrogenation (Martin [Mar 1989] and Burch [Bur 1999] studied the methane (CH_4) hydrogenation as well). The first study deals with the reaction over platinum (Pt) and platinum rhodium (Pt – Rh) gauzes for a residence time of 10^{-5} s, the other three studies treat about the reaction in a fixed bed reactor, which packaging consists of a lithium promoted magnesium oxide catalyst with a long residence time, and the fourth study considered further the use of tin promoted magnesium oxide catalyst. Morales [Mor 1989] conclude that the homogeneous reactions are dominant over 948 K. From this temperature the ethyl radicals (CH_2CH_3) generated on the surface are transported into the gas phase and then react with molecular oxygen (O_2) to form ethylene (C_2H_4). Although Martin [Mar 1989] reported a notable effect of the gas phase, they argued against the concept that carbon – based radicals generated by heterogeneous processes are important for the homogeneous one. Lødeng [Lød 1999] argues that gas phase reactions dominate the process under the considered conditions and that the heterogeneous process provides heat for homogeneous dehydrogenation as well. Burch [Bur 1999] highlighted that the non – catalyzed oxidative dehydrogenation of C_2H_6 is at least as good as that on any known pure oxide catalyst, in which there is not promotion treatment. Against the results of Morales [Mor 1989], Burch [Bur 1999] reported that the ethane conversion in the gas phase begins at 873 K.

Davis [Dav 2000] and Raimondeu [Rai 2002] studied the catalytic oxidation of CH_4 over different types of noble metal gauzes. In the case of Pt, they found that under low temperature conditions, the gas phase combustion could be neglected.

Zhou [Zho 2009] studied the flame stability of CH_4 combustion in three catalytic micro reactors made of different materials (quartz, alumina ceramic and copper – Cu –). They concluded that the flame stability envelopes of gas phase process in the quartz combustor are broader due to the higher flame temperature.

Gniot [Gni 2009] and Dathar [Dat 2014] have studied the oxidative dehydrogenation of isobutane (C_4H_{10}) using layered graphene catalysts and modified activated carbon as catalysts, respectively. They have observed that an increase of only 323 K in the inlet temperature decrease up to 20.0 % the selectivity because of the generation of CH_4, C_2H_4, and propylene (C_3H_6) via homogeneous processes. To offset these undesired gas phase contributions, they have put they efforts to develop catalysts able to operate at lower temperatures, although this may sacrifice conversion and therefore performance. Studing the same chemical procees, Li [Li 2010] considered filling the PFR reactor type with quartz chips to minimize the volume available for homogeneous reactions. Even expecting that it implies an increase of the pressure drop of the reactor, which could make the results unsuitable for a process at industrial scale.

Ramirez [Ram 2019] have studied the oxidative dehydrogenation of C_4H_{10} using a standard V / Al_2O_3 catalyst suported over commercial silicon carbide (SiC) monoliths and using wicrowaves as heat source at temperatures between 848 and 948 K. They found that the rates of formation of gas phase products become significant only at high gas phase temperatures, speccially above 923 K. They confirmed that the microwave heating increases the catalyst temperature maintaining coooler the gas phase. As such, it is a powerful tool to boost reaction selectivity and the productivity in catalytic systems, where homogeneous contributions become critical at high reaction temperatures.

3.2. Experimental investigation about the effect of gas phase reactions in catalytic oxidation of NH_3

Busby [Bus 1975] referenced several works, which since 1941 tried to study the effect of the gas phase process in the catalytic oxidation of NH_3. There have been comments, according to which the NH_3 oxidation starts on the surface and moves into the gas phase, providing a mixed heterogeneous – homogeneous mechanism. It had been said, that the NH_3 consumption is a heterogeneous – homogeneous reaction, involving an exothermic reaction away from the catalyst.

Busby [Bus 1975] reported that in the catalytic oxidation of NH_3, short contact times are involved, of the order of 10^{-3} s and that this time requires very rapid mass transport to the catalyst for the reaction to be completely heterogeneous. If the mass transport rate is insufficient, then a heterogeneous initiation of a homogeneous chain reaction is possible. At temperatures below 773 K, the N_2O formation is favored ($4\ NH_3 + 4\ O_2 \leftrightarrow 2\ N_2O + 6\ H_2O$). The higher the temperature, and the greater the contact time, then the greater the NO decomposition ($2\ NO \leftrightarrow O_2 + N_2$).

Geus [Geu 1999] resume the use of monoliths in catalytic oxidation, focusing on the NH_3 / NO_X system, they comment that at higher temperatures the gas phase combustion sets on. At atmospheric pressure, the homogeneous reactions set on at about 1023 K, while the experimental evidence available indicates that at higher pressures the ignition temperature of the gas phase reaction is of the same order of magnitude.

It is difficult to prevent the gas phase reaction to proceed at temperatures above about 1073 K. To suppress the homogeneous process, the radical intermediates must be removed effectively by exposure to a sufficiently large surface area quenching the radicals. Finally, they suggest that since metal gauzes are used in industrial processes successfully, the research on the development of stable alloys and on the use of gauzes in ignition of homogeneous gas phase reactions must be further carried on [Geu 1999].

Sadykov [Sad 2000] summarize the results of long – term efforts aimed at research and development of industrial oxide catalysts for NH_3 oxidation in the HNO_3 production within two – bed

(platinum gauzes and monolithic oxide layers) technology of the high – pressure process. They noted that the global reaction $\left(NH_3 + {}^3/_2\ NO \leftrightarrow {}^5/_4\ N_2 + {}^3/_2\ H_2O\right)$ may occur via both homogeneous and heterogeneous mechanisms. The rate of heterogeneous oxidation far exceeds that of the homogeneous route. The homogeneous reduction of NO_X by NH_3 is mostly efficient between 1173 – 1273 K.

The reduction of NO_X by NH_3 was found to be of a chain type involving many stages and intermediates being well described by the second order equation with respect to reagents. Referring to oxide catalysts, the contact time usually ranges from 10^{-2} to 10^{-1} s, which is essentially longer than on platinum gauzes. Moreover, the NO selectivity in oxide catalysts is always lower than that in platinum gauzes. They explain that it had been ascribed to a larger chemical sorption capacity of oxides, but it may also be caused by a larger impact of the homogeneous reaction between NH_3 and NO. Note that the mention to larger impact do not dismiss the effect of the gas phase process in the oxidation with platinum gauzes [Sad 2000].

In the monolith, as the gas velocity profile stabilizes along the channel, the mass transfer rate decreases, and the homogeneous reaction contribution increases. Even known that its rate is far lower than that of the desired reaction, it has a great effect on a choice of the monolith channel configuration [Sad 2000].

Baerns [Bae 2005] studied the NH_3 oxidation over platinum. The reaction was studied for a range of pressures between 10^{-5} and 1.0 bar, temperatures between 293 and 1073 K, in an isothermal configuration, and with different platinum catalysts: stepped Pt (533) single crystal, knitted gauze and polycrystalline foil. For these purposes, a micro structured quartz reactor was used considering TAP (temporal analysis of products) and UHV (ultrahigh – vacuum) configurations. Knowing that the gas transport in the catalytic reactor is determined by either Knudsen or molecular diffusion. Their experiments were performed in the Knudsen diffusion regime ($< 10^{15}$ molecules pulse^{-1}) in which solely heterogeneous interactions could be observed. In experiments under Knudsen diffusion regime, the short – lived intermediates such as NH_2, NH, and HNO were not detected because under these conditions the interactions in the gas phase are unlikely. This also opens but leave the possibility for detecting short – lived reaction intermediates or radical directly formed in the gas phase or released from the surface.

The N_2O is preferentially formed over polycrystalline catalyst. However, Baerns [Bae 2005] assume that the total pressure plays the most important role, in contrast to the lower pressures (Knudsen diffusion regime), at which all homogeneous reaction steps are suppressed, at higher pressures, that is, in the regime of molecular diffusion, N_2O formation might be also influenced by gas phase interactions. Finally, they presumed that in the catalytic process N_2O is formed via recombination of two assumed HNO intermediates $(2\ HNO_{-S} \rightarrow N_2O + H_2O + 2s)$, in the gas phase process N_2O is formed via interaction between NH_X and NO especially at high pressures.

Gong [Gon 2006] have studied the selective catalytic oxidation of NH_3 to N_2 on O – atom pre – covered Au (111). They considered experiments carried out in a molecular beam surface scattering apparatus at UHV pressure $< 2.0 \times 10^{-13}$ bar and temperatures between 77.0 and 600 K. Since the researchers was unable to detect desorbing H – atom or any H – based species (always presented in the gas phase process) other than NH_3 and H_2O, it is possible to conclude that those researchers do not detect the occurrence of the gas phase reactions in the process.

Kraehnert [Kra 2008] have derived a kinetical mechanism for the NH_3 oxidation over Pt. To conduct the experimental study, they used a micro – structured quartz – reactor operating at partial pressures of NH_3 and O_2 up to 0.06 bar and temperatures between 559 and 658 K. They proposed that the results illustrate the correct trends since they predict NO selectivity to increase with temperature, and only small amounts of N_2O to be formed, although the actual value of NO selectivity is lower than

the practically observed 95.0 w%. The remaining deviation between simulated and real values in practice may be attributed, among other causes, to neglected gas phase reactions.

Song [Son 2016] have studied experimentally the homogeneous NH_3 oxidation and have compared their experimental results with one – dimensional simulations. Their experiments were conducted in laminar flow reactors, made of quartz or alumina, at high – pressure (30.0 bar and 100 bar) under oxidizing and stoichiometric conditions, and medium – temperatures ranging from 450 to 925 K. They found that independent on temperature and pressure, the homogeneous oxidation of NH_3 was slow under stoichiometric conditions (inlet composition of NH_3 between 0.0714 and 0.0772 v% and inlet composition of O_2 between 0.0864 and 0.0929 v%). Under oxidizing conditions (inlet composition of NH_3 between 0.0729 and 0.0789 v% and inlet composition of O_2 between 3.95 and 4.07 v%), the onset temperature for reaction was between 850 and 875 K at 30.0 bar, while at 100 bar it was about 800 and 875 K, it is a complete consumption of NH_3 in the gas phase at higher pressures and low initial concentrations. The products of reaction were N_2 and N_2O, while NO and NO_2 concentrations were below the detection limit even under oxidizing conditions. The simulation model predicts any formation of NO or NO_2 and the concentration of N_2O is underpredicted at the highest pressure.

Resta [Res 2020] have studied experimentally the NH_3 oxidation on a chamber that allows standard UHV techniques, such as sputtering / annealing cycles to prepare a $Pt_{25}Rh_{75}$ (001) surface within a 10.0 ml flow reactor in the pressure range between 0.10 to 1.0 bar. The sample was exposed to 300 mbar total pressure with 3.50 mbar of NH_3, and an O_2 pressure ranging from 0.0 to 20.0 mbar. The total gas flow was 8.33×10^{-7} m^3 s^{-1} and Ar as carrier gas. The temperature could span from 300 to 1000 K. They found that in the gas phase there is only some NO production for the O_2 : NH_3 molar ratio equal to 6.0.

As an especial case, Segond [Seg 2002] studied the NH_3 oxidation in sub – and supercritical water conditions in two isothermal, isobaric plug flow reactors made of stainless steel and having different surface – to – volume ratios, at temperatures ranging from 803 to 903 K and pressures ranging from 1400 to 2800 bar under O_2 addition between 53.0 and 267 % over the stoichiometry conditions. They proved that NH_3 oxidation in supercritical H_2O proceeds through both homogeneous and heterogeneous mechanisms. In fact, they noted that at high temperature, less N_2O was observed because, as the temperature increases, produced N_2O react with NH_3 to produce N_2.

NO_3^- is produced as well, specially with the increment on O_2 composition. The effect of increasing the O_2 composition has no effect on the catalyzed reactions. They concluded too that the NO_3^- production is thus independent of the surface – to – volume ratio and only occur in the gas phase and decreased with the residence time. They found that the pressure has no or a small negative effect on the heterogeneous reaction but a pronounced effect on the homogeneous reaction [Seg 2002].

As other and final especial case, Patil [Pat 2020] have studied experimentally the NH_3 synthesis in plasma – catalytic process on a barrier discharge (DBD) reactor. They investigated 16 different transition metal and oxide catalysts supported on $\gamma - Al_2O_3$ under mild process conditions. According to their results, there is NH_3 decomposition depending on the gas phase and hydrogenated species conditions. For example, they explained that under excess of activated H – based species is known to facilitate decomposition and under high temperature conditions this process is conducted as well due to thermal decomposition. It is also a combined effect between the temperature and the NH_3 reactions over the catalytic surfaces: a higher reaction temperature there is a lower H – atom adsorption on the catalyst surface, thus reducing the probability of the heterogeneous reaction with activated N – based species and increasing the probability of the homogeneous reactions.

From this previous research report, the following observations can be made:

- The availability of chemisorbed O – atom activates NH_3 – adsorption and controls the selectivity towards NO formation [Imb 2007].

- Adsorbed NH and NH_2 have been identified as intermediates of the $NH_3 + O_2$ reaction on Pt (111). In other words, the primary step of NH_3 activation is the abstraction of H – atoms from NH_3 by adsorbed O – atom. This step is accompanied by the formation of NH_2 and OH species [Imb 2007]. The formation of OH, N and NH_X species in the catalytic surface was founded by Resta [Res 2020] as well.
- The direct interaction of chemisorbed oxygen (as O – atom and OH) with adsorbed NH_3 initiates the abstraction of hydrogen from NH_3. The OH promotes the initial step (NH_3 to NH_2) less effectively but in contrast to adsorbed O – atom it also promotes the subsequent steps via adsorbed NH_2, NH or N. But the absorption of NH_X radicals depend on the surface configuration as well.
- Apparently, a clean platinum surface exhibits a negligible activity for NH_3 decomposition. However, a Pt gauze catalyst pre – treated in a flow of O_2 at 1073 K revealed a remarkably high activity towards NH_3 conversion to N_2, H_2O and H_2 even in the absence of O_2 in the gas phase [Imb 2007].
- As is described by the gas phase mechanism, stripping of H – atoms from the NH_3 by O – based species, like O – atom or OH, are the dominating primary reaction steps in the activation of catalytic NH_3 oxidation [Bae 2005].
- For any H – atom containing fuel the H – O chemistry plays a fundamental role. The chemical kinetics involving H, O, OH, HO_2, H_2O and H_2O_2 also determine the radical pool in the gas phase of those reaction systems [Shr 2018].

3.3. Experimental investigation and simulation about the catalytic combustion and the gas phase effects

Using computational fluid dynamics and simulation tools, different investigations have studied the effect of gas phase processes on catalytic combustion. The hydrocarbon combustion approach has been widely considered and, therefore, based on it, recommendations have been generated and considerations that facilitate computational exercise have been validated. This section lists some relatively recent research and summarizes the observations made regarding the implementation of the simulations.

Following a simulation methodology like which was proposed by Deutschmann [Deu 1998] [Deu 1998 – 02], Zerkle [Zer 2000] used a nonuniform grid, finer near the wall and the entrance to the catalytic section, because in those regions, the largest gradients for the dependent variables was expected. For the gas phase they used a detailed kinetic mechanism with Arrhenius expressions, which can be subject to third body collision enhancement factors, low pressure treatments, and a Troe [Gil 1983] bimolecular pressure fall off treatment. The calculation capability of ANSYS FLUENT [Flu 16 – 01] with the gas phase process is more advanced than that for surface chemistry; except for some lacks in the flexibility to allow pressure dependences.

Deutschmann [Deu 1998 – 01] [Deu 1998 – 02] simulated a continuous stirring tank reactor (CSTR) for the conversion of CH_4 to synthesis gas over Rh and Pt. A two dimensions model with full mass transport and heterogeneous reaction chemistry using a coupling between FLUENT and FORTRAN was conducted. In the gas phase, the heat transfer simulation took an isothermal boundary condition on the wall according to experimental observations. The results shown a complex interaction between heterogeneous chemistry and the mass and heat transfer. Later the investigation considered a homogeneous chemistry showing that, for pressure higher than 10.0 bar, the gas phase process plays a strong role. This author characterized the increase in the total computational time due to the reaction model in the gas phase as dramatic.

Veser [Ves 2000] modeled catalytic oxidation of CH_4 in a monolith reactor of Pt. Although the investigation proposes a multistep kinetic mechanism for the heterogeneous process, which fixed the experimental and simulated data for a one – dimensional plug flow reactor (PFR), the authors report that gas phase reactions do not play a major role in this catalytic system.

Zerkle [Zer 2000] studied the C_2H_6 / O_2 / hydrogen (H_2) cracking to C_2H_4 and H_2 over Pt in a CSTR reactor that have a residence time typically lower than 5.0×10^{-3} s and temperatures between 1173 and 1273 K, including chemical kinetic models for the pure catalytic process and for the gas phase process, coupled in bidimensional simulation with full heat and mass transport, and simulation of the heat transport in the walls as well. Their results indicated that both reaction processes play key role in the conversion of C_2H_6 to C_2H_4, while heterogeneous chemistry is responsible for the generation of CO, CO_2, and CH_4. Specifically, depending on the conditions of operation, due to the heterogeneous process there is an oxidation of C – atoms and H – atoms on the surface and the heat, which is generated by the surface reactions and released into the gas phase drives its endothermic chemical process. The C_2H_4 and H_2 are produced in the gas phase for the leanest mixtures (oxidant – fuel mixtures in which the fuel composition is lower than the stoquiometric required for combustion) with the surface as a net consumer of H_2 under this condition. With the increase in the C_2H_6 composition, the homogeneous production of those both species decreases, while their production comes from the surface. The higher is the temperature higher is the net reaction rate in the gas phase.

Finally, the simulations of Zerkle [Zer 2000] summarized the process as a heterogeneous production of CO, CO_2, and H_2O, coupled to both homogeneous and heterogeneous C_2H_4 and H_2 production. In the reactor outlet, the process results in an additional H_2, CO, and CH_4 from heterogeneous process.

Zerkle [Zer 2000] employed a direct calculation of chemical source terms and found that this procedure results in a stable behaviour from the point of view of the numerical convergence. It also permits the inclusion of homogeneous chemical reactions without drastically increasing the computational time. The definition of the temperature profile plays an important role in determining the homogeneous contribution to the overall process. That inclusion of full heat transport in the wall is essential to the accurate simulation of the reactor performance.

Stefanidis [Stef 2009] and Chen [Che 2016] studied the effect of gas phase reactions on the C_3H_8 combustion over Pt in a catalytic plate microreactor. Under their conditions, they proved that in catalytic micro combustor, there is a strong interaction between gas phase and catalytic reactions.

Li [Li 2017] studied the H_2 combustion over Pt in a catalytic micro reactor. The study explains who the computational fluid dynamics (CFD) simulations allow the reaction mode to be artificially controlled. For instance, one can suppress the surface reactions, decouple the processes and examine the contribution of each individual one. The results shown that on one hand, catalytic reactions weaken the gas phase combustion either by consuming part of the fuel before the gas phase ignition occurs or by the inhibition of the gas phase ignition due to the H_2O formation and the H – atom adsorption on the surface. On the other hand, the heat generated by the catalytic reactions enhances the wall temperature, promotes heat recirculation, and favors the gas phase ignition. They concluded that the effect of the gas phase process is highly dependent on both the type of fuel and the type of catalyst, for example in the case of the H_2 combustion, the Pt catalyst suppresses gas phase combustion rather than assisting it. This conclusion is like the finding reported by Davis [Dav 2000].

3.4. Chemical mechanism for the catalytic oxidation of NH_3 over platinum

The mechanism presented by Krähner [Kra 2008] has been selected to carry out the simulation of the selective oxidation of NH_3 to NO over Pt containing catalyst. This kinetic model describes NH_3 conversion, N_2 selectivity and N_2O selectivity using nine elementary reactions steps and one

lumped reaction as Figure 5 shows. This model had been developed under conditions where significant amounts of all the N – atom containing products are formed. Platinum wire gauzes are used since the implementation of the Ostwald process on large scale production in the 1920s [Res 2020]. The Pt (1 1 1) and Pt (2 1 1) surfaces provide better bases to develop fundamental microkinetics of surface reactions in the NH_3 combustion when it takes part at typicall conditions of temperature between 1023 and 1173 K, and pressures between 1.0 and 15.0 bar [Gon 2017]. The Table 1 presents the reactions considered in the Krähner [Kra 2008] mechanism with their respective kinetic parameters.

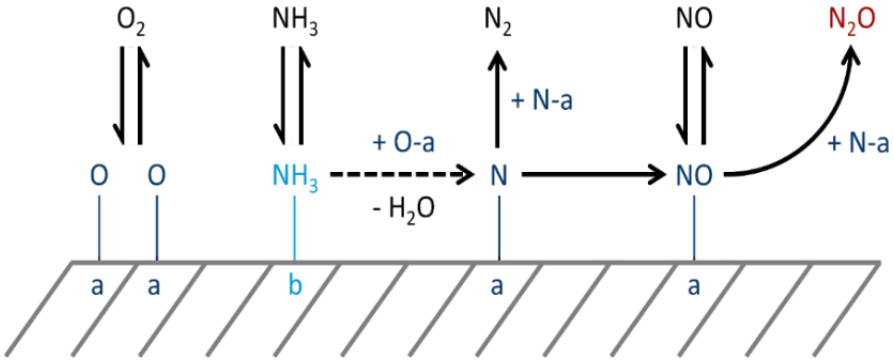

Figure 5. Mechanistic scheme of the reaction steps of catalytic NH_3 oxidation over platinum.

Table 1. Reactions and kinetical parameters of catalytic process.

Where:

A_i is the Arrhenius factor for the calculation of the forward rate constant of reaction *i*, (the units are dependent on the order of the chemical reaction).

b_i is the exponent of temperature for the calculation of the forward rate constant of reaction *i*, dimensionless.

E_{A_i} is the activation energy of reaction *i*, J kmol^{-1}.

	Chemical reaction	k (*)	E_A J kmol^{-1}	B ---
(RC001)	$NH_3 + Pt_b \rightarrow Pt_b\_NH_3$	1.95 $\times 10^{6}$	0.0	1.0
(RC002)	$Pt_b\_NH_3 \rightarrow NH_3 + Pt_b$	5.45 $\times 10^{10}$	6.09 $\times 10^{7}$	0.0
(RC003)	$O_2 + 2\,Pt_a \rightarrow 2\,Pt_a\_O$	3.3219 $\times 10^{13}$	0.0	1.0
(RC004)	$2\,Pt_a\_O \rightarrow O_2 + 2\,Pt_a$	3.4623 $\times 10^{17}$	1.81 $\times 10^{8}$	0.0
(RC005)	$NO + Pt_a \rightarrow Pt_a\_NO$	8.84 $\times 10^{10}$	6.35 $\times 10^{7}$	1.0
(RC006)	$Pt_a\_NO \rightarrow NO + Pt_a$	8.87 $\times 10^{17}$	1.548 $\times 10^{8}$	0.0
(RC007)	$Pt_b\_NH_3 + {}^3/_2\ Pt_a\_O \rightarrow Pt_a\_N + {}^3/_2\ H_2O + {}^1/_2\ Pt_a + Pt_b$	3.8634 $\times 10^{27}$	9.95 $\times 10^{7}$	0.0
(RC008)	$2\,Pt_a\_N \rightarrow N_2 + 2\,Pt_a$	9.4594 $\times 10^{25}$	1.39 $\times 10^{8}$	0.0
(RC009)	$Pt_a\_N + Pt_a\_O \rightarrow Pt_a\_NO + Pt_a$	7.1315 $\times 10^{24}$	1.354 $\times 10^{8}$	0.0
(RC010)	$Pt_a\_NO + Pt_a\_N \rightarrow N_2O + 2\,Pt_a$	1.478 $\times 10^{25}$	1.552 $\times 10^{8}$	0.0

(*) the units are dependent on the equation in which the parameter is used.

Obviously, between reactions RC001 and RC006, pairs of equilibrium reactions are formed. To facilitate its use in process simulations, these reactions have been presented in each of their direct forms and with their respective parameters. The kinetic parameters of the reverse reactions, obtained from the information of Krähner [Kra 2008], have been reported by Klingenberger [Kli 2017]. The first six reactions constitute the adsorption and desorption subgroup, the reaction RC007 describes the step of H – atom abstraction from NH_3 and the later three reactions constitute the subgroup of product formation.

This mechanism considers two active sites on the Pt surface (Pt_a and Pt_b). Krähner [Kra 2008] considers that the surface density of sites is equal to 1.64×10^{19} sites m^{-2} or 2.71×10^{-8} kmol m^{-2} according to the information reported by Zerkle [Zer 2000].

The NO formation is often described as recombination of absorbed O and N atoms. NO desorbs, decomposes, or reacts to N_2O. the competition between these reactions determines the selectivity towards NO and N_2O. The H – atom abstracted in NH_3 activation contributes to the H_2O formation, the only H – atom containing product of NH_3 oxidation detected in the development of this mechanism. It is possible that secondary reactions of NO and N_2O on the surface, and bi molecular NO adsorption followed by reactions of adsorbed NO take place. The N_2 interactions with the surface are negligible between 293 and 1073 K.

The experimental data reported by Krähner [Kra 2008] have clearly shown that NO inhibits the reaction between NH_3 and O_2 and contributes to N_2O formation. Hence, the NO adsorption is an essential part of the kinetic model for the investigated temperature and pressure range. The increase in the rate of N_2 formation with increasing temperature is not fully described by the kinetic model. The concentration of active sites on the surface was supposed to be independent of reaction conditions and time.

Krähner [Kra 2008] have suggest that the influence of feed composition on rates of product formation is described well for all products, although the model predicts slightly too low N_2O formation rates in large O_2 excess. Moreover, the influence of raising the temperature is reproduced well by the model for the NO and N_2O formation but deviates slightly for N_2 formation.

According to Imbihl [Imb 2007], in the mechanism proposed by Krähner [Kra 2008], the N_2 formation is the dominant reaction pathway at low temperature whereas at high temperature NO production prevails. The rate of N_2 formation increases with the partial pressure of NH_3 as well as with the partial pressure of O_2. Similarly, production rates for significant amounts of NO require partial pressures of O_2 exceeding those of NH_3.

Since the signals of N_2 and N_2O appear after the NO pulse in the temporal analysis reactor, these products are supposed to be formed via secondary NO transformations in the gas phase: (i) direct NO decomposition or / and (ii) NH_3 – NO interactions, it is selective reduction of NO. Then, they therefore suggested that N_2O, which is formed via secondary NO transformations is subsequently converted to N_2 [Imb 2007].

Imbihl [Imb 2007] suggested that the route of absorbed N – atom and NO to produce N_2O evidently contributes little to N_2O formation under their conditions. The N_2O reaction rate increases with the O_2 content of the feed, but in contrast to N_2, decreases in NH_3 excess. The later could be due to the selective reduction of N_2O in presence of NH_3. However, they stablish that their mechanism had been formulated for the formation of N_2O only in a speculative way.

Imbihl [Imb 2007] reports that N_2O is only formed in small quantities under UHV conditions and therefore, no comprehensive mechanistic information on its formation in NH_3 oxidation was available. Apparently different reaction pathways are leading to N_2O. According to the literature, the N_2O formation can occur either via recombination of two adsorbed NO molecules or via interaction between NO and NH_3 fragments. The recombination of two adsorbed NO molecules alone, however, cannot explain the experimental results. The reaction of NO and NH_3 fragments as the only reaction pathway of N_2O formation is also unlikely, since NH_X species necessary for N_2O formation cannot be

formed under oxidative conditions in the NO pulse. Since N_2O forms via a bimolecular step the reason why N_2O formation requires a higher pressure is probably because the bimolecular step requires both, a high enough NO coverage and a high enough temperature to overcome the activation barrier.

3.5. Detailed chemical mechanism for the process in the gas phase

Researchers from the Group of Inorganic Chemistry of the Abo Akademi in Finland [Kil 1999] [Cod 2001] developed a chemical mechanism that describes the NH_3 oxidation and its interaction with NO_X (NO, NO_2 and N_2O) in the gas phase. Traversac [Tra 2007] noted that this is a plausible chemical mechanism for simulation of the process that occurs in the gas phase during NH_3 oxidation over Pt. Wiser [Wis 2020] highlighted the annotation made by Traversac regarding the usefulness of this mechanism, not without considering that there is no agreement in the research about the role of gas phase reactions during NH_3 combustion.

The mechanism describes the possibility to convert NH_3 to N_2 by homogeneous reactions in the gas phase. Kilpinen [Kil 1999] and Coda Zabetta [Cod 2001] shows that additions of small amounts of NO in the fuel gas (composed primarily of NH_3) before the combustion stage, may convert parts of the NH_3 to N_2 at temperatures between 1073 and 1273 K.

The detailed reaction mechanism consists of 250 elementary reactions and 49 species, among which the CH_4 is the hydrocarbon of the process. After removing the reactions that include C – atom, the mechanism is reduced to 25 species and 145 elementary reactions. Appendix 1 presents this detailed mechanism based on nitrogenous species and O_2 and is defined as "AA – Mech". It should be noted that the numbering of the chemical reactions presented in this document corresponds to the list of Appendix 1.

A distinguishing feature of N – atom chemistry is the participation of long – lived radicals, for example H_2NO. These molecules require substantially more energy than their hydrocarbon analogs to form an unsaturated molecule and smaller radical. The increased endothermicity for these reactions in nitrogen chemistry results in much lower rate coefficients for dissociation. As a result, Gardiner [Gar 2000] shown that radical – radical reactions are more important in nitrogen than in carbon chemistry, and both O_2 and NO are suitable oxidizers for NH_3. With O_2 the NH_3 conversion is faster. With NO, the reaction is slower, and the conversion required more time. H_2 is another important compound affecting the chemistry of NH_3 oxidation.

During the writing of this document, Shrestha [Shr 2018] introduced a newly developed reaction mechanism for the NH_3 oxidation in freely propagating and burner stabilized premixed flames as well as in shock tubes, jet stirred reactors and plug flow reactors experiments. The reaction mechanism also considers the formation of NO_X, as well as the NO_X reduction depending on the conditions of the surrounding gas phase.

The Section 4.3.1 of this document shows the comparison between the AA – mech and the mechanism proposed by Glarborg [Gla 2018]. Quantitatively, the comparison is made between the values of the mechanism parameters through the equation (1).

$$R_I = \frac{I_{GLARBORG}}{I_{AA}} \qquad \textbf{(1)}$$

Where I can be any of the kinetic parameters referred to the modified Arrhenius expressions or to the parameters of the pressure dependent reactions.

3.6. Methodologies for the reduction and analysis of detailed chemical mechanisms

Stegelmann [Steg 2009] explained that in the kinetics model involving any multistep reaction mechanism, the net reaction rate is a complex function of the rate constants for all its elementary steps and the thermodynamic of all its reaction intermediates. However, under specific conditions, even the most complex mechanism can be limited to several rate determining steps, in which case the kinetic description is greatly simplified.

In the fiel of NH_3 combustion in the gas phase, Duynslägher [Duy 2012] indicate that the reduced mechanisms allow to reduce the computational cost in CFD simulations and allow a better understanding of the complete NO_X formation pathways.

The reduction procedure is essentially a trial – and – error methodology, which uses objective parameters, which describe the effect of the kinetic constants on the net rate of generation or consumption of the involved species. These methods were reported previously by several autors [Tur 2014] [Steg 2009] [Gla 1986] to reduce detailed chemical mechanisms. Duynslägher [Duy 2012] propouse that the choice of the fundamental reactions is based on a contribution rates calculation and sensitivity analysis. In detailed mechanisms the reactions set is established to be used for several conditions, a lot of reactions are added to be sure to have the more complete version of the mechanism. However, to have a mechanism only for specific combustion conditions some species and some reactions can be removed.

The first tool for the reduction and analysis of detailed chemical mechanisms is the ***"rate production analysis"***. Duynslägher [Duy 2012] explain that the calculation of the contribution rates allows to find the most important reactions for the formation and consumption of each species in the gas phase. According to what is proposed by Turányi [Tur 2014] for the analysis of chemical mechanisms, in which it is preferred to decrease the number of reactions instead of quantity of species, the molar conservation of elements is its basis. The flux of element *A* from species *j* to species *k* through reaction step i can be calculated according to equation (2).

$$A_{i_{j\to k}} = \frac{n_{A,j} \cdot n_{A,k} \cdot r_i}{N_{A,i}} \qquad \textbf{(2)}$$

Where:

$A_{i_{j\to k}}$ is the flux of element *A* from species *j* to species *k* through reaction step *i*, kmol m^{-3} s^{-1}.

$n_{A,j}; n_{A,k}$ is the number of atoms *A* in species *j* or *k*, dimensionless.

r_i is the rate of reaction *i*, kmol m^{-3} s^{-1}.

$N_{A,i}$ is the sum of number of atoms *A* on both side of reaction step *i*, dimensionless.

Considering all possible reaction steps that transform species j to other species k, the sum of the element fluxes at given reaction time is defined by equation (3).

$$A_{j\to k}(t) = \sum_i A_{i_{j\to k}}(t) \qquad \textbf{(3)}$$

Hence, the effect of a reaction step i ($F_{i_{j\to k}}(t)$) over the transformation of one species j to other species k by means of an element *A* is given by equation (4).

$$F_{i_{j\to k}}(t) = \frac{A_{i_{j\to k}}(t)}{\sum_i A_{i_{j\to k}}(t)} \quad \textbf{(4)}$$

The value of this effect is 1.0 when reaction *i* is the responsible for the transformation of species *j* into species *k*. On the other hand, the value is 0.0, when reaction *i* has no effect on the transformation of one species into another.

The second tool for the reduction and analysis of detailed chemical mechanisms is the ***"degree of rate control"***. The procedure of the degree of rate control, proposed by Stegelmann [Steg 2009] quantifies the extent to which a differential change in the standard state free energy of any given elementary step influences the net reaction rate. The equation (5) defines this parameter. The degree of rate control can only be quantitatively evaluated for microkinetic models (i.e., models with estimates of the rate constants for all the elementary steps).

$$X_{RC,i} = \frac{k_i}{r}\left(\frac{\partial r}{\partial k_i}\right)_{k_{m\neq i}, K_{C_i}} = \left(\frac{\partial \ln r}{\partial \ln k_i}\right)_{k_{m\neq i}, K_{C_i}} \quad \textbf{(5)}$$

Where:

$X_{RC,i}$	is the degree of rate control of reaction *i*, dimensionless.
k_i	is the forward rate constant of reaction *i*, (the units are dependent on the order of the chemical reaction).
r	is the overall rate of reaction, kmol m^{-3} s^{-1}.
K_{C_i}	is the equilibrium constant of reaction *i* based in concentration, dimensionless.

Where the partial derivative is taken holding constant the rate constants, for all other steps $m \neq i$ and the equilibrium constant. Note that keeping the equilibrium constant means that both k_i and k_{-i} (the backward rate constant of reaction *i*) must be varied by equal factors so that their ratio remains constant. The general rule explained by Stegelmann [Steg 2009] indicates that this variation should not exceed ±10.0 %. Fundamentally, equation (5) implies changing the transition state of elementary step i while nothing else is changed in the reaction mechanism and determining how this influences the overall rate.

As larger is the numeric value of $X_{RC,i}$ for a step *i*, bigger is the influence of its rate constant on the overall reaction rate r for a specific molecule. A positive value indicates that increasing k_i will increase the net rate r, and such steps are termed rate limiting steps. A negative value indicates the opposite, and such steps are termed inhibition steps.

The third tool for the reduction and analysis of detailed chemical mechanisms is the ***"sensivity analysis"***. Like the degree of rate control, Glarborg [Gla 1986] indicated that the sensitivity coefficients are normalized in the form of logarithmic derivatives, as the equation (6) shows.

$$S_{C,i} = \frac{k_i}{Y_j}\left(\frac{\partial Y_j}{\partial k_i}\right)_{k_{m\neq i}, K_{C_i}} = \left(\frac{\partial \ln Y_j}{\partial \ln k_i}\right)_{k_{m\neq i}, K_{C_i}} \quad \textbf{(6)}$$

Where:

$S_{C,i}$	is the sensitivity coefficients of reaction i, dimensionless.
Y_j	is the mass fraction of molecule *j*, dimensionless.

The sensitivity coefficients thus provide information about the rate limiting steps in the production and consumption of species. The sensitivity coefficients depend strongly on the reaction mechanism used and can only be interpreted in terms of it. Furthermore, the sensitivity analysis does not necessarily provide information about the actual pathways for production and destruction of species. Such information must be derived from the analysis of production rate.

3.7. Mathematical model for the computational simulations

The CFD simuation consists in solving all conservation equations for mass, momentum, and energy. For the species mixing and reactions, a species conservation equation is solved [Flu 2012 – 02]. In this section the conservation equations are presented for the laminar flow in an inertial (non – accelerating) reference frame.

3.7.1. The equation of mass conservation

The equation (7) or continuity equation, models the conservation of mass for compressible and incompressible flows. All the cases devoted to this investigation can be considered as incompressible flows [Flu 2012 – 02].

$$\frac{\partial \rho}{\partial t} + \nabla \cdot (\rho \vec{v}) = R_j \qquad \textbf{(7)}$$

Where:

ρ is the density, kg m^{-3}.

t is the time, s.

$\vec{v}$ is the velocity vector, m s^{-1}.

R_j is the net reaction rate of species *j*, kmol m^{-3} s^{-1}

The term $\left(\frac{\partial \rho}{\partial t}\right)$ refers to the change of the density during the process time and has effect on the results of non – stationary simulations.

Since multiple simultaneous chemical reactions can be modeled, with reactions occurring in the bulk phase (volumetric reactions) and/or on surfaces (catalytic reactions), it is necessary to define R_j [Flu 2012 – 02].

To solve the mass conservation equation for chemical species, it is necessary to predict the local mass fraction of each species (Y_j), through the solution of a convection – diffusion equation for the j_{th} species. The mass conservation takes general form described by equation (8). An equation of this form will be solved for $N_S - 1$ species where N_S is the total number of chemical species present in the system. Since the mass fraction of the species must sum to unity, the N_S mass fraction is determined as one minus the sum of the $N_S - 1$ solved mass fractions [Flu 2012 – 02].

$$\frac{\partial}{\partial t}(\rho Y_j) + \nabla \cdot (\rho \vec{v} Y_j) = -\nabla \cdot \vec{J}_j + R_j \qquad \textbf{(8)}$$

In equation (8), the diffusion flux of species $(\vec{J}_j)$ arises due to gradients of concentration and temperature. In this investigation, the use of Fick's law (dilute approximation) allows to model mass diffusion due to concentration gradients according to equation (9) [Flu 2012 – 02]:

$$\vec{J}_j = -\rho D_{j,m} \nabla Y_j - \rho D_{T,j} \frac{\nabla T}{T} \quad \textbf{(9)}$$

Where:

$D_{j,m}$ is the mass diffusion coeficients, $m^2\ s^{-1}$.

D_{T_n} is the thermal diffusion coefficient of species *n*, $m^2\ s^{-1}$.

T is the temperature, K.

For two dimensions, planar geometries like the cases of the catalytic square mesh (one or six parallel wires, to be shown in Section 6) or the planar channel reactor (one or six catalytic surfaces, to be shown in Section 8), the conservation of mass or continuity [equation (8)] is simplified to the equation (10) [Bir 2018]:

$$\frac{\partial}{\partial t}(\rho Y_j) + \frac{\partial}{\partial x}(\rho v_x Y_j) + \frac{\partial}{\partial y}(\rho v_y Y_j) = -\nabla \vec{J}_j + R_j \quad \textbf{(10)}$$

Where (v_i) is the velocity component in orthogonal coordinate *i*, $m\ s^{-1}$.

For two dimensional, axisymmetric geometries like the case of the stagnation point reactor, to be shown in Section 7, the conservation of mass or continuity [equation (8)] is simplified to the equation (11):

$$\frac{\partial}{\partial t}(\rho Y_j) + \frac{\partial}{\partial z}(\rho v_z Y_j) + \frac{\partial}{\partial r}(\rho v_r Y_j) + \frac{\rho v_r Y_j}{r} = -\nabla \vec{J}_j + R_j \quad \textbf{(11)}$$

The net reaction rate (R_j) that appear as source terms in equations (8), (10) and (11)are computed in this investigation by the laminar finite – rate model. In which the effect of turbulent fluctuations is ignored, and reaction rates are determined by Arrhenius kinetic expressions [Flu 2012 – 02], whose elementary reactions obey the law of mass action as default formulation [Chem 2015].

Consider elementary reversible (or irreversible) reactions involving *j* chemical species that can be represented in the general form of the equation (12):

$$\sum_{j=1}^{N_s} v'_{ji} \chi_j \leftrightarrow \sum_{j=1}^{N_s} v''_{ji} \chi_j \quad \textbf{(12)}$$

Where:

v'_{ji} is the stoichiometric coefficient of species *j* as reactive in reaction *i*, dimensionless.

v''_{ji} is the stoichiometric coefficient of species *j* as product in reaction *i*, dimensionless.

χ_j is the generical formula of chemical species *j*.

The reaction rate of the *j* chemical species is computed as the sum of the Arrhenius reaction sources over the N_R reactions that the species participate in, as equation (13) presents [Chem 2015]. The global stoichiometric coefficient (v_{ji}) is defined according to equation (14) [Chem 2015].

$$R_j = Mw_j \sum_{i=1}^{N_R} v_{ji} r_i \quad \textbf{(13)}$$

$$\upsilon_{ji} = \upsilon''_{ji} - \upsilon'_{ji} \quad \textbf{(14)}$$

Where (Mw_j) is the molecular weight of component *j*, kg kmol^{-1}.

The rate of reaction i (r_i) is given by the difference of the forward and reverse rates as equation (15) describes [Chem 2015]:

$$r_i = \left(\sum_{j=1}^{N_S} a_{ji} C_j\right)\left(k_i \sum_{j=1}^{N_S} C_j^{\upsilon'_{ji}} - k_{-i} \sum_{j=1}^{N_S} C_j^{\upsilon''_{ji}}\right) \quad \textbf{(15)}$$

Where:

a_{ji} is the factor of the effect of the species *j* in the reaction *i* as third body, m^3 kmol^{-1}.

C_j is the molar concentration of species *j*, kmol m^{-3}

As indicated in equation (15), the rate of reaction *i* is evaluated, by default, using the concentration of each reactant or product species raised to the power of its stoichiometric coefficient. The forward rate constants for the i reactions are generally assumed to have the modified Arrhenius temperature dependence indicated by equation (16) [Chem 2015]:

$$k_i = A_i T^{b_i} exp\left(\frac{-E_{A_i}}{RT}\right) \quad \textbf{(16)}$$

Where (R) is the universal constant of gases, 8.3143, kJ kmol^{-1} K^{-1}.

The three parameters of equation (16) are required as input to solve the model of the mass balance or continuity equation. They have been defined in Table 1 for the catalytic reactions and in Appendix I for the gas phase reactions. In thermal systems, the reverse rate constants (k_{-i}) in equation (15) are related to the forward rate constants through the equilibrium constants (K_{c_i}) according to equation (17) [Chem 2015]:

$$k_{-i} = \frac{k_i}{K_{c_i}} \quad \textbf{(17)}$$

Although (K_{c_i}) is given in concentration units, the equilibrium constants are more easily determined from the thermodynamic properties in pressure units; they are related by equation (18) [Chem 2015]:

$$K_{c_i} = K_{p_i}\left(\frac{P^0}{RT}\right)^{\sum_{j=1}^{N_S} \upsilon_{ji}} \quad \textbf{(18)}$$

The reference pressure (P^0) is 1.0 atm, and the equilibrium constants based on pressure (K_{p_i}) are obtained with the relationship indicated by equation (19) [Chem 2015]:

$$K_{p_i} = exp\left(\frac{\Delta S_i^o}{R} - \frac{\Delta H_i^o}{RT}\right) \quad \textbf{(19)}$$

The (Δ) refers to the change that occurs in passing completely from reactants to products in the i_{th} reaction; specifically, in cases of entrophy $\left(\Delta S_i^o/_R\right)$ and enthalpy $\left(\Delta H_i^o/_{RT}\right)$ according to equations (20) and (21) [Chem 2015]:

$$\frac{\Delta S_i^o}{R} = \sum_{j=1}^{N_S} v_{ji} \frac{S_j^0}{R} \quad \textbf{(20)}$$

$$\frac{\Delta H_i^o}{RT} = \sum_{j=1}^{N_S} v_{ji} \frac{H_j^0}{RT} \quad \textbf{(21)}$$

Where:

S_j^0 is the entrophy of species j, kJ kmol^{-1} K^{-1}.

H_j^0 is the enthalpy of species j, kJ kmol^{-1}.

The first factor $\left(\sum_{j=1}^{N_S} a_{ji}\, C_j\right)$ in equation (15) refers to the "third body" effect, wich is reflected in the chemical mechanism as "M". It is often the case in dissociation or recombination reactions to proceed. If all species in the mixture contribute equally as third bodies, then $a_{ji} = 1.0$ for each species, and the first factor is the total concentration of the mixture according to equation (22). However, it is often the case that some species act more efficiently as third bodies than others. The a_{ji} that differ from 1.0 must be specified by auxiliary input to the model [Chem 2015].

$$C = \sum_{j=1}^{N_S} C_j \quad \textbf{(22)}$$

Where (C) is the molar concentration of species in the gas phase, kmol m^{-3}.

Under certain conditions, some reaction rate expressions depend on pressure as well as temperature. This is the case of the unimolecular / recombination fall – off reactions, in which the reaction rate increases with increasing pressure. There are several methods of representing the rate expressions in this fall – off region. The simplest one is due to Lindemann. The parameters of the Arrhenius model are required for both the high – and low – pressure limiting cases, and the Lindemann form for the rate coefficient relates them in a pressure dependent rate expression. It is necessary to define parameter for both high – pressure limit (k_∞) and the low – pressure limit (k_0). The relationship between the actual forward rate constant (k_i) and the high and low – pressure constants is gived by equations (23). The definition of the rate constant for the high and low – pressure limits obey the form of Arrhenius expressions as was indicated in equation (16) [Chem 2015].

$$k_i = \frac{k_\infty k_0 C}{k_\infty + k_0 C} F \quad \textbf{(23)}$$

The fall of reaction parameter (F) in equation (23) have been defined by Troe [Gil 1983] by the use of equations between (24) and (28) [Chem 2015]:

$$lg(F) = \left\{1 + \left[\frac{lg(P_r) + c_f}{n_f - 0.14 \cdot [lg(P_r) + C_f]}\right]^2\right\}^{-1} lg(F_c) \quad \textbf{(24)}$$

$$P_r = \frac{k_0}{k_\infty} C \quad \textbf{(25)}$$

$$c_f = -0.4 - 0.67 \cdot lg(F_c) \quad \textbf{(26)}$$

$$n_f = 0.75 - 1.27 \cdot lg(F_c) \quad \textbf{(27)}$$

$$F_c = (1 - \alpha_f) \cdot exp\left(-\frac{T}{T_{f1}}\right) + \alpha_f \cdot exp\left(-\frac{T}{T_{f2}}\right) + exp\left(-\frac{T_{f3}}{T}\right) \quad \textbf{(28)}$$

Where:

P_r is the fall of parameter related to pressure limited parameters, kmol m^{-3}.

c_f is a temperature dependent fall – of parameter.

n_f is a temperature dependent fall – of parameter.

The four parameters of equation (28) $(\alpha_f,\ T_{f1},\ T_{f2},\ T_{f3})$ are required as input to solve the model of the mass balance or continuity equation.

3.7.2. Equations of momentum conservation

Conservation of momentum in an inertial (non – accelerating) reference frame is described by equation (29) [Flu 2012 – 02]:

$$\frac{\partial}{\partial t}(\rho\vec{v}) + \nabla \cdot (\rho\vec{v}\vec{v}) = -\nabla P + \nabla \cdot (\bar{\bar{\tau}}) + \rho\vec{g} + \vec{F} \quad \textbf{(29)}$$

Where:

P is the pressure, bar.

$\bar{\bar{\tau}}$ is the stress tensor, kg m s^{-2}.

$\vec{g}$ is gravity vector, m s^{-2}.

In equation (29) the terms $(\rho\vec{g})$ and $(\vec{F})$ are the gravitational body force and external body forces (source terms in the equation). Since those effects are not considered during this investigation, those terms are neglegted and lead to the equation (30):

$$\frac{\partial}{\partial t}(\rho\vec{v}) + \nabla \cdot (\rho\vec{v}\vec{v}) = -\nabla P + \nabla \cdot (\bar{\bar{\tau}}) \quad \textbf{(30)}$$

The term $\left[\frac{\partial}{\partial t}(\rho\vec{v})\right]$ refers to the effect of the changes of the density in the motion of the fluid during the process time and is taked into account to conduct non – stationary simulations. The stress tensor is defined according to the equation (31) [Flu 2012 – 02]:

$$\bar{\bar{\tau}} = \mu_M \left[(\nabla\vec{v} + (\nabla\vec{v})^T) - \frac{2}{3}\nabla \cdot \vec{v}\bar{\bar{I}}\right] \quad \textbf{(31)}$$

Where:

μ_M is the dinamic viscosity of the mixture of gases, Pa s.

$\bar{\bar{I}}$ is the unity tensor, kg m s^{-2}.

T denotes the transposition of vector $(\nabla\vec{v})$.

In the equation (31) the term $[(\nabla\vec{v})^T]$ reflects the effect of the volume dilation [Flu 2012 – 02].

For two dimensions, planar geometries like the cases of the catalytic square mesh (one or six parallel wires, to be shown in Section 6) or the planar channel reactor (one or six catalytic surfaces, to be shown in Section 8), the conservation of momentum [equation (30)] in these kind of computational domain is simplified to its components according to the equations (32) and (33). In the x – and y – axis components of momentum conservation, equations (32) and (33), the effects of the stress tensor are defined by equations (34) and (35) respectively [Bir 2018]:

x – axis component: $$\frac{\partial}{\partial t}(\rho v_x) + \frac{\partial}{\partial x}(\rho v_x v_x) + \frac{\partial}{\partial y}(\rho v_x v_y) = -\frac{\partial P}{\partial x} + \nabla\cdot(\bar{\bar{\tau}}) \quad \textbf{(32)}$$

y – axis component: $$\frac{\partial}{\partial t}(\rho v_y) + \frac{\partial}{\partial x}(v_x v_y) + \frac{\partial}{\partial y}(v_y v_y) = -\frac{\partial P}{\partial r} + \nabla\cdot(\bar{\bar{\tau}}) \quad \textbf{(33)}$$

x – axis component: $$\nabla\cdot(\bar{\bar{\tau}}) = \frac{\partial \tau_{xx}}{\partial x} + \frac{\partial \tau_{yx}}{\partial y} \quad \textbf{(34)}$$

y – axis component: $$\nabla\cdot(\bar{\bar{\tau}}) = \frac{\partial \tau_{xy}}{\partial x} + \frac{\partial \tau_{yy}}{\partial y} \quad \textbf{(35)}$$

Where (τ_{ij}) is the stress tensor component in orthogonal coordinate, kg m^{-1} s^{-2}.

The derivatives of the effects of the stress tensor in the equations (34) and (35) are defined between the equations (36) and (39) respectively [Bir 2018]:

$$\frac{\partial \tau_{xx}}{\partial x} = -\left(\frac{4}{3}\mu + \kappa\right)\frac{\partial^2 v_x}{\partial x^2} - \left(\frac{4}{3}\frac{\partial \mu}{\partial x} + \frac{\partial \kappa}{\partial x}\right)\frac{\partial v_x}{\partial x} + \left(\frac{2}{3}\mu - \kappa\right)\frac{\partial^2 v_y}{\partial x \partial y} + \left(\frac{2}{3}\frac{\partial \mu}{\partial x} - \frac{\partial \kappa}{\partial x}\right)\frac{\partial v_y}{\partial y} \quad \textbf{(36)}$$

$$\frac{\partial \tau_{yx}}{\partial y} = -\mu\left(\frac{\partial^2 v_x}{\partial y \partial x} + \frac{\partial^2 v_y}{\partial y^2}\right) - \frac{\partial \mu}{\partial y}\left(\frac{\partial v_y}{\partial x} + \frac{\partial v_x}{\partial y}\right) \quad \textbf{(37)}$$

$$\frac{\partial \tau_{xy}}{\partial x} = -\mu\left(\frac{\partial^2 v_x}{\partial x \partial y} + \frac{\partial^2 v_y}{\partial x^2}\right) - \frac{\partial \mu}{\partial x}\left(\frac{\partial v_y}{\partial x} + \frac{\partial v_x}{\partial y}\right) \quad \textbf{(38)}$$

$$\frac{\partial \tau_{yy}}{\partial y} = -\left(\frac{4}{3}\mu + \kappa\right)\frac{\partial^2 v_y}{\partial y^2} - \left(\frac{4}{3}\frac{\partial \mu}{\partial y} + \frac{\partial \kappa}{\partial y}\right)\frac{\partial v_y}{\partial y} + \left(\frac{2}{3}\mu - \kappa\right)\frac{\partial^2 v_x}{\partial y \partial x} + \left(\frac{2}{3}\frac{\partial \mu}{\partial y} - \frac{\partial \kappa}{\partial y}\right)\frac{\partial v_x}{\partial x} \quad \textbf{(39)}$$

For two dimensional, axisymmetric geometries like the case of the stagnation point reactor, the conservation of momentum [equation (30)] is simplified to its components according to the equations (40) and (41). In the axial and radial components of momentum conservation, the effects of the stress tensor are defined by equations (42) and (43) respectively. In both cases the term $(\nabla\cdot\vec{v})$ is defined by equation (44) [Flu 2012 – 02]:

Axial component: $$\frac{\partial}{\partial t}(\rho v_z) + \frac{1}{r}\left[\frac{\partial}{\partial z}(r\rho v_z v_z) + \frac{\partial}{\partial r}(r\rho v_r v_z)\right] = -\frac{\partial P}{\partial z} + \nabla\cdot(\bar{\bar{\tau}}) \quad \textbf{(40)}$$

Radial component: $$\frac{\partial}{\partial t}(\rho v_r) + \frac{1}{r}\left[\frac{\partial}{\partial z}(r\rho v_z v_r) + \frac{\partial}{\partial r}(r\rho v_r v_r)\right] = -\frac{\partial P}{\partial r} + \nabla \cdot (\bar{\bar{\tau}}) \quad \textbf{(41)}$$

Axial component: $$\nabla \cdot (\bar{\bar{\tau}}) = \frac{1}{r}\frac{\partial}{\partial z}\left[r\mu_M\left(2\frac{\partial v_z}{\partial z} - \frac{2}{3}(\nabla \cdot \vec{v})\right)\right] + \frac{1}{r}\frac{\partial}{\partial r}\left[r\mu_M\left(\frac{\partial v_z}{\partial r} + \frac{\partial v_r}{\partial z}\right)\right] \quad \textbf{(42)}$$

Radial component: $$\nabla \cdot (\bar{\bar{\tau}}) = \frac{1}{r}\frac{\partial}{\partial z}\left[r\mu_M\left(\frac{\partial v_r}{\partial z} + \frac{\partial v_x}{\partial r}\right)\right] + \frac{1}{r}\frac{\partial}{\partial r}\left[r\mu_M\left(2\frac{\partial v_r}{\partial r} - \frac{2}{3}(\nabla \cdot \vec{v})\right)\right] - 2\mu_M\frac{v_r}{r^2} + \frac{2}{3}\frac{\mu}{r}(\nabla \cdot \vec{v}) + \rho\frac{v_z^2}{r} \quad \textbf{(43)}$$

$$\nabla \cdot \vec{v} = \frac{\partial v_z}{\partial z} + \frac{\partial v_r}{\partial r} + \frac{v_r}{r} \quad \textbf{(44)}$$

3.7.3. Equations of energy conservation

Conservation of energy is described by equation (45) [Flu 2012 – 02]:

$$\frac{\partial}{\partial t}(\rho E) + \nabla \cdot [\vec{v}(\rho E + P)] = \nabla \cdot \left[k_M \nabla T - \sum_j h_j \vec{J}_j + (\bar{\bar{\tau}} \cdot \vec{v})\right] + S_h \quad \textbf{(45)}$$

Where:

E is the total energy, J.

k_M is the thermal conductivity of mixture of gases, W m^{-1} K^{-1}.

h_j is the sensible enthalpy of component *j*, J.

$\vec{J}_j$ is the diffusion flux of species *j*, kg m^{-2} s^{-1}.

S_h is the energy (heat) source due to chemical reactions, kW m^{-2}.

The term $\left[\frac{\partial}{\partial t}(\rho E)\right]$ refers to the effect of the changes of the total energy during the process time and is taked into account to conduct non – stationary simulations. The total energy is defined according to equation (46). The enthalpy due to sensible heat of a mixture of ideal gases is defined according to equation (47) [Flu 2012 – 02].

$$E = h_M - \frac{P}{\rho} + \frac{v_0^2}{2} \quad \textbf{(46)}$$

Where:

h_M is the enthalpy due to sensible heat of mixture of gases, J.

v_0 is the magnitude of the velocity, J.

$$h_M = \sum_{j=1}^{N_S} Y_j \cdot \int_{T_{ref}}^{T_f} C_{P_j}\, dT \quad \textbf{(47)}$$

Where:

T_{ref} is the reference temperature, 298.15 K.

T_f is the bulk temperature in the fluid, K.

C_{P_j} is the heat capacity at constant pressure of species *j*, kJ kmol^{-1} K^{-1}.

In equation (45) the source term (S_h) is the source of energy due to chemical reactions, eighter superficial or gas phase ones. It is defined by the equation (48) [Flu 2012 – 02]. It is important to indicate that along this investigation the source effects for the energy devoted to radiation processes are not included.

$$S_h = -\sum_{j=1}^{N_S} \frac{H_j^0}{Mw_j} R_j \qquad \textbf{(48)}$$

In equation (45) the term $\left(\nabla \cdot \sum_j h_j \vec{J}_j\right)$ corresponds to the transport of enthalpy due to species diffusion. This phenomenon can have a significant effect on the enthalpy field and should not be neglected. According to the equation (49), when the dimensionless Lewis number (Le) for any species is far from unity, neglecting this term can lead to significant error [Wal 1927] [Flu 2012 – 02]. In fact, since the order of magnitude of thermal conductivity, density, heat capacity and diffusivities are respectively: 10^{-2}, 10^{-1}, 10^{3} and 10^{5}, the Lewis number could have values even to 2.0, it means that the transport of enthalpy due to species diffusion must not be neglegted.

$$\mathrm{Le} = \frac{k_M}{\rho C_{P_M} D_{nj}} \qquad \textbf{(49)}$$

Where:

C_{P_M} is the heat capacity at constant pressure of mixture of gases, kJ kmol^{-1} K^{-1}.

T_f is the bulk temperature in the fluid, K.

D_{nj} is the mass diffusion coeficients, m^2 s^{-1}.

The term $(\bar{\bar{\tau}} \cdot \vec{v})$ in equation (45) refers to the viscous dissipation of the energy [Bir 2018]. The dimensionless Brinkman number (Br), according to the equation (50) gives account of the importance of the viscous dissipation term [Bri 1951] [Bir 2018]. Since the order of magnitude of the dynamic viscosity, flow velocity, thermal conductivity and temperature difference are respectively: 10^{-5}, 10^{0}, 10^{-2} and 10^{2}, the Brinkman number has an order of magnitude of 10^{-5}, it means that the flux of heat transported by molecular conduccion is largely higher than the heat produced by viscous dissipation in the models of this investigation and the viscous dissipation term can be neglegted.

$$\mathrm{Br} = \frac{\mu_M v_0^2}{k_M (T_w - T)} \qquad \textbf{(50)}$$

Where (T_w) is the temperature in the wall, K.

3.7.4. Thermodynamic and transport properties

To carry out simulations it is necessary to set the parameters for the calculation of thermodynamic and transport properties of the gas phase species. Since the reactions describe interactions of gas phase species. Each species in a reaction must be associated with thermodynamic data. The thermodynamic data are used to calculate equilibrium constants and reverse rate coefficients for a reaction [Chem 2015].

The model for the properties is based on previously described and used by Chemkin developers. The adjustment of properties has seven coefficients for each temperature range. It is important to note that the coefficients are presented in descending order for different temperature ranges, i.e., starting with

upper and ending in the lower range [Chem 2015]. The model for the thermodynamic properties corresponds to the equations between (51) and (53). For the species considered in this investigation, the value of coefficients (a_{6j}) and (a_{7j}) is equal to zero. The value for the rest of coefficients is in Appendix 4.

$$\frac{C_{P\,j}^{o}}{R} = a_{1\,j} + a_{2\,j} \cdot T + a_{3\,j} \cdot T^2 + a_{4\,j} \cdot T^3 + a_{5\,j} \cdot T^4 \quad \textbf{(51)}$$

$$\frac{H_j^o}{RT} = a_{1\,j} + \frac{a_{2\,j}}{2} \cdot T + \frac{a_{3\,j}}{3} \cdot T^2 + \frac{a_{4\,j}}{4} \cdot T^3 + \frac{a_{5\,j}}{5} \cdot T^4 + \frac{a_{6\,j}}{T} \quad \textbf{(52)}$$

$$\frac{S_j^o}{R} = a_{1\,j} \cdot Ln(T) + a_{2\,j} \cdot T + \frac{a_{3\,j}}{2} \cdot T^2 + \frac{a_{4\,j}}{3} \cdot T^3 + \frac{a_{5\,j}}{4} \cdot T^4 + a_{7\,j} \quad \textbf{(53)}$$

To model of the transport equations, it is necessary to define the called transport properties, which are defined as follows. The simulations devoted to this investigation was modeled with the use of the **dynamic viscosity** calculated from the kinetic theory according to the equation (54). The collision integral for dynamic viscosity $\left(\Omega_{\mu_j}\right)$ is defined by the equation (55). The dimensionless temperature $\left(T_j^*\right)$ is calculated according to equation (56) [Flu 2012 – 02] [Bir 2018]:

$$\mu_j = 2.67 \times 10^{-6} \frac{\sqrt{Mw_j\, T}}{\sigma_j^2 \Omega_{\mu_j}} \quad \textbf{(54)}$$

$$\Omega_{\mu_j} = \frac{1.16145}{T_j^{*\,0.14874}} + \frac{0.52487}{exp\left(0.77320 \cdot T_j^*\right)} + \frac{2.16178}{exp\left(2.43787 \cdot T_j^*\right)} \quad \textbf{(55)}$$

$$T_j^* = \frac{T}{{\varepsilon_j}/{k_B}} \quad \textbf{(56)}$$

Where:

μ_j is the dynamic viscosity of species *j*, Pa s.

σ_j is the Lennard – Jones parameter based on the species size, Å.

Ω_{μ_j} is the collision integral for the dynamic viscosity of species *j*, $m^2\ s^{-1}$.

T_j^* is the dimensionless temperature for calculation of transport properties.

${\varepsilon_j}/{k_B}$ Is the Lennard – Jones parameter based on the species vibration mode, K.

In the determination of viscositity based on equation (54), the required Lennard – Jones parameters (σ_j) and $\left({\varepsilon_j}/{k_B}\right)$ are listed in Appendix 5 [Boy 2005] [Rud 1996] [Clo 2000]. To compute the dynamic viscosity of the mixture, based on kinetic theory, the equation (57) is applied. Where the interaction parameter (ϕ_{nj}) is defined according to equation (58) [Flu 2012 – 02]:

$$\mu_M = \sum_{n=1}^{N_s} \frac{x_n^f \mu_n}{\sum_{j=1}^{N_s} x_j^f \phi_{nj}} \quad \textbf{(57)}$$

Where $\left(x_j^f\right)$ is the molar fraction of species *j* in the fluid, dimensionless.

$$\phi_{nj} = \frac{\left[1 + \left(\frac{\mu_n}{\mu_j}\right)^{1/2} \left(\frac{Mw_j}{Mw_n}\right)^{1/4}\right]^2}{\left[8\left(1 + \frac{Mw_n}{Mw_j}\right)\right]^{1/2}} \quad \textbf{(58)}$$

The simulations devoted to this investigation was modeled with the use of the **thermal conductivity** (k_j) calculated from the kinetic theory according to the equation (59). Equivalent to the dynamic viscosity of the mixture, to compute the thermal capacity of the mixture, based on kinetic theory, the equation (60) is applied. Where the interaction parameter (ϕ_{nj}) is defined according to equation (58) [Flu 2012 – 02]:

$$k_j = \frac{15}{4}\frac{R}{Mw_j}\mu_j\left[\frac{4}{15}\frac{C_{P_j}Mw_j}{R} + \frac{1}{3}\right] \quad \textbf{(59)}$$

$$k_M = \sum_{n=1}^{N_s} \frac{x_n^f k_n}{\sum_{j=1}^{N_s} x_j^f \phi_{nj}} \quad \textbf{(60)}$$

A careful treatment of chemical species diffusion in the species transport and energy equations is important when details of the molecular transport processes are significant for example in laminar flow – based processes [Flu 2012 – 02].

For multicomponent systems it is not possible, in general, to derive relations for the diffusion fluxes containing the gradient of only one component. Here, the Maxwell – Stefan equations will be used to obtain the diffusive mass flux. This will lead to the definition of generalized diffusion coefficients of the Fick's law. This method is preferred over computing the multicomponent diffusion coefficients since their evaluation requires the computation of (N_S^2) cofactor determinants of size $(N_S - 1) \times (N_S - 1)$, and one determinant of size $N_S \times N_S$. The Maxwell – Stefan equations can be written as equation (61) shows. Where, for an ideal gas the Maxwell diffusion coefficients are equal to the binary diffusion coefficients, the external force is assumed to be the same on all species and the pressure diffusion is negligible, then $(\overline{d_J} = \nabla X_j)$. Considering that the diffusive mass flux vector is $(\overrightarrow{J_J} = \rho_j \overrightarrow{V_j})$ [Flu 2012 – 02].

$$\sum_{\substack{j=1 \\ j \neq n}}^{N_S} \frac{x_n^f x_j^f}{D_{nj}}\left(\frac{\overrightarrow{J_J}}{\rho_j} - \frac{\overrightarrow{J_n}}{\rho_n}\right) = \nabla x_n^f \quad \textbf{(61)}$$

Where (D_{T_n}) is the thermal diffusion coefficient of species *n*, $m^2\ s^{-1}$.

After some mathematical manipulations, the diffusive mass flux vector, $\vec{J}_n$, can be obtained from equation (62) [Flu 2012 – 02]:

$$\vec{J}_n = -\sum_{j=1}^{N_S - 1} \rho D_{nj} \nabla Y_j \quad \textbf{(62)}$$

Where the different terms are defined according to the equations between the (63) and (68) [Flu 2012 – 02]:

$$D_{nj} = [D] = [A]^{-1}[B] \quad \textbf{(63)}$$

$$Mw_M = \sum_{j=1}^{N_S} \frac{Y_j}{Mw_j} \quad \textbf{(64)}$$

$$A_{nn} = -\left[\frac{x_n^f}{D_{nN_S}}\frac{Mw_M}{Mw_{N_S}} + \sum_{\substack{j=1 \\ j\neq n}}^{N_S} \frac{x_j^f}{D_{nj}}\frac{Mw_M}{Mw_n}\right] \quad \textbf{(65)}$$

$$A_{nj} = x_n^f\left[\frac{1}{D_{nj}}\frac{Mw_M}{Mw_j} - \frac{1}{D_{nN_S}}\frac{Mw_M}{Mw_{N_S}}\right] \quad \textbf{(66)}$$

$$B_{nn} = -\left[x_n^f\frac{Mw_M}{Mw_{N_S}} + \left(1 + x_n^f\right)\frac{Mw_M}{Mw_n}\right] \quad \textbf{(67)}$$

$$B_{nj} = x_n^f\left[\frac{Mw_M}{Mw_j} - \frac{Mw_M}{Mw_{N_S}}\right] \quad \textbf{(68)}$$

Where:

$[D]$ is the matrix of the generalized coefficients of the Fick's law, $m^2\ s^{-1}$.

A_{nn} are the terms (*nn*) of the matrix *A* for the calculation of D_{nj}

A_{nj} are the terms (*nj*) of the matrix *A* for the calculation of D_{nj}

B_{nn} are the terms (*nn*) of the matrix *B* for the calculation of D_{nj}

B_{nj} are the terms (*nj*) of the matrix *B* for the calculation of D_{nj}

The simulations devoted to this investigation was modeled with the use of the **mass diffusion coefficients** calculated from the kinetic theory according to the equation (69). The collision integral for diffusion coefficients (Ω_D) is defined by the equation (70). The dimensionless temperature $\left(T_{nj}^*\right)$ is calculated according to equation (71). [Flu 2012 – 02] [Bir 2018]:

$$D_{nj} = 0.00188\frac{\left[T^3\left(\frac{1}{Mw_n} + \frac{1}{Mw_j}\right)\right]^{1/2}}{P\sigma_{nj}^2\Omega_D} \quad \textbf{(69)}$$

$$\Omega_D = \frac{1.06036}{T_{nj}^{*\,0.15610}} + \frac{0.193}{exp\left(0.47635\cdot T_{nj}^*\right)} + \frac{1.03587}{exp\left(1.52996\cdot T_{nj}^*\right)} + \frac{1.76474}{exp\left(3.89411\cdot T_{nj}^*\right)} \quad \textbf{(70)}$$

$$T_{nj}^* = \frac{T}{\left[\varepsilon/k_B\right]_{nj}} \quad \textbf{(71)}$$

The case of the binary Lennard – Jones parameters is such as: (σ_{nj}) is calculated as the arithmetic average of the individual (σ_j), $\left(\left[\varepsilon/k_B\right]_{nj}\right)$ is calculated as the geometric average of the individual $\left(\varepsilon_j/k_B\right)$. The required Lennard – Jones parameters (σ_j) and $\left(\varepsilon_j/k_B\right)$ for each species are listed in Appendix 5 [Boy 2005] [Rud 1996] [Clo 2000].

3.7.5. Boundary conditions

The mathematicl model of the boundary conditions, which have been used in the models of this investigation are described as follows.

An **inlet mass flow** refers to a fixed mass flow ($\dot{m}$) is defined for an inlet boundary, the definition in this part of the domain obeys to the equation (72) [Com 2020]. Since the density must be calculated, it is required to specify the inlet conditions of temperature, pressure, and composition.

$$\dot{m} = -\int_{\partial\Omega} \rho(\vec{v} \cdot \vec{n}) dS \quad \textbf{(72)}$$

Where:

$\vec{n}$ is the normal vector to surface, dimensionless.

dS is the differencial of surface, m^2.

The **inlet velocity** as boundary condition refers to a fixed magnitude of velocity (v_0) defined for an inlet boundary, the definition in this part of the domain obeys to the equation (73) [Com 2020]. From the velocity vector ($\vec{v}$) the mass flow is calculated according to equation (72), for that it is required to specify the inlet conditions of temperature, pressure, and composition as well.

$$\vec{v} = v_0 \vec{n} \quad \textbf{(73)}$$

When **a wall is considered as closed boundary** thorough which there is no flow and meets the non displacement condition, the velocity vector simply takes the null value ($\vec{v} = 0$). The no flow condition applies for all transport enties $(\vec{S})$ as momentum, energy, or mass according to equation (74) [Com 2020]:

$$-\vec{n} \cdot \vec{S} = 0 \quad \textbf{(74)}$$

When a **fixed temperature condition** is applied at the wall, the heat flux to the wall from a fluid cell without radiation is computed according to equation (75). The heat transfer coefficient in the fluid – side (h_f) is computed based on the local flow – field conditions (temperature and velocity profiles), using Fourier's law applied at the walls, as described by equation (76) [Flu 2012 – 02]:

$$\dot{Q}_w = h_f(T_w - T_f) \quad \textbf{(75)}$$

$$\dot{Q}_w = h_f \left.\frac{\partial T}{\partial n}\right|_{wall} \quad \textbf{(76)}$$

Where $(\dot{Q}_w)$ is the heat flux to the wall from a fluid, kW m^{-2}.

When a **fixed composition condition** for a species *j* is applied at the wall, the mass flux from the wall to a fluid cell is computed according to equation (77). The mass transfer coefficient in the fluid – side $\left(k_{m_j}\right)$ is computed based on the local flow – field conditions (temperature, composition, and velocity profiles), using Fick's law applied at the walls, as described by equation (78) [Flu 2012 – 02]:

$$\dot{M}_j^w = k_{m_j}\left(x_j^w - x_j^f\right) \quad \textbf{(77)}$$

$$\dot{M}_j^w = k_{m_j} \left. \frac{\partial x_j}{\partial n} \right|_{wall} \quad \textbf{(78)}$$

Where:

$\dot{M}_j^w$ is the mass flux of species *j* at boundary *w*, kg m^{-3} s^{-1}.

x_j^w is the molar fraction of species *j* at boundary *w*, dimensionless.

The definition of the **pressure outlet** condition specifies the normal stress, which in most cases is approximately equal to the pressure. The tangential stress component is set to zero. The software was configured and used in such a way that the value of the pressure (p_0), at the boundary, is the absolute pressure. This boundary condition obeys the equation (79):

$$\left[-P\bar{\bar{I}} + \mu_M(\nabla\vec{v} + (\nabla\vec{v})^T)\right]\vec{n} = -p_0\vec{n} \quad \textbf{(79)}$$

The **symmetry boundary condition** prescribes no penetration and vanishing shear stresses. The boundary condition is a combination of a Dirichlet condition and a Neumann condition according to equations between (80) and (83) [Com 2020]:

Dirichlet conditions:

$$\vec{v} \cdot \vec{n} = 0 \quad \textbf{(80)}$$

$$\left(-P\bar{\bar{I}} + \bar{\bar{\tau}}\right)\vec{n} = 0 \quad \textbf{(81)}$$

Neumann conditions:

$$\vec{v} \cdot \vec{n} = 0 \quad \textbf{(82)}$$

$$\left[-P\bar{\bar{I}} + \mu(\nabla\vec{v} + (\nabla\vec{v})^T)\right]\vec{n} = 0 \quad \textbf{(83)}$$

For the special case of the one – dimensional simulation, to be shown in Section 7, CANTERA [Goo 2017] models the problem by computing the stagnation streamline for the radius $r = 0$. The equations used are (84) for continuity, (85) for radial momentum, (86) for energy and (87) for species. These four equations are the similarity equations for the flow in a finite – height gap of infinite radial extent. The scaled radial velocity (V) is defined according to the equation (88):

$$\frac{\partial \rho v_z}{\partial z} + 2\rho V = 0 \quad \textbf{(84)}$$

$$\rho v_z \frac{\partial V}{\partial z} + \rho V^2 = -\Lambda + \frac{\partial}{\partial z}\left(\mu \frac{\partial V}{\partial z}\right) \quad \textbf{(85)}$$

$$\rho C_P v_z \frac{\partial T}{\partial z} = \frac{\partial}{\partial z}\left(k_M \frac{\partial T}{\partial z}\right) - \sum_{j=1}^{N_S} \vec{J}_j C_{P_j} \frac{\partial T}{\partial z} - \sum_{j=1}^{N_S} h_j M w_j R_j \quad \textbf{(86)}$$

$$\rho v_z \frac{\partial Y_j}{\partial z} = -\frac{\partial \vec{J}_j}{\partial z} + M w_j R_j \quad \textbf{(87)}$$

$$\mathrm{V} = \frac{v_r}{r} \quad \textbf{(88)}$$

Where (V) is the scaled radial velocity, s^{-1}.

The pressure eigenvalue (Λ) equals the pressure curvature independent of z and is defined according to the equation (89). For this kind of discretized problem, it is acceptable that $\left(\frac{d\Lambda}{dz} = 0\right)$.

$$\Lambda = \frac{1}{r}\frac{\partial P}{\partial r} \tag{89}$$

To define the diffusive fluxes $(\vec{J}_j)$, CANTERA [Goo 2017] offers a mixture averaged model according to equation (90):

$$\vec{J}_j = -\rho \frac{Mw_j}{Mw_M} D_{jn} \frac{\partial x_j}{\partial z} \tag{90}$$

For the calculation of the diffusive fluxes, CANTERA [Goo 2017] offers a multicomponent formulation as well based on equation (62), which considers the thermal diffusion. However, this term is very small for hevier species and generall affects only light species such as H_2. Because of this, iti is often not worth the additional computational effort and will also not be used in the CANTERA [Goo 2017] simulations.

3.7.6. Parameters to describe the performance of the chemical reactions

The **NH_3 consumption** (X_{NH_3}) defines porcentualy, how much NH_3 have been consumed during the progress of the reaction. When the reactor is constituded for several catalytic surfaces (CS), it is possible to define the NH_3 consumption for each catalytic surface or accumulated throughout the reactor. Those two cases are defined by equations (91) and (92) respectively:

$$X_{NH_3}\Big|_{CS_i}^{local} = 100 \cdot \frac{\dot{m}_{NH_3}^{inlet}\big|_{CS_{i-1}} - \dot{m}_{NH_3}^{outlet}\big|_{CS_i}}{\dot{m}_{NH_3}^{inlet}\big|_{CS_{i-1}}} \tag{91}$$

$$X_{NH_3}\Big|_{CS_i}^{global} = 100 \cdot \frac{\dot{m}_{NH_3}^{inlet} - \dot{m}_{NH_3}^{outlet}\big|_{CS_i}}{\dot{m}_{NH_3}^{inlet}} \tag{92}$$

Where the subscript (CS) refers to the catalytic surface and (i) refers to the counting of the catalytic surface, particulary when $(i = 1 \rightarrow CS_{i-1} = CS_0)$ it is the inlet condition.

The **NO selectivity** (S_{NO}) defines porcentualy, how much NH_3 is consumed to form NO during the progress of the reaction. When the reactor is constituded for several catalytic surfaces (CS), it is possible to define the NO selectivity for each catalytic surface or accumulated throughout the reactor. Those two cases are defined by equations (93) and (94) respectively:

$$S_{NO}\Big|_{CS_i}^{local} = 100 \cdot \frac{x_{NO}^{outlet}\big|_{CS_i} - x_{NO}^{inlet}\big|_{CS_{i-1}}}{x_{NH_3}^{inlet}\Big|_{CS_{i-1}} - x_{NH_3}^{outlet}\Big|_{CS_i}} \cdot \frac{Mw_{NH_3}}{Mw_{NO}} \tag{93}$$

$$S_{NO}\Big|_{CS_i}^{global} = 100 \cdot \frac{x_{NO}^{outlet}\big|_{CS_i}}{x_{NH_3}^{inlet} - x_{NH_3}^{outlet}\Big|_{CS_i}} \cdot \frac{Mw_{NH_3}}{Mw_{NO}} \tag{94}$$

The **N_2O selectivity** (S_{N_2O}) defines porcentualy, how much NH_3 is consumed to form N_2O during the progress of the reaction. When the reactor is constituded for several catalytic surfaces (CS), it is possible to define the N_2O selectivity for each catalytic surface or accumulated throughout the reactor. Those two cases are defined by equations (95) and (96) respectively:

$$S_{N_2O}\Big|_{CS_i}^{local} = 100 \cdot 2 \cdot \frac{x_{N_2O}^{outlet}\Big|_{CS_i} - x_{N_2O}^{inlet}\Big|_{CS_{i-1}}}{x_{NH_3}^{inlet}\Big|_{CS_{i-1}} - x_{NH_3}^{outlet}\Big|_{CS_i}} \cdot \frac{Mw_{NH_3}}{Mw_{N_2O}} \quad \textbf{(95)}$$

$$S_{N_2O}\Big|_{CS_i}^{global} = 100 \cdot 2 \cdot \frac{x_{N_2O}^{outlet}\Big|_{CS_i}}{x_{NH_3}^{inlet} - x_{NH_3}^{outlet}\Big|_{CS_i}} \cdot \frac{Mw_{NH_3}}{Mw_{N_2O}} \quad \textbf{(96)}$$

The **N_2 selectivity** (S_{N_2}) defines porcentualy, how much NH_3 is consumed to form N_2 during the progress of the reaction. When the reactor is constituded for several catalytic surfaces (CS), it is possible to define the N_2 selectivity for each catalytic surface or accumulated throughout the reactor. Those two cases are defined by equations (97) and (98) respectively:

$$S_{N_2}\Big|_{CS_i}^{local} = 100 \cdot 2 \cdot \frac{x_{N_2}^{outlet}\Big|_{CS_i} - x_{N_2}^{inlet}\Big|_{CS_{i-1}}}{x_{NH_3}^{inlet}\Big|_{CS_{i-1}} - x_{NH_3}^{outlet}\Big|_{CS_i}} \cdot \frac{Mw_{NH_3}}{Mw_{N_2}} \quad \textbf{(97)}$$

$$S_{N_2}\Big|_{CS_i}^{global} = 100 \cdot 2 \cdot \frac{x_{N_2}^{outlet}\Big|_{CS_i}}{x_{NH_3}^{inlet} - x_{NH_3}^{outlet}\Big|_{CS_i}} \cdot \frac{Mw_{NH_3}}{Mw_{N_2}} \quad \textbf{(98)}$$

Between the equations (93) and (98) the subscript (CS) refers to the catalytic surface and (i) refers to the counting of the catalytic surface, particulary when $(i = 1 \rightarrow CS_{i-1} = CS_0)$ it is the inlet condition. The referred compositions (x_j) are ~~molar~~ mass fractions defined according to (99):

$$x_j = \frac{\dot{m}_j}{\dot{m}_T} \quad \textbf{(99)}$$

To analyse the results of the CFD simulations, the **net reaction rate** for a single catalytic surface is calculated by equation (100), and according to equation (101) when the reactor is composed bz several catalytic surfaces:

$$R_j\Big|_{CS_i}^{local} = \frac{\dot{m}_j^{outlet}\Big|_{CS_i} - \dot{m}_j^{inlet}\Big|_{CS_{i-1}}}{V^{CS_i}} \quad \textbf{(100)}$$

$$R_j\Big|_{CS_i}^{global} = \frac{\dot{m}_j^{outlet}\Big|_{CS_i} - \dot{m}_j^{inlet}}{\sum_{i=1}^{CS} V^{CS_i}} \quad \textbf{(101)}$$

Where (V^{CS_i}) is the reaction volume associated to the catalytic surface (i).

In the same analysis of results, it is important to compare the change in the parameters of the reactor performance (conversion and selectivity of species) due to the inclusion of gas phase rections. If ϕ is a specific parameter, then the change due to the CatOxGP process is defined according to the equation (102). In analogous way, for the net reaction rate the change due to the CatOxGP process is defined according to the equation (103):

$$\Delta\phi = \phi_{CatOxGP} - \phi_{CatOx} \quad \textbf{(102)}$$

$$\Delta R_j = 100 \cdot \frac{R_{j_{CatOxGP}} - R_{j_{CatOx}}}{R_{j_{CatOxGP}}} \quad \textbf{(103)}$$

For the performance parameters (ϕ), the difference between types of reactors (for example Squared Mesh Reactor – SMR – and Planar Channel Flow Reactor – PCFR –) is defined according to the equation (104). For the net reaction rate the change due to the CatOxGP process is defined according to the equation (105):

$$\Delta\phi = \phi_{SMR} - \phi_{PCFR} \quad \textbf{(104)}$$

$$\Delta R_j = 100 \cdot \frac{R_{j_{SMR}} - R_{j_{PCFR}}}{R_{j_{SMR}}} \quad \textbf{(105)}$$

3.8. Process conditions at industrial scale used for simulations

Umicore AG & Co. KG [Born 2018] reported information obtained from the Ostwald reactor at industrial conditions. This information is presented in this section. Figure 6 shows the inlet pressure and temperature, Figure 11 (a) shows the initial NH_3 composition and Figure 11 (b) shows the inlet velocity. All that information has been reported from data of industrial process in a reactor with a typical square catalytic mesh. The characteristics presented at inlet pressure higher than 10.0 bar are not representative of the general process. However, since it is the information available, it is part of the observations that this document considers. From this information, Table 2 presents the process values used for the simulation of the CatOx (catalytic oxidation) process.

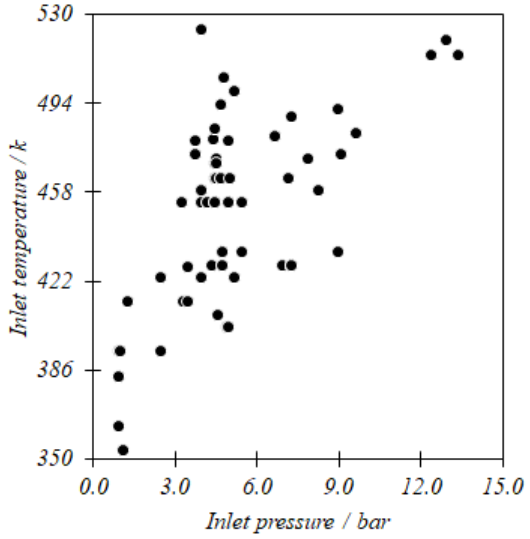

Figure 6. Industrial conditions in CatOx process. Inlet temperature and pressure. Based on information reported by Umicore AG & Co. KG [Born 2018].

The reported information of the process not only presents the inlet, but also the outlet conditions of the industrial reactor. To validate the simulation results and obtain a better understanding of the process, they must agree with this information.

Figure 8 shows some final response of the process variables to changes in inlet pressure. The NO selectivity is in any case higher than 90.0 % and the joint N_2O and N_2 selectivity is less than 10.0 %. The general process trend is that the NO selectivity decreases with the increment of the inlet pressure.

For inlet pressure lower than 5.0 bar, the pressure effect over the N_2O and N_2 selectivity is lower than which occurs for higher pressures.

Figures 9 and 10 show some final response of the process variables to changes in inlet temperature and NH_3 composition, respectively. The process trend is that NO selectivity slightly increases with the increment of these parameters. Certainly, the effect over the N_2O + NO selectivity is contrary.

The increments of inlet pressure and temperature significantly increase the outlet temperature. Since the concentration of the gas phase is practically invariant due to the high N_2 composition, the increase of the inlet NH_3 composition has not an important effect over the outlet temperature.

Table 2. Industrial conditions in CatOx process used for the simulations.
Based on information reported by Umicore AG & Co. KG [Bor 2018].

Pressure	Temperature	NH_3 composition	Velocity
bar	**K**	**v%**	**m s^{-1}**
P < 5.0	350 – 425 – 462 – 500	10.0 – 11.0 – 12.5	0.25 – 0.75 – 1.75
5.0 < P < 10.0	425 – 462 – 500	10.0 – 11.0 – 12.5	0.25 – 0.75 – 1.75 – 2.50
P > 10.0	500 – 515 – 530	10.0 – 11.0	1.40 – 1.60 – 1.75

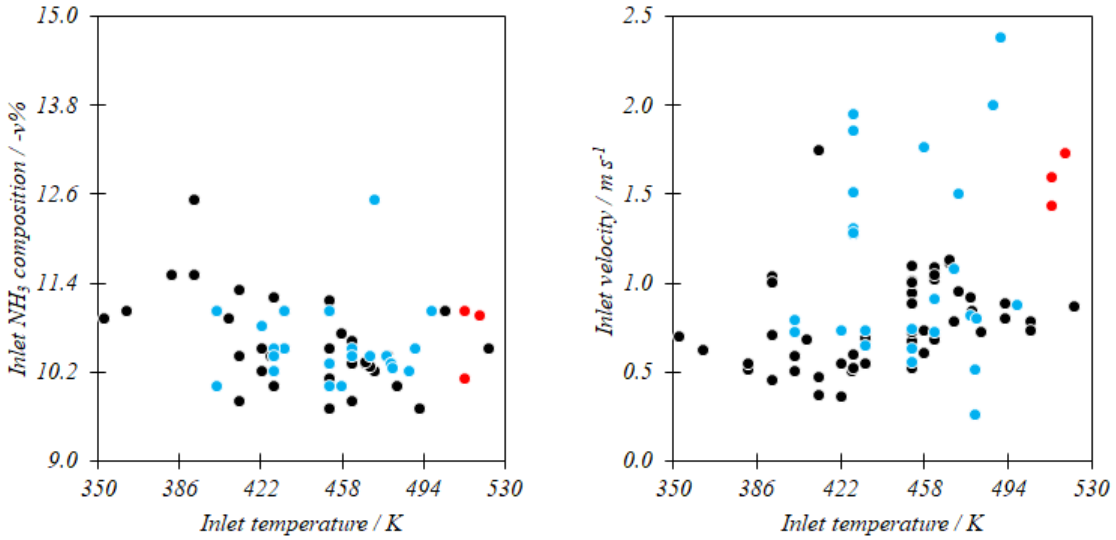

(a) Inlet NH_3 composition, temperature, and pressure.

(b) Inlet velocity, temperature, and pressure.

(●) P < 5.0 bar (●) 5.0 bar < P < 10.0 bar (●) P > 10.0 bar.

Figure 11. Industrial conditions in CatOx process. Inlet temperature, NH_3 composition and velocity.
Based on information reported by Umicore AG & Co. KG [Bor 2018].

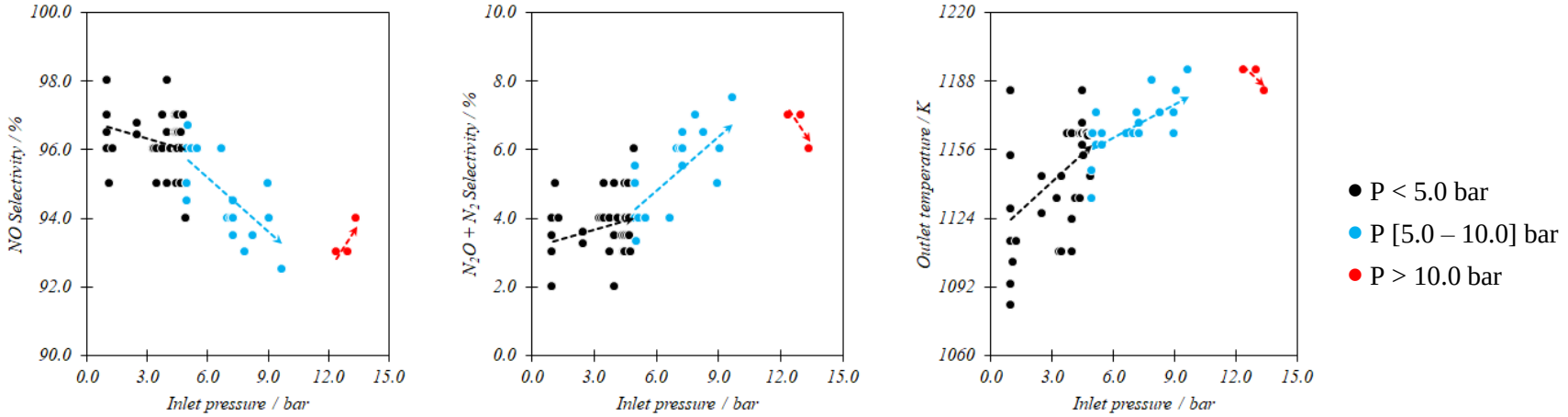

(a) NO Selectivity *(b) N_2O + NO Selectivity* *(c) Outlet temperature*

Figure 8. Matching of reported conditions in in the industrial CatOx process. Inlet pressure effect over outlet parameters. Based on information reported by Umicore AG & Co. KG [Born 2018].

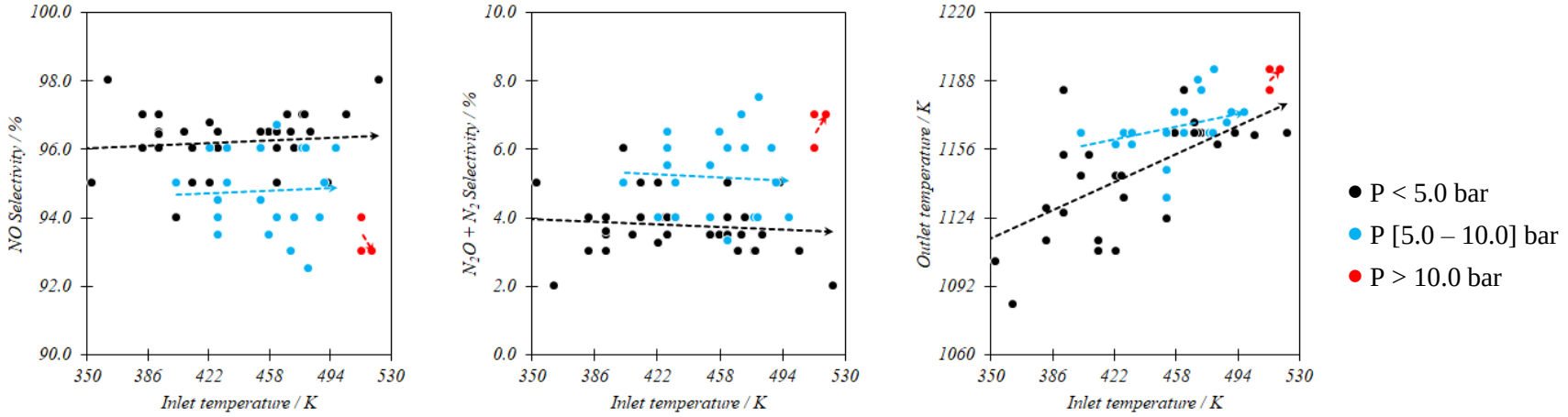

(a) NO Selectivity *(b) N_2O + NO Selectivity* *(c) Outlet temperature*

Figure 9. Matching of reported conditions in in the industrial CatOx process. Inlet temperature effect over outlet parameters. Based on information reported by Umicore AG & Co. KG [Bor 2018].

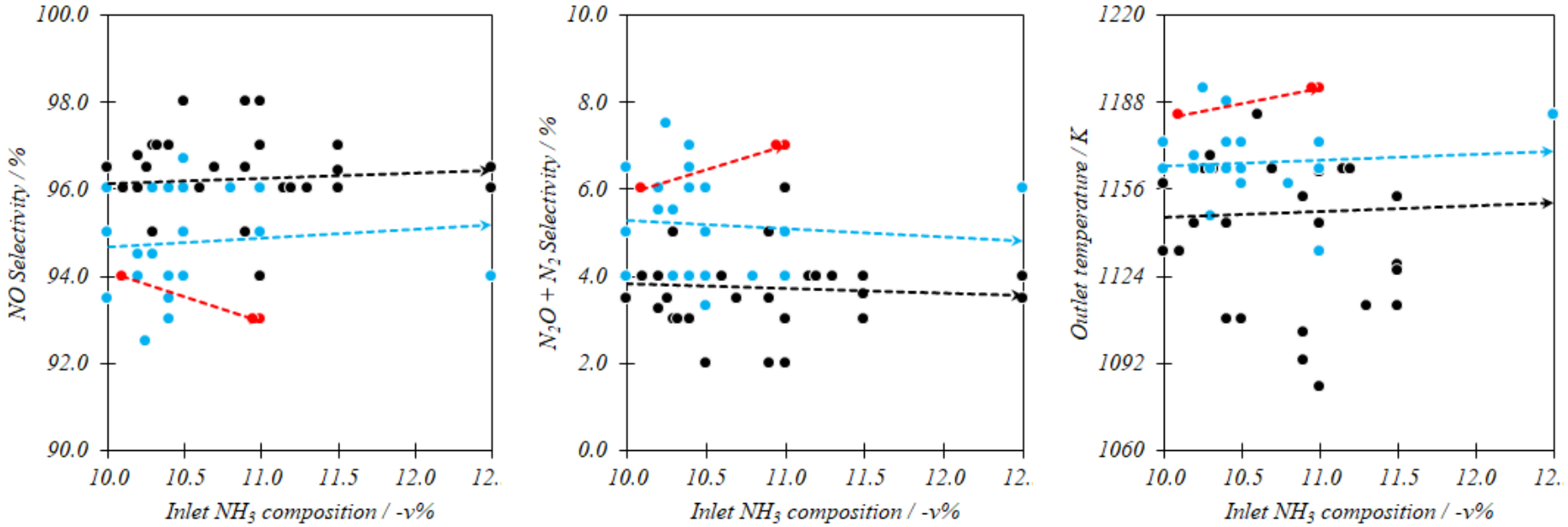

(a) NO Selectivity *(b) N_2O + NO Selectivity* *(c) Outlet temperature*

● P < 5.0 bar ● P [5.0 – 10.0] bar ● P > 10.0 bar

Figure 10. Matching of reported conditions in in the industrial CatOx process. Inlet NH_3 composition effect over outlet parameters. Based on information reported by Umicore AG & Co. KG [Bor 2018].

4. Characteristics and pathway analysis of the chemical mechanism in the gas phase

This chapter presents the characteristics of the detailed chemical mechanism used for the simulation of the process in the gas phase, which could exist during the catalytic oxidation of NH_3. The methodology is presented, by means of which this detailed mechanism is reduced to be used to carry out CFD (Computational Fluid Dynamics) simulations. It is expected that with the reduced mechanism, these simulations can be carried out with greater computational efficiency, obtaining results comparable with those that would be obtained by the application of the detailed mechanism and that allow understanding in a more synthetic way the possible chemical routes that are presented in the gas phase. The reduction of the detailed mechanism considers the application of the rate production analysis [Tur 2014], degree of rate control method [Steg 2009] and sensitivity analysis [Gla 1986]. The reduced mechanism that is obtained, which consists of 34 reactions and 17 species, is compared with the detailed mechanism by means of the application of simulations of PFR (Plug Flow Reactor) at pressure of 5.0 bar. The presumed chemical pathway in the gas phase is presented in detail.

Finally, since the parameters reported for the mechanism in the gas phase is not modified and there are other mechanisms reported to describe the same effect, this section presents a comparison between the use of the AA – Mech [Kil 1999] [Cod 2001] and the mechanism reported by Glarborg [Gla 2018].

4.1. Application of method for the reduction of the detailed mechanism and validation of reduced chemical mechanism

To facilitate the use of the AA – Mech for the process in the gas phase, in the development of simulations using CFD tools, it is preferable to use a reactive scheme that contains the least possible number of reactions and species, but at the same time allows to achieve the expected results of the process. In this reduction method, the following process condition has been considered:

- Composition and temperature according to the progress of the reaction RI, from an initial mixture of 10.0 v% NH_3, 90.0 v% Dry Air.
- Inlet temperature of 1223 K.
- Inlet pressure of 5.0 bar.
- The residence time of 2.80 ms, which is the residence time for the process in a catalytic square mesh reactor with 10 wires at those conditions of pressure and temperature.

The reaction RI is important since describes the main route to NH_3 oxidation. Equation (106) defines the progress of reaction.

$$4NH_3 + 5O_2 \rightarrow 4NO + 6H_2O \qquad \textbf{RI}$$

$$\xi_{RI} = 100 \times \frac{\dot{N}_{NO}}{\dot{N}_{NO} + \dot{N}_{NH_3}} \qquad \textbf{(106)}$$

Under this operating conditions, Figure 11 presents the results of the degree of rate control and sensitivity analysis for 80.0 % ξ_{RI}. Several researchers [Lyo 1975] [Mill 1983] explain that under these conditions, the composition of NH_3 and NO in the gases is such that the selective non – catalytic reduction process can occur in the gas phase. Figure 11 shows the results of the steps, which have values

of $X_{RC,i}$ greater than 10^{-4}. Appendix 2 presents the results for the other reactions. Figures 12 and 13 show the concentration profiles of species when a mixture generated after 80.0 % ξ_{RI} reacts at 5.0 bar and 1223 K.

The following observations come from the analysis of Figures 11 to 13, and from the results of the analysis of the rate production:

- The Figure 11 shows that the results of the degree of rate control and the sensitivity analysis are coincident.
- The Figure 11 shows that the effect of the variation of the pre – exponential factor is greater for the NH_3 net reaction rate of than for the net reaction rate of NO, N_2 and N_2O.
- Several investigations [Lin 1994] [Mill 1989] have shown that the N_2O concentration is highly dependent on the reactions that dominate the NO concentration. Such is the case of the reactions R071 ($NH_2 + NO \rightarrow N_2 + H_2O$), R072 ($N_2 + H_2O \rightarrow NH_2 + NO$), and R073 ($NH_2 + NO \rightarrow OH + NNH$).
- The following molecules and radicals: H_2O_2, NO_3, N_2H_2, NH, N_2H_4, N_2H_3, HNNO, and N – atom, have concentrations below 10^{-5} mol m^{-3}, as is shown in Figure 13. The reactions associated with these species could be removed from mechanism according to consideration of quasi stationary state (i. e. rate of production near or equal to rate of destruction). This approach had been previously reported [Cre 2000] [Duy 2012]. Miller [Mill 1989] indicated that the N – atom is a dominant species for the abstraction of H – atom from NH_3 under fuel – rich flame conditions, this characteristic had been pointed by Mathieu [Mat 2015] as well. This is not the case of the mixture conditions in this investigation.
- Gardiner [Gar 2000] explained that the N_2H_3 is an unusually long – lived radical and therefore can be excluded from the model.
- Gardiner [Gar 2000] had explained that the N_2H_2 is unusual since its H – N bond dissociation energy is only 258 kJ mol^{-1}, quite small for a stable molecule. Moreover, Lindstedt [Lin 1994] explained that the addition reactions to N_2H_2 (like R057, $N_2H_2 + NO \leftrightarrow NH_2 + N_2O$) are probably not important. Consequently, the isomerization barriers are above the entrance channel, and the overall rates to non adduct products are slow. And therefore, this molecule can be omitted from the reaction mechanism.
- The importance of NH in the mechanism would be limited. In fact, previous investigations [Lin 1994] [Mil 1989] explained that its formation increases under stoichiometric and NH_3 rich conditions, which are not presented in the chemical process that is the subject of this study.
- From this condition of quasi – stationary state and considering the low levels of degree of rate control, this analysis allows removing 73 reactions from the detailed reaction mechanism.
- According to the analysis of the rate production, reactions that induce an effect less than 10.0 % on atoms conversion ($F_{i_{j\rightarrow k}}$) are not considered as important reactions in the reaction mechanism.

  Then 22 reactions of the detailed mechanism are excluded (R001 – R003, R007, R008, R010, R026, R046, R005, R006, R041, R047, R067, R079, R088, R092, R096, R097, R101, R114, R118, and R121). For example, in the case of reaction R096 ($H_2NO + M \rightarrow HNO + H + M$), Gardiner [Gar 2000] had explained that this H_2NO dissociation will be unimportant compared to reactions with radicals. For the reaction R092 ($H + HONO \rightarrow H_2 + NO_2$), this direct abstraction is less important than the adduct formation for instance the reaction R126 ($HONO + M \rightarrow M + NO + OH$).
- In agreement with Duynslägher [Duy 2012], Figure 12 shows that the concentration profiles of main species (NH_3, O_2, NO, N_2) do not present special changes due to use of the reduced mechanism.

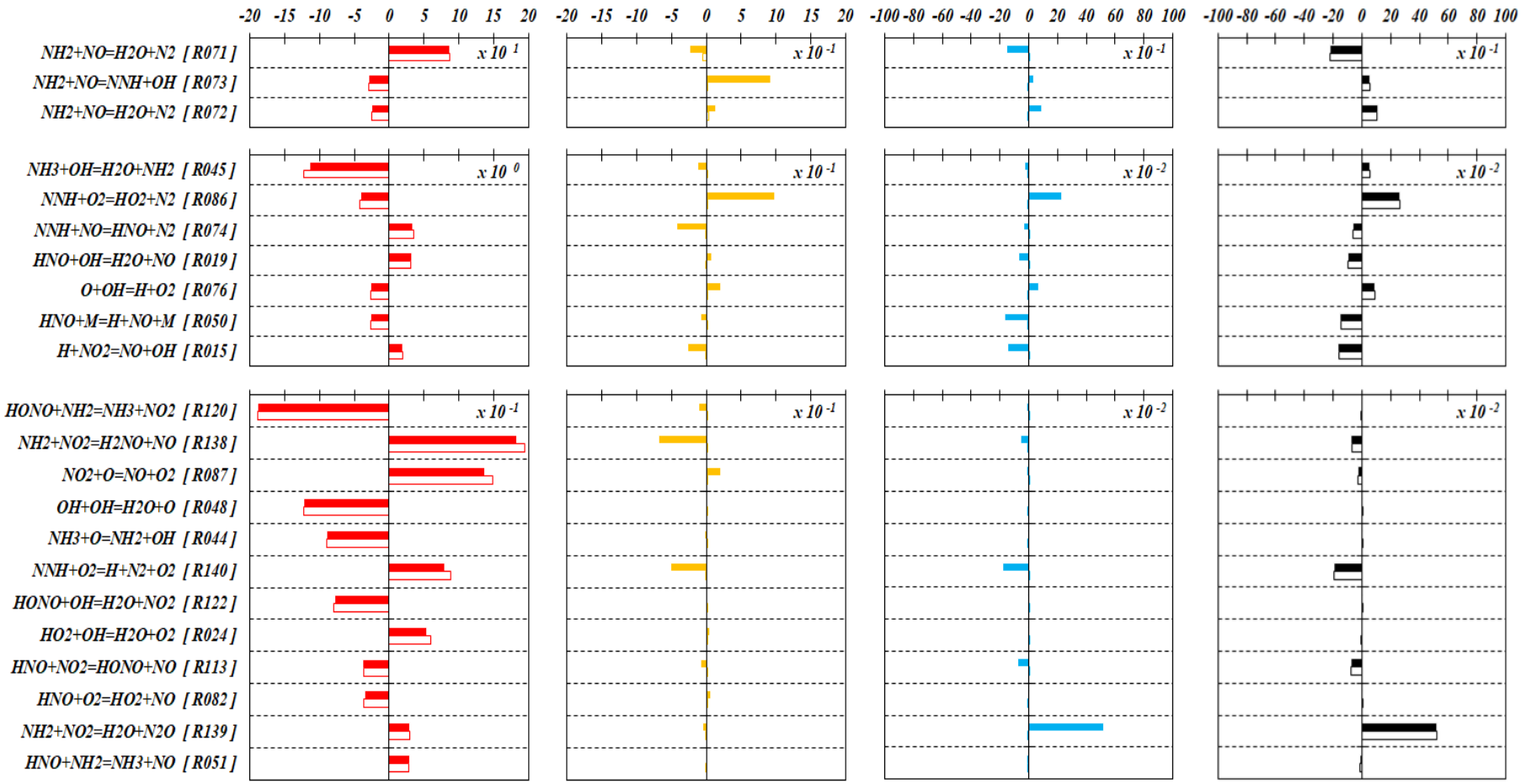

Boxes: Filled, Degree of rate control / Empty, Sensitivity coefficient

■□ NH_3 / ■□ NO / ■□ N_2 / ■□ N_2O

Figure 11. Results of the degree of rate control and sensitivity analysis. Inlet conditions: 1223 K, 5.0 bar. (10.0 NH_3 / 90.0 N_2) v% → 80.0 % ξ_{RI} → (2.01 NH_3 / 8.02 NO / 12.0 H_2O / 6.86 O_2 / − N_2) v%. Simulations made with CANTERA [Goo 2017].

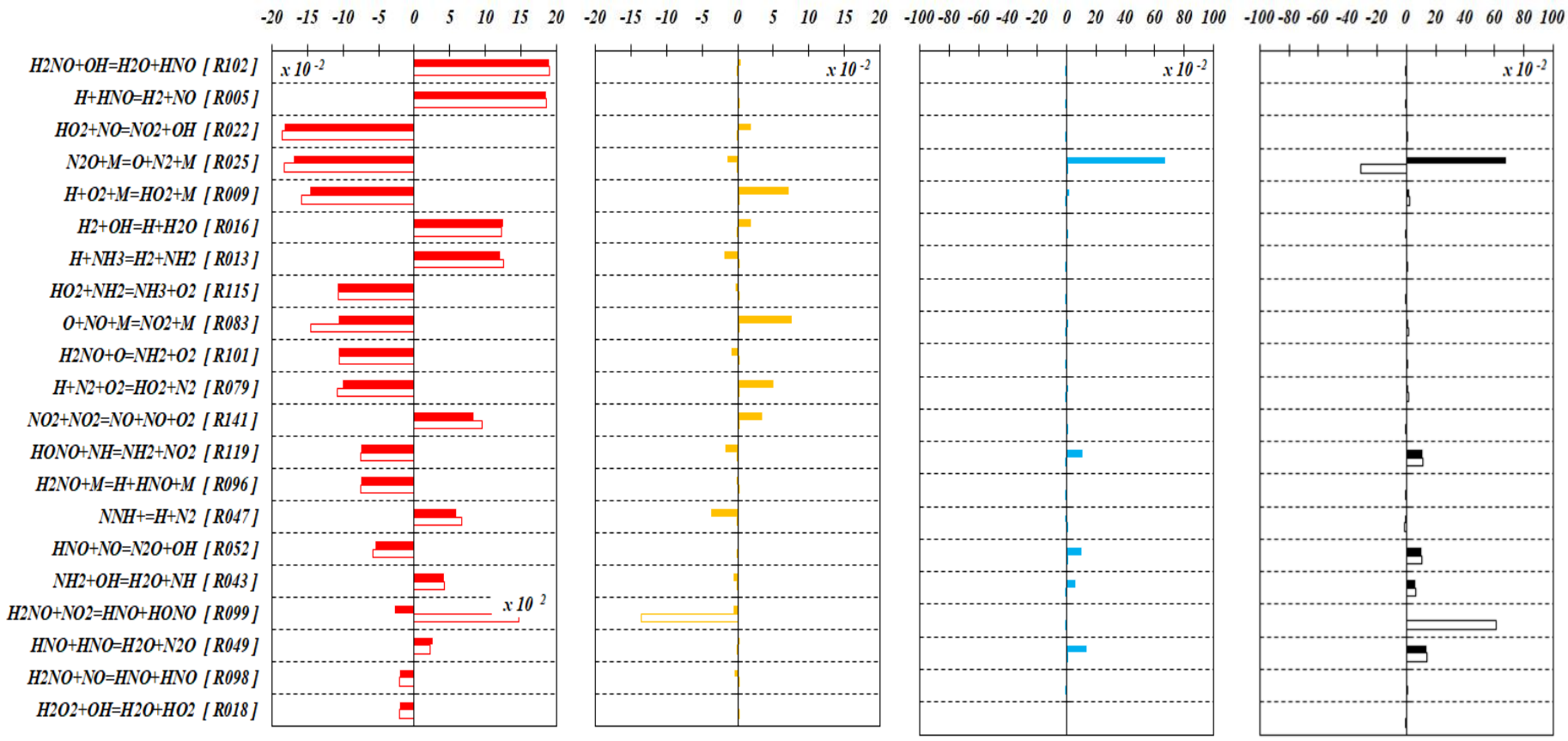

Boxes: Filled, Degree of rate control / Empty, Sensitivity coefficient

■□ NH_3 / ■□ NO / ■□ N_2 / ■□ N_2O

Figure 11. **(Continuation)** Results of the degree of rate control and sensitivity analysis. Inlet conditions: 1223 K, 5.0 bar. (10.0 NH_3 / 90.0 N_2) v% → 80.0 % ξ_{RI} → (2.01 NH_3 / 8.02 NO / 12.0 H_2O / 6.86 O_2 / − N_2) v%. Simulations made with CANTERA [Goo 2017].

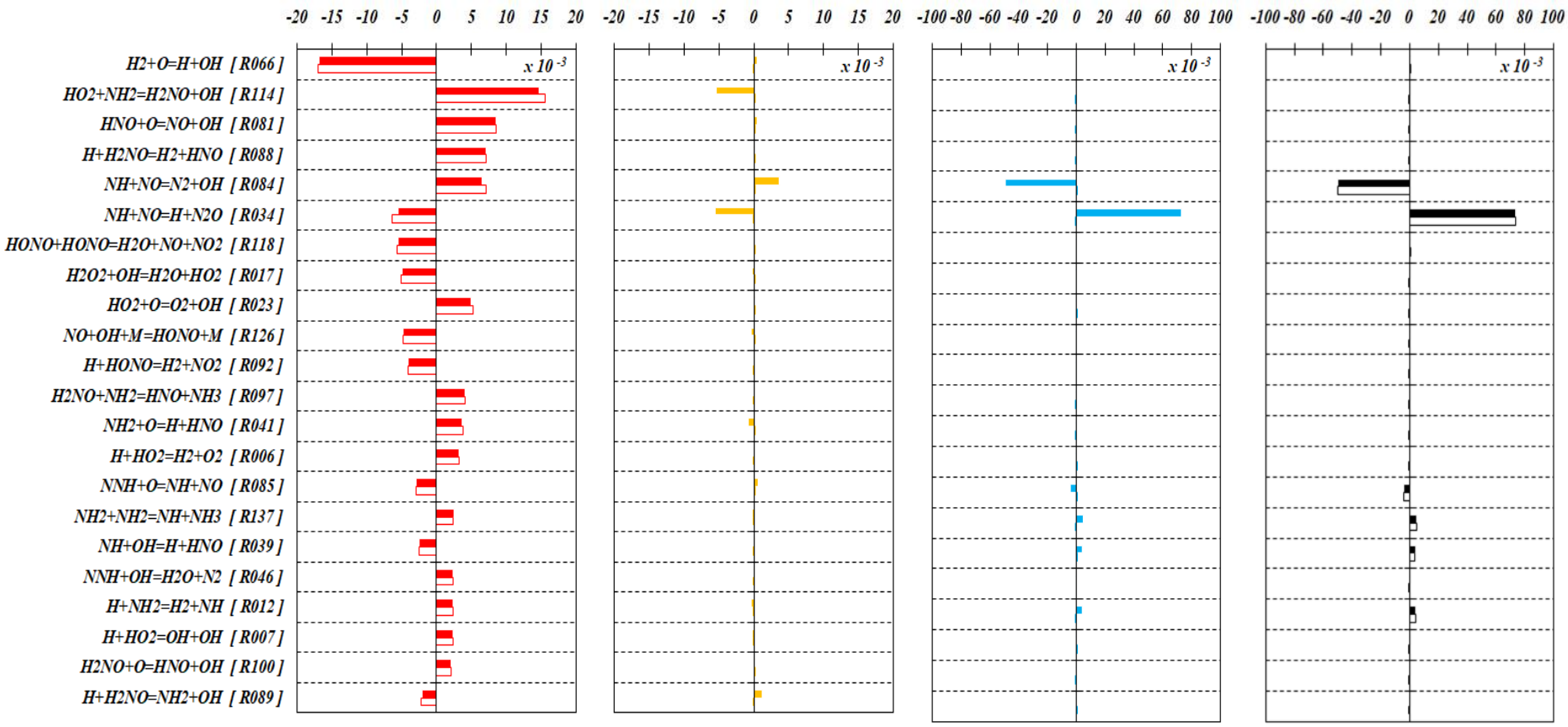

Boxes: Filled, Degree of rate control / Empty, Sensitivity coefficient

■□ NH_3 / ■□ NO / ■□ N_2 / ■□ N_2O

Figure 11. **(Continuation)** Results of the degree of rate control and sensitivity analysis. Inlet conditions: 1223 K, 5.0 bar. (10.0 NH_3 / 90.0 N_2) v% → 80.0 % ξ_{RI} → (2.01 NH_3 / 8.02 NO / 12.0 H_2O / 6.86 O_2 / − N_2) v%. Simulations made with CANTERA [Goo 2017].

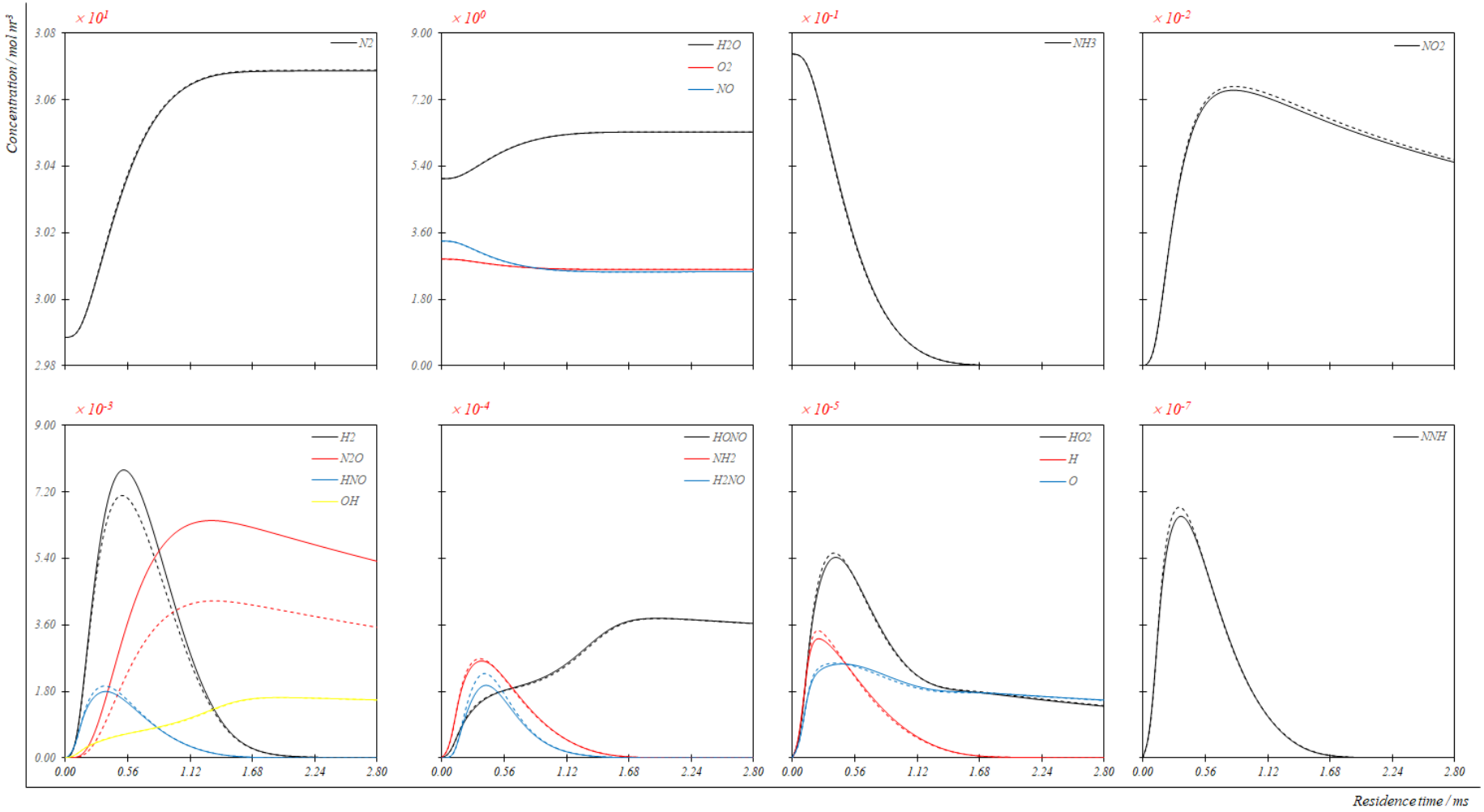

Figure 12. Concentration profiles of the species present in the gas phase process. Calculated from the detailed (continuous line) and reduced (dashed line) mechanisms.
Inlet conditions: 1223 K, 5.0 bar.
(10.0 NH_3 / 90.0 N_2) v% → 80.0 % ξRI → (2.01 NH_3 / 8.02 NO / 12.0 H_2O / 6.86 O_2 / − N_2) v%.
Simulations made with CANTERA [Goo 2017].

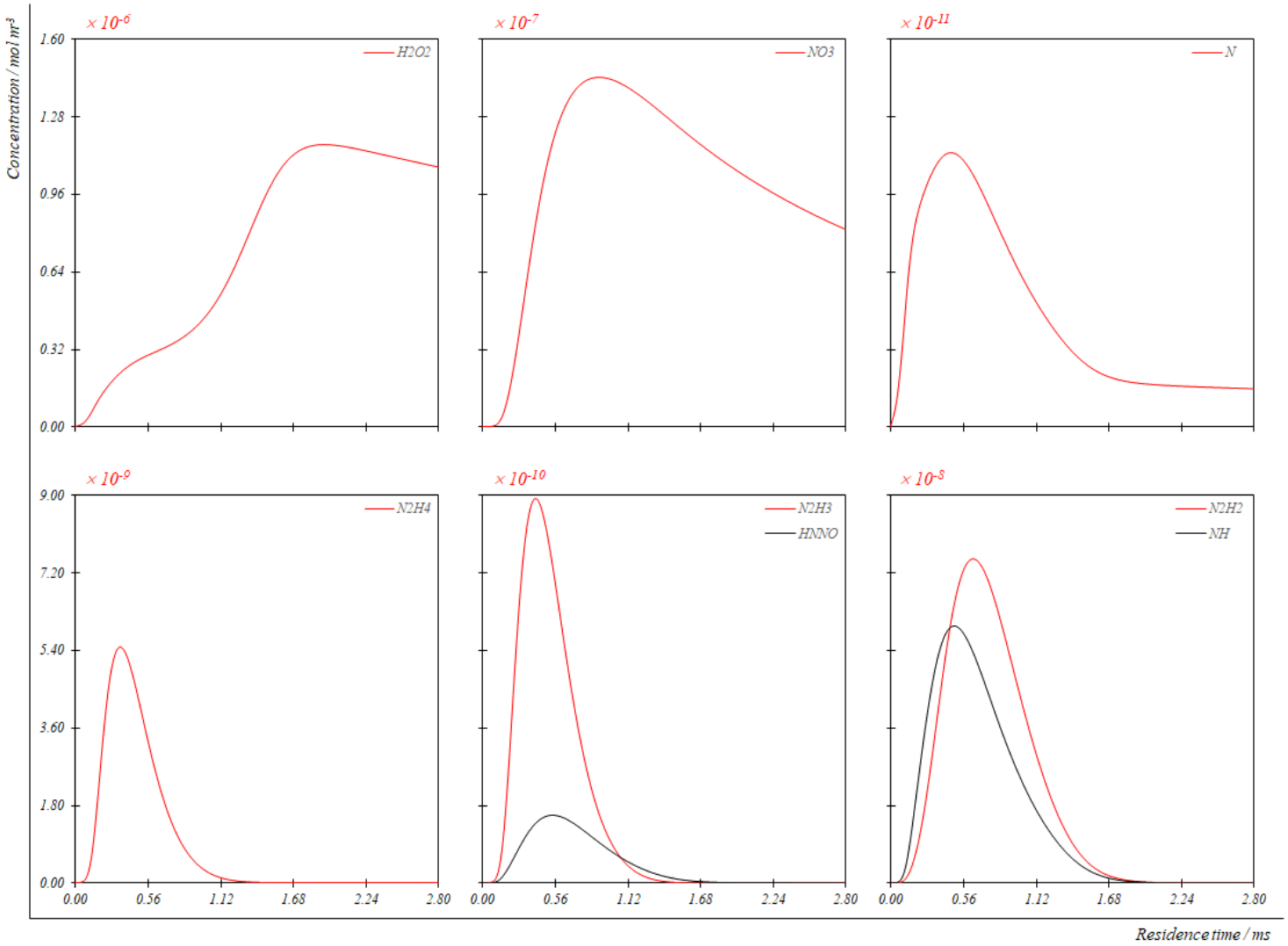

Figure 13. Concentration profiles of species considered at quasi stationary state. Calculated from the detailed mechanism. Inlet conditions: 1223 K, 5.0 bar. (10.0 NH_3 / 90.0 N_2) v% → 80.0 % ξ_{RI} → (2.01 NH_3 / 8.02 NO / 12.0 H_2O / 6.86 O_2 / − N_2) v%.
Simulations made with CANTERA [Goo 2017].

- Due to the change in species concentration over time, the flow of each element *A* is also variable. For this reason, it is possible to determine both the average flow of each element during the residence time and the standard deviation of this flow with respect to this average value. It is inferred that in cases where standard deviation tends to zero, the flow of each element tends to be constant and close to average value throughout residence time. In this sense, the reaction steps whose flow is less than 10^{-9} mol m^{-3} s^{-1} and have a standard deviation of less than 1.0 % are eliminated. Then, 9 reactions of the detailed reaction mechanism are excluded.
- The following reactions: R031 – R033, R070, R075, R078, and R125, have a degree of rate control values lower than 10^{-4}. Since up to this point all reactions with degrees lower than this magnitude order have been eliminated, then these 7 associated reactions are excluded from the detailed reaction mechanism.

Under these conditions, Appendix 3 presents the reduced mechanism. It consists of 34 reactions and 17 species. Figure 12 presents the concentration profiles of the process species, calculated from the detailed and reduced mechanisms. Gas phase concentration of the major species (N_2, NH_3, NO, O_2, H_2O, N_2O), which are considered in the catalytic process, have a similar behaviour throughout the residence time.

4.2. Pathway analysis

From the rate production analysis applied to the reduced mechanism, Figure 14 presents the fundamental routes between the reagents and the products.

Each amine radical (NH_i) can undergo a subsequent reaction by one of two ways: (i) reaction with NO leading to the N_2 formation, (ii) oxidation leading to formation of NO_X (NO, N_2O, NO_2). Miller [Mill 1989] expleind that for very lean mixes, the critical NH_i is the amidogen radical (NH_2), but as the equivalence ratio increases the greater abundance of H – atoms, results in a shift in the critical NH_i radicals from NH_2 to NH to N. Since the process of catalytic oxidation of NH_3 occurs under lean conditions, this behaviour is consistent with the results presented in section 4.1, according to which the reduced mechanism does not consider NH or N – atom. This pathway agrees with one proposed shor time ago for Song [Son 2016] or with the patway proposed for Duynslägher [Duy 2012]. They agreed that species like HNO the NO_2 equilibrium governs the gas phase process in the NH_3 oxidation.

In the same line of analysis, Shresta [Shr 2018] indicate that NH_3 undergoes H – atom abstraction by O – atom, H – atom and OH radical and decomposes to amidogen radical (NH_2). It is a very reactive species and its reactions with H – atom, O – atom, OH radical and NO control the overall reactivity of the system in the gas phase.

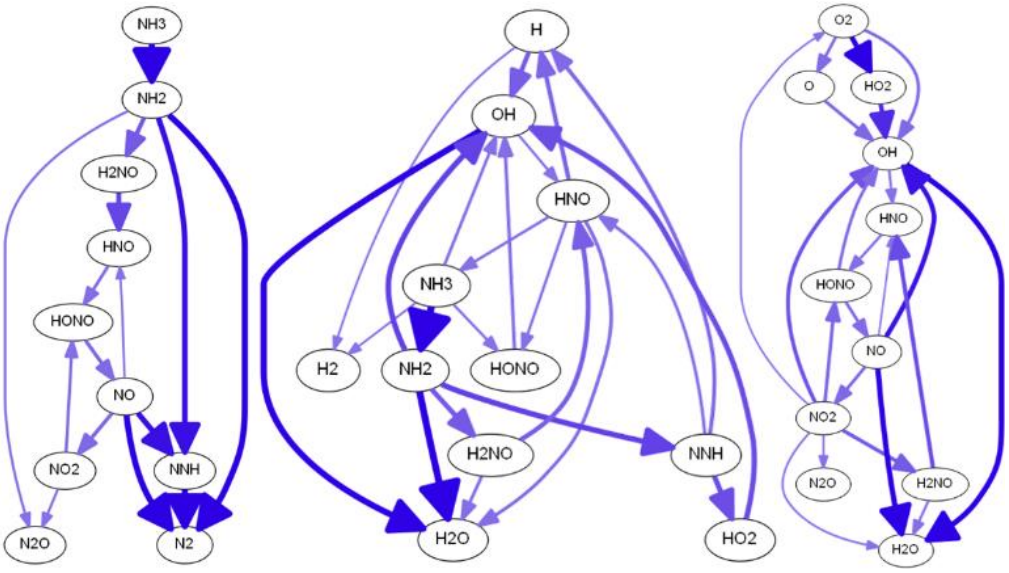

Figure 14. Pathway of the NH_3 / NO / N_2 / O_2 system in the gas phase process based on the reduced reaction mechanism. Simulations made with CANTERA [Goo 2017].

4.2.1. N_2 formation

The main route for the consumption of NH_3 and NO in gas phase leads to the N_2 formation. The progress of the reaction RI ($4NH_3 + 5O_2 \rightarrow 4NO + 6H_2O$), or what is the same, the increase of the NO concentration maintains and increases this process route. The N_2 formation requires the presence of NH_2 in the reactive medium as the main radical or the presence of NNH as an intermediate radical, as presented in Figure 14 and as Miller [Mill 1989] reported previously. The selectivity for forming NO or N_2 from N – volatiles in combustion depends largely on the fate of amine radicals such as NH_2 [Son 2016].

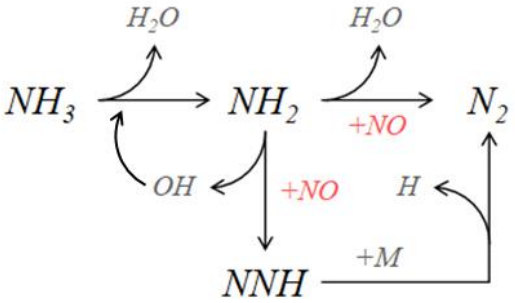

Figure 14. Mean reaction route for the N_2 formation in the gas phase.

Duynslägher [Duy 2012] explain that the NH_2 problem is fundamental since this species is the main intermediate in the NH_3 degradation and thus also the precursor for the gas phase products. Tayyeb Javed [Tay 2007] explained that the NH_2 is highly selective to NO and causes their reduction even in oxidizing conditions and Miller [Mill 1989] and Takeyama [Tak 1967] have explained that the NH_2 formation is governed by the reaction R045, as has been reported for the NH_3 oxidation and as Figure 11 indicates, where reaction R045 appears as the step that involves NH_3 with higher degree of rate control and sensitivity coefficient. Specially in low pressure flames this reaction plays a significant role [Mac 1967]. The reaction R071 governs the NO reduction, which will preferably take place if there is presence of NH_3 in the reactive medium. Indeed, Figure 11 shows that reaction R071 is a limiting step of the rate of NH_3 oxidation in the gas phase. This reaction has the highest values of both the degree of

rate control and the sensitivity coefficient. Additionally, this step limits the NO formation in the gas phase, as expected due to its reduction to N_2. Accordly, Song [Son 2016] have stablished that the reaction R071 is a main chain – terminating step. Regardless of the progress of the reaction RI ($4NH_3 + 5O_2 \rightarrow 4NO + 6H_2O$) ($\xi_{RI}$), the reaction R045 has the highest net rate in the entire process.

$$NH_3 + OH \rightarrow NH_2 + H_2O \qquad \textbf{R045}$$

$$NH_2 + NO \rightarrow N_2 + H_2O \qquad \textbf{R071}$$

The parameters for the determination of the rate constant of the reaction R071 have been recent discussed and detailed described according to what was reported by Song [Son 2016]. These same parameters have been reported in the AA – Mech [Kil 1999] [Cod 2001] and are used in this investigation.

Gardiner [Gar 2000] indicated that the NH_2 production, the key intermediate in the reduction process for NO, can be regarded as reasonably well understood. The NH_2 production according to reaction R045 is an inhibitory rate step of the process in the gas phase, as shown in Figure 11. If the NH_3 does not oxidize in the gas phase to form NH_2, the process in this phase is scarce or not carried out at all.

The NH_3 dehydrogenation does not only occur through the reaction R045, in this process the reactions R013 and R115 also participate. Fujji [Fuj 1981] reported that reaction R115 is one of the initial reactions for the oxidation of NH_3. It should be noted that the net rates of reactions R045 and R013 are progressive. That is, with the increase in the progress of the reaction RI ($4NH_3 + 5O_2 \rightarrow 4NO + 6H_2O$) ($\xi_{RI}$), the net rate of the reactions increases.

The parameters for the determination of the rate constant of the reaction R045 in the AA – Mech [Kil 1999] [Cod 2001] are the same that habe been recent reported by Song [Son 2016]. It is important since this investigation stablished that the reaction R045 is the main route for the consumption of NH_3 in the gas phase.

Considering the information of the Figure 11, the reaction R013 is a limiting step in the NH_3 oxidation in the gas phase and, in turn, due to the NH_2 formation, which subsequently reacts with NO, inhibits the formation of the latter species. This inhibitory effect had been previously reported [Mat 2015]. On the other hand, by controlling the O_2 effect in the gas phase, the reaction R115 limits the NH_3 oxidation and the NO generation by controlling the NH_2 formation, which subsequently acts in the NO reduction. In fact, Song [Son 2016] have stablished that the interaction ($NH_2 + HO_2$), as in reaction R115, is a promoting chemical process for the consumption of NH_3 to finally forming OH radicals.

$$NH_3 + H \rightarrow NH_2 + H_2 \qquad \textbf{R013}$$

$$NH_3 + O_2 \rightarrow NH_2 + HO_2 \qquad \textbf{R115}$$

Figure 15 presents indeed the comparison of the net rates of the three reactions that control the first NH_3 dehydrogenation. The reaction R045 effect reaches longer residence times and has a net rate up to two orders of magnitude higher than the net rate of the reactions R013 and R115. For example, for a progress of the reaction RI (ξ_{RI}) equal to 80.0 %, the reaction R045 occurs up to 1.80 ms, while the reactions R013 and R115 occur only up to 1.50 and 1.20 ms respectively.

The reverse route of reaction R071 ($NH_2 + NO \rightarrow N_2 + H_2O$), reaction R072, has similar behaviour but with half the net rate. Which confirms that the trend of the process leads to the N_2 formation. The behaviour of this reaction as an inverse route to reaction R071 is confirmed by means

of the information of the Figure 11, which shows the opposite effect. That is, the inhibition in the NH_3 oxidation and the control of the NO formation.

$$N_2 + H_2O \rightarrow NH_2 + NO \qquad \textbf{R072}$$

Several reserchers [Lin 1994] [Lyo 1975] have indicated that the reaction R073 is the main route for the OH formation in the process and is favorable to NO reduction. Klippenstein [Klip 2011] indicate that the importance of NNH for formation and reduction of NO depends on its thermal stability and its consumption channels. Reaction R071 is equally unfavorable because causes the process ends since it controls the N_2 formation. According to the information in Figure 11, the reaction R073 qualitatively presents the same effect of rate control on the NH_3 consumption and NO generation as the reaction R072. However, from the quantitative point of view, the reaction R073 significantly limits the NO formation compared to the reaction R072. This means that the gas phase process has a preferable tendency to reduce NO from NH_2 than to NO formation due to the N_2 oxidation. This is the same conclusion at wich Song [Son 2016] have come.

$$NH_2 + NO \rightarrow OH + NNH \qquad \textbf{R073}$$

The comments presented util this point, which are related to reactions R071 $(NH_2 + NO \rightarrow N_2 + H_2O)$ and R073, are in accordance with the observations made for Shrestha [Shr 2018]. They suggested that the chain branching channel by reaction R073 and the terminating channel by reaction R071 are important in the selective non – catalytic reduction of NO with NH_3. The NNH interacts with the O_2 according to the reactions R086 and R140 to produce N_2. In the reaction R140, O_2 acts as a third body.

$$NNH + O_2 \rightarrow N_2 + HO_2 \qquad \textbf{R086}$$

$$NNH + O_2 \rightarrow N_2 + H + O_2 \qquad \textbf{R140}$$

When two reactions (i, j) have the same reagents and one of them generates termination products, as is the case of reactions R086 and R140, the branching ratio defined as $BR_i = k_i \cdot (k_i + k_j)^{-1}$, is the rate at which one reaction is preferable in the chemical process over another.

Although Gardiner [Gar 2000] indicates that the reaction R086 is too slow to be of interest in this type of chemical systems, the difference in the kinetic parameters reported by Gardiner [Gar 2000] and the same reported in the AA – Mech [Kil 1999] [Cod 2001] for the reactions R086 and R140, induces the branching ratio of these reactions to be 0.80 and 0.20 respectively, regardless of temperature. According to this, and according to the explanation of Kilpinen [Kil 1999] and Coda Zabetta [Cod 2001] about the reaction R086 is indeed more important than the reaction R140. In fact, Shrestha [Shr 2018] argued that the reaction R086 is the major channel for the NHH consumption. The information of the Figure 11 confims this.

From a qualitative point of view, the control effect of the reactions R086 and R140 on the NH_3 oxidation and the NO formation is contrary. The degree of rate control of the reaction R086 is in any case higher (up to one order of magnitude) than the degree of rate control of reaction R140. For that, the reaction R086 inhibits the NH_3 consumption by limiting its oxidation due to the O_2 consumption to oxidize the NNH.

Figure 16 a) and b) show, that at fixed O – atom or OH concentration (which is formed by reaction R073), the increase in the progress of the reaction RI ($4NH_3 + 5O_2 \rightarrow 4NO + 6H_2O$) ($\xi_{RI}$) inhibits the NO reduction. The inhibition effect is greater with the increase in the O – atom or NO concentration.

In agreement with Caton [Cat 1989], Figure 16 c) and d) indicates that under oxidizing conditions, the high O – atoms and OH concentrations, not only inhibits the NO reduction but also favors the NH_3 oxidation through the reactions associated with the NH_2 formation from NH_3. Gardiner [Gar 2000] also indicated that simulation results are particularly sensitive to the branching ratio of reactions R071 ($NH_2 + NO \rightarrow N_2 + H_2O$) and R073 ($NH_2 + NO \rightarrow OH + NNH$).

Considering that H_2O is formed in reactions R045 ($NH_3 + OH \rightarrow NH_2 + H_2O$) and R071 and that to these reactions the analysis of sensitivity and rate control attach so much importance, Miller [Mill 1989] indicated that the presence of H_2O inhibits the reduction of NO. In fact, Figure 17 shows that at a given concentration of H_2O, the NO reduction percentage decreases with the increase in the progress of the reaction RI (ξ_{RI}), or what is the same, with the NH_3 consumption or with the increase in process temperature.

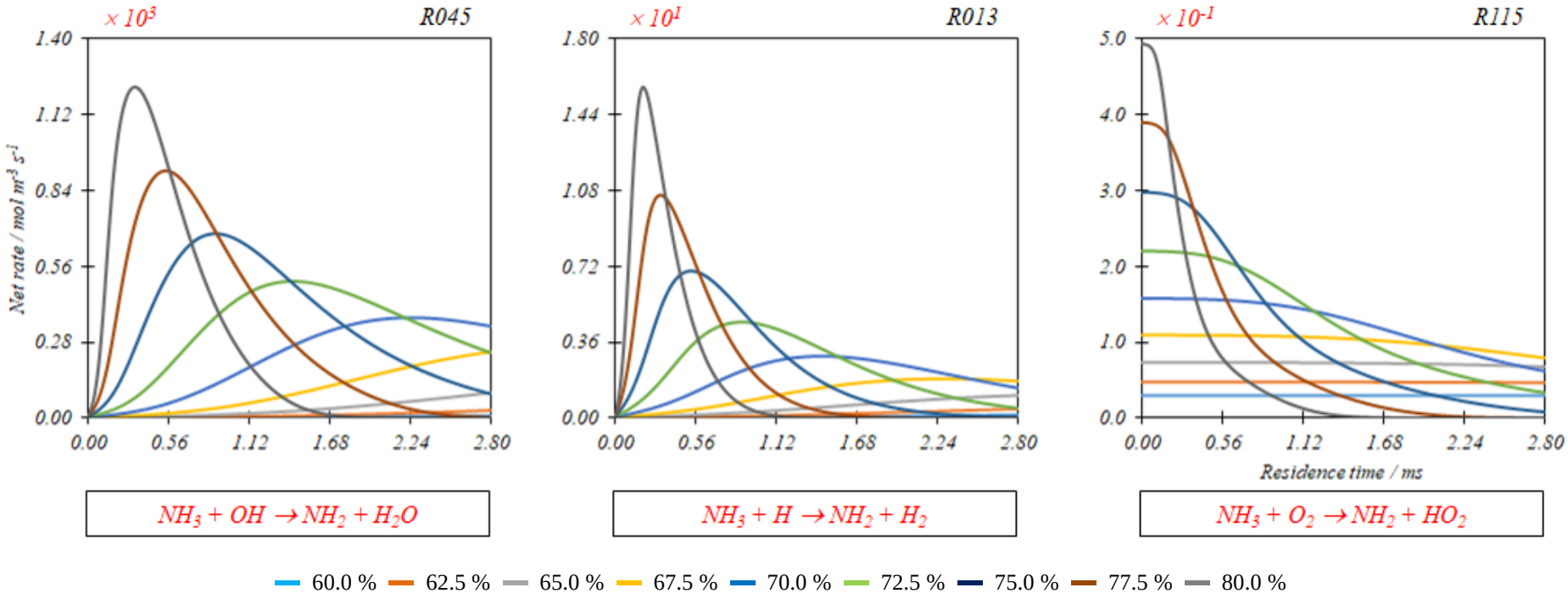

Figure 15. The net rate of reactions associated with the NH_3 dehydrogenation (R045, R013, and R115).
Parameter: progress of the reaction RI ($4NH_3 + 5O_2 \rightarrow 4NO + 6H_2O$) ($\xi_{RI}$) according to equation 106.
Simulations made with CANTERA [Goo 2017].

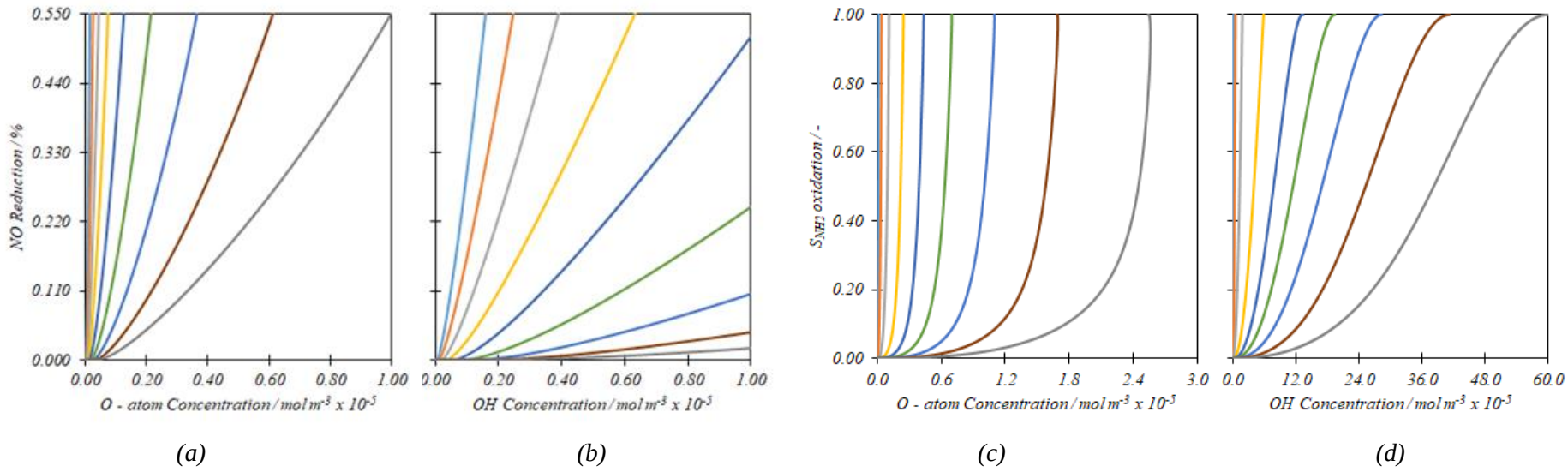

(a) Effect of O – atom Concentration on the NO reduction in the gas phase.
(b) Effect of radical OH Concentration on the NO reduction in the gas phase.
(c) Effect of O – atom Concentration on the selectivity to NH_2 oxidation in the gas phase.
(d) Effect of radical OH Concentration on the selectivity to NH_2 oxidation in the gas phase.

60.0 % 62.5 % 65.0 % 67.5 % 70.0 % 72.5 % 75.0 % 77.5 % 80.0 %

Figure 16. Characteristics of the NH_2 + NO chemical system.
Parameter: progress of the reaction RI ($4NH_3 + 5O_2 \rightarrow 4NO + 6H_2O$) ($\xi_{RI}$) according to equation 106.
Simulations made with CANTERA [Goo 2017].

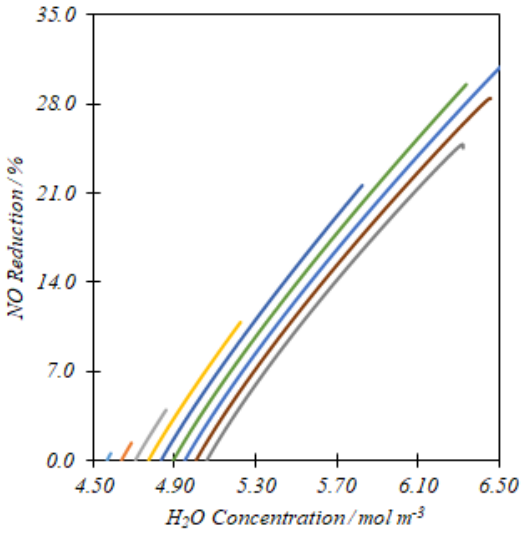

Figure 17. Effect of H_2O concentration in the NO reduction.
Parameter: progress of the reaction RI ($4NH_3 + 5O_2 \rightarrow 4NO + 6H_2O$) ($\xi_{RI}$). according to equation 106.
Simulations made with CANTERA [Goo 2017].

4.2.2. Formation of NO_X (NO, NO_2, N_2O)

As Figure 18 shows, the second route of NH_3 and NO consumption in the gas phase tends to the NO_X formation, either directly from NH_2 to form N_2O through NO_2 or previously through the NO and NO_2 formation due to the interactions between the NO_X and HO_2. For values of the progress of the reaction RI (ξ_{RI}) above of the 75.0 %, the N_2O formation is no longer relevant, and the oxidation route only forms NO and NO_2.

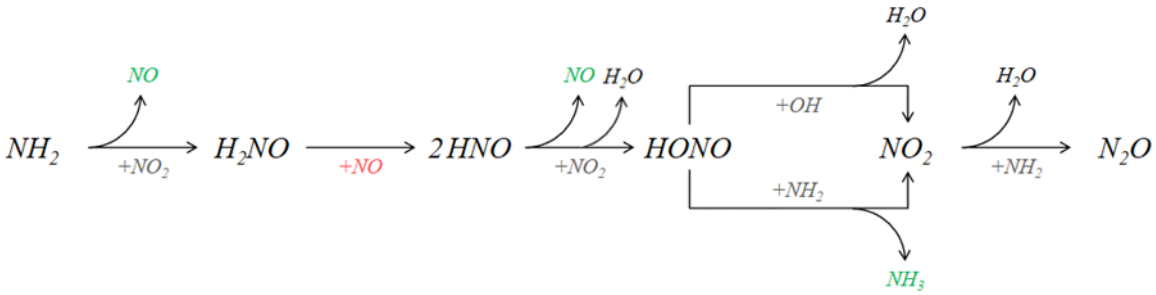

Figure 18. Reaction route for the NO_X (NO, N_2O, NO_2) generation in the gas phase.

Shrestha [Shr 2018] commented that the NO_2 kinetics is one of the most important sub – mechanisms in almost all the cases of NH_3 – NO reaction systems in the gas phase and suggested that all reactions involving NO_2 are found to have increasing sentitivities with increasing temperature. NO_2 participates in the reactive process that ultimately leads to the N_2O formation. Reaction R022 forms NO_2, and then it can be oxidized by means of reaction R139. Since HO_2 is an important precursor of NO_2, it is reasonable to consider that it is formed preferably in oxidant conditions. In fact, Zheivot [Zhe 2007] noted that in the catalytic oxidation of NH_3, probably, the loss of NO was related to its oxidation to NO_2 in the gas phase in the presence of oxygen. Therefore, it was reasonable to reduce the residence time of the product principal (NO) in the oxidative medium.

$$NO + HO_2 \rightarrow OH + NO_2 \qquad \textbf{R022}$$

$$NO_2 + NH_2 \rightarrow H_2O + N_2O \qquad \textbf{R139}$$

According to Figure 11, qualitatively the effect of rate control of reactions R022 and R139 on the NH_3 oxidation and the NO formation are contrary. The grade of rate control of reaction R139 is one order of magnitude greater than the grade of rate control of the reaction R022. Reaction R139 limits the rate of NH_3 consumption since it governs the NH_2 consumption. As much as the NH_2 consumption is limited, the NH_3 oxidation in the gas phase decrease. In addition, due to the N_2O formation, the reaction R139 limits the NO formation as an oxidation product of NH_3. In the presence of NO, the reduction route is direct through the sucesive process drived by reactions R022 and R139. This behaviour due to the reaction R139 is coherent with was stablished by Song [Son 2016] saying that this reaction is part of the main chain – terminating species. Shresta [Shr 2018] have indicated that the reaction R022 ($NO + HO_2 \rightarrow OH + NO_2$) is particulary important in the formation NO_2 and its sensitivity increases with increasing the temperature.

Shrestha [Shr 2018] have indicated that additionally to the reaction R022, there are other reactions like ($NO_2 + HO_2 \leftrightarrow HONO + O_2$) not included in the AA – Mech [Kil 1999] [Cod 2001] which compites in the consumption of the HO_2 radicals.

Another way to produce N_2O is the reaction R052. A study of Diau [Dia 1995] of the NO – H_2 system showed this reaction as a rate limiting in the N_2O formation, as was shown in the results presented in Figure 11. The N_2O formation by means of this reaction limits the NH_3 oxidation in the gas phase since it competes with its oxidation to N_2O. Finally, from the information in Figure 11, it follows that reaction R052 has no significant effect on the rate of NO formation.

$$HNO + NO \rightarrow N_2O + OH \qquad \textbf{R052}$$

Miller [Mill 1983] reported that the increase of NO reduction is coincident with the increase in the N_2O concentration in the gas phase. Figure 19 shows it, this effect is practically independent of the progress of the reaction RI ($4NH_3 + 5O_2 \rightarrow 4NO + 6H_2O$) ($\xi_{RI}$).

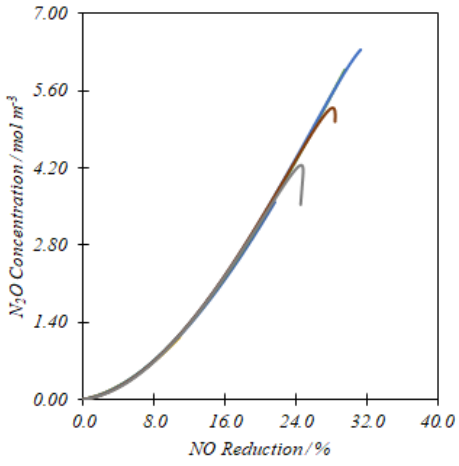

Figure 19. Effect of the NO reduction over the N_2O generation.
Parameter: progress of the reaction RI ($4NH_3 + 5O_2 \rightarrow 4NO + 6H_2O$) ($\xi_{RI}$) according to equation 106.Simulations made with CANTERA [Goo 2017].

There are different inhibitory effects on the NO_2 formation. First, as Figure 20 shows, reactions R087 and R141 are inhibitory for long residence times and high progresses of reaction RI (ξ_{RI}). These conditions favor the reduction of NO_2 to NO instead of its formation. The same figure shows that since the net rate of the reaction R087 can be up to 8 times greater than it for the reaction R141, the N_2O formation, according to these reactions, takes place mainly before 67.5% of NH_3 consumption ($\xi_{RI} < 67.5\%$) and for residence times less than 2.0 s. Secondly, the reaction R024 has an inhibitory effect on the NO_2 formation since it consumes part of the available HO_2, which in other case reacts according to the reaction R022 ($NO + HO_2 \rightarrow OH + NO_2$) to produce NO_2.

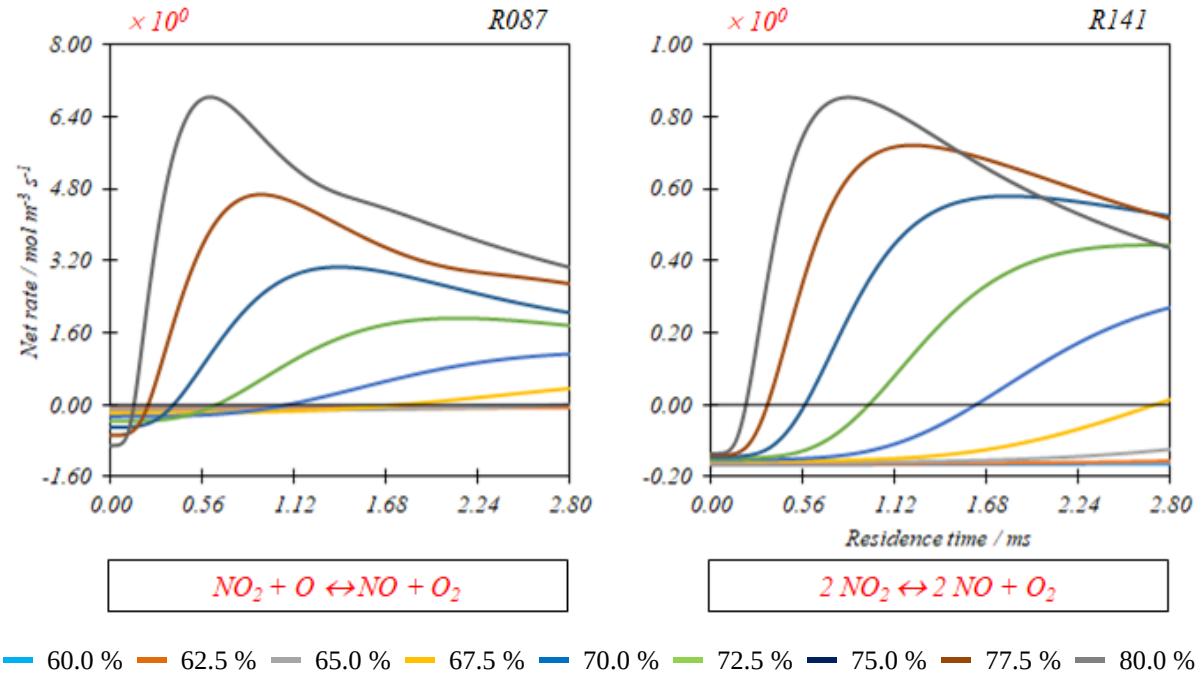

Figure 20. The net rate of reactions associated with the NO_2 / NO system (R087 and R141). Parameter: progress of the reaction RI ($4NH_3 + 5O_2 \rightarrow 4NO + 6H_2O$) ($\xi_{RI}$). according to equation 106.
Simulations made with CANTERA [Goo 2017].

$$NO_2 + O \leftrightarrow NO + O_2 \qquad \textbf{R087}$$

$$2NO_2 \leftrightarrow 2NO + O_2 \qquad \textbf{R141}$$

$$HO_2 + OH \rightarrow H_2O + O_2 \qquad \textbf{R024}$$

By means of the interaction between NH_2 and HO_2 throug the reaction R114 ($HO_2 + NH_2 \leftrightarrow H_2NO + OH$), Song [Son 2016] described part of the HO_2 conversion to OH. Even know that the AA – Mech [Kil 1999] [Cod 2001] propouse the same reaction parameters, this reaction has not significant role under the conditions of this investigation. In fact, in Figure 11, it was shown that this reaction has a control effect in order of magnitude of 10^{-3} for each mayor species.

From the information in Figure 11, it is observed that reactions R087 and R141 have the same qualitative control effect on the rate of the NH_3 consumption and the NO formation in the gas phase. However, the effect of reaction R087 is one order of magnitude greater. The reaction R087 limits the NH_3 oxidation in the gas phase due to the O – atom consumption for the NO_2 reduction instead of the NH_3 oxidation. Additionally, the reaction R087 is a limiting step of the NO formation in the gas phase,

since it has both possibilities: to favor its formation and to favor its oxidation according to the equilibrium described by it.

From the information in Figure 11, it is observed that the reaction R083 inhibits the NH_3 oxidation in the gas phase and is a limiting step in the rate of NO formation. According to this reaction, the N – atom oxidation occurs by a route contrary to oxidation leaded by NH_3. Allen [All 1995] indicated that reactions R022 ($NO + HO_2 \rightarrow OH + NO_2$), R083 and R087 ($NO_2 + O \leftrightarrow NO + O_2$) dominate the consumption of O – atoms, leaving few to be consumed through reaction R048.

$$NO + O + M \leftrightarrow M + NO_2 \quad \textbf{R083}$$

$$H_2O + O \rightarrow 2OH \quad \textbf{R048}$$

According to Figure 11, the reaction R048 is a limiting step for the NH_3 oxidation in the gas phase. This is because it favors the OH formation which is an important radical in the process of NH_3 oxidation in the gas phase. On the other hand, this reaction does not directly have an important effect on the rate of NO generation.

The NO_2 reacts according to the reactions R138 and R113, respectively. The reaction R083 ($NO + O + M \leftrightarrow M + NO_2$) also contributes to the NO_2 formation. Figure 21 presents the comparison between the net rates of reactions for the NO_2 formation. The control of NO_2 formation by means of the reaction R022 ($NO + HO_2 \rightarrow OH + NO_2$) (which has been presented in section 5.3.2) had been earlier reported by Miller [Mill 1989].

For low values of residence time (less than 2.0 ms) and for values of the progress of the reaction RI ($4NH_3 + 5O_2 \rightarrow 4NO + 6H_2O$) ($\xi_{RI}$) less than 75.0 %, the effect of the reaction R083 is like the effect of the reaction R138, both contribute to the NO_2 formation. However, the rate of NO_2 generation due to the reaction R138 is up to three times higher. With the increase in the progress of the reaction RI (ξ_{RI}), the general tendency of these two reactions is to consume NO_2. Song [Son 2016] and Klippenstein [Klip 2013] have reported that the NH_3 oxidation in the gas phase occurs to a significant extent through the H_2NO intermediate. However, the rate constants for the reactions that consider this species are still quite uncertain, for that reason certain studies suggest that the H_2NO chemistry was not a significant contribution in the NO reduction [Shr 2018].

$$NO_2 + NH_2 \leftrightarrow H_2NO + NO \quad \textbf{R138}$$

$$NO_2 + HNO \rightarrow HONO + NO \quad \textbf{R113}$$

From the point of view of the degree of rate control, reactions R138 and R113 inhibit the NO formation. However, the effect of reaction R113 is almost null. Shrestha [Shr 2018] sugested that the reaction R138 is the more important channel recycling NO_2 back to NO, behaviour that have been observed in experimental studies. Meanwhile, the reaction R113 inhibits the NH_3 oxidation in the gas phase because it does not promote the NO_X reduction.

Klippenstein [2013] have reported that the branching ratio between reactions R138 and R139 ($NO_2 + NH_2 \rightarrow H_2O + N_2O$) is determinating in the effect of NO_2 in the gas phase process between NH_3 and NO where NO_2 is converted first to NO then to minor amounts of N_2O.

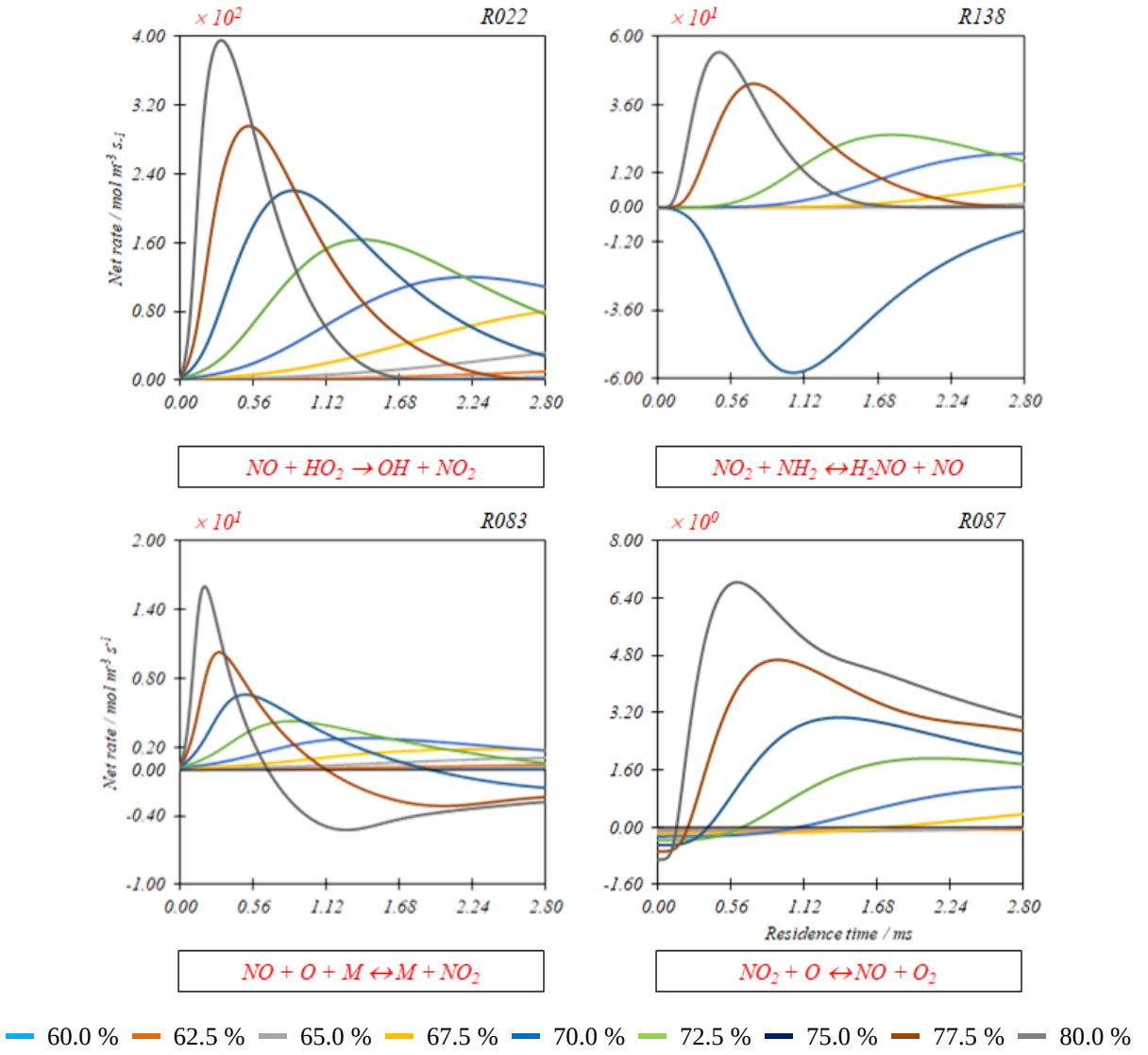

Figure 21. The net rate of reactions associated with NO_2 (R022, R138, and R083).
Parameter: progress of the reaction RI ($4NH_3 + 5O_2 \rightarrow 4NO + 6H_2O$) ($\xi_{RI}$) according to equation 106.
Simulations made with CANTERA [Goo 2017].

Reaction R086 ($NNH + O_2 \rightarrow N_2 + HO_2$) (which was presented in section 5.3.1) is the main HO_2 production route required for NO oxidation according to the reaction R022 ($NO + HO_2 \rightarrow OH + NO_2$). Additionally, the previously presented reaction R115 ($NH_3 + O_2 \rightarrow NH_2 + HO_2$) and the following reactions R009 and R082 also contribute to HO_2 formation.

$$H + O_2 + M \rightarrow M + HO_2 \qquad \textbf{R009}$$

$$HNO + O_2 \rightarrow NO + HO_2 \qquad \textbf{R082}$$

Figure 22 shows the comparison between net rates for reactions associated with HO_2 formation. The net rates of reactions R009 and R082 are practically the same, and their effect is similar over time. Therefore, these reactions occur simultaneously and produce a synergistic effect. However, according to Figure 11, although both reactions inhibit the NH_3 consumption, the effect of reaction R082 is lower than the effect of reaction R009. In fact, Shrestha [Shr 2018] indicated that the reactions involving HO_2

like R009 are generally found to be more sensitive at high pressure. However, reaction R082 has been considered an important step on the path to the formation of NO in the gas phase. Without being the same, the parameters for calculating the reaction rate using the AA – Mech [Kil 1999] [Cod 2001] have the same order of magnitude as the parameters previously reported [Son 2016].

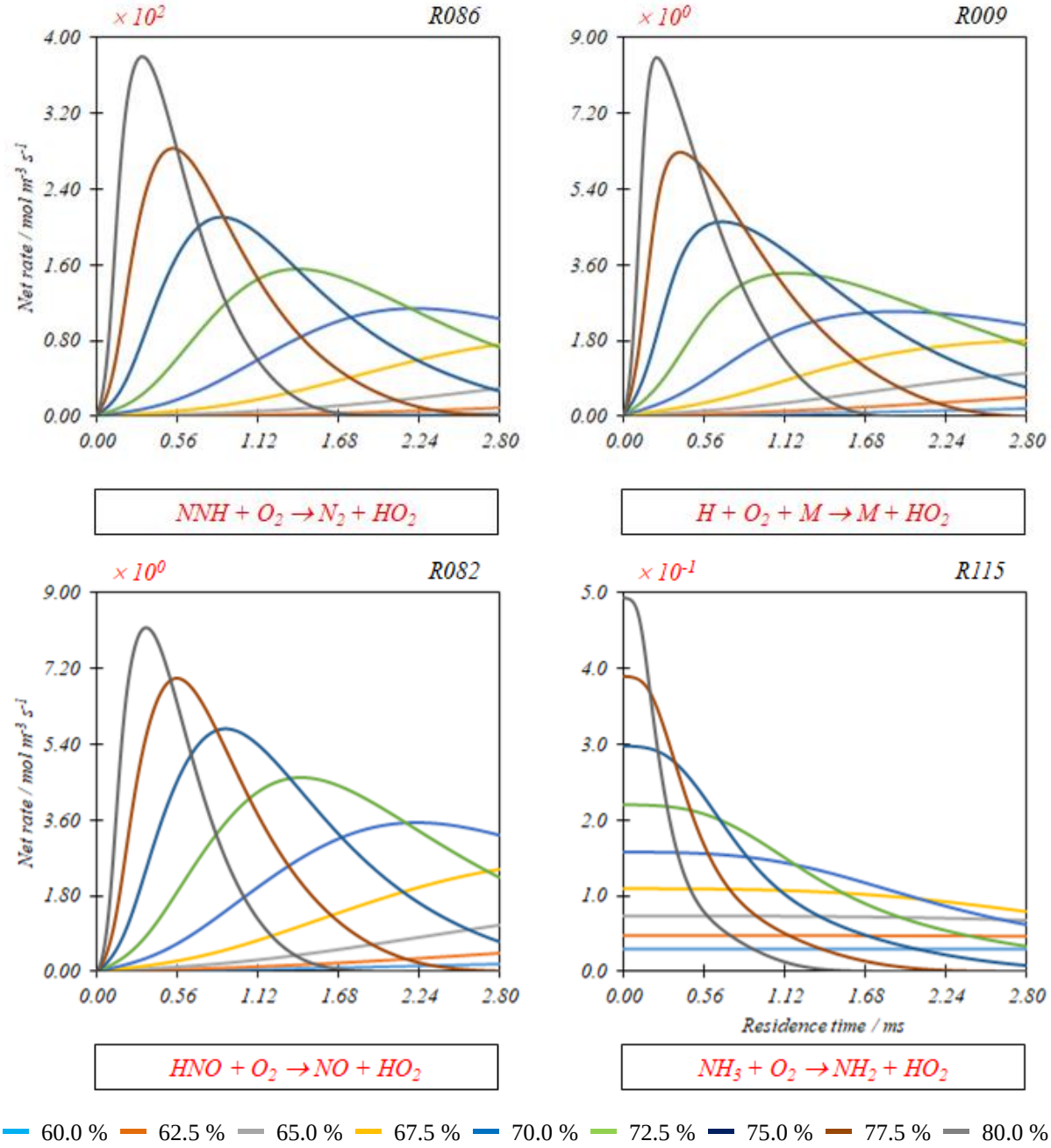

Figure 22. The net rate of reactions associated with the HO_2 generation (R086, R009, R082, and R115).
Parameter: progress of the reaction RI ($4NH_3 + 5O_2 \rightarrow 4NO + 6H_2O$) ($\xi_{RI}$) according to equation 106.
Simulations made with CANTERA [Goo 2017].

The effect of reaction R115 ($NH_3 + O_2 \rightarrow NH_2 + HO_2$) remains for the entire process time. Of course, the decrease in NH_3 concentration causes the net rate of this reaction to decrease but never be

zero. Therefore, under simulation conditions, if there is NH_3, there is NH_2 generation in the gas phase and an eventual NO reduction during the process.

Figure 11 shows that like the reaction R009, the reaction R082 is a step that inhibits the NH_3 oxidation in the gas phase and limits the NO formation. Although qualitatively the effect of reaction R009 is the same, from a quantitative point of view the effect of rate control of reaction R082 is one order of magnitude greater.

The inhibition of NH_3 oxidation in the gas phase due to these reactions is a product of the O_2 consumption for the oxidation of other species rather than NH_3. The effect as a limiting step of the rate of NO generation, although not significant, is evidently due to the direct NO formation from the process that drived by these reactions.

The HNO, required for the NO and NO_2 formation due to reactions R052 ($HNO + NO \rightarrow N_2O + OH$) and R082 ($HNO + O_2 \rightarrow NO + HO_2$), reacts according to reaction R019 as well. Due to the OH formation for short residence times, this reaction constitutes a route of process termination.

$$HNO + OH \rightarrow H_2O + NO \qquad \textbf{R019}$$

According to the information in Figure 11, the reaction R019 is a limiting step of both the rate of the NH_3 oxidation and the NO generation in the gas phase. This is particularly because this reaction constitutes a step of process completion. In fact, Song [Son 2016] have reported that the interaction between the radicals HNO and OH plays a significant role as a chain terminate step and inhibiton of NH_3 consumption.

Reactions R098 and R102 form HNO. Figure 23 shows that the effect of both reactions has a similar duration in the process time. However, for a given value of the progress of the reaction RI ($4NH_3 + 5O_2 \rightarrow 4NO + 6H_2O$) ($\xi_{RI}$), the net rate of reaction R098 is slightly higher.

$$H_2NO + NO \rightarrow 2HNO \qquad \textbf{R098}$$

$$H_2NO + OH \rightarrow HNO + H_2O \qquad \textbf{R102}$$

From the point of view of the degree of rate control, neither the reaction R098, nor the reaction R102 has an important effect on the NO generation in the gas phase. Considering the NH_3 oxidation the gas phase, the reaction R102 limits this chemical process by being a step in which the process is finished (H_2O formation) and at the same time generates an important radical (HNO) for the selective non – catalytic reduction of NO. On the other hand, the reaction R098 inhibits the NH_3 oxidation as it favors an alternative route for the NO reduction.

Klippenstein [Klip 2013] and Song [Son 2016] stablished that other important route to consume H_2NO is due to the reaction R099 ($H_2NO + NO_2 \rightarrow HNO + HONO$) and although the parameters for calculating the reaction rate are the same as those proposed in the AA – Mech [Kil 1999] [Cod 2001], this reaction has not been included in the reduced mechanism, as shown in Figure 11, the control effect of the reaction R099 has an order of magnitude near to 10^{-3}.

Song discussed as well about the importance of the interaction between the radical H_2NO and the O_2 througt the reaction ($H_2NO + O_2 \rightarrow HNO + HO_2$). They have found a high positive sensitivity coefficient at their process conditions and is favored by oxidizing conditions. It yields HO_2 radicals, which is converted to the more reactive OH radical. This reaction is not considered in the AA – Mech [Kil 1999] [Cod 2001].

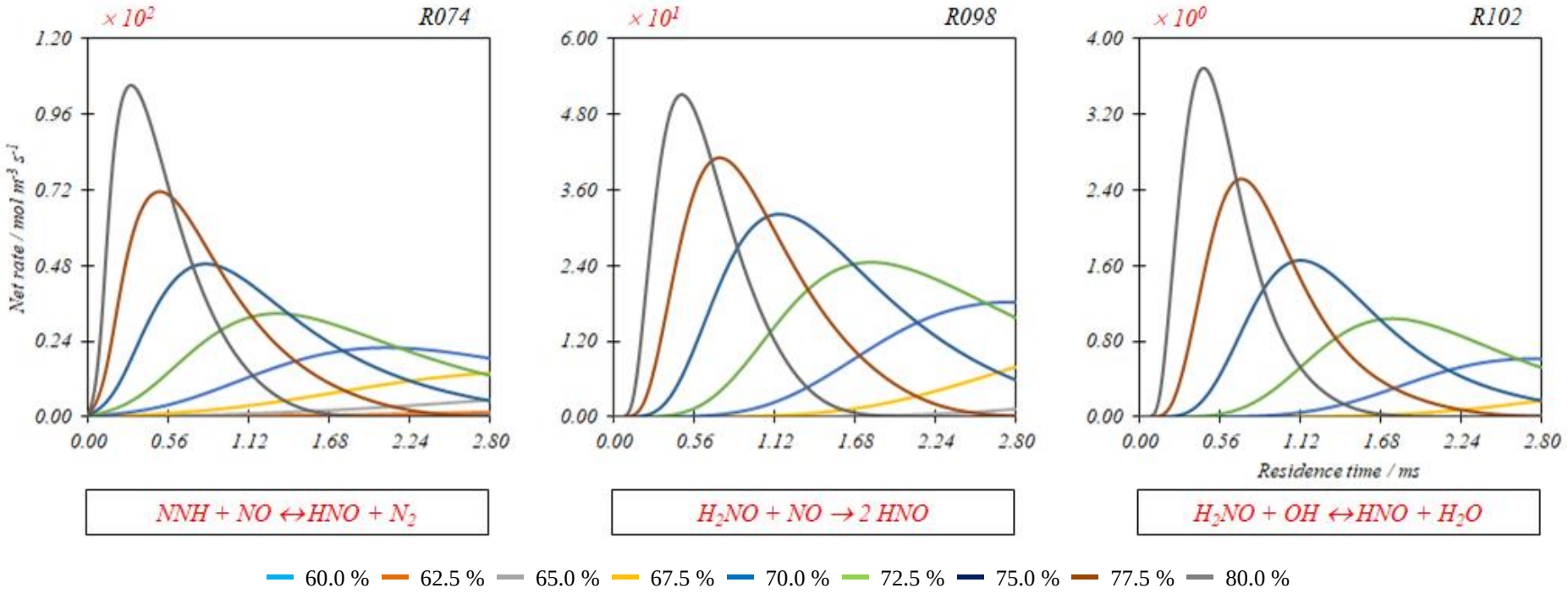

Figure 23. The net rate of reactions associated with the HNO generation.
Parameter: progress of the reaction RI ($4NH_3 + 5O_2 \rightarrow 4NO + 6H_2O$) ($\xi_{RI}$) according to equation 106.
Simulations made with CANTERA [Goo 2017].

Another route for the NO formation is the HONO decomposition according to the reaction R126.

$$HONO + M \rightarrow M + NO + OH \qquad \textbf{R126}$$

Although from the point of view of Figure 11, this reaction does not have an important control effect on the rate of the NO generation. Evidently the NO formation described by it acts as a limiting step in the NH_3 oxidation in the gas phase. The same conclusion has been proposed be Shrestha [Shr 2018].

Reaction R025 favors the N_2 formation of by means of the N_2O decomposition. Lindstedt [Lin 1994] and Miller [Mill 1989] indicated that for lean and moderately rich NH_3 / air mixtures, the principal N_2O reduction is due by this reaction. Shrestha [Shr 2018] indicated this reaction to be an important route for the activity of N_2O as an oxidizing agent. In early studies using static and flow reactors, Allen [All 1995] showed that N_2O decomposes heterogeneously on even relatively inert surfaces such as quartz and silica with overall energy of activation that is small in comparison to that for the gas phase reaction. Gardiner [Gar 2000] stablished the thermo molecular character of the reaction R025 implies that it becomes more important at higher pressures. In a study of N_2O decomposition Allen [Allen 1994] suggests that using the Miller [Mill 1989] parameters predict too much NO_2 and few NO. The direct N_2O reduction to N_2 according to the reaction R025 is of course a step that inhibits both the NH_3 oxidation and the NO generation in the gas phase. In is interesting that the N_2O descomposition in the gas phase was reported in an exclusively dedicated study made by Gonzalez [Gon 2017] about the catalytic oxidation of NH_3 over Pt. Gonzalez indicates that the homogeneous gas – phase decomposition of N_2O occurs to a significant extent in the reactor system at temperatures higher than 1100 K. This is consistent with what is presented in Figure 11.

$$N_2O + M \rightarrow M + O + N_2 \qquad \textbf{R025}$$

4.2.3. OH formation

Although the routes for the OH formation through the reactions R073 ($NH_2 + NO \rightarrow OH + NNH$) and R022 ($NO + HO_2 \rightarrow OH + NO_2$) are the most important, there are other additional routes for the formation of this fundamental radical of the gas phase process, such as reactions R015, R016, and R076 based on the H – atom. Several authors [Mill 1989] [Tay 2007] [Mat 2015] have reported that the reaction R076 is a source of important intermediate species for the NH_3 reactions in the gas phase.

$$H + NO_2 \rightarrow NO + OH \qquad \textbf{R015}$$

$$H + H_2O \leftrightarrow H_2 + OH \qquad \textbf{R016}$$

$$H + O_2 \rightarrow O + OH \qquad \textbf{R076}$$

When the progress of the reaction RI ($4NH_3 + 5O_2 \rightarrow 4NO + 6H_2O$) ($\xi_{RI}$) is greater than 70.0 %, which implies the H_2O presence in the reactive system, the reaction R016 allows the OH formation. For lower progress of the reaction RI (ξ_{RI}), this OH formation path is irrelevant. Indeed, Figure 24 shows that the increase in the H_2O concentration (increase in the progress of the reaction RI (ξ_{RI})) increases the OH formation in short residence times.

The comparison between Figures 21 and 24 shows that the principal NO_2 removal step is reaction R015. The reaction R087 ($NO_2 + O \leftrightarrow NO + O_2$) has a lower effect over the NO_2 abatement.

For this last reaction, removal occurs when the progress of the reaction RI (ξ_{RI}) is greater than 67.5 %. As greater the progress of the reaction RI (ξ_{RI}), greater the range of residence times in which the NO_2 reduction is effective. These characteristics of the NO_2 consumption have already been reported by Miller [Mill 1989] and Shrestha [Shr 2018]. The accuracy of the predictions of the NO_2 concentrations in the gas phase is dependent both on the accuracy of the kinetic parameters of reactions R022 ($NO + HO_2 \rightarrow OH + NO_2$) and R015, and on the accuracy of the calculation of the diffusional transport of the molecules, especially for NO (reaction R022) and H – atoms (reaction R015). Gardiner [Gar 2000] had reported that the reaction R015 is expected to be fast, and the pressure has a low effect on it.

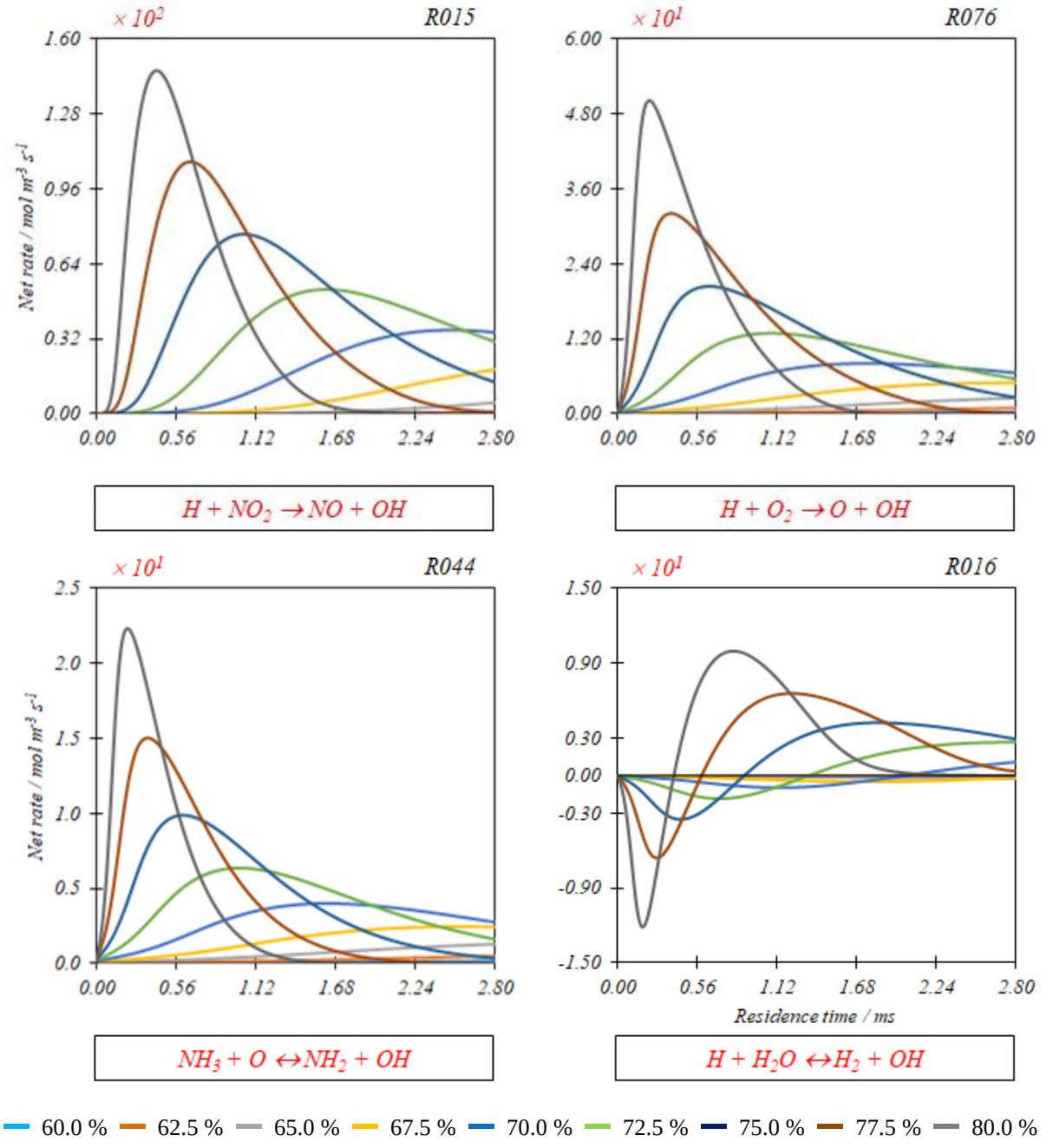

Figure 24. The net rate of reactions associated with the OH formation (R015, R076 and, R016). Parameter: progress of the reaction RI ($4NH_3 + 5O_2 \rightarrow 4NO + 6H_2O$) ($\xi_{RI}$) according to equation 106.
Simulations made with CANTERA [Goo 2017].

According to the information presented in Figure 11, the effect of reactions R015 and R076 ($H + O_2 \rightarrow O + OH$) on the degree of rate control is the same, even in quantitative terms. Both reactions are limiting steps for the rate of the NH_3 oxidation in the gas phase because in both the H – atom produced by the successive extractions from NH_3 interacts with other species in the reactive medium. Additionally, because the reaction R015 is an unlikely route of NO formation from NO_2 and the reaction R076 favors the O_2 interaction with H – atom instead of its reaction with NH_2 or any of the other nitrogenous species, both reactions inhibit the NO formation in the gas phase. Shrestha [Shr 2018] reported that the reaction R015 is particulary important in the consumption of NO_2, they argued that this reaction has been discussed as a step that promots the reactivity of the system by forming OH even when its rate constant is decreased by 50.0 % to fit several experimental results.

On the other hand, the reaction R16 ($H + H_2O \leftrightarrow H_2 + OH$) is a limiting step for the rates of NH_3 oxidation and NO formation in the gas phase. This is due to its potential to form H – atom and OH, which are essential to carry out both processes. In particular, the effect on the rate of NH_3 oxidation in the gas phase is greater since the formed radicals participate in reactions that favor this process instead of those that contribute to the NO formation in the gas phase.

Reaction R044 has a rate lower than the rate of reaction R126 ($HONO + M \rightarrow M + NO + OH$), which forms OH from HONO. Reaction R076, is the main route for the formation of required O – atom for reaction R044. Several authors [Mill 1989] [Tay 2007] have reported that the reaction R048 ($H_2O + O \rightarrow 2OH$), contributes to the OH formation as well, certainly at a lower level.

$$NH_3 + O \rightarrow NH_2 + OH \qquad \textbf{R044}$$

The effect of rate control of the reaction R044 ($NH_3 + O \rightarrow NH_2 + OH$) is obviously the inhibition of the NH_3 oxidation since, through this reaction, the process is carried out by means of O – atom, which is much less related to interact with the NH_3 than, for example, O_2 or OH.

4.2.4. Effect of HNO

Reaction R140 ($NNH + O_2 \rightarrow N_2 + H + O_2$), is the main production route of the H – atom required for the OH formation. However, H – atom can also be formed by means of the reaction R050, as has been reported by Takeyama [Tak 1967], Miller [Mill 1989] and Tayyeb Javed [Tay 2007]. Lindstedt [Lin 1994] reported that in $NH_3 - O_2$ mixtures reaction R050 dominates the HNO consumption.

$$HNO + M \rightarrow M + H + NO \qquad \textbf{R050}$$

Figure 25 shows how the effect of the reactions R050 and R140 ($NNH + O_2 \rightarrow N_2 + H + O_2$) is similar during the residence time of the process. According to this figure, the net rate of the reaction R050 is only higher than the net rate of the reaction R140 for the progress of the reaction RI ($4NH_3 + 5O_2 \rightarrow 4NO + 6H_2O$) ($\xi_{RI}$) equal to 80.0 %.

Figure 26 shows how reactions R113 ($NO_2 + HNO \rightarrow HONO + NO$) and R019 ($HNO + OH \rightarrow H_2O + NO$) reinforce the HNO reaction. Particularly reaction R113 has a relevant effect for the progress of the reaction RI (ξ_{RI}) greater than 65.0 %. The reaction R019 is relevant when the same parameter is higher than 67.5 %.

According to the information in Figure 11, the reaction R050 ($HNO + M \rightarrow M + H + NO$) inhibits both the NO formation and the NH_3 oxidation in the gas phase, although the effect on this last

process is greater. Further, it inhibits the NH_3 oxidation, as it constitutes an alternative route for NO formation.

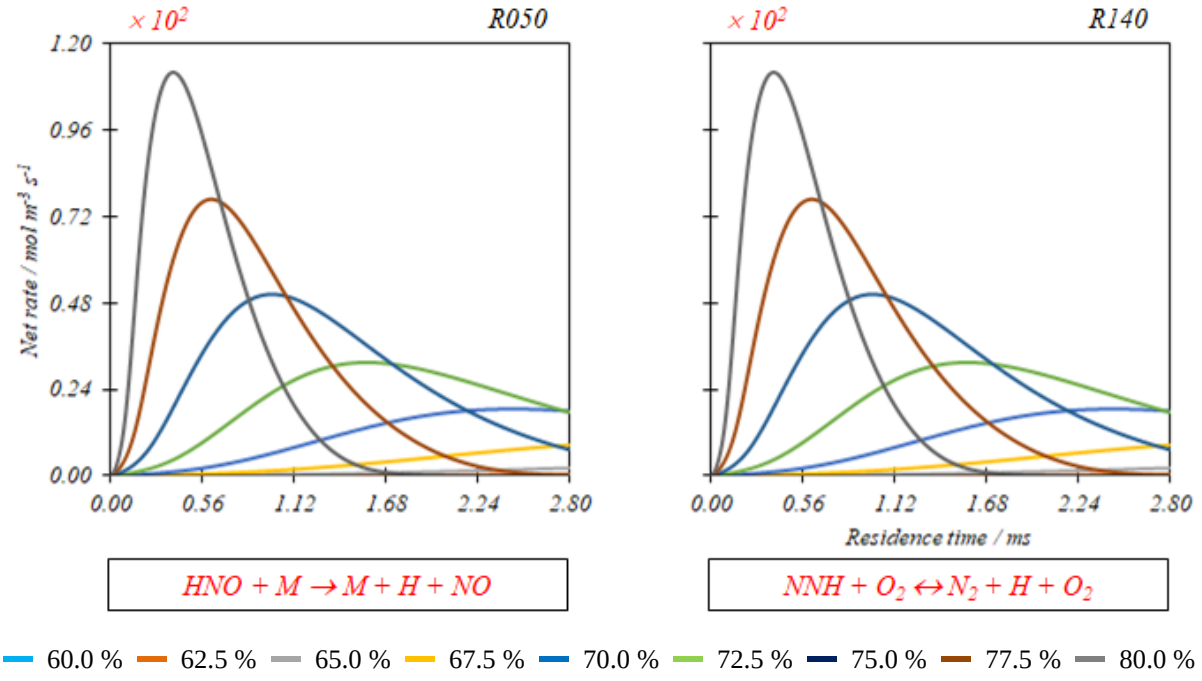

Figure 25. The net rate of reactions associated with the H – atom formation (R050 and R140). Parameter: progress of the reaction RI ($4NH_3 + 5O_2 \rightarrow 4NO + 6H_2O$) ($\xi_{RI}$) according to equation 106.
Simulations made with CANTERA [Goo 2017].

Klippenstein [Klip 2011] have studied widly the effect of NNH over the NO formation and consumption in the gas phase. Their results agree with the pathway propoused in this study. Beginning with the NH_3 convertion to NH_2 with the O / H radical pool, specially thorough OH and reaction R045 ($NH_3 + OH \rightarrow NH_2 + H_2O$), the reactions R071, R072 ($NH_2 + NO \rightarrow N_2 + H_2O$), and R073 ($NH_2 + NO \rightarrow OH + NNH$) are key steps in the process. Those reactions simultaneously remove No and produce free radicals to sustain the reaction. The effect of reactions R076 ($H + O_2 \rightarrow O + OH$) and R048 ($H_2O + O \rightarrow 2OH$) leeds to the formation of hydroxyl radicals due to R073 and mantein the process in the gas phase specially at high temperatures.

4.2.5. Self – sustainability of the NO reduction

After considering the reactions for NH_2 formation due to H – atom abstraction [R045 ($NH_3 + OH \rightarrow NH_2 + H_2O$), R120 ($HONO + NH_2 \rightarrow NO_2 + NH_3$), R044 ($NH_3 + O \rightarrow NH_2 + OH$), R013 ($NH_3 + H \rightarrow NH_2 + H_2$), and R115 ($NH_3 + O_2 \rightarrow NH_2 + HO_2$)], for most conditions, the primary abstraction reaction is the reaction R045. However, Miller [Mill 1989] had reported that for lean conditions reaction with O – atoms as R044 and for rich conditions reaction with H – atoms as R013 also make significant contributions to the NH_2 formation. Indeed, under the conditions presented here, in which the mixing conditions are always lean in NH_3, the reaction R013 presents the lowest net rate, as was shown in Figure 11. The rate constants for the above reactions do not have significant scatter. For these reactions Lindstedt [Lin 1994] had found good agreement between the values reported by different authors. As

had been reported by Tayyeb Javed [Tay 2007] the chemical reactions R044 and R045 show that it is possible to start the process both in the absence and presence of H_2O.

Reactions R009 ($H + O_2 + M \rightarrow M + HO_2$), R016 ($H + H_2O \leftrightarrow H_2 + OH$), and R076 ($H + O_2 \rightarrow O + OH$) are those of the system of H and O – atoms, and reactions R045, R013 and R044 are the main reactions for NH_3 consumption. As had been reported by Fujji [Fuj 1981], the Figure 11 shows that the reactions R044 and R045 are retarding reactions for the NH_3 oxydation in the gas phase.

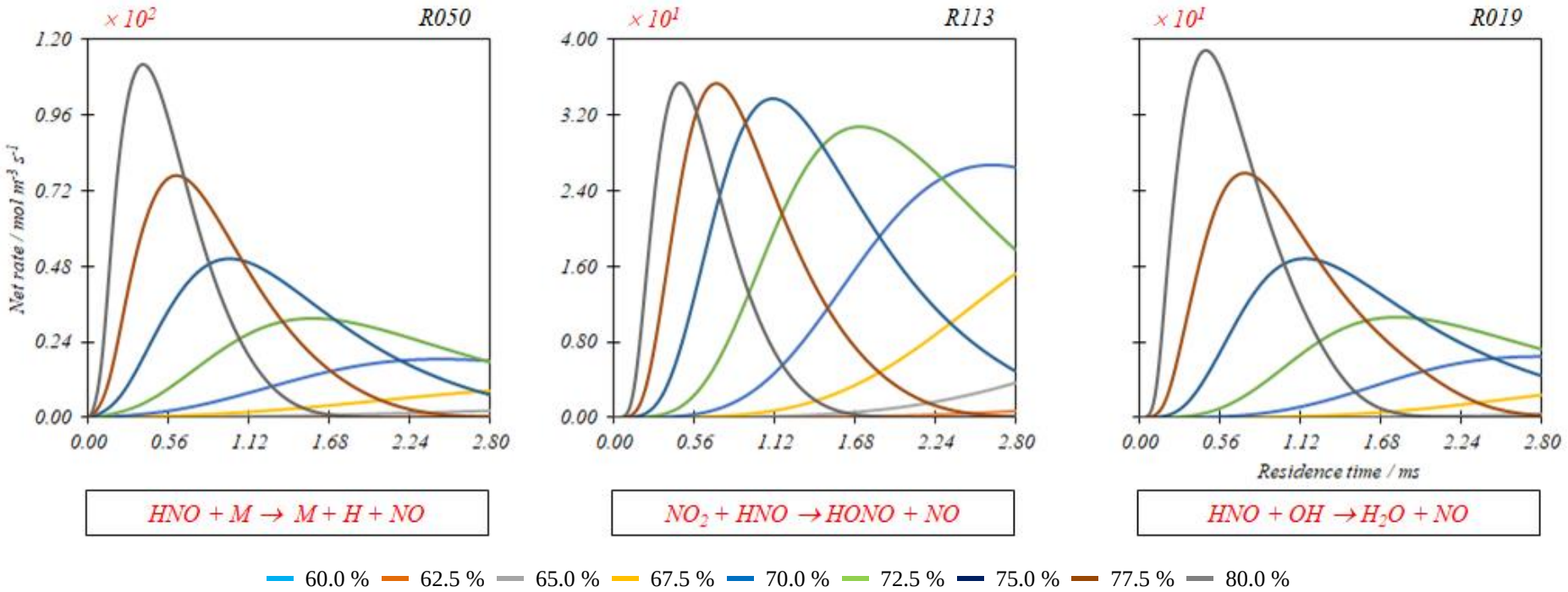

Figure 26. The net rate of reactions associated with the HNO reactions (R050, R113, and R019).
Parameter: progress of the reaction RI ($4NH_3 + 5O_2 \rightarrow 4NO + 6H_2O$) ($\xi_{RI}$) according to equation 106.
Simulations made with CANTERA [Goo 2017].

As is showed in Figure 27, to be self – sustaining, the NH_2 + NO reactions must directly or indirectly regenerate OH and O – atom to continue the NH_3 abstraction to NH_2 via reactions R044 and R045. The reactions R071 ($NH_2 + NO \rightarrow N_2 + H_2O$), R072 ($N_2 + H_2O \rightarrow NH_2 + NO$), and R073 ($NH_2 + NO \rightarrow OH + NNH$) are dependent on the formation of the NH_2 from reactions R013, R044 and R045, which in turn depend on the O – atom and OH concentrations. The above indicates that if the reaction R073 occurs, the OH radical is regenerated to continue the NH_3 conversion as had been shown by Tayyed Javed [Tay 2007].

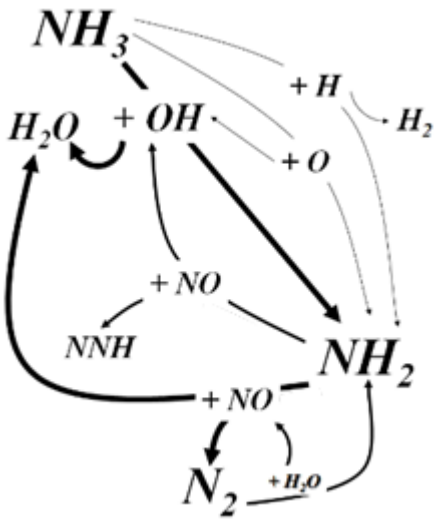

Figure 27. Self – sustainability of the NO reduction.

At lower temperatures reactions R076 ($H + O_2 \rightarrow O + OH$) and R048 ($H_2O + O \rightarrow 2OH$), which are strongly dependent on temperature, have a low rate and do not form enough OH to convert NH_3 to NH_2. Caton [Cat 1989] explained that it is because reaction R048 competes for O – atoms and inhibits the NH_2 formation by the reaction R044, shifting the NO reduction to slightly higher temperatures. With this behaviour, Tayyeb Javed [Tay 2007] explained that the low amount of formed NH_2 cannot follow the path of the reaction R071 for the NO reduction.

4.2.6. Cyclic processes in the NOx formation

In any case, there are two chemical cycles between the HNO, HONO, NO, and NO_2. Figure 28 presents these cycles. First, the reaction R120 produces NO_2. This also interacts with H_2O according to reaction R122. The increase in the progress of the reaction RI ($4NH_3 + 5O_2 \rightarrow 4NO + 6H_2O$) ($\xi_{RI}$) also favors these reactions.

$$HONO + NH_2 \rightarrow NO_2 + NH_3 \qquad \textbf{R120}$$

$$NO_2 + H_2O \rightarrow HONO + OH \qquad \textbf{R122}$$

According to the information in Figure 11, the reaction R120 is a limiting step for both the NO formation and the NH_3 oxidation, although the effect on the NH_3 oxidation is greater. However, it is an oxidation path of NH_3 for the successive NH_2 formation, it is a very low – rate step compared to others that favor the extraction of H – atom from NH_3.

In agreement with Duynslägher [Duy 2012] several reactions are involved in the NO_2 formation and consumption. Produced through reactions R120 and R022 ($NO + HO_2 \rightarrow OH + NO_2$) , and

consumed by the reaction R015 ($H + NO_2 \rightarrow NO + OH$). Mean while NH_3 exist and produce NH_2, the reaction R120 takes place along all gas phase and allow to explain its presence at outlet of reactor.

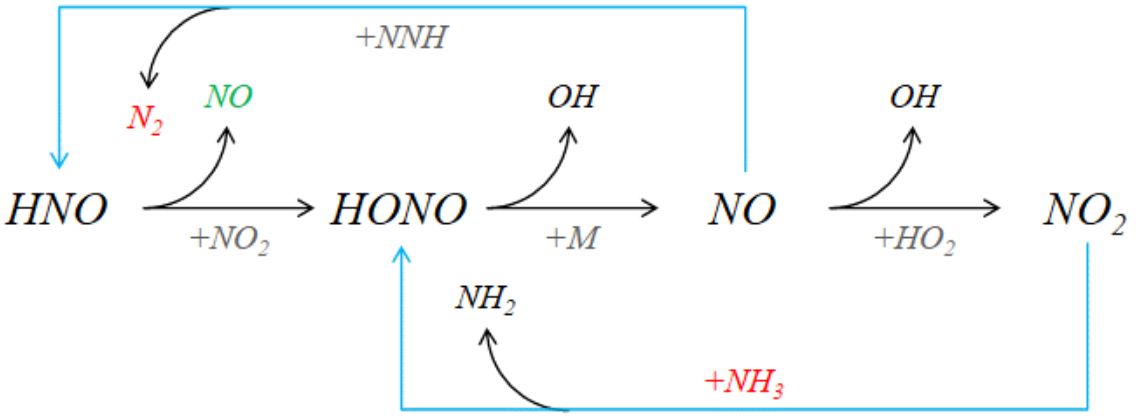

Figure 28. Cyclic processes in the NO_X formation.

Shrestha [Shr 2018] indicated that knowing that the reaction R126 ($HONO + M \rightarrow M + NO + OH$) is more important at low NO concentrations, with its increment the reaction R122 becomes important and together with reactions R133 and R050 ($HNO + M \rightarrow M + H + NO$) it forms a chain terminating sequence in the process.

Figure 29 shows that for the progress of the reaction RI (ξ_{RI}) greater than 65.0 %, the effect of the reaction R122 remains throughout the residence time. According to the information in Figure 11, the reaction R120 is a limiting step for the NH_3 oxidation and has an almost null control effect on NO formation. However, it is an OH formation route for the successive NH_2 formation from the NH_3 dehydrogenation, it is a very low – rate step compared to others that favor OH formation.

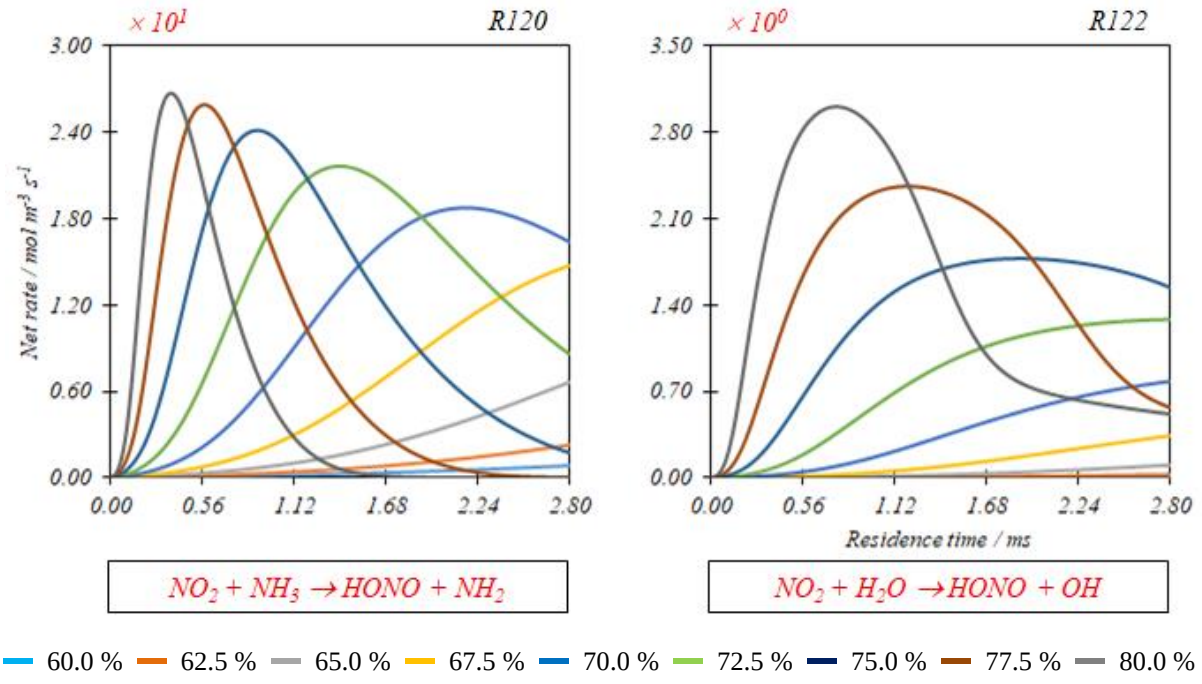

Figure 29. The net rate of reactions associated with the HONO generation (R120 and R122). Parameter: progress of the reaction RI ($4NH_3 + 5O_2 \rightarrow 4NO + 6H_2O$) ($\xi_{RI}$) according to equation 106.
Simulations made with CANTERA [Goo 2017].

Second, the NO reacts with the NNH according to the reaction R074. Due to the NO requirement, this reaction is more important with the progress of the reaction RI ($4NH_3 + 5O_2 \rightarrow 4NO + 6H_2O$) ($\xi_{RI}$). The reaction R051 regenerates the initial substances of the process.

$$NO + NNH \rightarrow HNO + N_2 \qquad \textbf{R074}$$

$$HNO + NH_2 \rightarrow NH_3 + NO \qquad \textbf{R051}$$

According to Figure 11, reactions R074 and R051 are limiting steps for the NH_3 oxidation in the gas phase, although the effect of reaction R074 is one order of magnitude greater. In both reactions, species from the NH_3 oxidation are consumed (NNH and NH_2). In addition, the reaction R074 is obviously a limiting step in the NO generation as it leads to its reduction, while the effect of reaction R051 on the rate control of the NO generation is almost null.

At this point, it should be noted that the NO reduction could also occur by means of the NNH according to the reactions R074 or R140 ($NNH + O_2 \rightarrow N_2 + H + O_2$). However, as shown in Figure 30, for the progress of the reaction RI (ξ_{RI}) greater than 77.5 %, the reaction R074 has a slightly higher net rate at a given residence time. As Miller [Mill 1989] had reported, to promote the NH_3 oxidation the reaction R074 is preferable, in which although there is a N_2 generation, also allows the HNO formation as an intermediate in the NH_3 oxidation to NO production. After presenting the reactions associated with NNH [R073 ($NH_2 + NO \rightarrow OH + NNH$), R074 ($NO + NNH \rightarrow HNO + N_2$), R086 ($NNH + O_2 \rightarrow N_2 + HO_2$), and R140 ($NNH + O_2 \rightarrow N_2 + H + O_2$)] it must be said as had been reported by Gardiner [Gar 2000] that, in effect, no pressure dependence is expected for any of the radical reactions with NNH.

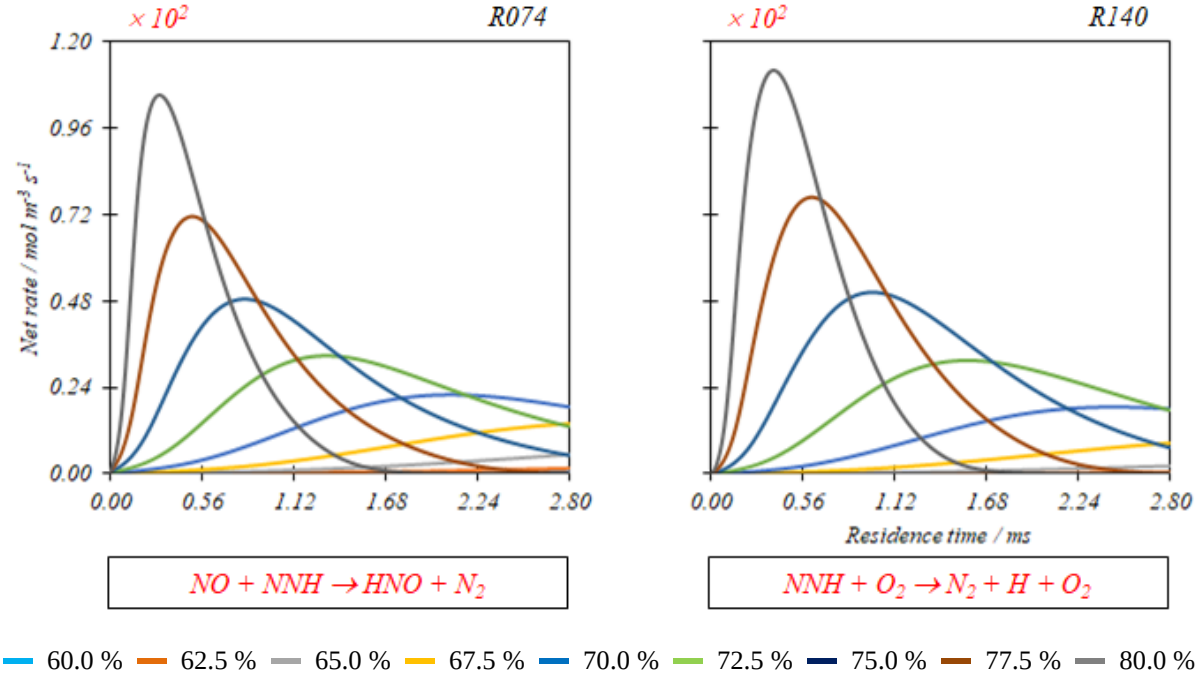

Figure 30. The net rate of reactions associated with the NO reduction by NNH (R074 and R140). Parameter: progress of the reaction RI ($4NH_3 + 5O_2 \rightarrow 4NO + 6H_2O$) ($\xi_{RI}$) according to equation 106.
Simulations made with CANTERA [Goo 2017].

At high temperatures, the reactions of NH_2 oxidation, which leads to the NO formation (reactions R138 ($NO_2 + NH_2 \leftrightarrow H_2NO + NO$) and R051) especially the reaction R051 competes with the reactions of NO reduction by NH_2 [reactions R071 ($NH_2 + NO \rightarrow N_2 + H_2O$) and R073), and eventually dominates the process as temperature increases. Figure 31 presents this behaviour. Caton [Cat 1989] reported the same behaviour.

It is interesting to note that the Zel'dovich mechanism, which has been widely reported by different investigations related gas chemistry of N – atom, for example in the case of the studie of Miller [Mill 1989], is not part of the reactions that control the process presented in this document. According to the numeration of the Appendix 1, the reactions R028, R029 and R030 constitute the extended Zel'dovich mechanism [Flu 2012 – 02] [Mill 1989] [Zel 1946].

$$N + NO \leftrightarrow O + N_2 \qquad \textbf{R028}$$

$$N + O_2 \leftrightarrow NO + O \qquad \textbf{R029}$$

$$N + OH \leftrightarrow H + NO \qquad \textbf{R030}$$

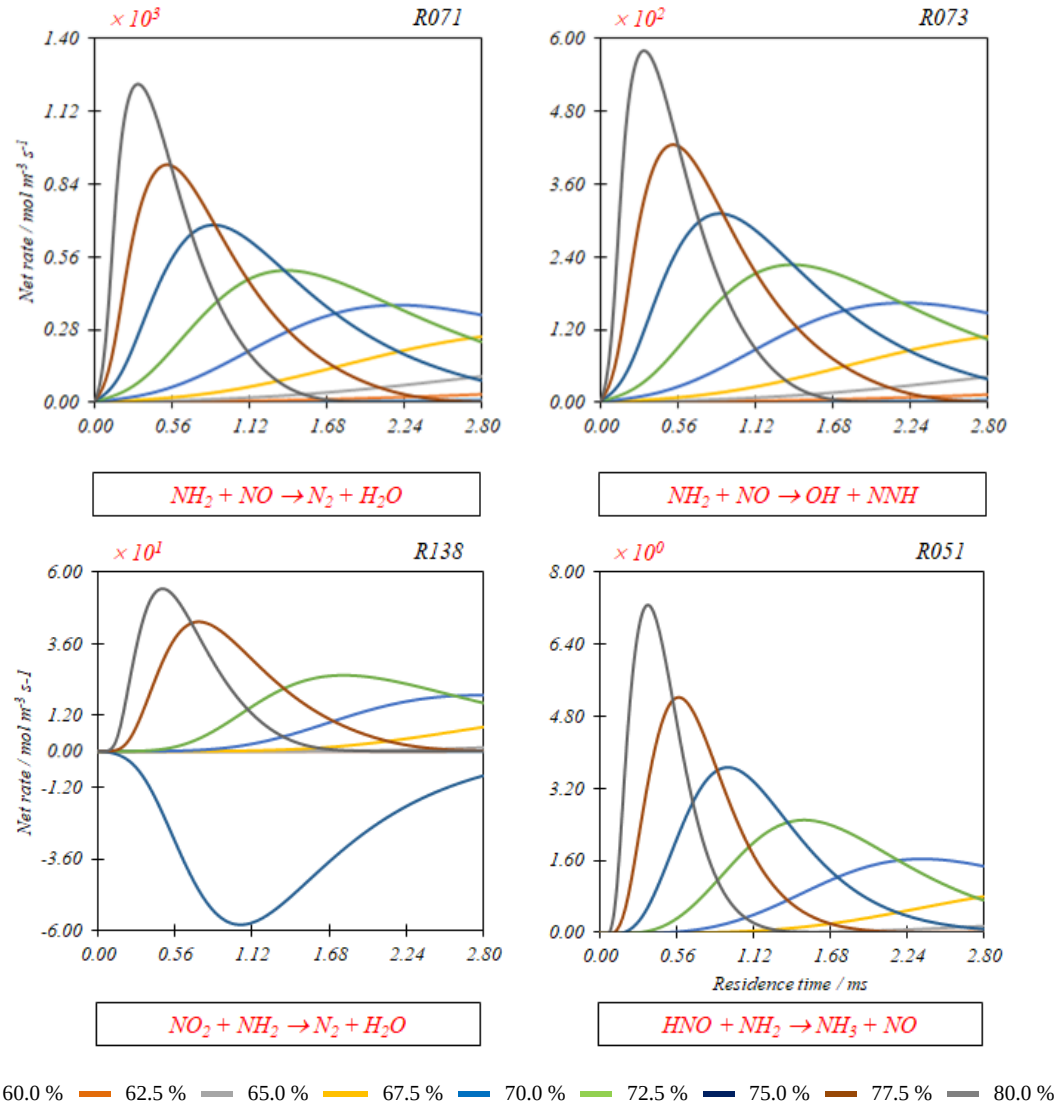

Figure 31. The net rate of reactions associated with the NH_2 / NO system (R071, R073, R138, and R051).
Parameter: progress of the reaction RI ($4NH_3 + 5O_2 \rightarrow 4NO + 6H_2O$) ($\xi_{RI}$) according to equation 106.
Simulations made with CANTERA [Goo 2017].

4.3. Comparison between the kinetic parameters of AA – Mech Kilpinen [Kil 1999] and Coda Zabetta [Cod 2001] and the mechanism proposed by Glarborg [Gla 2018] for the gas phase reactions.

The objective of the research of Glarborg [Gla 2018] was to establish and evaluate a state of the art, non optimized chemical kinetic model for homogeneous nitrogen chemistry in combustion at atmospheric or sub atmospheric pressure. These mechanisms involve fixation of the N_2 contained in the combustion air and NH_3 oxidation in the gas phase. According to these investigation, homogeneous fixation of N_2 involves the attack of reactive atoms (O, H) on the triple N – N bond of the N_2. The studies of Glarborg devoted to the oxidation process of NH_3 have by spredelly reported and taked into account [Bra 2016].

4.3.1. Comparison between the kinetic parameters

Table 3 presents a general comparison of the mechanisms according to their general characteristics. The parameters for the calculation of thermodynamics properties, allow to obtain comparable results between the two mechanisms.

Table 3. General characteristics of the mechanisms for the gas phase process.

Mechanism	**AA – Mechanism [Kil 1999] [Cod 2001]**	**Glarborg mechanism [Gla 2018]**
Reactions associated with N, H and O	145	213
Species	25	31
Exclusive species of the mechanism	HNNO	H_2NN – HNO_2 NH_2OH – $HONO_2$ NH_2OH – HON
Species present in both mechanism	H – H_2 – H_2NO – H_2O – H_2O_2 – HNO – HO_2 HONO – N – N_2 – N_2H_2 – N_2H_3 – N_2H_4 – N_2O NH – NH_2 – NH_3 – NNH – NO – NO_2 – NO_3 – O – O_2 – OH	
Exclusive reactions related with the exclusive species	12	59
Exclusive reactions related with shared species	9	30
Shared reactions	124	

To carry out the comparison of the shared 124 reactions the equation (1) previously presented in Section 3.5 was used. According to this analysis, only 26 of the 124 comparable reactions have the same parameters in both mechanisms. These reactions are listed below. The reactions R013, R044, R045, and R074 have been considered important according to was previously reported in the section 4.2. The numbering of the reactions listed in this section corresponds to the numbering used in Appendix 1.

$$NH_3 + H \leftrightarrow NH_2 + H_2 \quad \textbf{R013}$$

$$NNH + H \leftrightarrow N_2 + H_2 \quad \textbf{R014}$$

$$NH + N \leftrightarrow N_2 + H \quad \textbf{R027}$$

$$N + OH \leftrightarrow NO + H \quad \textbf{R030}$$

$$NH + O \leftrightarrow NO + H \quad \textbf{R036}$$

$$NH_2 + O \leftrightarrow HNO + H \quad \textbf{R041}$$

$$\boldsymbol{NH_3 + O \leftrightarrow NH_2 + OH} \quad \textbf{R044}$$

$$\boldsymbol{NH_3 + OH \leftrightarrow NH_2 + H_2O} \quad \textbf{R045}$$

$$NNH + OH \leftrightarrow N_2 + H_2O$$ **R046**

$$NH_2 + N \leftrightarrow N_2 + 2H$$ **R054**

$$NNH + NH \leftrightarrow N_2 + NH_2$$ **R063**

$$NNH + NH_2 \leftrightarrow N_2 + NH_3$$ **R070**

$$\boldsymbol{NNH + NO \leftrightarrow N_2 + HNO}$$ **R074**

$$H_2NO + H \leftrightarrow HNO + H_2$$ **R088**

$$H_2NO + H \leftrightarrow NH_2 + OH$$ **R089**

$$NO_3 + H \leftrightarrow NO_2 + OH$$ **R095**

$$H_2NO + NH_2 \leftrightarrow HNO + NH_3$$ **R097**

$$H_2NO + O \leftrightarrow HNO + OH$$ **R100**

$$NH_3 + HO_2 \leftrightarrow NH_2 + H_2O_2$$ **R116**

$$NO_3 + HO_2 \leftrightarrow NO_2 + O_2 + OH$$ **R117**

$$NH + HONO \leftrightarrow NH_2 + NO_2$$ **R119**

$$N_2H_3 + NH \leftrightarrow N_2H_2 + NH_2$$ **R128**

$$N_2H_3 + OH \leftrightarrow NH_3 + HNO$$ **R132**

$$NO_2 + NO_2 \leftrightarrow NO_3 + NO$$ **R142**

$$NO_3 + O \leftrightarrow NO_2 + O_2$$ **R144**

$$NO_3 + OH \leftrightarrow NO_2 + HO_2$$ **R145**

Another category of comparable reactions is composed of those in which the AA – Mech [Kil 1999] [Cod 2001] considers the "forward" kinetic parameters and the Glarborg mechanism [Gla 2018] presents them as "backward". These reactions are presented below, the reactions R050, R052, and R076 should be highlighted, since they have been considered as fundamental reactions for the process in the gas phase according to was explaind in section 5.3.

$$2H + M \leftrightarrow H_2 + M$$ **R003**

$$H + OH + M \leftrightarrow H_2O + M$$ **R010**

$$H + NH_2 \leftrightarrow H_2 + NH$$ **R012**

$$H + HONO \leftrightarrow H_2 + NO_2$$ **R092**

$$H_2NO + O \leftrightarrow NH_2 + O_2$$ **R101**

$$NH_3 + M \leftrightarrow H + NH_2 + M \qquad \textbf{R125}$$

$\boldsymbol{HNO + M \leftrightarrow H + NO + M}$	**R050**
$\boldsymbol{HNO + NO \leftrightarrow N_2O + OH}$	**R052**
$\boldsymbol{O + OH \leftrightarrow H + O_2}$	**R076**

The comparison of the dependence with the temperature for the kinetic constants, calculated from the equilibrium models, shows important differences between the kinetic parameters used in the two mechanisms. The difference between the behaviours of the kinetical constants under the temperature does not depend strongly on the thermodynamic properties since they are almost the same for the two mechanisms.

The figures in Appendix 6 present the value of the parameter relationship for the reactions that are common to the two mechanisms and have been considered as fundamental reactions in section 5.3. In general, for these reactions, the parameters differ significantly between the two mechanisms. When no value bar of the relation between parameters is presented, this means that in some of the mechanisms has a parameter value equal to zero, while in the other the value is different from zero. An important feature that considers the Glarborg [Gla 2018] mechanism for certain reactions is the existence of pressure dependency parameters according to Low and Troe [Gil 1983] formulations. This happens specifically for reactions R009, R025, R083, and R126. For these reactions, the AA – Mech [Kil 1999] [Cod 2001] does not consider effects of pressure.

Glarborg [Gla 2018] reports reactions such as the reaction R025 as fundamental in the process of NO oxidation in the gas phase. Indeed, additional reaction paths to NO from N_2 are initiated by N_2 recombination with O – atom followed by oxidation of a N – atom intermediate to NO. The N_2O scheme may be important under lean conditions at high pressure and moderate temperatures. Glarborg [Gla 2018] indicated that the behaviour of the N_2O is quite well established by their mechanism.

$$N_2O + M \rightarrow M + O + N_2 \qquad \textbf{R025}$$

The figures in Appendix 7 present the value of the parameter ratio for the other reactions common to the two mechanisms, which were not considered relevant according to the information presented in section 5.2. Again, important differences are observed between the two mechanisms. Although not shown in these graphs, the difference between the parameters that describe the dependence with the pressure for reactions R124 and R127 is also high. On the other hand, in the mechanism of Glarborg [Gla 2018], the reaction R065 has Troe [Gil 1983] approach parameters to consider the dependency with the pressure.

4.3.2. Comparison between simulation results

Figure 32 (a) shows results for NH_3 oxidation in the presence of NO for concentrations between 25.0 – 100 ppm at constant NH_3 concentration (1000 ppm) and O_2 composition (40.0 v%). The inlet pressure of the reactor in the Vilas tests [Vil 2004] and the simulations of Glarborg [Gla 2018], has not been reported. Therefore, 1.0 atm is used according to the general condition reported by Glarborg [Gla 2018]. In addition, they refer to the presence of traces of H_2O at the reactor inlet without

specifying its concentration. Hence the application of the AA – Mech [Kil 1999] [Cod 2001] considers it as zero.

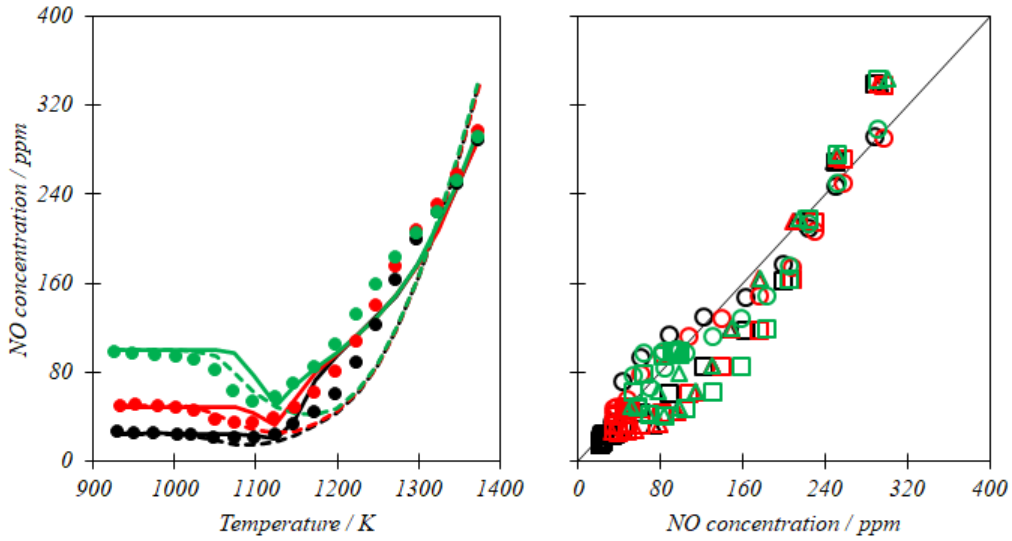

(a) Concentration vs. Temperature profile *(b) Comparison*

Black	25.0 ppm NO at the inlet.
Red	50.0 ppm NO at the inlet.
Green	100 ppm NO at the inlet.
Dots	Experimental data reported by Vilas.
Continuous line	Simulation predictions reported by Glarborg.
Dashed line	Simulation predictions based on AA – Mech.
Circles	Comparison between Vilas and Glarborg.
Squares	Comparison between Vilas and AA – Mech.
Triangles	Comparison between Glarborg and AA – Mech.

Figure 32 Comparison of experimental data reported by Vilas [Vil 2004], simulation predictions reported by Glarborg [Gla 2018] and simulation predictions based on AA – Mech [Kil 1999] [Cod 2001] for the NH_3 oxidation in a flow reactor made of quartz.
Simulations made with CANTERA [Goo 2017].
Inlet conditions: 1000 ppm NH_3 / NO as variable parameter / 40.0 v% O_2 / balance N_2, 1.0 atm (supposed), $\tau[s] = 48.7/T[K]$.
The inlet conditions have been reported by Glarborg [Gla 2018], those process conditions do not correspond with the Ostwald process but do correspond with the selective non – catalytic reduction of NO_X with NH_3.

Glarborg [Gla 2018] indicate that the important features of NH_3 oxidation, including the selectivity to forming NO and N_2, are well described by their model. The onset temperature for the reaction is independent of the NO level. Even at the smallest NO concentration of 25.0 ppm, a minimum in NO is observed just above the initiation temperature, and inspection of the data shows that the fractional conversion of NO at the minimum is quite similar over the range of NO concentrations. At

higher temperatures, up to 1200 K, the outlet NO concentration approaches asymptotically to a value, which is independent of the inlet temperature and inlet NO concentration.

The use of the AA – Mech [Kil 1999] [Cod 2001] shows a general behaviour like reported by Glarborg [Gla 2018]. At low temperatures, the results from the AA – Mech [Kil 1999] [Cod 2001] fix better the experimental results of Vilas [Vil 2004] than the simulation results reported by Glarborg [Gla 2018]. Both results indicate that from 1200 K, the final NO concentration is no longer dependent on the inlet NO concentration. For the case of AA – Mech [Kil 1999] [Cod 2001] this condition induces lower final NO compositions up to 1350 K. Above this temperature the prediction of the AA – Mech [Kil 1999] [Cod 2001] presents higher values than the experimental results obtained by Vilas [Vil 2004]. Despite this difference between the two mechanisms, for all inlet NO compositions, at temperatures lower than 1100 K, the results with the AA – Mech [Kil 1999] [Cod 2001] are better adjusted to the experimental results proposed by Vilas [Vil 2004]. Figure 32 (b) indicates that the use of both mechanisms allows obtaining similar simulation results under these process conditions. This shows that the predictions from the AA – Mech [Kil 1999] [Cod 2001] capture the process trends as well as the predictions from the Glarborg [Gla 2018] mechanism.

Figure 33 compare simulation results for outlet composition with experimental data reported by Kasuya [Kas 1995]. They performed a series of flow reactor experiments to investigate the effect of O_2 composition from 1.0 to 50.0 v% on the process of non – catalytic reduction of NO_x with NH_3.

Glarborg [Gla 2018] indicate that an increase in the oxygen concentration shifts the minimum of the outlet NO concentration towards lower temperatures and widens the possibility of decreasing the final NO concentration over the entire temperature range. These characteristics are well described by both chemical mechanisms. The predicted minimum of temperature is slightly shifted for some conditions. The simulation with the AA – Mech [Kil 1999] [Cod 2001] shows that at temperatures around 1200 K the simulation results are closer to the experimental conditions than the results presented from the use of the Glarborg mechanism [Gla 2018], especially for O_2 compositions between 4.0 and 20.0 v% O_2. At high temperatures, the Glarborg mechanism [Gla 2018] fits better to the experimental conditions, however, in general, both mechanisms have the same behaviour to predict the outlet NO concentration under these conditions. The greatest differences between the results are presented for O_2 compositions higher than 20.0 v%. Under those conditions, the mechanism is not expected to be useful since the processes of NH_3 oxidation and NO reduction are not usually carried out under these high levels of O_2 compositions. The similitude between the simulation results and the experimental results at O_2 compositions between 4.0 and 10.0 v% indicate the possibility of using both mechanisms for the simulation of the gas phase process during the catalytic oxidation of NH_3.

Kasuya [Kas 1995] was the first to report the detection of NO_2 in the process of non – catalytic reduction of NO_x with NH_3; NO_2 is now believed to be a key intermediate in the process. It is seen to form in significant quantities at high O_2 compositions, but the level drops off rapidly as O_2 decreases. Glarborg [Gla 2018] indicated that the simulation results are in qualitative agreement with the measurements, but the predicted window for NO_2 extends to higher temperatures than observed experimentally.

Glarborg [Gla 2018] reported that the competition between reactions of HNO and H_2NO with O_2 and with the radical pool is important for the peak concentration of NO_2, as well as the width of the NO_2 formation window.

Glarborg [Gla 2018] stablished as well that the formation of N_2O is a complex function of temperature and oxygen concentration. The N_2O peak shifts from high temperature to low temperature as the O_2 composition increases. The predictions with the Glarborg mechanism agree qualitatively with the measured profiles, but the model overpredicts N_2O under conditions where the NH + NO reaction is the main source.

For O_2 compositions greater than 10.0 v%, neither mechanism predicts well the outlet N_2O or NO_2 concentrations. The obtained results with the AA – Mech [Kil 1999] [Cod 2001] show similar trends in NO_2 and N_2O concentrations. For O_2 compositions up to 4.0 v% O_2 (which can occur near the surface of the catalyst). In the case of N_2O, the AA – Mech [Kil 1999] [Cod 2001] meets more adequately to the experimental results.

Despite the differences between the parameters of both mechanisms, their application shows generally similar results that allow inducing that the use of AA – Mech [Kil 1999] [Cod 2001] is suitable for the simulation of the gas phase process that may take place during the catalytic oxidation of NH_3.

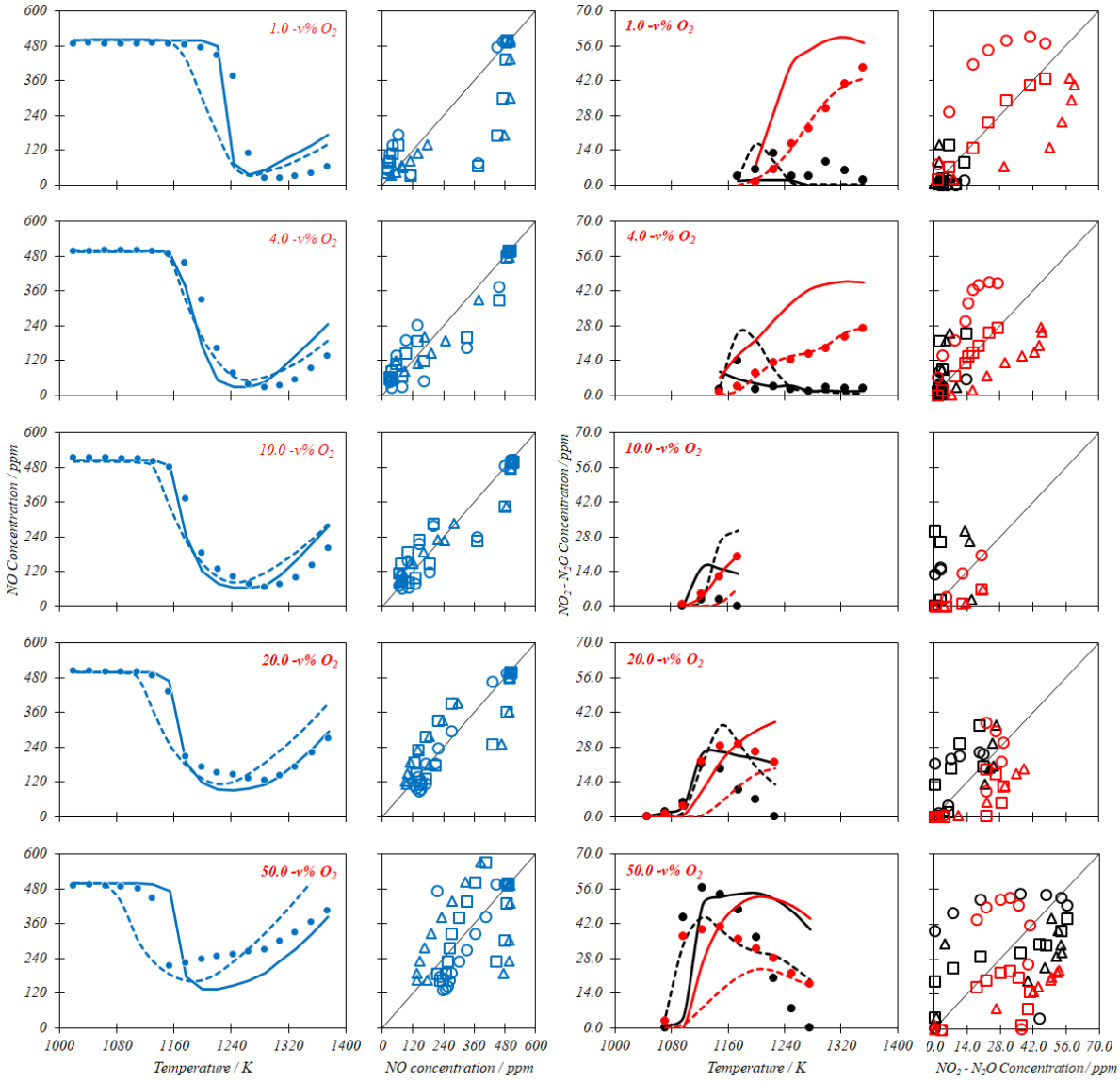

Blue		NO Concentration
Black		NO_2 Concentration.
Red		N_2O Concentration.
Dots	●	Experimental data reported by Kasuya.
Continuous line	———	Simulation predictions reported by Glarborg.
Dashed line	- - - - - -	Simulation predictions based on AA – Mech.
Circles	○	Comparison between Kasuya and Glarborg.
Squares	□	Comparison between Kasuya and AA – Mech.
Triangles	△	Comparison between Glarborg and AA – Mech.

Figure 33. Comparison of experimental data reported by Kasuya [Kas 1995], simulation predictions reported by Glarborg [Gla 2018] and simulation predictions based on AA – Mech [Kil 1999] [Cod 2001] for NO reduction by NH_3 in a flow reactor made of quartz and the effect of O_2 concentration.
Inlet conditions: 1000 ppm NH_3 / 500 ppm NO / 5.0 v% H_2O / balance N_2, 1.0 atm (reported), $\tau[s] = 88.0/T[K]$.

5. Configuration of the software for the simulation [Flu 2012 – 01]

This section presents the configuration considered for the use of the commercial software package ANSYS FLUENT [Flu 16 – 01] as platform to conduct the simulations devoted to this investigation, which is a finite – volume element software. In this section the titles, and options of the Graphical User Interface of ANSYS FLUENT [Flu 16 – 01] are presented in *Cursive letters*.

To conduct the simulations, the *Pressure – based Solver* was used in a *Transient time* consideration and with and *Absolute Velocity Formulation*. The calculation with the *Energy Equation* was enabled and the *Viscous Model* was set up as *Laminar*.

To use boundaries conditions as inlet velocity (section 6.5.5.2), fixed temperature in a wall (section 6.5.5.4) or fixed composition in a wall (section 6.5.5.4), it is necessary to select the *Pressure – based Solver*. It traditionally has been used for incompressible and mildly comprensible flows. For this investigation, the coupled algorithm of the *Pressure – based Solver* had been taked into account. In this algorithm the momentum equations and the pressure – based continuity ecuation are solved in a coupled manner. In general, the coupled algorithm significantly improves the convergence speed and requires higher memory disponibility.

In the *Species Model*, the *Species Transport Model* was selected, *Wall Surface Reactions* have been used for the simulation of the CatOx process and *Volumetric Reactions* for the simulation of CatOxGP process. *Laminar Finite – Rate* was considered as *Turbulence – Chemistry Interaction*. Furthermore, the following options have been taked into account:

- *Inlet diffusion*

The net transport of species at inlets consists of both convection and diffusion components. The convection component is fixed by the specified inlet species mole fraction, whereas the diffusion component depends on the gradient of the computed species concentration field. At small inlet velocities, substantial mass can be gained or lost through the inlet due to diffusion.

- *Diffusion Energy Source*

Neglecting the species diffusion term implies that errors may be introduced to the prediction of temperature in problems involving mixing of species with significantly different heat capacities, especially for components with a Lewis number far from unity.

- *Full Multicomponent Diffusion*

According to the explained in section 6.5.3.

Obtaining a converged solution in a reacting flow can be difficult for several reasons. First, the impact of chemical reaction on the basic flow pattern may be strong, leading to a model in which there is strong coupling between the mass / momentum balances and the species transport equations (section 6). This is especially true in combustion, where the reactions lead to a large heat release and subsequent density changes and large acceleration in the flow. All reacting systems have coupling when the flow properties depend on the species concentrations.

A second convergence issue in reacting flows involves the magnitude of the reaction source term (R_j). When the model involves very rapid reaction rates (reaction time scales are much faster than convection and diffusion time scales), the solution of the species transport equations becomes numerically difficult. Such systems are termed “stiff” systems. When those systems are laminar as well,

they can be solved with the *Stiff Chemistry Solver*. In unsteady simulations, this solver option applies a fractional step algorithm.

The coupling issues are best addressed using a two – steps solution procedure. In this process, you begin by solving the flow, energy, and species equations with the reactions disabled. When the basic flow pattern has therefore been established, the reactions are re – enable and the calculation continues.

Since the detailed chemical mechanisms are invariably numerically stiff and compute – intensive, it is useful to use the *Integration Parameters* available to face the integration of the chemical source term (S_m) in the equation (7), then the *ISAT* (In – Situ Adaptive Tabulation) was selected as *Integral Method*. All parameters stablished by defect was used in the solver configuration. NH_3 and O_2 are the *Fuel / Oxidizer Species*.

ISAT is a storage – retrieval method that constructs a chemistry table at run – time (in – situ) with a user – specified interpolation accuracy (adaptative tabulation). ANSYS FLUENT [Flu 16 – 01] uses an ODE solver with two error tolerances (the *Absolute Error Tolerance* and the *Relative Error Tolerance*) to integrate the stiff chemical kinetics. The default values of those tolerances, 10^{-8} and 10^{-9} respectively are manteined to conduct the simulations in this investigation. There is a specific *ISAT Parameter* called the *ISAT Error Tolerance*, which control the numerical error in the *ISAT* table, it is seted and manteined by default as 10^{-3}. This value may be sufficiently accurate for temperature and major species.

In the *Solution Methods*, it is necessary to configurate: (i) the *Scheme of Pressure – Velocity Coupling*, (ii) The *Spatial Discretization* and (iii) the *Transient Formulation*.

Regarding the *Pressure – Velocity Coupling*, the *PISO* (Pressure – Implicit with Splitting Operators) *Scheme* was used as segregated algorithm to compute this coupling. The *PISO* algorithm with *Neighbor Correction* is highly recommended for all transient flow calculations. *PISO* with *Skewness correction* was specially used in the case of catalytic square mesh reactor (section 9) due to its distortioned mesh.

Regarding the *Spatial Discretization*, it is necessary to configure the spatial discretization for: (i) the *Gradient*, (ii) the *Pressure*, (iii) Density, (iv) the *Momentum*, (v) *Species* and (vi) *Energy*. When the flow is not aligned with the mesh (that is, when it crosses the mesh lines obliquely), second – order convestive discretization decreases the numerical discretization error (numerical diffusion). For triangular meshes, since the flow is never aligned with the mesh, the model generally obtains more accurate results by using the second – order discretization. In the case of the *Density*, the second – order upwind scheme provides reasonable stability for the discretization of the pressure – correction equation and gives good results for most classes of flows. Based on those considerations the *Second – order Upwind* was used as general scheme for the *Spatial Discretization*.

Regarding the *Transient Formulation*, the *First Order Implicit* was used.

The *Pressure – based Solver* uses under – relaxation of equations to control the update of computed variables at each iteration. This means that all equations will have under – relaxation factors associated with them. For most flows, the default *under – relaxation factors* do not usually require modification.

By using the *PISO neighbor* and *skewness correction*, it was necessary to set the *under – relaxation factors* for *momentum* and *pressure* so that they sum to 1.0 (for example, 0.30 for *pressure* and 0.70 for *momentum*).

For energy equation: in problems where the energy field impacts the flud flow (via temperature – dependent properties) under – relaxation factor in the range 0f 0.80 – 1.0 should be used. For this invstigation the value was set as 0.90.

Where density is strongly coupled with temperature, it is that there are large changes in temperature that cause large changes in density, which can in turn, cause instabilities in the flow solution. By the under – relaxing of the change in density, is is possible to minimice this difficulty. Then

the under – relaxation factor in the range of 0.50 – 1.0 should be used. For this invstigation the value was set as 0.50.

To improve the startup and the general solution behaviour of flow simulations when higher order spatial discretizations are used, is usual to consider the *Relaxation of High Order Terms*. Such high – order terms can be significant and prevent convergence stalling, particularly at aggressive solution settings. The default values for the *Relaxation Factor* are 0.75 for transient cases. This value was used and applied to all equations solved.

For other scalar equations, the default underrelaxation may be too aggressive for some problems, especially at the start of the calculation. The factors of 0.80 to facilitate convergence.

For most problems, the default convergence criterion in ANSYS FLUENT is sufficient. This criterion requires that the globally scaled residuals decrease to 10^{-3} for all equations except the energy, for which the criterion is 10^{-6}.

Specially to carry out the simulation of the stagnation point reactor, which is reported in the Chapter 10 of this documment, the model suggested by the free package for simulation of physicochemical processes CANTERA [Goo 2017] were used. This package propouses a one – dimensional model, which is developed in the axis of symmetry of the simulation domain.

The following hardware was used for the calculations:

Machine 1: Four processors Intel ® Core ™ i5 – 4590 with 4 cores

CPU 3.30 GHz

RAM 32 Gb

Microsoft Windows 10, 64 bits

All capacity used.

Machine 2: Intel Xeon Processor E5-2660 v3 with 10 cores

CPU 2.60 GHz

RAM 128 Gb

Microsoft Windows 10, 64 bits.

Partial capacity used (shared).

6. Simulation of the catalytic square mesh reactor

Two dimensional simulations have been carried out with the commercial software package ANSYS FLUENT [Flu 16 – 01], which uses the finite volume method for spatial discretization of the governing Navier Stokes equations [Amo 2017]. This research considered three different reactor configurations, namely: (i) catalytic square mesh reactor, (ii) stagnation point reactor and (iii) planar channel reactor.

This chapter presents the methodology, results, and discussion about the simulation of the catalytic square mesh reactor. This type of configuration, in which the catalyst wires form parallel networks, is the most widely applied on an industrial scale [Ull 2012]. For this reason, this type of geometry is of particular interest as an object of research. In this regard, this chapter presents the results of the following simulation cases:

- Simulation of the CatOx process at basic operating conditions and other process conditions. In section 9.5.1.
- Simulation of the CatOxGP process in the first catalytic wire. In section 9.5.2.

The simulation of the CatOx process is carried out only up to the sixth wire. Up to this length of the reactor, is the presence of NH_3 and therefore in successive wires, no effect of the process in the gas phase is expected. Due to the numerical difficulty represented by the simulation of the CatOxGP process, together with the geometry of the calculation domain, the CatOxGP simulation for the sucesive wires is ruled out for the purposes of this research.

6.1. Geometry and mesh

With the aim of simulate the NH_3 oxidation in the catalytic square mesh reactor, the geometry consists in 0.10 mm inlet and outlet lengths, and six catalytic wires whose diameter is 0.10 mm. Two successive lines are separated by 0.20 and 0.050 mm gaps in x and y directions respectively. The cross section of the inlet of the reactor consists of a rectangle with 1.0 m wide and 0.15 mm high. The calculation domain considers the axial symmetry of the reactor.

ANSYS MESHING [Flu 16 – 02] was used for the generation of the domain of the numerical simulation. Figure 34 shows a detail of the geometry and the mesh up to the second catalytic wire. The mesh of the six wires reactor has 195456 triangular cells. This has been detailed in the flow zone around the catalytic surface by means of an edge sizing procedure. Since it is considered that during the process, the temperature of the catalytic wires is uniform and stable, its internal mesh has not been considered for simulation purposes. This mesh has a maximum aspect ratio (MAR) equal to 4.13, minimum orthogonal quality (MOQ) equal to 0.648 and maximum orthogonal skewness (MOS) equal to 0.261. Since MOQ values close to 0.0 and MOS values close to 1.0 correspond to low quality [Flu 2012 – 01] [Flu 2012 – 02], this mesh can be used for simulation proposes.

For the simulation of the CatOxGP process in the square mesh type reactor, the geometry consists in 0.10 mm inlet and outlet lengths, and one catalytic wire with diameter equal to 0.10 mm. The cross section of the inlet to the reactor consists of a rectangle with 1.0 m wide and 0.15 mm high. The calculation domain considers the axial symmetry of the reactor.

Figure 35 shows a detail of the geometry and the mesh used to carry out the simulation of the CatOxGP process in the catalytic square mesh reactor. This mesh has 282624 triangular cells, has been detailed in the flow zone around the catalyst by means of an edge sizing procedure. Since it is considered that during the process, the temperature of the catalytic wires is uniform and stable, its internal mesh

has not been considered for simulation purposes. This mesh has MAR = 5.90, MOQ = 0.465 and MOS = 0.416. Where MAR is Maxumun Aspect Ratio, MOQ is Minimum Orthogonal Quality and MOS is Maximum Orthogonal Skewness. Therefore, it can be used for simulation proposes.

It is important to note that due to the numerical complexity involved in the simulation of the CatOxGP process, the meshing presented in Figure 35 is finer than the meshing presented in Figure 34, especially in the region near the catalytic surface, where it expects a higher temperature, NO concentrations and therefore a possible effect of gas phase reactions.

6.2. Spatial convergence of the mesh

Slater [Sla 2012] presented a methodology for the examination of the spatial convergence. It is a method for determining the ordered discretization error in a CFD simulation. The method involves performing the simulation on two or more successively finer meshes. As the grid is refined the error of the spatial discretization should asymptotically approaches zero, excluding round off error of the computer.

A CFD code uses a numerical algorithm that will provide a theoretical order of convergence; however, the boundary conditions, numerical models, and mesh will reduce the value of this characteristic.

By means of the index MCI (Mesh Convergence Index) it is possible reporting the results of studies of the convergence of the mesh. The MCI should be computed using three levels of meshing to accurately estimate the order of convergence and to check that the solutions fix the asymptotic range of convergence. The procedure consists of to start with a mesh resolution and then conduct a series of refinements to define the effect of mesh resolution. This is known as astudy of the refinement of the mesh.

The MCI is a measure of the percentage the computed value is away from the value of the asymptotic numerical value. It indicates how much the solution would change with a further refinement of the mesh. A small value of MCI indicates that the computation is within the asymptotic range.

According to the methodology presented by Slater [Sla 2012], two refinements were applied on the catalytic square mesh reactor presented on Figure 35 (195456 cells) obtaining meshes of 392867 and 789662 cells respectively (which implies a refining ratio of 2.01). With these calculation domains, the simulation of the CatOx process was applied and with the operating conditions, which had been reported as typical for the catalytic oxidation of NH_3:

- The inlet velocity of 0.75 m s^{-1}.
- The inlet temperature of 423 K.
- The pressure of 5.0 bar.
- The volumetric composition of 10.0 v% NH_3 and 90.0 v% dry air.

Figure 36 presents the results of the analysis of spatial convergence for the catalytic square mesh reactor. The NSR (Normalized Simulation Result) refer to the relationship between the calculated value for the finest mesh and the analog for any other less refined mesh. The NCQ (Normalized cell Quantity) is the ratio between the number of cells in the refined mesh and in other less refined meshes. It is observed that the results do not differ significantly for each computational domain. In the worst case, the total outlet pressure, calculated with the least refined mesh (195456 cells) is 0.650 % lower than that obtained in the simulation with the most refined mesh (789662 cells). It indicates that the mesh presented in Figure 35 (195456 cells) is useful for the simulation proposes.

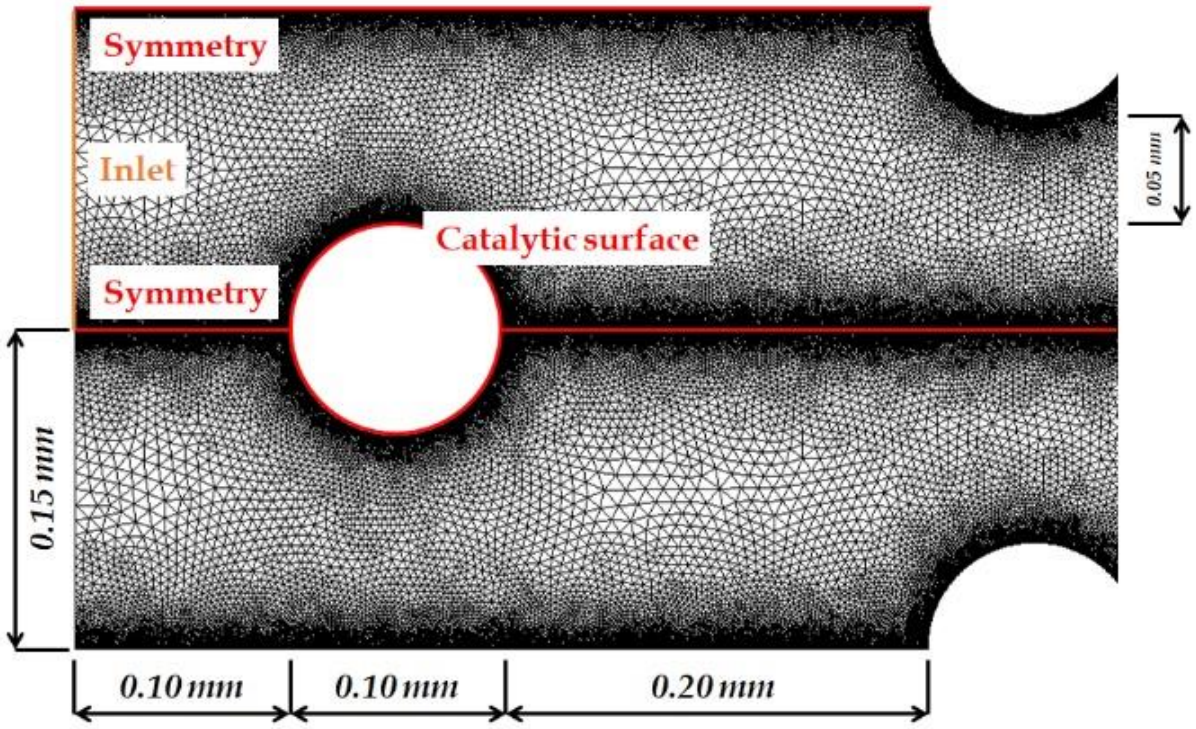

Figure 34. Detail of geometry and meshing of catalytic square mesh reactor (six parallel wires).

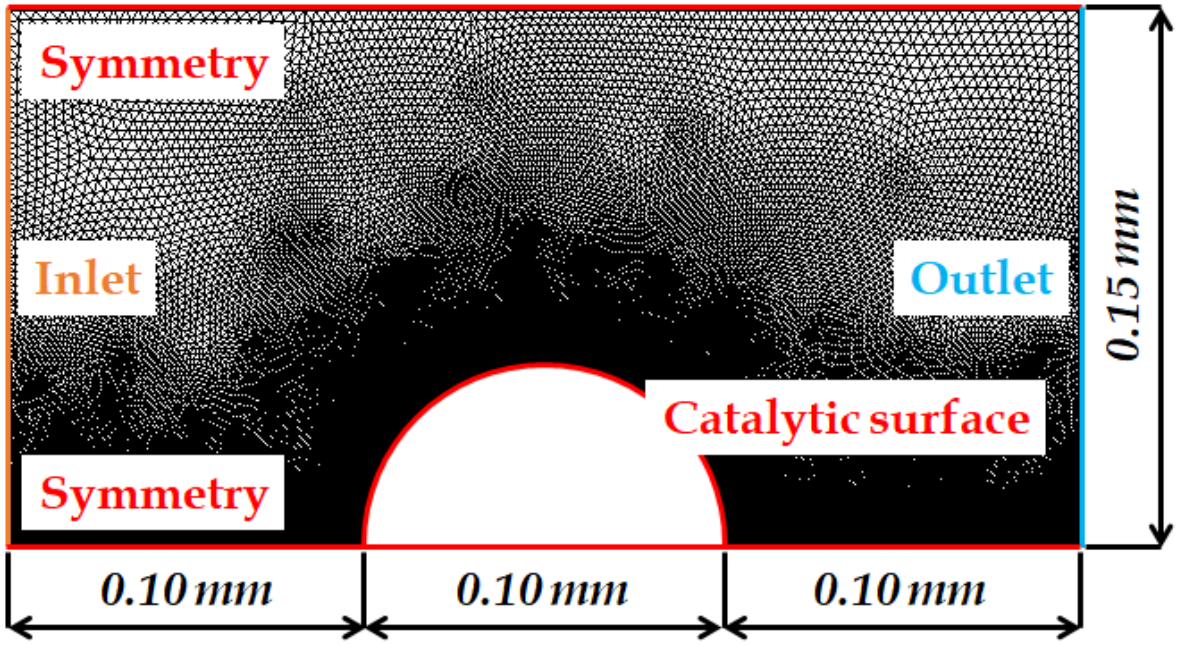

Figure 35. Geometry and meshing of single catalytic wire reactor for the simulation of the CatOxGP process.

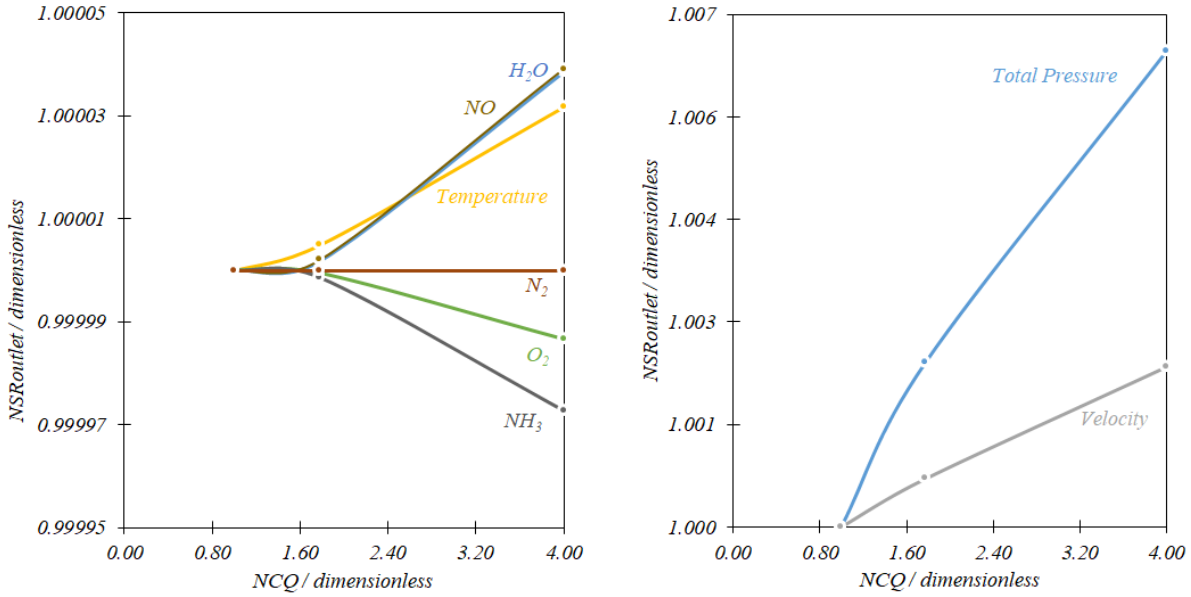

Figure 36. Results of the analysis of the spatial convergence of the mesh. NSR vs. NCQ for the catalytic square mesh reactor.

6.3. Boundary conditions and configuration of the simulation

To carry out the simulation of the cases associated with the square mesh reactor, the conditions described in this section were used. For the CatOx process, the Table 4 shows the inlet conditions used for the ANSYS FLUENT [Flu 16 – 01] simulation. Sections refered to simulation results, discusión and análisis (section 9.5) present the especific configuración of the inlet conditions which are used in each case. For the CatOxGP process, the Table 5 shows the inlet conditions used for the ANSYS FLUENT [Flu 16 – 01] simulation.

In any case, to carry out the simulation, the following definitions are considered at the boundaries of the computational domain:

- The inlet boundaries shown in Figures 34 and 35, are velocity inlets according to equation (73).
- The outlet boundaries shown in Figures 34 and 35, are pressure outlets according to equation (79).
- The horizontal, upper and lower boundaries, which do not correspond to the catalyst surface and which were shown in Figures 34 and 35, are considered symmetry boundaries and are defined by the equations between (80) and (83).

For the simulation of the CatOx process, the boundaries corresponding to the catalytic surface, as was shown in the Figure 34, is defined as closed wall according with the equation (74), in which the reactions of the catalytic mechanism, presented in the Section 3.4, take place.

In the case of the simulation of the CatOxGP process in the first catalytic wire, the boundary corresponding to the catalytic surface is defined as a closed wall according to the equation (74), which is at temperature and composition conditions obtained in the simulation of the CatOx process considering the same inlet conditions. When the standard deviation with respect to the average value is less than 10.0 %, then the average value (eigther of temperature or composition) is considered as a boundary condition for the simulation of the CatOxGP process. When this condition is not fullfit, the profile in the wire from the CatOx simulation is taked as a boundary condition.

Table 4. Inlet conditions for the simulation of catalytic square mesh reactor in the CatOx process.

Pressure	Temperature	NH_3 composition	Velocity
Bar	**K**	**v%**	**m s^{-1}**
5.0 – 10.0 – 15.0	423 – 462 – 500 – 530	10.0 – 11.0 – 12.5	0.25 – 0.75 – 1.75 – 2.50

Table 5. Inlet conditions for the simulation of the CatOxGP process in the first wire of the catalytic square mesh reactor

Velocity	m s^{-1}	0.75
Temperature	K	423
Pressure	bar	5.0
Composition		
NH_3	v%	10.0
Dry air	v%	90.0

6.4. Simulation results, discussion, and analysis

This section is focused on the presentation, discussion and analysis of the results associated with the simulations of the CatOx and CatOxGP processes carried out in the the catalytic square mesh reactor.

6.4.1. CatOx process

This section presents the results of the CatOx process under the basic operation conditions at industrial scale in a catalytic square mesh reactor. Then, to predict the response of the process, it presents and compares the results due to the change in operating conditions (increases in pressure and temperature).

6.4.1.1. Operation basic case

Once the process simulations have been carried out for all the possible combinations that result from the conditions presented in Table 2 (i.e., 93 simulations), the results show that the trend in the behaviour of the analyzed variables is the same although there are the expected variations due to increases and decreases in the inlet conditions. For this reason, to present all the results is excessive and monotonous. It is preferable to explain in detail an operational base case and from it indicate the variations resulting due to the modifications in the inlet conditions. Consequently, the simulations corresponding to the following inlet conditions: 423 K, 5.0 bar, the NH_3 composition between 10.0 and 12.5 v%, and velocity between 0.25 and 2.50 m s^{-1}, are taken as operation basic cases for this report. It is important to note that the most research results concerning CatOx have been published at these inlet conditions.

6.4.1.1.1. Residence time

Figure 37 shows the behaviour of the residence time in each wire and throughout the reactor. Under these inlet conditions (423 K, 5.0 bar), independent of the inlet NH_3 composition, increasing the inlet velocity decreases up to 7 times the residence time along the reactor. In any case, at fixed inlet velocity, the increase in the inlet NH_3 composition implies an increase of up to 12.0 % in the residence time along the reactor.

This behaviour indicates that the inlet NH_3 composition has not an important effect over the residence time. The principal effect over the residence time is clearly due to the inlet velocity. For all cases, the residence time has a maximum in the first wire. Especially at velocity inlet of 0.25 m s^{-1}, the residence time decreases until it becomes almost constant in the following wires.

6.4.1.1.2. NH_3 consumption

Figure 38 shows the behaviour of the NH_3 consumption in each wire and throughout the reactor. The NH_3 consumption or conversion between the wires is defined according to the equation (91) for the local case and the equation (92) for the global case. Those equations were presented in Section 3.7.6.

Under these inlet conditions (423 K, 5.0 bar), independent of the inlet NH_3 composition, increasing the inlet velocity decreases up to 56.0 % the NH_3 consumption. At fixed inlet velocity, increasing inlet NH_3 composition increases up to 2.0 % the NH_3 consumption along the reactor. This behaviour indicates that the process carried out in the first wire governs the NH_3 consumption.

For inlet velocity of 0.25 m s^{-1}, independent of the inlet NH_3 composition, the NH_3 concentration is practically zero from the fourth wire. At inlet velocity of 0.25 m s^{-1}, up to the fourth wire, the NH_3 consumption in each wire is higher than which is obtained at other velocities. This is because, from the fourth wire, there is not enough NH_3 composition for the process. At the same inlet velocity, between the first and third wires, independent of the inlet NH_3 composition, there is a maximum of the NH_3 consumption. With the increment of the inlet velocity, this maximum is shifted towards following wires, until finally tends to remain constant, as the results show at an inlet velocity of 2.50 m s^{-1}. As the velocity increases, the residence time is shorter, the NH_3 concentration is greater, and there is NH_3 even up to the sixth wire (as it happens at inlet velocities of 1.75 and 2.50 m s^{-1}).

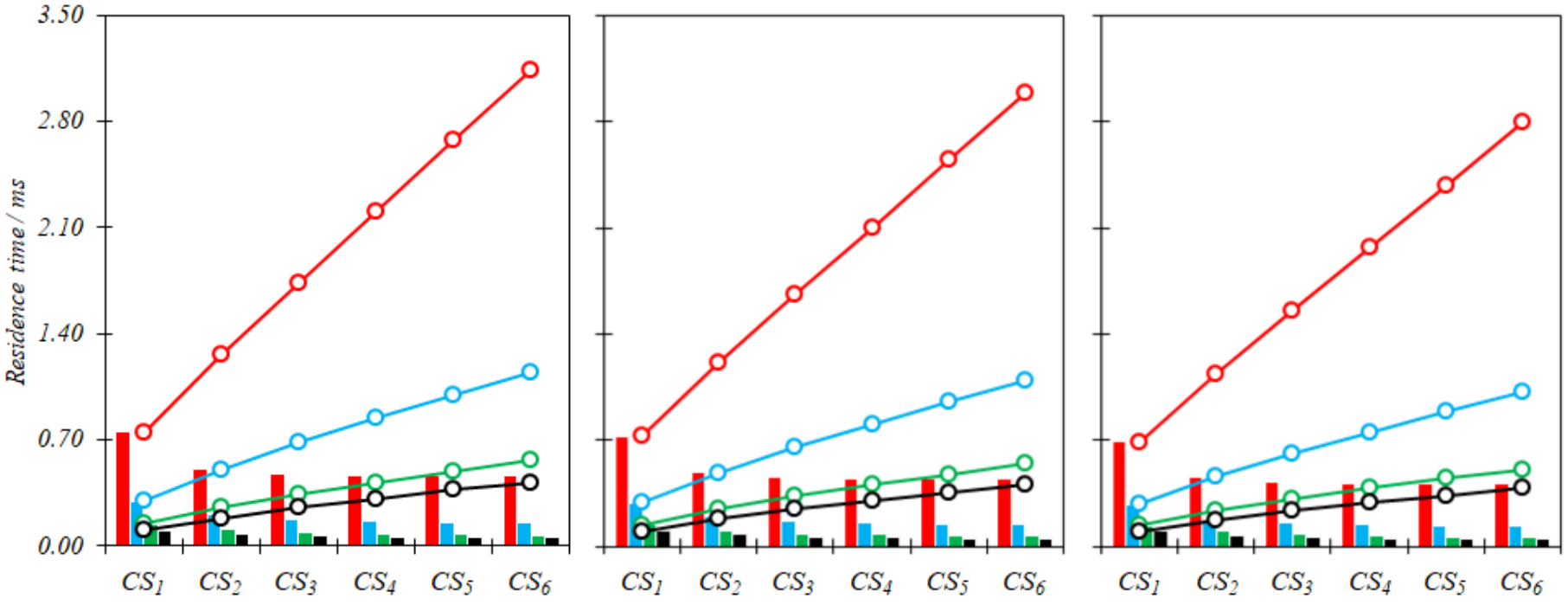

(a) 10.0 v% *(b) 11.0 v%* *(c) 12.5 v%*

Bars, a specific value in the wire.
Lines, accumulated throughout the reactor.

Inlet velocity: (■) 0.25 (■) 0.75 (■) 1.75 (■) 2.50 m s^{-1}.

Figure 37. Simulation results of the CatOx process in a catalytic square mesh reactor with six wires. Residence time in each wire and accumulated throughout the reactor.
Inlet conditions: 423 K, 5.0 bar, NH_3 + Dry air as balance mixture.

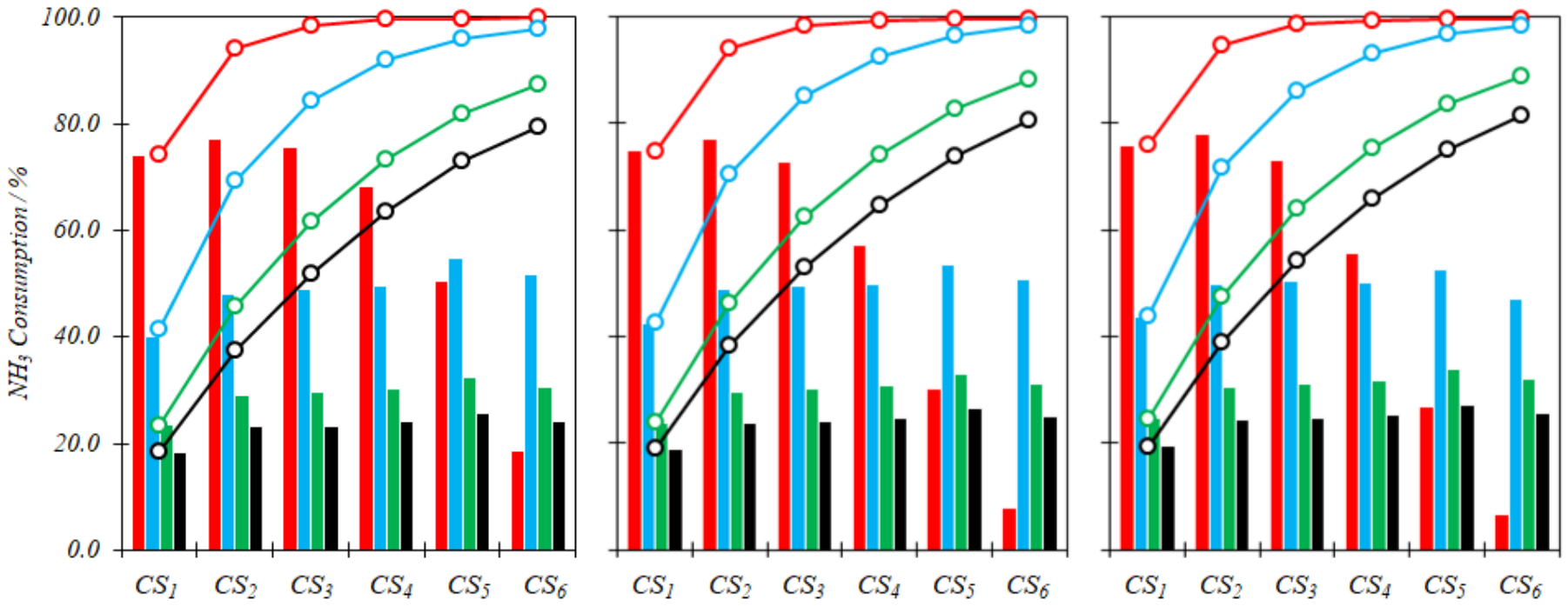

(a) 10.0 v% *(b) 11.0 v%* *(c) 12.5 v%*

Bars, a specific value in the wire.
Lines, accumulated throughout the reactor.

Inlet velocity: (■) 0.25 (■) 0.75 (■) 1.75 (■) 2.50 m s^{-1}.

Figure 38 Simulation results of the CatOx process in a catalytic square mesh reactor with six wires. NH_3 consumption in each wire and accumulated throughout the reactor.
Inlet conditions: 423 K, 5.0 bar, NH_3 + Dry air as balance mixture.

6.4.1.1.3. NO selectivity

Figure 39 shows the behaviour of the NO selectivity behaviour in each wire and throughout the reactor. The NO selectivity is defined according to with the equation (93) for the local case and the equation (94) for the global case. Those equations were presented in Section 3.7.6.

Under these inlet conditions (423 K, 5.0 bar), independent of the inlet NH_3 composition increasing the inlet velocity decreases up to 1.0 % the NO selectivity along the reactor. In any case, at fixed inlet velocity, the increase in the inlet NH_3 composition implies a decrease of up to 10.0 % in the NO selectivity along the reactor.

This behaviour indicates that when the inlet NH_3 composition is lower than 11.0 v%, the global NO production is practically independent of the inlet velocity of the reagent. For an inlet NH_3 composition of 12.5 v%, especially in the first wire, the increment of the inlet velocity decreases the global NO production. At inlet velocity of 0.25 m s^{-1}, the global NO production is practically independent of the inlet NH_3 composition. At inlet velocity of 2.50 m s^{-1}, the global NO production is highly dependent on the inlet NH_3 composition.

Both the mass flow of each species $(\dot{m}_j^B)$ and the total mass flow $(\dot{m}_T^B)$ in a specific boundary are direct results of the simulations carried out in ANSYS FLUENT [Flu 16 – 01].

Where the subscript (CS) refers to the catalytic surface and (i) refers to the counting of the catalytic surface, particulary when $(i = 1 \rightarrow CS_{i-1} = CS_0)$ it is the inlet condition.

There is no case in which the NO selectivity is 100 %. Therefore, according to the considerations of the catalytic mechanism considerations, the process can form N_2O or N_2. When the inlet NH_3 composition is high, the NO selectivity decreases significantly along the reactor, compared to what occurs at low NH_3 compositions. Then, the increment of the inlet NH_3 composition induces an increase in the formation of another nitrogenous species.

The results of Figure 39 correspond to the reported information of the process presented between Figures 8 and 10. Indeed, it is observed that the NO selectivity after the sixth wire is in all cases, for inlet NH_3 compositions between 10.0 and 11.0 v%, higher than 97.5 %. In the case of the inlet NH_3 composition of 12.5 v%, this selectivity is only achieved with an inlet velocity of 0.25 m s^{-1}. For higher inlet velocities the residence time is not enough to achieve the NO selectivity observed in the industrial process.

6.4.1.1.4. N_2O selectivity

Figure 40 shows the behaviour of the N_2O selectivity in each wire and throughout the reactor. The N_2O selectivity is defined according to the equation (95) for the local case and the equation (96) for the global case. Those equations were presented in Section 3.7.6.

Under these inlet conditions (462 K, 5.0 bar), increasing the inlet velocity increases up to 5.0 % the N_2O selectivity along the reactor. In any case, at fixed inlet velocity, the increase in the inlet NH_3 composition implies an increase of up to 10.0 % in the N_2O selectivity along the reactor.

This behaviour indicates that when the inlet NH_3 composition is lower than 11.0 v%, the process of N_2O production is practically independent of the inlet velocity of the reagent. For an inlet NH_3 composition of 12.5 v%, especially in the first wire, the increment of the inlet velocity decreases the global N_2O production. At inlet velocity of 0.25 m s^{-1}, the global N_2O production is practically independent of the inlet NH_3 composition. At the inlet velocity of 2.50 m s^{-1}, the global N_2O production is highly dependent on the inlet NH_3 composition.

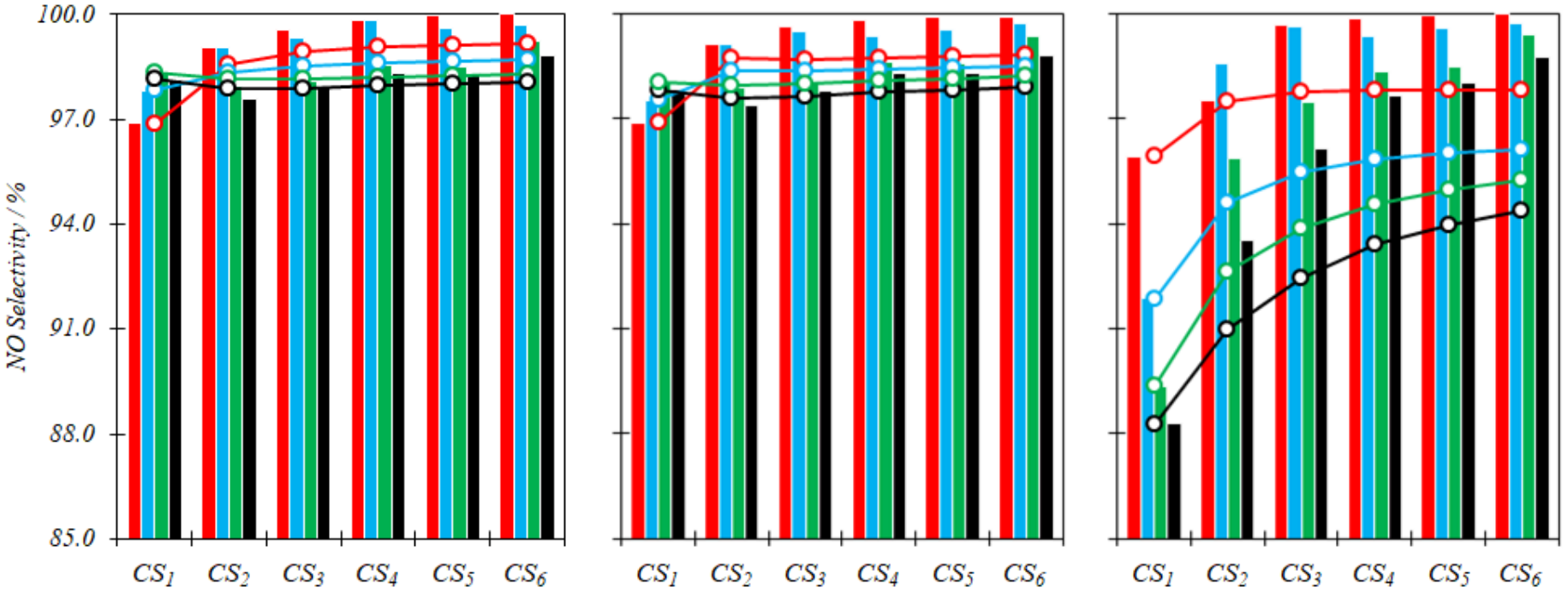

(a) 10.0 v% *(b) 11.0 v%* *(c) 12.5 v%*

Bars, a specific value in the wire.
Lines, accumulated throughout the reactor.

Inlet velocity: (■) 0.25 (■) 0.75 (■) 1.75 (■) 2.50 m s^{-1}.

Figure 39. Simulation results of the CatOx process in a catalytic square mesh reactor with six wires. NO selectivity in each wire and accumulated throughout the reactor.
Inlet conditions: 423 K, 5.0 bar, NH_3 + Dry air as balance mixture.

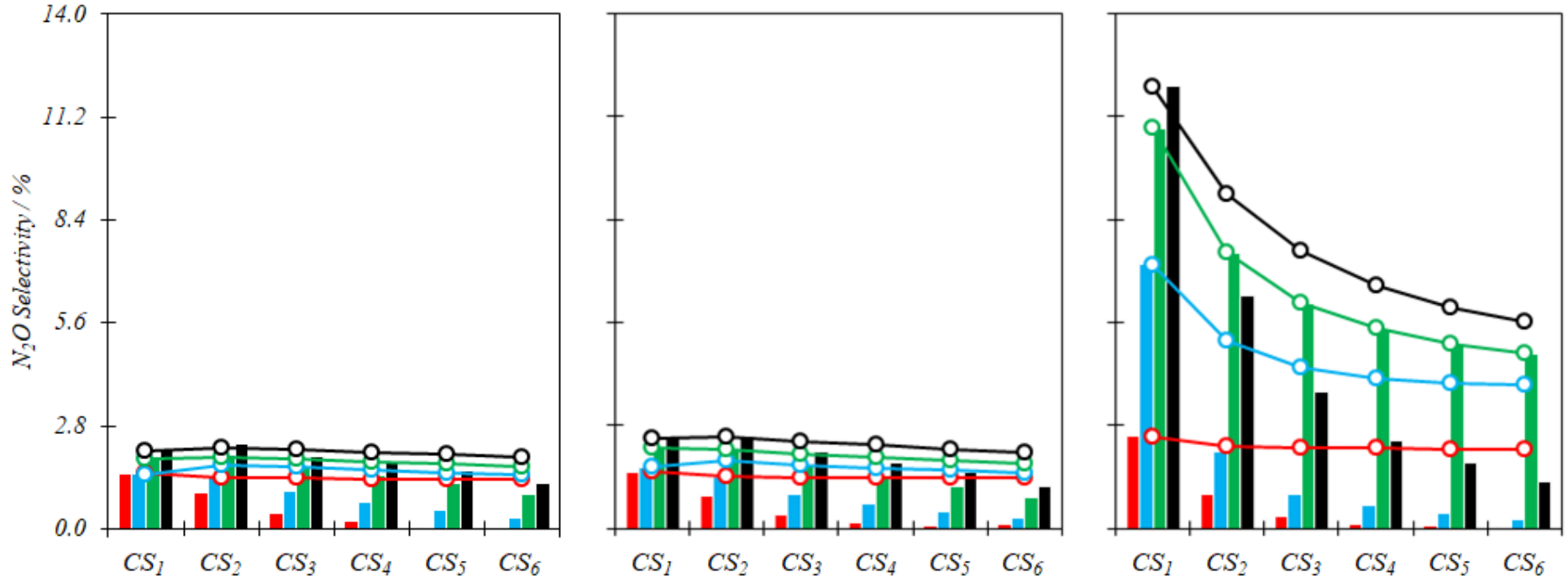

(a) 10.0 v% *(b) 11.0 v%* *(c) 12.5 v%*

Bars, a specific value in the wire.
Lines, accumulated throughout the reactor.

Inlet velocity: (■) 0.25 (■) 0.75 (■) 1.75 (■) 2.50 m s^{-1}.

Figure 40. Simulation results of the CatOx process in a catalytic square mesh reactor with six wires. N_2O selectivity in each wire and accumulated throughout the reactor.
Inlet conditions: 423 K, 5.0 bar, NH_3 + Dry air as balance mixture.

The results show for each wire that, independent of the inlet velocity and at inlet NH_3 composition between 10.0 and 11.0 v%, the N_2O selectivity is higher in the first wire and decreases along the reactor. For an inlet velocity of 2.50 m s^{-1}, the N_2O selectivity in each wire is similar. With the decrease of the inlet velocity, this behaviour changes until 0.25 m s^{-1}, from where the N_2O selectivity decreases considerably between consecutive wires.

The results of Figure 40 correspond to the reported information of the process presented in Section 3.8. Indeed, it is observed that the N_2O selectivity after the sixth wire is in all cases, for inlet NH_3 compositions between 10.0 and 11.0 v%, lower than 4.0 %. In the case of the inlet NH_3 composition of 12.5 v%, this selectivity is only achieved with an inlet velocity of 0.25 m s^{-1}. For higher inlet velocities the N_2O selectivity is significantly higher.

6.4.1.1.5. Average temperature on the surface ($\overline{T_w}$)

Figure 41 shows the behaviour of the $\overline{T_w}$ in each wire. Under these inlet conditions (423 K, 5.0 bar), increasing the inlet velocity increases up to 11.0 % the $\overline{T_w}$. In any case, at fixed inlet velocity, the increase in the inlet NH_3 composition implies an increase of up to 16.0 % in the $\overline{T_w}$ along the reactor.

This behaviour indicates that, for a given inlet NH_3 composition, the effect of the inlet velocity over the $\overline{T_w}$ is greater in the first catalyst wire. Furthermore, the changes of the inlet NH_3 composition have quantitatively the same effect over the $\overline{T_w}$ at both low and high inlet velocity.

The simulation results indicate that the superficial temperature shows a greater standard deviation with respect to its average value as the inlet velocity and the NH_3 composition increase. For fixed inlet velocity and NH_3 composition, due to the higher values of the second parameter, the deviation of the superficial temperature is greater in the first wire.

The maximum standard deviation in superficial temperature with respect to its average value is 1.31 %. Then, the $\overline{T_w}$ obtained in the CatOx simulations at 5.0 bar and 423 K as inlet conditions, is a useful boundary condition for the CatOxGP simulation.

For a fixed inlet NH_3 composition, in the first wire, the $\overline{T_w}$ is similar for all cases of inlet velocities. At inlet velocity of 0.25 m s^{-1}, the $\overline{T_w}$ remains practically constant from the third wire. For higher inlet velocities and NH_3 compositions, this process characteristic tends to disappear.

6.4.1.1.6. Average NH_3 and NO composition on the surface ($\overline{x^w_{NH_3}}$, $\overline{x^w_{NO}}$)

Figure 42 shows the behaviour of $\overline{x^w_{NH_3}}$ and $\overline{x^w_{NO}}$ in each wire. Regarding the $\overline{x^w_{NH_3}}$ in Figure 42 (a), under these inlet conditions (423 K, 5.0 bar), increasing the inlet velocity increases even up to 55.0 $\times 10^{-3}$ v% $\overline{x^w_{NH_3}}$. In any case, at fixed inlet velocity, the increase in the inlet NH_3 composition implies an increase of up to 33.0 % in the $\overline{x^w_{NH_3}}$ along the reactor.

The simulations results indicate that the NH_3 superficial composition shows a greater standard deviation with respect to its average value as the inlet velocity and NH_3 composition increase. For fixed inlet velocity and NH_3 composition, due to the higher values of the second parameter, the deviation of the NH_3 composition at the surface is greater in the first wire.

The minimum standard deviation in NH_3 composition at the surface with respect to its average value is 8.36 % and occurs for inlet NH_3 composition of 12.5 %−v on the sixth wire. Then, the $\overline{x^w_{NH_3}}$ obtained in the CatOx simulations at 5.0 bar and 423 K as inlet conditions, is not a useful boundary condition in the CatOxGP simulation. Instead, the profile of the NH_3 composition in the catalytic surface should be used.

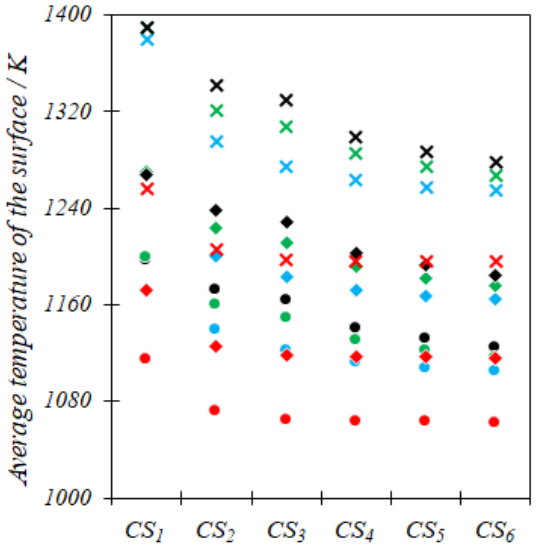

Inlet NH_3 composition: (●) 10.0 (◆) 11.0 (×) 12.5 v%.

Inlet velocity: (■) 0.25 (■) 0.75 (■) 1.75 (■) 2.50 m s^{-1}.

Figure 41. Simulation results of the CatOx process in a catalytic square mesh reactor with six wires. The $\overline{T_w}$ in each wire.
Inlet conditions: 423 K, 5.0 bar, NH_3 + Dry air as balance mixture.

This behaviour indicates that, a given inlet NH_3 composition, the effect of the inlet velocity on the $\overline{x_{NH_3}^w}$ is significantly greater in the latest wires. Furthermore, at high inlet velocity, the changes of the inlet NH_3 composition have a slightly big effect over the $\overline{x_{NH_3}^w}$.

Regarding the $\overline{x_{NO}^w}$ in Figure 42 (b), under these inlet conditions (423 K, 5.0 bar), increasing the inlet velocity increases up to 5.0 % the $\overline{x_{NO}^w}$ along the reactor. In any case, at fixed inlet velocity, the increase in the inlet NH_3 composition implies an increase of up to 23.0 % in the $\overline{x_{NO}^w}$ along the reactor.

The simulations results indicate that the NO superficial composition shows a greater standard deviation with respect to its average value as the inlet velocity and NH_3 composition increase. For fixed inlet conditions, due to the higher values of the NH_3 consumption in the reaction, the deviation NO composition at the surface is greater in the first wire.

The maximum standard deviation in NO composition at the surface with respect to its average value is 2.70 %. Then, the $\overline{x_{NO}^w}$ obtained in the CatOx simulations at 5.0 bar and 423 K as inlet conditions, is a useful boundary condition in the CatOxGP simulation.

This behaviour indicates that, a given initial NH_3 composition, the effect of the inlet velocity over the $\overline{x_{NO}^w}$ is slightly big in the first wire. In the latest wires, the effect of increasing the inlet velocity on the $\overline{x_{NO}^w}$ is greater at lower inlet NH_3 composition. Furthermore, the initial NH_3 composition changes have a slightly big effect over the $\overline{x_{NO}^w}$ practically independent of the inlet velocity.

At inlet velocity of 0.25 m s^{-1}, from the third wire, independent of the inlet NH_3 composition, the $\overline{x_{NH_3}^w}$ tends to be zero. At fixed inlet velocity, the change in inlet NH_3 composition does not generate a substantial change in the $\overline{x_{NH_3}^w}$. This change is greater when the inlet velocity increases.

With increments of the inlet velocity and the NH_3 composition, there is greater NH_3 composition in the final wires. Up to 2.50 m s^{-1} and inlet NH_3 composition of 12.5 v%, the $\overline{x_{NH_3}^w}$ is greater than

0.50 ×10^{-3} v%, even in the sixth wire. This behaviour suggests that there may be a gas phase effect in the process at inlet velocities higher than 1.75 m s^{-1}.

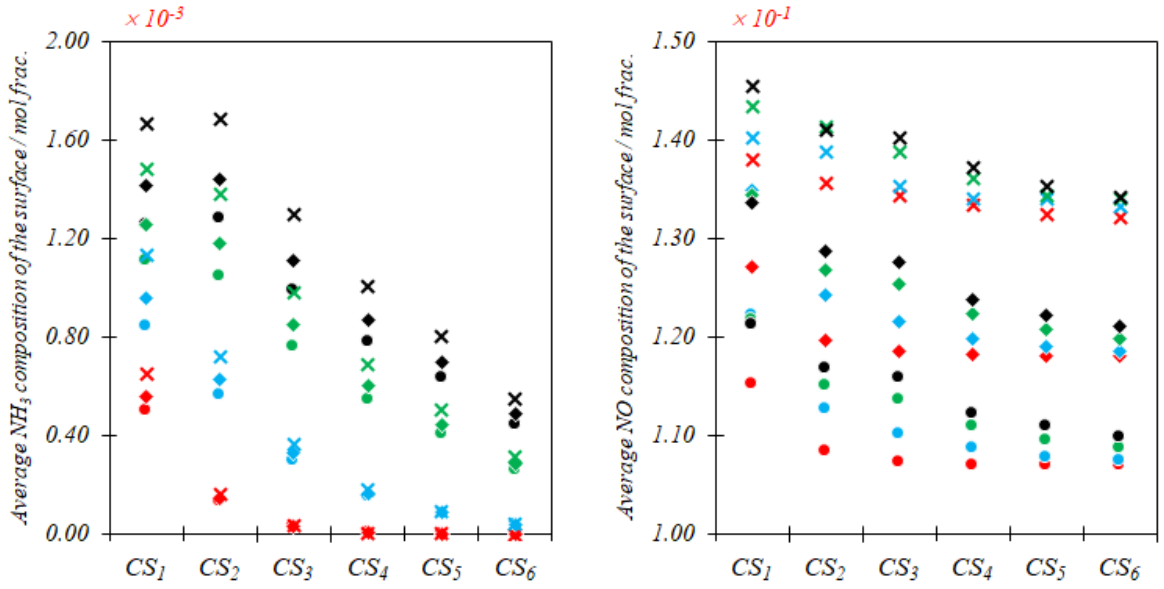

(a) $\overline{x_{NH_3}^{w}}$ *(b)* $\overline{x_{NO}^{w}}$

Inlet NH_3 composition: (●) 10.0 (◆) 11.0 (×) 12.5 v%.

Inlet velocity: (■) 0.25 (■) 0.75 (■) 1.75 (■) 2.50 m s^{-1}.

Figure 42. Simulation results of the CatOx process in a catalytic square mesh reactor with six wires. $\overline{x_{NH_3}^{w}}$ and $\overline{x_{NO}^{w}}$ in each wire.
Inlet conditions: 423 K, 5.0 bar, NH_3 + Dry air as balance mixture.

6.4.1.1.7. Average N_2O and N_2 composition of the surface ($\overline{x_{N_2O}^{w}}$, $\overline{x_{N_2}^{w}}$)

Figure 43 shows the behaviour of the $\overline{x_{N_2O}^{w}}$ and $\overline{x_{N_2}^{w}}$ in each wire. Regarding the $\overline{x_{N_2O}^{w}}$ in Figure 43 (a), under these inlet conditions (423 K, 5.0 bar), increasing the inlet velocity increases up to 5 times the $\overline{x_{N_2O}^{w}}$ along the reactor. In any case, at fixed inlet velocity, the increase in the inlet NH_3 composition implies an increase of up to 7 times in the $\overline{x_{N_2O}^{w}}$ along the reactor.

Simulation results indicate that the N_2O composition at the surface shows a greater standard deviation with respect to its average value as inlet velocity and NH_3 composition increase. For fixed inlet conditions, due to the higher N_2O generation, the deviation of the N_2O composition at the surface is greater in the first wire.

For inlet velocities lower than 0.75 m s^{-1} and for all inlet NH_3 compositions, the minimum standard deviation in the N_2O composition at the surface with respect to its average value is 11.4 % for the first wire and lower than this value for other wires.

Then, the $\overline{x_{N_2O}^{w}}$ in the first wire, obtained in the CatOx simulations at 5.0 bar, 423 K and velocities lower than 0.75 m s^{-1} as inlet conditions, is not a useful boundary condition in the CatOxGP simulation. Instead, the N_2O composition profile on the surface should be used. On the other hand, from the second wire, the $\overline{x_{N_2O}^{w}}$ obtained in the CatOx simulations is a useful boundary condition in the CatOxGP simulation.

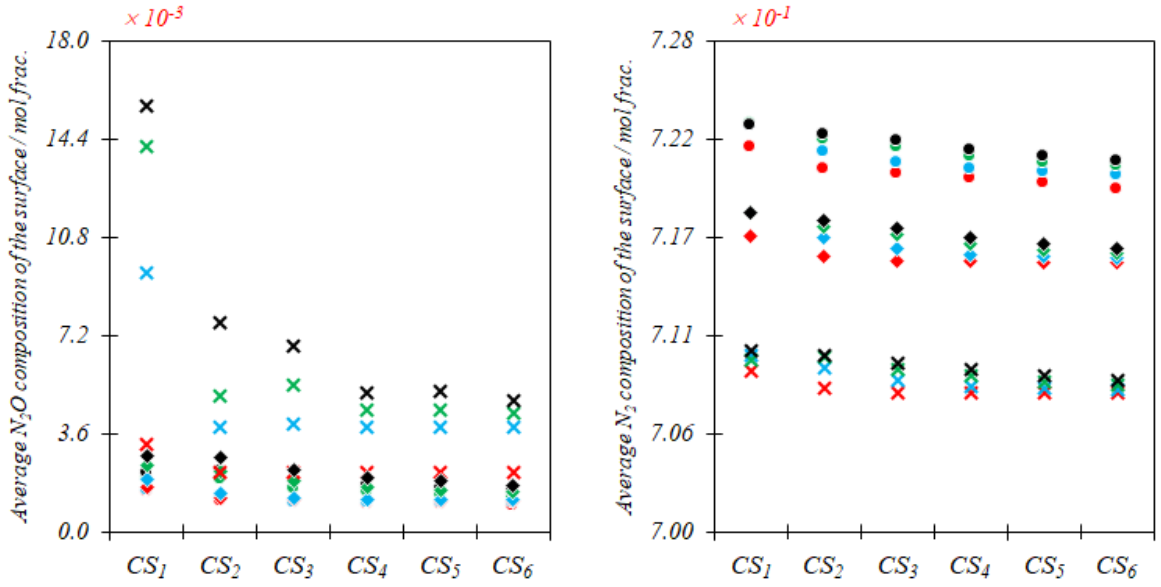

(a) $\overline{x_{N_2O}^{w}}$ (b) $\overline{x_{N_2}^{w}}$

Inlet NH_3 composition: (●) 10.0 (◆) 11.0 (×) 12.5 v%.

Inlet velocity: (■) 0.25 (■) 0.75 (■) 1.75 (■) 2.50 m s^{-1}.

Figure 43. Simulation results of the CatOx process in a catalytic square mesh reactor with six wires. $\overline{x_{N_2O}^{w}}$ and $\overline{x_{N_2}^{w}}$ in each wire.
Inlet conditions: 423 K, 5.0 bar, NH_3 + Dry air as balance mixture.

For inlet velocities higher than 1.75 m s^{-1} and all inlet NH_3 composition, the minimum standard deviation of the N_2O composition at the surface with respect to its average value is 10.7 % between the first and third wire and lower than this value for other wires.

Then, the $\overline{x_{N_2O}^{w}}$ in the three initial wires, obtained in the CatOx simulations at 5.0 bar, 423 K and inlet velocities higher than 1.75 m s^{-1} as initial conditions, is not a useful boundary condition in the CatOxGP simulation. Instead, the N_2O composition profile on the surface should be used. On the other hand, between the fourth and sixth wire, the $\overline{x_{N_2O}^{w}}$ obtained in the CatOx simulations is a useful boundary condition in the CatOxGP simulation.

This behaviour indicates that, the effect of the inlet velocity on the $\overline{x_{N_2O}^{w}}$ is small when the inlet NH_3 composition is lower than 11.0 v% and big when it is higher than this value. Furthermore, at high inlet velocities, the changes of inlet NH_3 composition have a bigger effect over the $\overline{x_{N_2O}^{w}}$ of the first wires.

Regarding the $\overline{x_{N_2}^{w}}$ in Figure 43 (b), under these inlet conditions (423 K, 5.0 bar), increasing the inlet velocity has not effect over $\overline{x_{N_2}^{w}}$. Independent of the inlet velocity, increasing the inlet NH_3 composition increases up to 2.0 % the $\overline{x_{N_2}^{w}}$ along the reactor.

The simulation results indicate that the N_2 composition at the surface shows a greater standard deviation with respect to its average value as the inlet velocity and NH_3 composition decrease. For fixed inlet velocity and NH_3 composition, the deviation of the N_2 composition at the surface is greater in the first wire.

The maximum standard deviation in N_2 composition at the surface with respect to its average value is 0.050 %. Then, the $\overline{x_{N_2}^w}$, obtained in the CatOx simulations at 5.0 bar and 423 K as inlet conditions, is a useful boundary condition for the CatOxGP simulation.

This behaviour indicates that, a given inlet NH_3 composition, the inlet velocity has not enough effect over the $\overline{x_{N_2}^w}$. Furthermore, independent of the velocity, the inlet NH_3 composition has slightly effect over the $\overline{x_{N_2}^w}$.

For inlet NH_3 composition lower than 12.5 v% and independent of the inlet velocity, the $\overline{x_{N_2O}^w}$ value of 0.20 v% seems to be typical for all simulation cases. In any other cases, the $\overline{x_{N_2O}^w}$ in the first wire is significantly higher. Since there is not a simulation case, in which the inlet N_2 composition is lower than 69.2 v%, with the increase in NH_3 consumption, the variation in the $\overline{x_{N_2}^w}$ is minimal between each wire.

This means that if there is any effect of the gas phase process on the catalytic oxidation of NH_3 (at 5.0 bar and 423 K as inlet conditions), this will increase with the initial velocity and NH_3 composition and will preferably occur in the first wires of the catalytic mesh.

6.4.1.2. Operational case: increase of inlet temperature to 462 or 500 K

When the inlet temperature increases from 423 K to 462 or 500 K and the inlet pressure remains at 5.0 bar, the simulation results of the CatOx process have the same behaviour as was shown between Figures 37 and 43 for the basic cases of operation, but the following characteristics are specific at this new temperature conditions:

- At inlet conditions of 462 or 500 K and 5.0 bar, independent of inlet NH_3 composition, increasing inlet velocity:
  - ✓ decreases up to 8 times the residence time, and 57.0 % the NH_3 consumption, along the reactor.
- At inlet conditions of 462 or 500 K and 5.0 bar, increasing inlet velocity:
  - ✓ decreases up to 7.0 % the NO selectivity along the reactor.
  - ✓ increases from zero to 48.0 $\times 10^{-3}$ v% the $\overline{x_{NH_3}^w}$.
  - ✓ has no effect over $\overline{x_{N_2}^w}$.
  - ✓ increases up to 9.0 % the N_2O selectivity, 12.0 % the $\overline{T_w}$, 7.0 % the $\overline{x_{NO}^w}$, and 6 times the $\overline{x_{N_2O}^w}$ along the reactor.
- In any case, at fixed inlet velocity, the increase in the inlet NH_3 composition:
  - ✓ decreases up to12.0 % the residence time and 10.0 % the NO selectivity along the reactor. along the reactor.
  - ✓ increases up to 2.0 % the NH_3 consumption, 9.0 % the N_2O selectivity, 15.0 % the $\overline{T_w}$, 33.0 % the $\overline{x_{NH_3}^w}$ along the reactor, 25.0 % the $\overline{x_{NO}^w}$, 8 times the $\overline{x_{N_2O}^w}$ and 2.0 % the $\overline{x_{N_2}^w}$ along the reactor.
- In relation to the basic cases, independent of the inlet NH_3 composition, the increase of the inlet temperature (up to 462 or 500 K):
  - ✓ increases the residence time along the reactor up to 6.0 or 11.0 % respectively.
  - ✓ increases the NH_3 consumption along the reactor up to 3.0 or 15.0 % respectively.
  - ✓ increases the $\overline{T_w}$ along the reactor up to 3.0 or 6.0 % respectively.
  - ✓ decrease the $\overline{x_{NH_3}^w}$ along the reactor up to 78.0 % or 2 times respectively.

- ✓ decrease the $\overline{x_{N_2O}^{w}}$ along the reactor up to 25.0 or 54.0 % respectively.
- ✓ has no effect over $\overline{x_{N_2}^{w}}$.

- In relation to the basic cases, independent of the inlet velocity, the increase of the inlet temperature up to 462 K has no effect over the NO selectivity. While the increase of the inlet temperature up to 500 K increases up to 1.0 % the NO selectivity along the reactor.
- In relation to the basic cases, independent of the inlet velocity and NH_3 composition, the increase of the inlet temperature (up to 462 or 500 K) increases the N_2O selectivity along the reactor by up to 1.0 %.
- In relation to the basic cases, independent of the inlet velocity, the increase of the inlet temperature (up to 462 or 500 K) increases up to 4.0 % the $\overline{x_{NH_3}^{w}}$ along the reactor.
- The increment of the inlet temperature, independent of the inlet NH_3 composition, influences the behaviour of:
  - ✓ the residence time specially at low inlet velocities.
  - ✓ the NH_3 consumption specially at high inlet velocities at the last wires.
- The increment of the inlet temperature influences especially the behaviour of:
  - ✓ the NO selectivity at inlet NH_3 composition of 12.5 v%.
  - ✓ the $\overline{x_{N_2O}^{w}}$ at inlet conditions of 0.25 m s^{-1} and 12.5 v%, or 2.50 m s^{-1} and 10.0 v% (velocity and NH_3 composition).
- At inlet inlet velocity of 2.50 m s^{-1} and inlet NH_3 composition of 12.5 v%, the increment of the inlet temperature influences especially the behaviour of the N_2O selectivity, the $\overline{x_{NH_3}^{w}}$ and the $\overline{x_{NO}^{w}}$.
- The increment of the inlet temperature influences especially the behaviour of the AST along the reactor at inlet velocity of 2.50 m s^{-1} and inlet NH_3 compositions between 10.0 and 11.0 v%.
- Compared with the basic cases of operation, the dependence of the residence time with the inlet velocity is not the same for all wires, being high for the latest wires. At fixed inlet velocity, especially at low values, the variation of the residence time respect to the inlet NH_3 composition is greater.
- It is noticeable that the effect of the increasing of temperature to 462 or 500 K over the NO selectivity corresponds to the information reported in Figure 9 for the process. That is, at 5.0 bar, the increase in the inlet temperature induces the increase in NO selectivity.

6.4.1.3. Operational case: increase of inlet pressure to 10.0 bar

When the inlet pressure increases from 5.0 bar to 10.0 bar and the inlet temperature remains at 423 K, the simulation results of the CatOx process have the same behaviour as was shown between Figures 37 and 43 for the basic cases of operation, but the following characteristics are specific at this new pressure condition:

- At inlet conditions of 423 K and 10.0 bar, independent of inlet NH_3 composition, increasing inlet velocity:
  - ✓ decreases 8 times the residence time, up to 44.0 % the NH_3 consumption and up to 5.0 % the NO selectivity along the reactor.
  - ✓ increases up to 7.0 % the N_2O selectivity, 5.0 % the $\overline{T_w}$, 6.0 % the $\overline{x_{NO}^{w}}$, 3 times the $\overline{x_{N_2O}^{w}}$ and from zero to 59.0 $\times 10^{-3}$ v% the $\overline{x_{NH_3}^{w}}$ along the reactor
  - ✓ has no effect over $\overline{x_{N_2}^{w}}$.

- In any case, at fixed inlet velocity, the increase in the inlet NH_3 composition increases up to 13.0 % the residence, 2.0 % the NH_3 consumption, 8.0 % the NO selectivity, 8.0 % the N_2O selectivity, 16.0 % the $\overline{T_w}$, 33.0 % the $\overline{x_{NH_3}^w}$, 24.0 % the $\overline{x_{NO}^w}$, 5 times the $\overline{x_{N_2O}^w}$ and 2.0 % the $\overline{x_{N_2}^w}$ along the reactor.
- In relation to the basic cases, independent of the inlet NH_3 composition, the increase of the inlet pressure up to 10.0 bar:
  - ✓ increases up to 12.0 % the residence time and 8.0 % the $\overline{T_w}$ along the reactor.
  - ✓ decreases up to 15 times the $\overline{x_{NH_3}^w}$ along the reactor.
- In relation to the basic cases, independent of the inlet velocity, the increase of the inlet pressure up to 10.0 bar increase up to 2.0 % the NO selectivity and the N_2O selectivity along the reactor.
- In relation to the basic cases, independent of the inlet velocity and of the inlet NH_3 composition, the increase of the inlet pressure up to 10.0 bar increase up to 2.0 % the NH_3 consumption, 5.0 % the $\overline{x_{NO}^w}$ and 82.0 % the $\overline{x_{N_2O}^w}$ along the reactor.
- The increment of the inlet pressure, independent of the inlet NH_3 composition, influences the behaviour of:
  - ✓ the residence time at low inlet velocities.
  - ✓ the NH_3 consumption at high inlet velocities at the last wires.
- The increment of the inlet pressure, at inlet velocity of 0.25 m s^{-1} and inlet NH_3 composition of 12.5 v%, influences the behaviour o the $\overline{x_{NH_3}^w}$, the $\overline{x_{NO}^w}$, and the $\overline{x_{N_2O}^w}$
- The increment of the inlet pressure, at inlet NH_3 composition of 12.5 v%, influences the behaviour of the NO selectivity along the reactor.
- The increment of inlet pressure, at inlet velocity of 2.50 m s^{-1} and inlet NH_3 composition 12.5 v%, influencesthe behaviour of the N_2O selectivity along the reactor.
- The increment of inlet pressure, at inlet velocity of 2.50 m s^{-1} and inlet NH_3 composition between 10.0 and 11.0 v%, influences the behaviour of the $\overline{T_w}$ along the reactor.
- The increment of inlet pressure, at inlet velocity of 2.50 m s^{-1} and inlet NH_3 composition of 10.0 v%, influences the behaviour of the the $\overline{x_{N_2O}^w}$.
- Compared with the basic cases of the operation, the dependence of the residence time with the inlet velocity is not the same for all wires, being high for the latest wires. At a fixed inlet velocity, especially at low values, the variation of the residence time respect to the inlet NH_3 composition is greater.
- Compared with the basic cases of the operation, the $\overline{x_{N_2O}^w}$ dependence with the inlet velocity is low, especially in the last wires. The variation of the $\overline{x_{N_2O}^w}$ respect to the inlet NH_3 composition is slightly high especially at inlet velocity of 2.50 m s^{-1}.

6.4.1.4. Operational case: simultaneous increase of inlet temperature to 462 or 500 K and inlet pressure to 10.0 bar, and inlet temperature to 500 or 530 K and inlet pressure to 15.0 bar

When the inlet temperature increases from 423 K to 462 or 500 K, and the inlet pressure increases from 5.0 bar to 10.0 bar or the inlet temperature increases from 423 K to 500 or 530 K, and the inlet pressure increases from 5.0 bar to 15.0 bar, the simulation results of the CatOx process have the same behaviour as was shown between Figures 37 and 43 for the basic cases of operation, but the following characteristics are specific at this new pressure condition:

- At inlet temperatures between 462 and 500 K and inlet pressure of 10.0 bar, independent of the inlet NH_3 composition, increasing the inlet velocity:
  - ✓ decreases up to 8 times the residence time, 49.0 % the NH_3 consumption and 5.0 % NO selectivity along the reactor.
  - ✓ increases up to 7.0 % N_2O selectivity and 5.0 % $\overline{T_w}$ along the reactor.
- At inlet temperatures between 462 and 500 K and inlet pressure of 10.0 bar, increasing the inlet velocity increases from zero to 55.0 $\times 10^{-3}$ v% the $\overline{x_{NH_3}^w}$, up to 6.0 % the $\overline{x_{NO}^w}$ and 3 times $\overline{x_{N_2O}^w}$ along the reactor.
- At inlet temperatures between 462 and 500 K and inlet pressure of 10.0 bar, increasing the inlet velocity has no effect over $\overline{x_{N_2}^w}$.
- At fixed inlet velocity, the increase in the inlet NH_3 composition:
  - ✓ decreases up to 12.0 % the residence time and 8.0 % the NO selectivity along the reactor.
  - ✓ increases up to 2.0 % NH_3 consumption, 8.0 % the N_2O selectivity, 18.0 % the $\overline{T_w}$, 32.0 % the $\overline{x_{NH_3}^w}$, 25.0 % the $\overline{x_{NO}^w}$ along the reactor, 5 times $\overline{x_{N_2O}^w}$ and 2.0 % $\overline{x_{N_2}^w}$ along the reactor along the reactor.
- At inlet temperatures between 500 and 530 K and inlet pressure of 15.0 bar, independent of the inlet NH_3 composition, increasing the inlet velocity:
  - ✓ decreases up to 27.0 % the residence time and 7.0 % the NH_3 consumption along the reactor.
  - ✓ increases up to 1.0 % the $\overline{T_w}$ and 10.0 % the $\overline{x_{NH_3}^w}$ along the reactor.
  - ✓ has no effect over $\overline{x_{NO}^w}$ or $\overline{x_{N_2}^w}$.
- At inlet temperatures between 500 and 530 K and inlet pressure of 15.0 bar, there is no effect over the NO selectivity or N_2O selectivity due to increment on inlet velocity or NH_3 composition.
- At inlet temperatures between 500 and 515 K and 15.0 bar, independent of the inlet velocity, increasing the inlet NH_3 composition increases up to 14.0 % the N_2O selectivity along the reactor.
- At inlet conditions of 530 K, 15.0 bar and 1.40 m s^{-1}, the increase in the inlet NH_3 composition implies an increase of up to 31.0 % the N_2O selectivity and 45.0 % the $\overline{x_{N_2O}^w}$ along the reactor along the reactor.
- For inlet temperature of 500 and 515 K, at an inlet pressure of 15.0 bar, independent of the inlet NH_3 composition, and for inlet temperature of 530 K at inlet NH_3 composition of 11.0 v% increasing the inlet velocity increases 10.0 % the $\overline{x_{N_2O}^w}$ along the reactor.
- For inlet temperature of 500 and 515 K, at fixed inlet velocity, increasing the inlet NH_3 composition increases up to 26.0 % the $\overline{x_{N_2O}^w}$ along the reactor.
- At inlet conditions of 530 K and 15.0 bar, independent of the inlet NH_3 composition, increasing the inlet velocity increase up to 2.0 % $\overline{x_{N_2}^w}$.
- At inlet temperatures between 500 and 530 K, 15.0 bar and fixed inlet velocity, increasing the inlet NH_3 composition has no effect over $\overline{x_{N_2}^w}$.
- At fixed inlet velocity, increasing the inlet NH_3 composition:
  - ✓ decreases up to 3.0 % the residence time along the reactor.
  - ✓ increases up to 1.0 % NH_3 consumption, 18.0 % the $\overline{T_w}$, 12.0 % the $\overline{x_{NH_3}^w}$ and 10.0 % $\overline{x_{NO}^w}$ along the reactor.
- In relation to the base case, independent of the inlet NH_3 composition, the simultaneous increase of the inlet temperature (up to 462 and 500 K) and pressure up to 10.0 bar:

- ✓ increase up to 88.0 % the residence time and 10.0 % the $\overline{T_w}$ along the reactor.
- ✓ decrease up to 16.0 % the NH_3 consumption along the reactor.

- In relation to the basic cases, the simultaneous increase of the inlet temperature (up to 462 or 500 K) and pressure up to 10.0 bar decrease up to 8 times the $\overline{x_{NH_3}^w}$ and 49.0 % the $\overline{x_{N_2O}^w}$ along the reactor.
- In relation to the basic cases, the simultaneous increase of the inlet temperature (up to 462 or 500 K) and pressure (up to 10.0 or 15.0 bar):
  - ✓ increase up to 3.0 % the $\overline{x_{NO}^w}$ along the reactor.
  - ✓ has no effect over $\overline{x_{N_2}^w}$.
- In case of the simultaneous increment of the inlet temperature (up to 500 and 530 K) and pressure up to 15.0 bar, independent of the inlet NH_3 composition:
  - ✓ increase up to 20.0 % the residence time, 9.0 % the NO selectivity, 74.0 % the N_2O selectivity and 41.0 % the $\overline{T_w}$, 11.0 % $\overline{x_{NO}^w}$ and 65.0 % $\overline{x_{N_2O}^w}$ along the reactor.
  - ✓ decrease up to 41.0 % the NH_3 consumption and 51.0 % $\overline{x_{NH_3}^w}$ along the reactor.
- In relation to the basic cases, independent of the inlet velocity, the simultaneous increase of the inlet temperature (up to 462 and 500 K) and pressure up to 10.0 bar:
  - ✓ decrease up to 2.0 % the NO selectivity along the reactor.
  - ✓ has no effect over the N_2O selectivity along the reactor.
- The increment of the inlet temperature, at low inlet velocities and independent of the NH_3 composition, influences the behaviour of the residence time.
- The increment of the inlet temperature, at high inlet velocities, independent of the NH_3 composition and in the last wires, influences the behaviour of the NH_3 consumption.
- The increment of the inlet temperature, at inlet NH_3 composition of 12.5 %, influences the behaviour of the NO selectivity along the reactor.
- The increment of the inlet temperature, at inlet velocity of 2.50 m s^{-1} and inlet NH_3 composition of 12.5 %, influences the behaviour of the N_2O selectivity along the reactor.
- The increment of the inlet temperature, at inlet velocity of 2.50 m s^{-1} and inlet NH_3 composition between 10.0 and 11.0 %, influences the behaviour of the $\overline{T_w}$ along the reactor.
- The increment of the inlet temperature, at inlet velocity of 1.40 m s^{-1} and inlet NH_3 composition of 12.5 v%, influences the behaviour of the $\overline{x_{NH_3}^w}$, the $\overline{x_{NO}^w}$ and the $\overline{x_{N_2O}^w}$ along the reactor.
- The increment of the inlet temperature, at inlet velocity of 2.50 m s^{-1} and inlet NH_3 composition of 10.0 v%, influences the behaviour of the $\overline{x_{N_2O}^w}$ along the reactor.
- Compared with the basic cases of the operation, the dependence of the residence time with the inlet velocity is not the same for all wires, being high for the latest wires. At fixed inlet velocity, especially at low values, the residence time variation respect to the inlet NH_3 composition is greater.
- Compared with the basic cases of the operation, the dependence of the $\overline{x_{N_2O}^w}$ with the inlet velocity is low, especially in the last wires. The variation of the $\overline{x_{N_2O}^w}$ respect to the inlet NH_3 composition is slightly high especially at an inlet velocity of 2.50 m s^{-1}.

6.4.2. Catalytic and gas phase process

This section presents the results of the CatOxGP process on the first catalytic wire and compares them with the results of the CatOx process presented in section 9.5.1. For the simulation of the CatOxGP process the reduced mechanism (Appendix 3) was used.

The Table 6 shows the results of the mass balance of nitrogen – based molecules and N – atoms associated with the simulation results, which are shown in Figure 44. This information implies that the simulation accomplishes the mass balance of nitrogen as a principal atom in the process. Indeed, the imbalance of –1.12 kg m^{-3} s^{-1} corresponds only with the 0.441 % of the nitrogen aported by the NH_3 oxidation (–254 kg m^{-3} s^{-1}). The Table 7 shows the net reaction rate and the composition at outlet of the non nitrogen – based species. Based on the results form Tables 6 and 7, it is possible to determinate that the global mass unbalance is 45.1 kg m^{-3} s^{-1}, it is the 4.38 % of the net reaction rate of the reactives that entrance into the reactor (NH_3, O_2). The simulation results are valid and useful from the point of view of the mass balance. It is notable that for the first wire the composition of the radical species corresponds to the formation of nitrogen based intermidiates. Those are highlighted in the Table 6. It is important to point that the net reaction rates presented in Tables 6 and 7 are global values, it means that considers the results of the simulaton on CatOxGP.

Table 8 shows the results of NH_3 conversion and selectivity of N_2O, NO and N_2. This table show the net reaction rate as well for these species. The NH_3 conversion was calculated according to equation (92). The NO, N_2O and N_2 selectivities were calculated according to equations (93), (95) and (97) respectively when $(i = 1 \rightarrow CS_{i-1} = CS_0)$. The net reaction rates were calculated according to equation (101) when $\sum_{i=1}^{CS} V^{CS_i} = V^{CS_1} = 4.50 \times 10^{-8} m^3$. The mencioned equations have been previously presented in Section 3.7.6.

The CatOxGP process induces the increment in the NH_3 conversion, N_2O selectivity and N_2 selectivity. The decrease in the NO selectivity and the increase in the N_2 selectivity evidence the effect of the gas phase process, which induces the selective non – catalytic reduction of NO in the chemical system.

Table 6. Results of the mass balance of nitrogen – based molecules and N – atoms in the simulation of the CatOxGP process in the catalytic square mesh reactor, single wire case.
Inlet conditions: 0.75 m s^{-1}, 423 K, 5.0 bar, 10.0 v% NH_3, 90.0 v% dry air.

Molecule	Net reaction rate		Molecule composition	
	of molecule	of constituent N – atom	at inlet	at outlet
	kg m^{-3} s^{-1}		v%	
H_2NO	9.50	**4.15**	0.0	6.73×10^{-2}
HNO	43.1	**19.4**	0.0	3.15×10^{-1}
HONO	125	**37.2**	0.0	6.03×10^{-1}
N_2	9.88×10^{-3}	9.88×10^{-3}	71.1	70.4
N_2O	5.97	3.80	0.0	3.08×10^{-2}
NH_3	−309	−254	10.0	5.78
NO	402	188	0.0	3.04
NO_2	9.88×10^{-3}	3.01×10^{-3}	0.0	4.87×10^{-5}
NH_2	4.96×10^{-3}	4.34×10^{-3}	0.0	1.14×10^{-5}
NNH	7.73×10^{-1}	7.47×10^{-1}	0.0	6.05×10^{-3}
Unbalance of nitrogen, kg m^{-3} s^{-1}:		*−1.12*		

Table 7. Results of net reaction rate and outlet composition for non nitrogen – based molecules in the simulation of the CatOxGP process for the catalytic square mesh reactor, single wire case.
Inlet conditions: 0.75 m s^{-1}, 423 K, 5.0 bar, 10.0 v% NH_3, 90.0 v% dry air.

Simulation result		**H**	**H_2**	**H_2O**	**HO_2**	**O**	**O_2**	**OH**
Net reaction rate	kg m^{-3} s^{-1}	4.28 $\times10^{-7}$	2.26 $\times10^{-4}$	487	4.50 $\times10^{-6}$	2.55 $\times10^{-7}$	−720	1.20 $\times10^{-4}$
Composition at outlet	v%	9.64 $\times10^{-8}$	2.55 $\times10^{-5}$	6.14	3.09 $\times10^{-8}$	3.62 $\times10^{-9}$	13.6	9.10 $\times10^{-7}$

Table 8. Simulation results of the catalytic square mesh reactor, single wire case.
Inlet conditions: 0.75 m s^{-1}, 423 K, 5.0 bar, 10.0 v% NH_3, 90.0 v% dry air.

Species	**Performance parameter**		**Change due to CatOxGP**	**Net reaction rate of**		**Change due to CatOxGP**
	CatOx	**CatOxGP**		**CatOx**	**CatOxGP**	
	%		%	kg m^{-3} s^{-1}		%
NH_3 (*)	40.1	41.4	+1.30	307	309	+ 0.647
N_2O (**)	1.49	1.50	+0.010	5.89	5.97	+ 1.340
NO (**)	98.3	97.8	–0.050	533	402	+24.6
N_2 (**)	0.203	0.674	+0.471	7.03 $\times10^{-3}$	9.88 $\times10^{-3}$	+28.8

Performance parameter: (*) Conversion, (**) Selectivity

Figure 44 show the results of the simulation of the catalytic square mesh reactor with a single wire for ANSYS FLUENT [Flu 16 – 01] model. These results refer to the nitrogenous species that participate simultaneously in the CatOx and CatOxGP processes.

Figure 44 shows the composition and net reaction rate for the principal species in the catalytic mechanism result of the simulation of the CatOxGP process. In the case of the net reaction rate, the numerical scale of the variable corresponds exclusively to the process carried out in the gas phase, that is, it does not consider the net reaction rate due to catalytic reactions.

The reaction rate contour in Figure 44 (a) shows the NH_3 consumption rate in the gas phase, especially in the posterior face of the catalytic wire. The contour of net reaction rate of NH_3 shows the clear tendency to consumption of the substance in the gas phase. The mechanisms for the NH_3 consumption in the gas phase correspond to its direct oxidation or its oxidation in the presence of NO. The amplitude of the profile of the net reaction rate of NH_3 is consistent with the radical formation zone.

Regarding N_2O, the contour in Figure 44 (b) shows this increase in the rate of the N_2O, especially in the posterior face of the catalytic wire. In the same area where NO formation occurs (behind the wire), the largest reaction rate in the gas phase takes place, in this region the highest reactor temperature is also observed. There occur simultaneously: i). the consumption in the gas phase of the remaining NH_3, ii). the consumption in the gas phase of the NO formed in the CatOx process and iii) the N_2O and N_2 formation. The contour of the net reaction rate of N_2O shows both consumption and generation zones. The genertion zones are wider than the consumption zones and this characteristic is reflected in the global reaction rate, which tends to the N_2O generation, as is shown in the Tables 6 and 8.

Regarding NO, the contour in Figure 44 (c) shows that this decrease in the global reaction rate is due to the NO consumption, especially in the posterior face of the catalytic wire, where the process in

the gas phase takes place. The contour of the net reaction rate of NO shows the clear tendency to consumption of the substance in the gas phase. The mechanisms for the NO consumption in the gas phase correspond to its direct oxidation or reduction in the presence of NH_3.

Regarding N_2, the contour in Figure 44 (d) shows that this increase in the global reaction rate is due to the N_2 generation, especially in the posterior face of the catalytic wire, where the selective non – catalytic reduction of NO to N_2 due to NH_3 take place. The contour of net reaction rate of N_2 shows the clear tendency to the generation of the substance in the gas phase as a product of the direct oxidation of NH_3 or NO, or as a product of the NO reduction in the presence of NH_3.

Appendix 8 presents the formation of some of the most important radicals considered in the gas phase process. The formation of these radicals agrees with the fact that gas phase reactions occur mainly on the back side of the catalytic wire, confirming, that in this region, processes in the gas phase are presented. In the case of the net reaction rate, the numerical scale of the variable corresponds exclusively to the process carried out in the gas phase, that is, it does not consider the net reaction rate due to catalytic reactions.

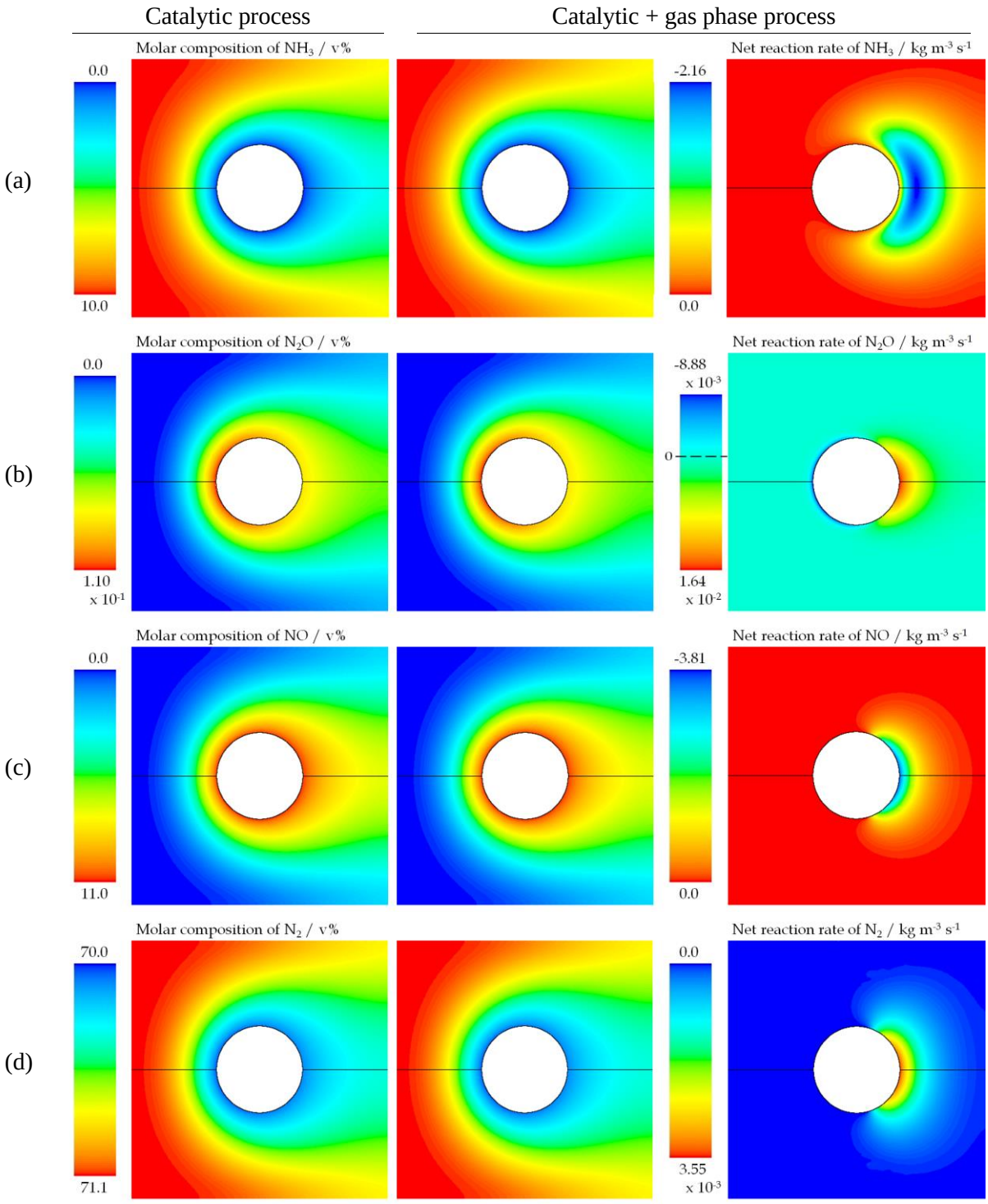

Figure 44. Results of the simulation of the CatOx and CatOxGP processes in the first wire of the square mesh reactor. Contours of composition and net reaction rate of NH_3, N_2O, NO and N_2.
Inlet conditions: 0.75 m s^{-1}, 423 K, 5.0 bar, 10.0 v% NH_3, 90.0 v% dry air.

7. Simulation of the stagnation point reactor

This chapter presents the methodology, results, and discussion about the simulation of the stagnation point reactor. It possesses an axial symmetric geometry with a fluid coming out of an inlet and flowing against a surface or flow straightener causing the fluid to flow out of the reactor in a radial direction. This type of reactor is often used to study heterogeneous combustion reactions with a catalyst on the surface because of its unique geometry all physical variables only change in the axial direction along the z – axis and are constant in the radial axis r. Because of this property of the reactor, this tridimensional problem can be reduced to a one – dimensional problem by using a similarity transformation making the problem much simpler and easier to study.

For this reason, this geometry is useful to simplify the simulation process and at the same time obtain results that allow to establish the influence of the CatOxGP process. In this regard, this chapter presents the results of the simulation of the CatOxGP process once the reduced mechanism (Appendix 3) was used. This simulation takes place in an area equivalent to the first catalytic wire of the square mesh reactor, whose simulation results were presented in the Section 6.4.1.

Although this CFD simulation model reduces the numerical difficulty to simulate the CatOxGP process with respect to the model of the first wire in the square mesh reactor, due to the consideration of axi – symmetry, this model does not favor the simulation sufficiently to consider the conditions like those that occur from the second catalytic wire.

To carry out the simulation of the stagnation point reactor, the CFD methodology with ANSYS FLUENT [Flu 16 – 01], from the domain shown in Figure 45, and the model suggested by the package for simulation of physicochemical processes CANTERA [Goo 2017] were used.

CANTERA [Goo 2017] propouses a one – dimensional model, which is developed in the axis of symmetry of the domain presented in Figure 45. For the simulation of the CatOxGP process using CANTERA, the reduced mechanism (Appendix 3) was used.

The chemical reactions for the gas phase will be described by the AA – Mech [Kil 1999] [Cod 2001]. For the surface reactions the mechanism presented by Krähner [Kra 2008] was used. The reactions are modelled by the model presented in Section 3.7. The reactions itself will be left untouched however there will be used only one active site for all species instead of two active sites with one site being exclusively used for NH_3 and the other one for the other species.

7.1. Geometry and mesh

With the aim of simulate the catalytic oxidation of NH_3 in the stagnation point reactor, the geometry consists in 0.15 mm gap (outlet) length, inlet, and catalytic surface, both with a diameter of 0.15 mm. The catalytic surface is located perpendicular to the inlet flow.

ANSYS MESHING [Flu 16 – 02] was used for the generation of the domain of the numerical simulation. Figure 45 shows a detail of the geometry and the mesh. This mesh has 8664 quadrilateral cells. Since it is considered that during the process, the temperature of the catalytic surface is uniform and stable, its internal mesh has not been considered for simulation purposes. This mesh has MAR = 1.48, MOQ = 0.997 and MOS = 2.89×10^{-3}. Therefore, it can be used for simulation proposes.

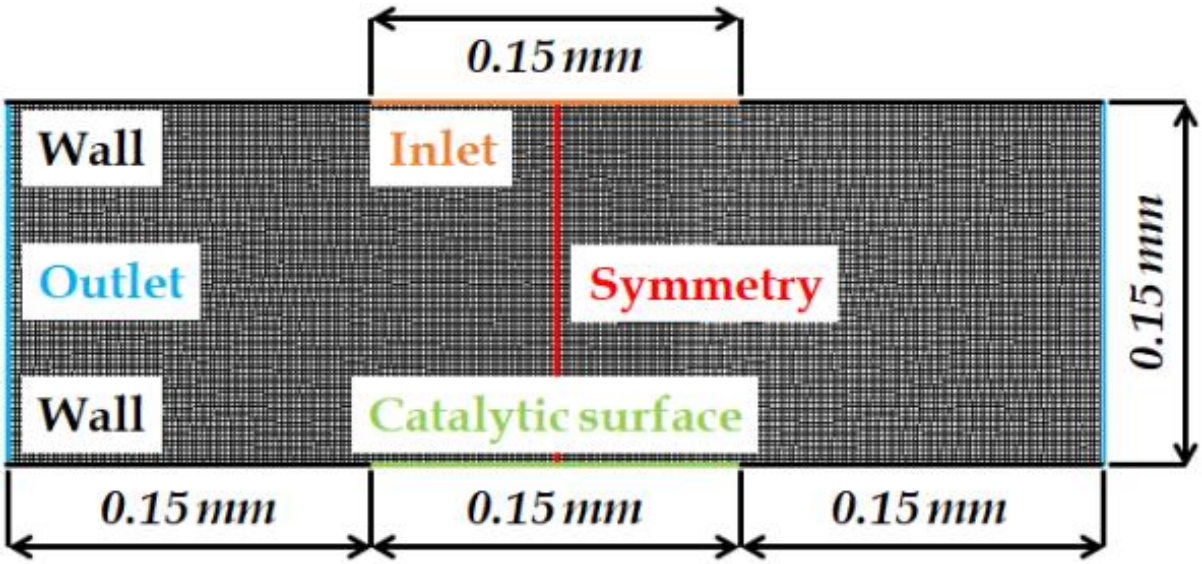

Figure 45. Geometry and meshing of stagnation point reactor.

7.2. Spatial convergence of the mesh

According to the methodology presented by Slater [Sla 2012], two refinements were applied on the stagnation point reactor presented on Figure 45 (8664 cells) obtaining meshes of 17415 and 35003 cells respectively (which implies a refining ratio of 2.01). With these calculation domains, the simulation of the CatOx process was applied and with the operating conditions:

- The mass flux of the inlet is 3.0 kg m^{-2} s^{-1}.
- The inlet temperature of 423 K.
- The pressure of 5.0 bar.
- The volumetric composition of 10.0 v% NH_3 and 90.0 v% dry air.

Figure 46 presents the results of the analysis of spatial convergence for the stagnation point reactor. It is observed that the results do not differ significantly for each computational domain. In the worst case, the outlet H_2O composition, calculated with the least refined mesh (8664 cells) is 0.828 % higher than that obtained in the simulation with the most refined mesh (35003 cells). It indicates that the mesh presented in Figure 45 (8664 cells) is useful for the simulation proposes.

7.3. Boundary conditions and configuration of the simulation

To carry out the simulation of the cases associated with the stagnation point reactor, the conditions described in this section were used. For the CatOxGP process, the Table 9 shows the inlet conditions used for the ANSYS FLUENT [Flu 16 – 01] and the CANTERA [Goo 2017] simulations.

The inlet conditions used for the simulation of the catalytic square mesh reactor are adjusted to the inlet conditions of the model of the stagnation point reactor. According to the conditions and the inlet geometry respectively presented in the Table 5 and in the Figure 35 for the square mesh reactor, considering that the inlet area for that domain is 300 mm^2, it is possible to determine the mass flux of 3.0 kg m^{-2} s^{-1}, which is reported in the Table 9. To carry out the simulation, the following definitions are considered at the boundaries of the computational domain:

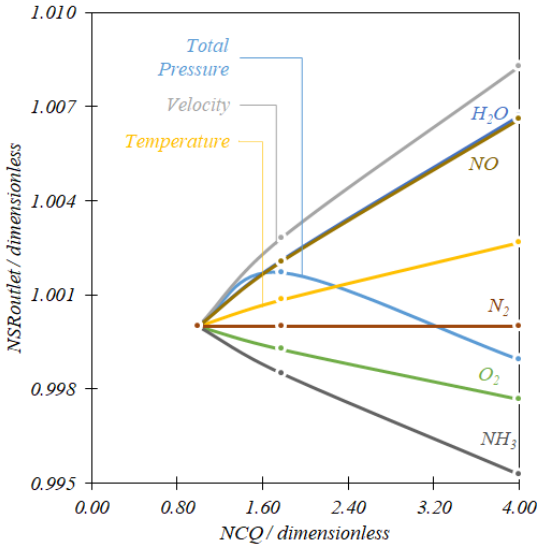

Figure 46. Results of the analysis of the spatial convergence of the mesh. NSR vs. NCQ for the stagnation point reactor.

- The inlet boundarie shown in the Figure 45, is mass flux inlet according to equation (72).
- The outlet boundaries shown in the Figure 45, are pressure outlets according to equation (79).
- The horizontal, upper, and lower boundaries, which do not correspond to the catalyst surface, and which were shown in the Figure 45, are defined as closed wall according with the equation (74).
- The axial axis is the symmetry axis of the reactor, by means of it the model is simplified.
- The boundary corresponding to the catalytic surface shown in the Figure 45, is defined as a closed wall according to equation (74), which is at temperature and composition conditions obtained in the simulation of the CatOx process in the first wire of the square mesh reactor, considering the same inlet conditions.
- The area of the catalytic surface for the simulation of the stagnation point reactor corresponds to a circumference whose diameter allows the same NH_3 conversion obtained in the first catalytic wire in the catalytic square mesh reactor case, around 40.0 %.

Figure 47 outlines and summarizes this methodology for the simulation of the stagnation point reactor.

Table 9. Inlet conditions for the simulation of the stagnation point reactor.

Mass flux	kg m^{-3} s^{-1}	3.0
Temperature	K	423
Pressure	bar	5.0
Composition		
NH_3	v%	10.0
Dry air	v%	90.0

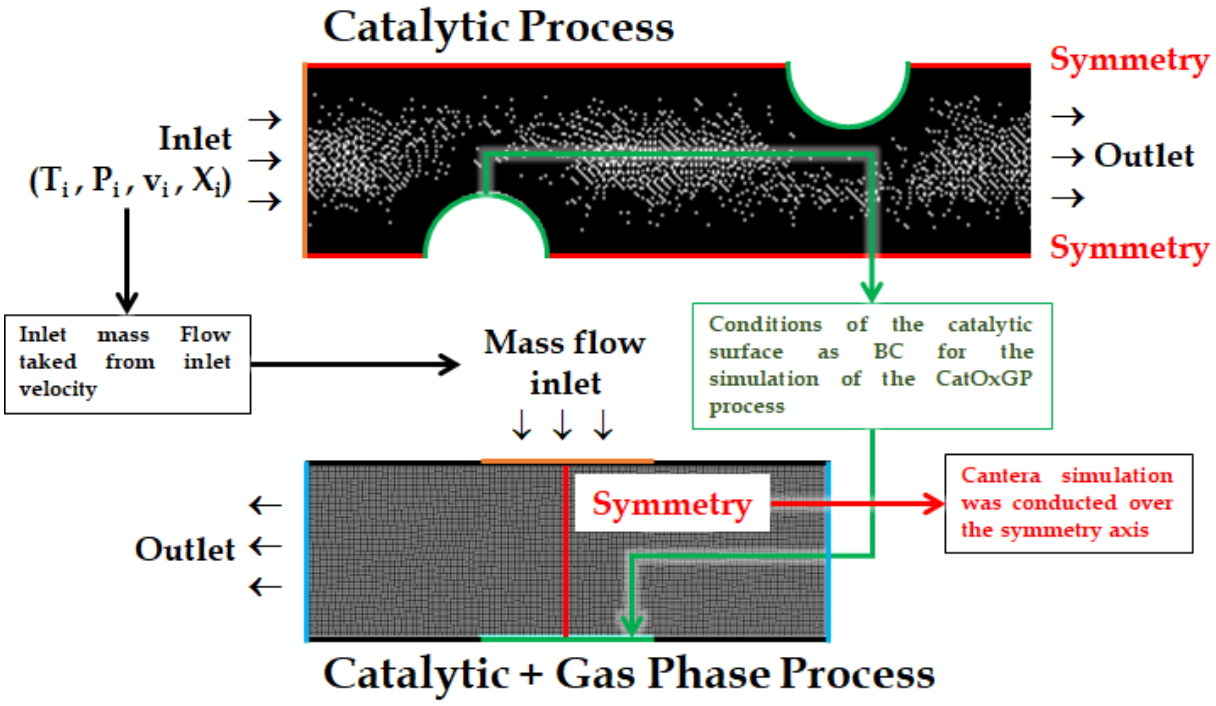

Figure 47. Methodology for the simulation of the stagnation point reactor.

7.4. Simulation results, discussion, and analysis

The Table 10 shows the results of the mass balance of nitrogen – based molecules and N – atoms associated with the simulation results, presented in this section. This information implies that the simulation accomplishes the mass balance of nitrogen as a principal atom in the process. Indeed, the imbalance of 0.127 kg m^{-3} s^{-1} corresponds only with the 0.128 % of the nitrogen aported by the NH_3 oxidation (–99.1 kg m^{-3} s^{-1}). The Table 11 shows the net reaction rate and the composition at outlet of the non nitrogen – based species. Based on the results form Tables 10 and 11, it is possible to determinate that the global mass unbalance is 4.33 kg m^{-3} s^{-1}, it is the 1.07 $\times 10^{-5}$ % of the net reaction rate of the reactives that entrance into the reactor (NH_3, O_2). The simulation results are valid and useful from the point of view of the mass balance. It is important to point that the net reaction rates presented in Tables 10 and 11 are global values, it means that considers the results of the simulaton on CatOxGP.

Table 12 shows the results of NH_3 conversion and selectivity of N_2O, NO and N_2. This table show the net reaction rate as well for these species. The NH_3 conversion was calculated according to equation (92). The NO, N_2O and N_2 selectivities were calculated according to equations (93), (95) and (97) respectively when $(i = 1 \rightarrow CS_{i-1} = CS_0)$. The net reaction rates were calculated according to equation (101) when $\sum_{i=1}^{CS} V^{CS_i} = V^{CS_1} = 2.39 \times 10^{-11} m^3$. The mencioned equations have been previously presented in Section 3.7.6.

The CatOxGP process induces the decrement in the NH_3 conversion, N_2O selectivity and NO selectivity. The decrease in the NO selectivity and the increase in the N_2 selectivity evidence the effect of the gas phase process, which induces the selective non – catalytic reduction of NO in the chemical system.

Figures 48 and 49 show the results of the simulation of the stagnation point reactor for both the ANSYS FLUENT [Flu 16 – 01] and the CANTERA [Goo 2017] models. These results refer to the nitrogenous species that participate simultaneously in the CatOx and CatOxGP processes. In the case of

the net reaction rate, the numerical scale of the variable corresponds exclusively to the process carried out in the gas phase, that is, it does not consider the net reaction rate due to catalytic reactions.

Table 10. Results of the mass balance of nitrogen – based molecules and N – atoms in the simulation of the CatOxGP process in the stagnation point reactor.
Inlet conditions: 3.0 kg m^{-2} s^{-1}, 423 K, 5.0 bar, 10.0 v% NH_3, 90.0 v% dry air.

Molecule	Net reaction rate		Molecule composition	
	of molecule	of constituent N – atom	at inlet	at outlet
	kg m^{-3} s^{-1}		v%	
H_2NO	1.94×10^{-8}	8.47×10^{-9}	0.0	2.67×10^{-10}
HNO	2.28×10^{-5}	1.03×10^{-5}	0.0	3.24×10^{-7}
HONO	1.77×10^{-4}	5.27×10^{-5}	0.0	1.66×10^{-6}
N_2	3.07×10^{-1}	3.07×10^{-1}	71.1	70.6
N_2O	1.70	1.08	0.0	1.71×10^{-2}
NH_3	−120	−99.1	10.0	6.80
NO	210	97.8	0.0	3.08
NO_2	3.26×10^{-2}	9.92×10^{-3}	0.0	3.12×10^{-4}
NH_2	3.18×10^{-9}	2.78×10^{-9}	0.0	8.76×10^{-11}
NNH	3.55×10^{-4}	3.42×10^{-4}	0.0	5.39×10^{-6}
Unbalance of nitrogen, kg m^{-3} s^{-1}:		0.127		

Table 11. Results of net reaction rate and outlet composition for non nitrogen – based molecules in the simulation of the CatOxGP process for the stagnation point reactor.
Inlet conditions: 3.0 kg m^{-2} s^{-1}, 423 K, 5.0 bar, 10.0 v% NH_3, 90.0 v% dry air.

Simulation result		H	H_2	H_2O	HO_2	O	O_2	OH
Net reaction rate	kg m^{-3} s^{-1}	7.30×10^{-11}	3.93×10^{-8}	191	1.48×10^{-9}	7.54×10^{-9}	−282	3.56×10^{-8}
Composition at outlet	v%	3.20×10^{-11}	8.61×10^{-9}	4.69	1.97×10^{-11}	2.08×10^{-10}	14.8	5.23×10^{-10}

Table 12. Simulation results of the stagnation point reactor.
Inlet conditions: 3.0 kg m^{-2} s^{-1}, 423 K, 5.0 bar, 10.0 v% NH_3, 90.0 v% dry air.

Species	Performance parameter		Change due to CatOxGP	Net reaction rate		Change due to CatOxGP
	CatOx	CatOxGP		CatOx	CatOxGP	
	%		%	kg m^{-3} s^{-1}		%
NH_3 (*)	31.51	31.46	–0.047	120.7	120.5	–0.166
N_2O (**)	1.35	1.09	–0.259	2.11	1.70	–24.1
NO (**)	98.7	98.6	–0.069	209.76	209.56	–0.0954
N_2 (**)	7.35×10^{-4}	0.189	+0.1898	2.38×10^{-3}	3.07×10^{-1}	

Performance parameter: (*) Conversion, (**) Selectivity

The contour in Figure 48 (a) shows, that despite a certain level of NH_3 consumption in the gas phase, especially near the catalytic surface, where there is also NO, the difference between the composition countours is imperceptible. The contour of net reaction rate of NH_3 shows the clear tendency to consumption of the substance in the gas phase. The mechanisms for the NH_3 consumption in the gas phase correspond to its direct oxidation or its oxidation in the presence of NO.

The net reaction rate of N_2O and NO shown in the profiles of the Figures 48 (d) and 49 (a) increase especially close to the catalytic surface due to the reactive process in the gas phase, rising to the N_2O and NO consumption and to reducing their global generation rate in the reactor. The contour of the net reaction rate of N_2O shows both consumption and generation zones. The genertion zones are wider than the consumption zones and this characteristic is reflected in the global reaction rate, which tends to the N_2O generation, as is shown in the Table 12. The contour of the net reaction rate of NO shows the clear tendency to consumption of the substance in the gas phase. The mechanisms for the NO consumption in the gas phase correspond to its direct oxidation or reduction in the presence of NH_3.

The contour in Figure 49 (d) shows that this increase in the global reaction rate is due to the N_2 generation, especially near to the catalytic surface, where the selective non – catalytic reduction of NO to N_2 by NH_3 takes place. In effect, the net reaction rate of N_2, increases especially close to the catalytic surface due to the reactive process in the gas phase, rising to the N_2 generation and its global generation rate in the reactor. The contour of net reaction rate of N_2 shows the clear tendency to the generation of the substance in the gas phase.

In Figures 48 and 49 [(b), (c), (e), (f)], the results of simulations from ANSYS FLUENT [Flu 16 – 01] and CANTERA [Goo 2017] in the symmetry axis of the reactor, show that when the CatOx and CatOxGP processes are compared, there is no appreciable difference in the behaviour of the principal nitrogen species (NH_3, N_2O, N_2 and NO). The results obtained with the one – dimensional model of CANTERA [Goo 2017], adjust satisfactorily to the results obtained with the ANSYS FLUENT [Flu 16 – 01] model. It is wortly to note that the composition of the species presented in those figures has mass fraction as unit instead of molar composition (v%) presented in the contours.

The largest calculated difference in composition occurs for the case of N_2O where the difference rises to 12.1 % near to the catalytic surface and where it is confirmed that the N_2O composition decreases due to the process in the gas phase as Figure 48 (e) shows. This decrease in N_2O composition coincides with the increase in its consumption, as shown in Figure 48 (f).

With respect to NH_3 and NO, the profiles in the symmetry axis of the reactor, allow observing that the selective non – catalytic reduction of NO is carried out by means of NH_3 within the fluid, just before the catalytic surface [Figures 48 (c) and 49 (c)]. This process is confirmed both with the N_2 generation that occurs in the same region of the reactor, as shown in Figure 49 (f), and with the appearance of the radicals, which participate in the CatOxGP process and begin to increase their composition in this same region, according to the contours shown in Appendix 9. The N_2 concentration profil shown in Figure 49 (e) has a minimum just in the area in which the largest generation of radicals in gas phase takes part.

By comparison of the two models, CANTERA [Goo 2017] and ANSYS FLUENT [Flu 16 – 01], a difference in the behaviour of the profiles of the net rate of generation for NH_3, NO and N_2 is observed [Figure 48 (c), Figure 49 (c) and (f)]. This difference is due fundamentally to the transport phenomena of momentum, mass and energy that take place in the radial direction and that are not considered by this CANTERA [Goo 2017] model.

Figure 50 presents the contours of temperature and beta ratio for this reactor. This shows the region in which the NO formed react in the gas phase, it is the zone of NH_3 – lean mixture [Mac 1967]. There is an extreme coincidence in the results of the process temperature, Figure 50 (b) presents this result. However, the temperature in the case of the CatOxGP process simulation is slightly lower than

that obtained in the CatOx process simulation. This decrease in temperature is consistent with the endothermic character of NO_X reduction. The contour of beta ratio presented in Figure 50 (c) allows to identify the zone in which the gas phase reactions are expected to occur. This region corresponds to the zone in which the increase in the net reaction rate of NH_3, N_2O, NO and N_2 occurs, which was presented between Figures 48 and 49.

For the information presented in the Apprendix 9, in the case of the net reaction rate, the numerical scale of the variable corresponds exclusively to the process carried out in the gas phase, that is, it does not consider the net reaction rate due to catalytic reactions.

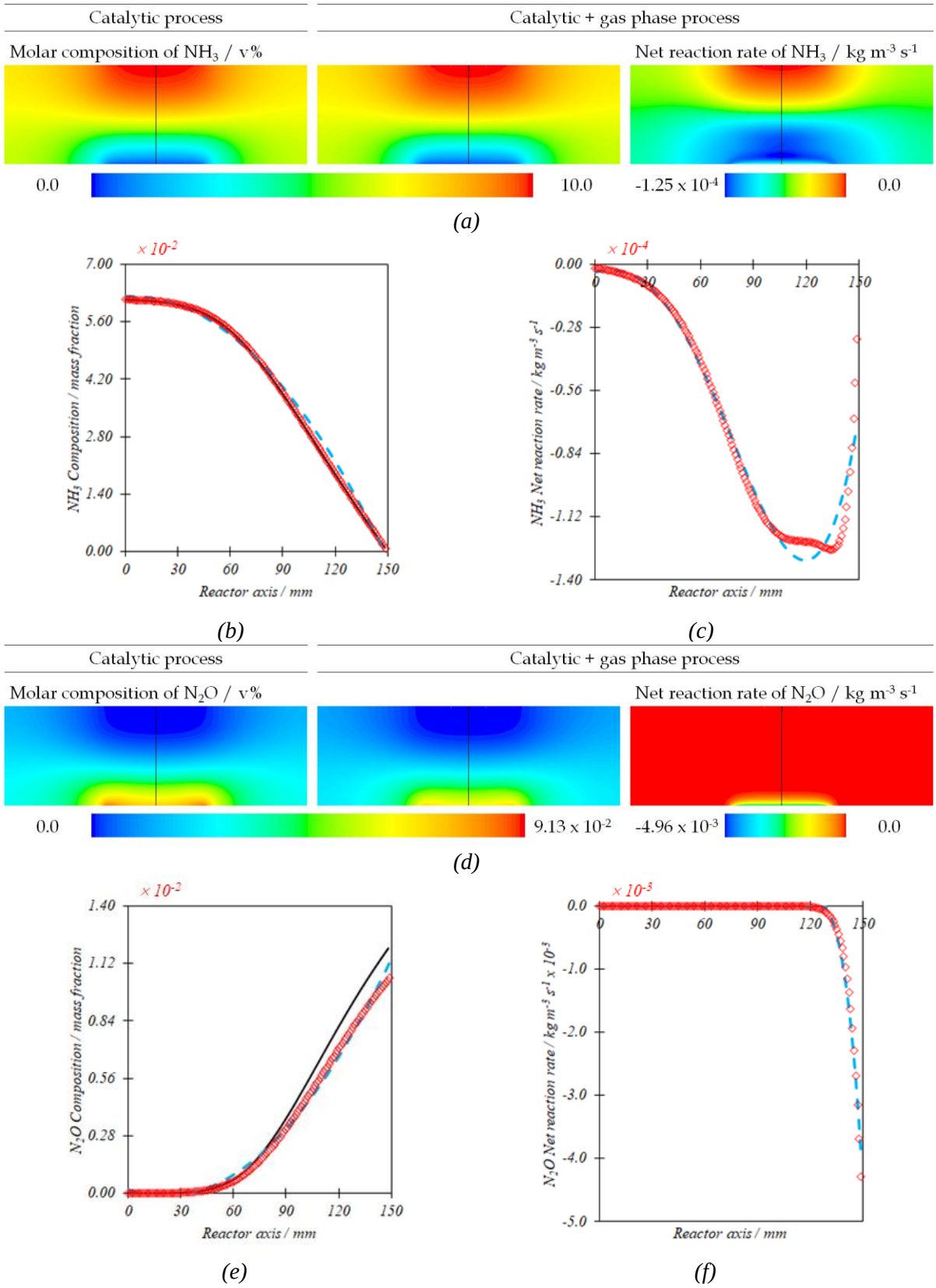

Figure 48. Results of the simulation of the CatOx and CatOxGP processes in a stagnation point reactor. Contours of the composition and net reaction rate of NH_3 and N_2O.
Inlet conditions: 3.0 kg m^{-2} s^{-1}, 423 K, 5.0 bar, 10.0 v% NH_3, 90.0 v% dry air.

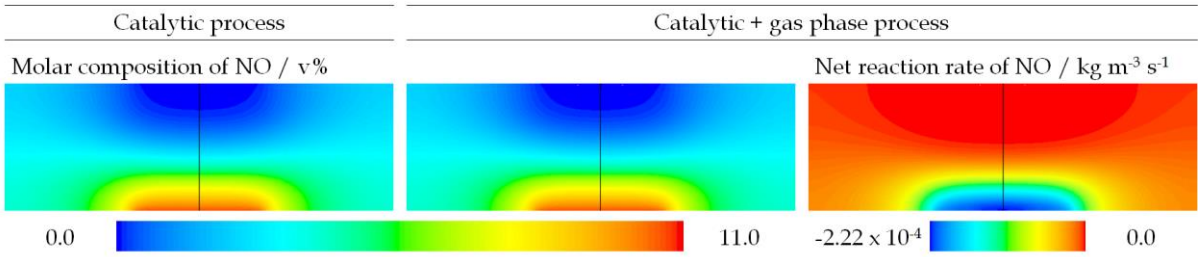

(a)

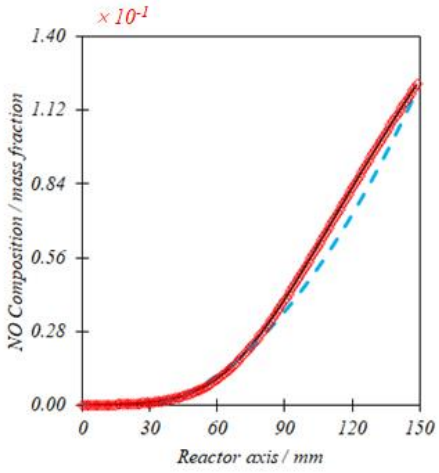

(b)

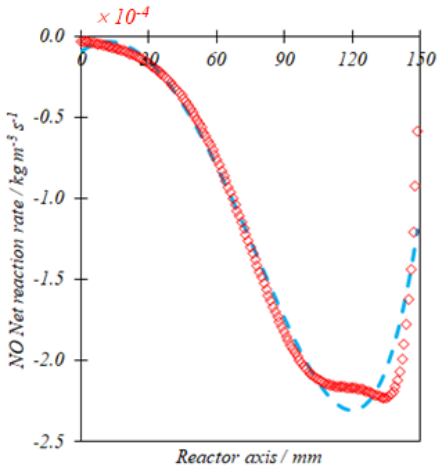

(c)

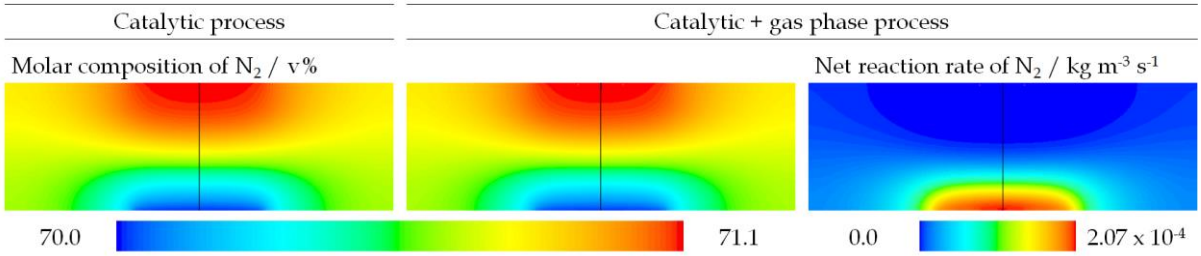

(d)

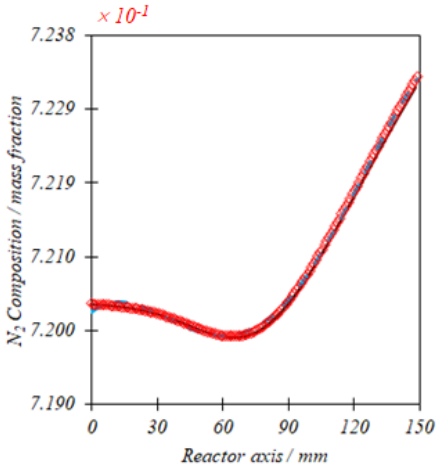

(e)

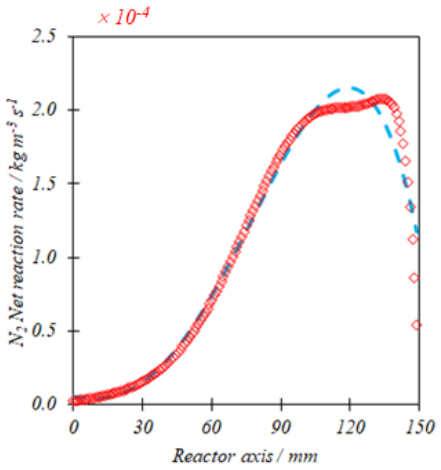

(f)

Meaning of lines according to the nomenclature of Figure 45.

Figure 49. Results of the simulation of the CatOx and CatOxGP processes in a stagnation point reactor. Contours of the composition and net reaction rate of NO and N_2.
Inlet conditions: 3.0 kg m^{-2} s^{-1}, 423 K, 5.0 bar, 10.0 v% NH_3, 90.0 v% dry air.

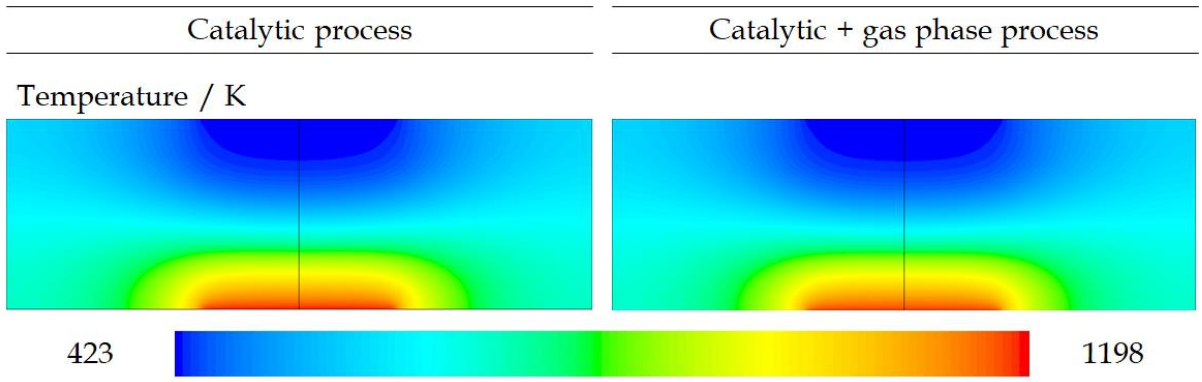

(a)

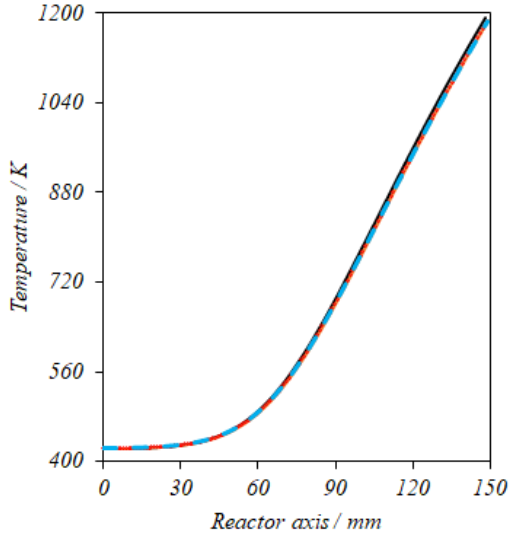

(b)

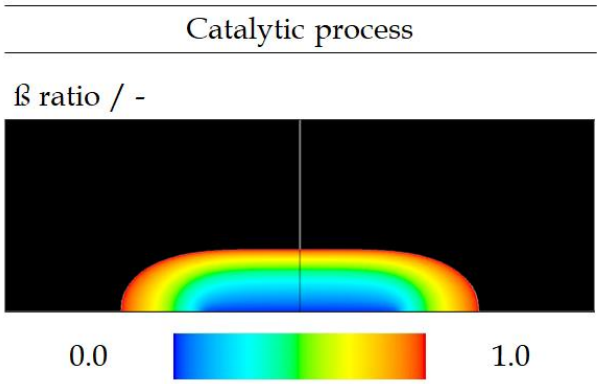

(c)

Meaning of lines according to the nomenclature of Figure 45.

Figure 50. Results of the simulation of the CatOx and CatOxGP processes in a stagnation point reactor. Contours of the temperature and ß ratio.
Inlet conditions: 3.0 kg m^{-2} s^{-1}, 423 K, 5.0 bar, 10.0 v% NH_3, 90.0 v% dry air.

8. Simulation of the planar channel flow reactor

This chapter presents the methodology, results, and discussion about the simulation of the planar channel flow reactor. Due to the ease of geometry, which is made up of quadrilateral elements, it is useful to simplify the simulation process and at the same time obtain results that allow to stablish the influence of the CatOxGP process. In this regard, this chapter presents the results of both the CatOx and the CatOxGP processes in the following simulation cases:

- Simulation on a surface equivalent to the first catalytic wire of the square mesh reactor, whose simulation results were presented in the Section 6.4.2.
- Simulation of the reactor with six catalytic surfaces equivalent to those of a square mesh reactor.

These models significantly reduce the numerical difficulty to simulate the CatOxGP process with respect to the model of the square mesh reactor. For the simulation of the CatOxGP process the reduced mechanism (Appendix 3) was used.

8.1. Geometry and mesh

With the aim of simulate of the catalytic oxidation of NH_3 in the planar channel reactor, the geometry consists in 0.10 mm inlet and outlet lengths, and a catalytic surface, located parallel to the inlet flow, with 0.15 mm length. The cross section of the inlet to the reactor consists of a rectangle with 1.0 m wide and 0.163 mm high.

ANSYS MESHING [Flu 16 – 02] was used for the generation of the domain of the numerical simulation. Figure 51 shows a detail of the geometry and the mesh. This mesh has 17152 quadrilateral cells. Since it is considered that during the process, the temperature of the catalytic surface is uniform and stable, its internal mesh has not been considered for simulation purposes. This mesh has MAR = 1.45, MOQ = 1.0 and MOS = 3.18×10^{-12}. Therefore, it can be used for simulation proposes.

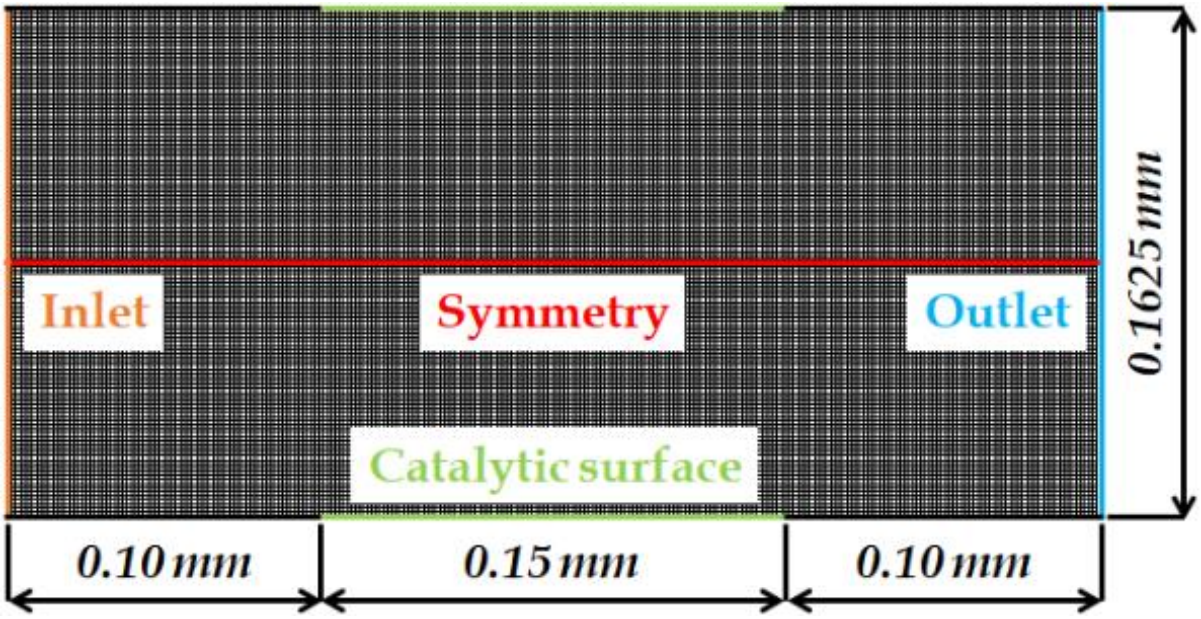

Figure 51. Geometry and meshing of planar channel reactor.

8.2. Spatial convergence of the mesh

According to the methodology presented by Slater [Sla 2012], two refinements were applied on the planar channel reactor presented on Figure 51 (17152 cells) obtaining meshes of 34476 and 69296 cells respectively (which implies a refining ratio of 2.01). With these calculation domains, the simulation of the CatOx process was applied and with the operating conditions:

- The inlet velocity of 1.20 m s^{-1}.
- The inlet temperature of 423 K.
- The pressure of 5.0 bar.
- The volumetric composition of 10.0 v% NH_3 and 90.0 v% dry air.

Figure 52 presents the results of the analysis of spatial convergence for the planar channel reactor. It is observed that the results do not differ significantly for each computational domain. In the worst case, the outlet H_2O composition, calculated with the least refined mesh (8664 cells) is 0.475 % lower than that obtained in the simulation with the most refined mesh (35003 cells). It indicates that the meshing presented in Figure 51 (17152 cells) is useful for the simulation proposes.

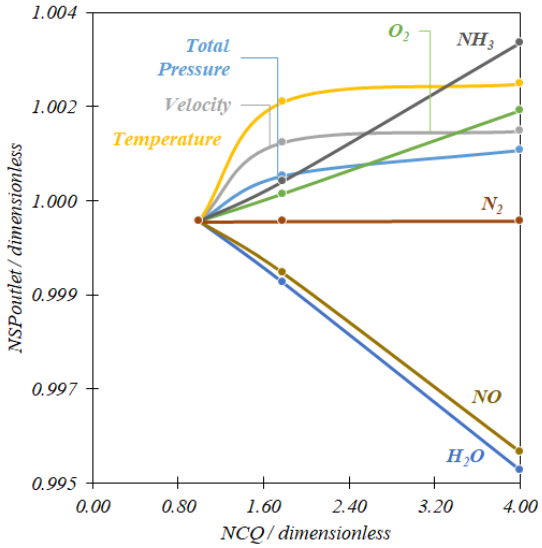

Figure 52. Results of the analysis of the spatial convergence of the mesh. NSR vs. NCQ for the planar channel reactor.

8.3. Boundary conditions and configuration of the simulation

To carry out the simulation of the cases associated with the planar channel flow reactor, the conditions described in this section were used. For the CatOx and CatOxGP process over the first and second catalytic surfaces, Table 13 shows the inlet conditions used for the ANSYS FLUENT [Flu 16 – 01] simulation until the second catalytic surface of the planar channel flow reactor. Note that in the simulation of the reactor with two catalytic surfaces a higher pressure was used (15.0 bar). For the CatOx and CatOxGP process with six catalytic surfaces, Table 14 shows the inlet conditions used for the ANSYS FLUENT [Flu 16 – 01] simulation.

The inlet conditions used for the simulation of the catalytic square mesh reactor are adjusted to the inlet conditions of the simulation of the planar channel flow reactor. It was intended that the average Reynolds number for both configurations be the same. Since the flow lines of both cases are different,

the Reynolds number was equalized by means of the change in the height of the entrance surface to the planar channel flow reactor. The length of the reactor in case of the planar channel has been modified in such a way that the residence time is the same as the obtained in the case of the catalytic square mesh reactor.

In any case, to carry out the simulation, the following definitions are considered at the boundaries of the computational domain:

- The inlet boundarie shown in the Figure 51, is a velocity inlet according to equation (73).
- The outlet boundaries shown in the Figure 51, is a pressure outlet according to equation (79).
- The horizontal lower boundaries, which do not correspond to the catalyst surface, and which were shown in Figure 51, are defined as closed wall according with the equation (74).
- The horizontal upper boundaries shown in the Figure 51, are symmetry boundaries according with equations between (80) and (83).

Table 13. Inlet conditions for the simulation of the first catalytic surface of the planar channel flow reactor.

Velocity	m s^{-1}	1.20
Temperature	K	423
Pressure	bar	5.0
Composition		
NH_3	v%	11.0
Dry air	v%	89.0

Table 14. Inlet conditions for the simulation of the first and second catalytic surfaces of the planar channel flow reactor.

Inlet condition		**Simulation case** (a)	(b)	(c)	(d)
Composition					
NH_3	v%	10.0			
Dry air	v%	90.0			
Velocity	m s^{-1}	1.20			
Temperature	K	423	500	423	530
Pressure	bar	5.0	5.0	15.0	15.0

For the simulation of the CatOx process, the boundaries corresponding to the catalytic surface, as was shown in the Figure 51, is defined as closed wall according with the equation (74), in which the reactions of the catalytic mechanism, presented in the Section 3.4, take place.

In the case of the simulation of the CatOxGP process in the first catalytic wire, the boundary corresponding to the catalytic surface is defined as a closed wall according to the equation (74) , which

is at temperature and composition conditions obtained in the simulation of the CatOx process considering the same inlet conditions.

The area of the catalytic surface for the simulation of the planar channel reactor is such allows the same NH_3 conversion obtained in the first catalytic wire in the catalytic square mesh reactor case, around 40.0 %.

8.4. Simulation results, discussion, and analysis

This section is focused on the presentation, discussion and analysis of the results associated with the simulations of the CatOx and CatOxGP processes carried out in the the planar channel flow reactor.

8.4.1. Simulation in the first catalytic surface

This section presents the results of the CatOxGP process on the first catalytic surface. For the simulation of the CatOxGP process the reduced mechanism (Appendix 3) was used.

The Table 15 shows the results of the mass balance of nitrogen – based molecules and N – atoms associated with the simulation results, which are shown in Figure 53. This information implies that the simulation accomplishes the mass balance of nitrogen as a principal atom in the process. Indeed, the imbalance of –3.36 kg m^{-3} s^{-1} corresponds only with the 0.971 % of the nitrogen aported by the NH_3 oxidation (–366 kg m^{-3} s^{-1}). The Table 16 shows the net reaction rate and the composition at outlet of the non nitrogen – based species.

Table 15. Results of the mass balance of nitrogen – based molecules and N – atoms in the simulation of the CatOxGP process in the planar channel flow reactor, first catalytic surface. Inlet conditions: 1.20 m s^{-1}, 423 K, 5.0 bar, 11.0 v% NH_3, 89.0 v% dry air.

Molecule	Net reaction rate		Molecule composition	
	of molecule	of constituent N – atom	at inlet	at outlet
	kg m^{-3} s^{-1}		v%	
H_2NO	4.18	**1.83**	0.0	2.62×10^{-2}
HNO	12.2	**5.50**	0.0	7.89×10^{-2}
HONO	73.5	**21.9**	0.0	3.14×10^{-1}
N_2	18.8	18.8	70.4	69.7×10^{-4}
N_2O	20.6	13.1	0.0	4.50×10^{-2}
NH_3	−445	−366	**11.0**	5.63
NO	595	278	0.0	3.98
NO_2	77.5	23.60	0.0	3.38×10^{-1}
NH_2	1.28×10^{-4}	1.12×10^{-4}	0.0	1.60×10^{-6}
NNH	1.76×10^{-1}	1.70×10^{-1}	0.0	1.22×10^{-3}
Unbalance of nitrogen, kg m^{-3} s^{-1}:		−3.36		

Table 16. Results of net reaction rate and outlet composition for non nitrogen – based molecules in the simulation of the CatOxGP process for the planar channel flow reactor, first catalytic surface.
Inlet conditions: 1.20 m s^{-1}, 423 K, 5.0 bar, 11.0 v% NH_3, 89.0 v% dry air.

Simulation result		H	H_2	H_2O	HO_2	O	O_2	OH
Net reaction rate	kg m^{-3} s^{-1}	8.05 $\times10^{-8}$	2.11 $\times10^{-4}$	670	1.11 $\times10^{-6}$	1.85 $\times10^{-8}$	−971	3.15 $\times10^{-5}$
Composition at outlet	v%	1.60 $\times10^{-8}$	2.10 $\times10^{-5}$	7.46	6.78 $\times10^{-9}$	2.32 $\times10^{-10}$	12.4	2.11 $\times10^{-7}$

Based on the results form Tables 15 and 16, it is possible to determinate that the global mass unbalance is 55.6 kg m^{-3} s^{-1}, it is the 3.93 % of the net reaction rate of the reactives that entrance into the reactor (NH_3, O_2). The simulation results are valid and useful from the point of view of the mass balance. It is notable that for the first wire the composition of the radical species corresponds to the formation of nitrogen based intermidiates. Those are highlighted in the Table 15. It is important to point that the net reaction rates presented in Tables 15 and 16 are global values, it means that considers the results of the simulaton on CatOxGP.

Table 17 shows the results of NH_3 conversion and selectivity of N_2O, NO and N_2. This table show the net reaction rate as well for these species. The NH_3 conversion was calculated according to equation (92). The NO, N_2O and N_2 selectivities were calculated according to equations (93), (95) and (97) respectively when $(i = 1 \rightarrow CS_{i-1} = CS_0)$. The net reaction rates were calculated according to equation (101) when $\sum_{i=1}^{CS} V^{CS_i} = V^{CS_1} = 2.84 \times 10^{-8} m^3$. The mencioned equations have been previously presented in Section 3.7.6.

Table 17. Simulation results of the first catalytic surface in the planar channel reactor.
Inlet conditions: 1.20 m s^{-1}, 423 K, 5.0 bar, 11.0 v% NH_3, 89.0 v% dry air.

Species	Performance Parameter		Change due to CatOxGP	Net reaction rate		Change due to CatOxGP
	CatOx	CatOxGP	%	CatOx	CatOxGP	%
	%			kg m^{-3} s^{-1}		
NH_3 (*)	38.0	48.2	+10.2	351	445	+21.2
N_2O (**)	1.79	1.88	+0.10	17.1	20.6	+17.0
NO (**)	96.2	89.6	–6.61	703	595	–15.4
N_2 (**)	0.0136	2.58	+2.57	7.88 $\times10^{-2}$	18.8	

(*) Performance parameter: (*) Conversion, (**) Selectivity

Figure 53 shows the contours of the composition and net reaction rate for NH_3, NO_2, NO and N_2, and the contour of the temperature when the CatOx and the CatOxGP processes are simulated at the first catalytic surface (equivalent to the first catalytic wire in the square mesch reactor) under: inlet velocity of 1.20 m s^{-1}, inlet temperature of 423 K, pressure of 5.0 bar and inlet NH_3 composition of 11.0 v%. In the case of the net reaction rate, the numerical scale of the variable corresponds exclusively to the process carried out in the gas phase, that is, it does not consider the net reaction rate due to catalytic reactions.

The temperature contours shown in Figure 53 (e) do not present substantial differences between the CatOx and CatOxGP processes, this is because the fundamental thermal effect of the process comes from its catalytic component.

The CatOxGP process induces the increment in the NH_3 conversion, N_2O selectivity and N_2 selectivity. The increase in the selectivities of these two species implies a decrease in the NO selectivity. This behaviour evidences the effect of the gas phase process, which induces the selective non – catalytic reduction of NO in the chemical system.

As Figure 53 shows, in the contours associated with the net generation rates of the substances, the gas phase process takes a significant place after the fluid crosses half of the catalytic surface. In this zone, the simultaneous presence of NH_3 and NO favors the selective non – catalytic reduction of NO. This effect is reflected, as previously indicated, by the increase in the NH_3 conversion, NO_2 and N_2 formation, and by the decrease in the global NO formation.

The reaction rate contour in Figure 53 (a) shows the NH_3 consumption rate in the gas phase. The contour of net reaction rate of NH_3 shows the clear tendency to consumption of the substance in the gas phase. The mechanisms for the NH_3 consumption in the gas phase correspond to its direct oxidation or its oxidation in the presence of NO. The amplitude of the profile of the net reaction rate of NH_3 is consistent with the radical formation zone.

Regarding N_2O, the contour in Figure 53 (b) net raction rate of the N_2O. In the same area where NO formation occurs, the largest reaction rate in the gas phase takes place, in this region the highest reactor temperature is also observed. The contour of the net reaction rate of N_2O shows both consumption and generation zones. The genertion zones are wider than the consumption zones and this characteristic is reflected in the global reaction rate, which tends to the N_2O generation, as is shown in the Tables 15 and 17.

Regarding NO, the contour in Figure 53 (c) shows that this decrease in the global reaction rate is due to the NO consumption, especially near to the catalytic surface, where the process in the gas phase takes place. The contour of the net reaction rate of NO shows the clear tendency to consumption of the substance in the gas phase. The mechanisms for the NO consumption in the gas phase correspond to its direct oxidation or reduction in the presence of NH_3.

Regarding N_2, the contour in Figure 53 (d) shows that this increase in the global reaction rate is due to the N_2 generation due to the selective non – catalytic reduction of NO to N_2 due to NH_3 take place. The contour of net reaction rate of N_2 shows the clear tendency to the generation of the substance in the gas phase as a product of the direct oxidation of NH_3 or NO, or as a product of the NO reduction in the presence of NH_3.

Figure 53 (f) shows the contours of the beta ratio, according to which, in the area in which this parameter takes values between 0.0 and 1.0, it is presented the highest net reaction rate of the substances associated with the selective non – catalytic reduction of NO.

Appendix 10 shows the contours of the concentration and net reaction rate associated with the radicals that participate in the CatOxGP process. In the case of the net reaction rate, the numerical scale of the variable corresponds exclusively to the process carried out in the gas phase, that is, it does not consider the net reaction rate due to catalytic reactions. It is observed that the radical formation takes place after the fluid has pased half of the catalytic surface. This behaviour is consistent with the fact that concentrations of NO, NH_3, H_2O and O_2 are enough in this region to promote the gas phase reactions.

Although the formation of the radicals takes place near the surface, a region in which the highest temperature of the fluid also occurs, substances such as H_2, H_2NO or NO_2 remain and diffuse in a wide region of the fluid, and other species such as O – atom, OH or NH_2 are close to the catalytic surface. This shows the behaviour of the half – lifetime of the substances.

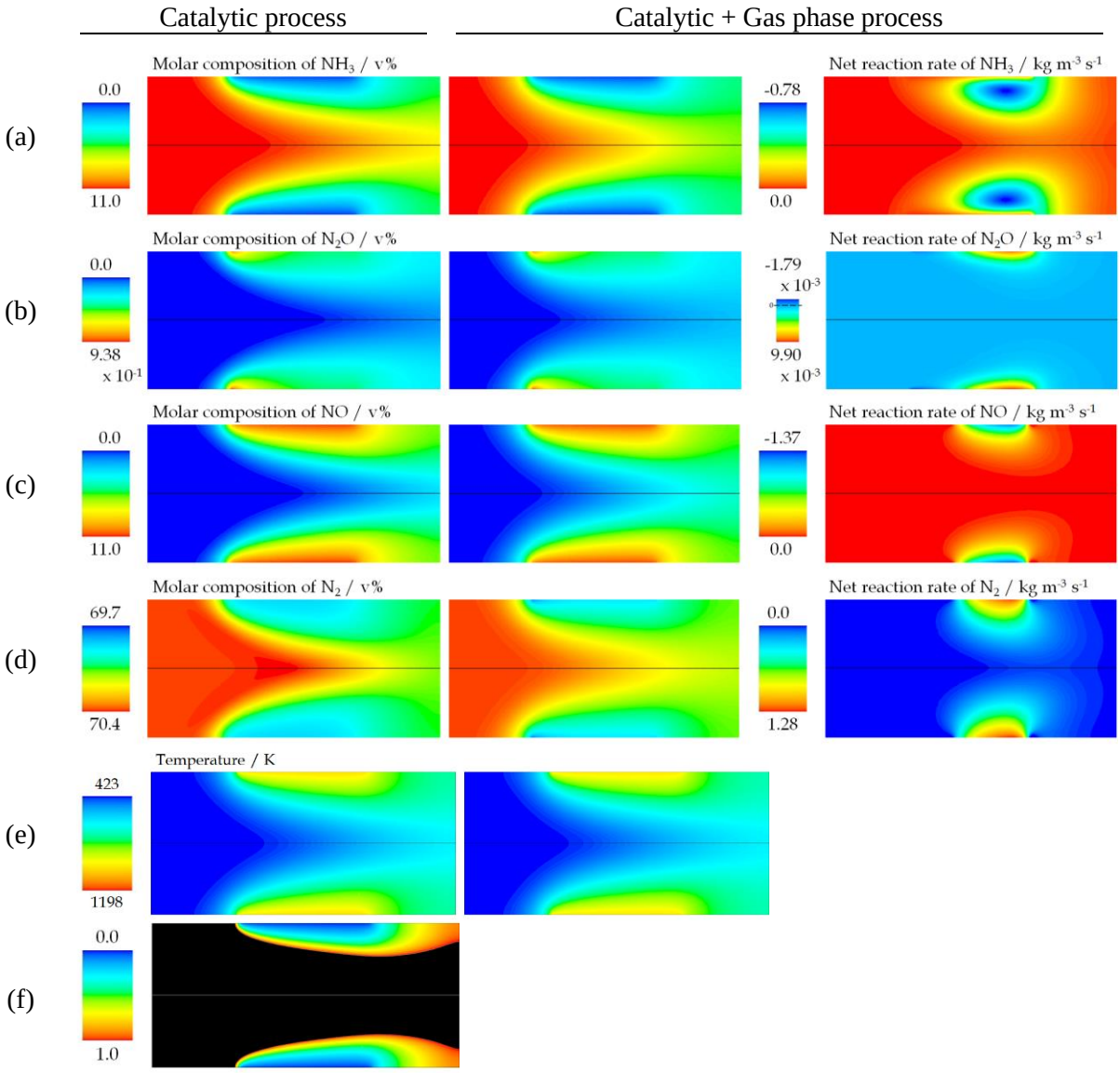

Figure 53. Results of the simulation of the CatOx and CatOxGP processes in a planar channel reactor. Contours of the composition and net reaction rate of NH_3, NO_2, NO and N_2. Contour of the temperature. Contour of beta ratio.
Inlet conditions: 1.20 m s^{-1}, 423 K, 5.0 bar, 11.0 v% NH_3, 89.0 v% dry air.

8.4.2. Simulation of the reactor with six catalytic surfaces

After having carried out the simulation on the first catalytic surface for the three reactor configurations, it is observed that from the point of view of understanding the process, the simulation of the case of the planar channel reactor reactor provides information like that of the single wire reactor and therefore, the simplest geometry will allow to obtain results on the other catalytic surfaces.

This section presents the results of the CatOxGP process on the planar channel reactor with six catalytic surfaces and compares them with the results of the CatOx process in the same reactor. For the simulation of the CatOxGP process the reduced mechanism (Appendix 3) was used.

Figure 54 shows the results of net reaction rate for every species along the reactor and for all conditions of pressure and temperature. From this information it is possible to determinate that the maximum imbalance of nitrogen occurs in the third catalytic surface at 15.0 bar and 530 K, in this point the imbalance is –31.1 kg m^{-3} s^{-1} this value corresponds with the 10.1 % of the nitrogen apported by the

NH_3 oxidation (–307 kg m^{-3} s^{-1}). These values implie that the simulation accomplishes the mass balance of nitrogen as a principal atom in the process.

The same analysis can be done with the imbalance of all species in the process. In that case, the maximum mass imbalance is in the fifth catalytic surface at 15.0 bar and 423 K, in this point the imbalance is – 65.6 kg m^{-3} s^{-1} this value corresponds with the 13.3 % of the net reaction rate of the reactives that entrance into that catalytic surface (NH_3, O_2).

Figure 55 shows the results of the composition for every species along the reactor and for all conditions of pressure and temperature. As expected, the composition of the radicals decays to zero or practically zero at the end of the reactor. In fact, as shown in Table 15, the maximum radical composition at the outlet of the first catalytic surface is 3.14×10^{-1} v% HONO. In the case of the reactor with six catalytic surfaces, this value decreases until the order of magnitude of 10^{-4}.

The figures that show the contours of composition and the net reaction rate of the species presented in this section are as follows:

- Figure 56. Contours of NH_3.
- Figure 58. Contours of NO.
- Figure 60. Contours of N_2.
- Figure 62. Contours of N_2O.

It should be noted that in these contours, the scales referring to the net reaction rates correspond exclusively to the process that takes place in the gas phase.

8.4.2.1. NH_3 contours

After the third catalytic surface, in all simulation cases, the NH_3 has been almost completely consumed. This behaviour occurs for the CatOx and the CatOxGP processes. However, in the CatOxGP process, the NH_3 composition throughout the reactor is less than that determined in the CatOx process. With respect to the contour of NH_3 net reaction rate, this species reacts in the gas phase throughout the reactor, mainly near the first catalytic surface. However, for the following catalytic surfaces, the NH_3 consumption in the gas phase continues to exist.

The increment of the pressure up to 15.0 bar mantein the NH_3 composition even up to the fifth catalytic surface. With the isothermal increase in pressure, the effect of the process in the gas phase remains, it means that the NH_3 composition throughout the reactor in the CatOxGP process is less than the composition in the CatOx process. Under this pressure condition, the NH_3 net reaction rate contour shows that it is possible to extend the contour of the NH_3 consumption in the gas phase even to near the second catalytic surface.

The effect of the isobaric increase in temperature is more noticeable for high pressures. At 15.0 bar, the increment in temperature causes the NH_3 composition to decrease markedly throughout the reactor. The local maximum value of the net reaction rate of NH_3, which occurs at 530 K and 15.0 bar, indicates that the increment of pressure and temperature increases the net reaction rate of NH_3 in the gas phase. Despite this, this increase does not induce the total consumption of NH_3 in the reactor.

Figure 57 shows the results of the NH_3 conversion throughout the reactor for the simulations of the CatOx process and the CatOxGP process. Conditions of inlet temperature and pressure have been differentiated by means of the color code explained in the lower part of the figures. Figure 57 (a) presents the information referring to the NH_3 conversion calculated for each catalytic surface. Figure 57 (b) presents the information about accumulated value throughout the reactor.

The NH_3 conversion, the NO, N_2O and N_2 selectivities, and the net reaction rates were calculated according to equations presented in Section 3.7.6.

Regardless of the inlet pressure and temperature, the results of the simulations of the CatOxGP process show that it increases the NH_3 conversion throughout the reactor. From the point of view of local results, that is, considering the NH_3 conversion in each catalytic surface presented in Figure 57 (a), the results of the simulations of the CatOxGP processes increase between 2.13 % (15.0 bar, 423 K, first catalytic surface) and 5.04 % (5.0 bar, 500 K, third catalytic surface) with respect to the results for the CatOx processes. The increase in NH_3 conversion due to the gas phase process contributes not only to the generation of the species included in the chemical mechanism of the gas phase process, but particularly to the NO reduction in the gas phase.

According to Figure 57 (b), for simulation cases at 5.0 bar, the final NH_3 conversions are greater than 90.0 w%. At 500 K, in the simulation of the CatOx process, this value of the NH_3 conversion occurs at the third catalytic surface, for the simulation of the CatOxGP process, this conversion occurs before. On the third catalytic surface the value of the NH_3 conversion in the simulation of the CatOxGP process is 2.74 % higher than the results of the simulation of the CatOx process. At 423 K, in the simulation of the CatOx process, the NH_3 conversion becomes 90.0 w% in the fourth catalytic surface. For the simulation of the CatOxGP process, this conversion occurs once the gases exceed the third catalytic surface. On the fourth catalytic surface the value of the NH_3 conversion in the simulation of the CatOxGP processes is 1.53 % higher than the result of the simulation of the CatOx process. At 5.0 bar, the simulation results of the CatOxGP process at 423 K are like the simulation results of the CatOx process at 500 K. As for in cases of simulation at 5.0 bar and 500 K, the results of the CatOx and the CatOxGP processes become similar after the fifth catalytic surface.

At 15.0 bar, only the cases at 530 K achieves the NH_3 conversion greater than 80.0 w%. In the simulation of the CatOx process, this value occurs after the fifth catalytic surface. For the simulation of the CatOxGP process, this value occurs before. On the fifth catalytic surface the value of the NH_3 conversion in the simulation of the CatOxGP process is 4.27 % higher than the results of the simulation of the CatOx process. At 15.0 bar and 530 K, the maximum NH_3 conversion in the simulation of the CatOxGP process is 89.0 w%.

At 15.0 bar and 423 K, the maximum NH_3 conversion in the simulation of the CatOxGP process is 81.1 w%. This NH_3 conversion value is 4.28 % higher than that obtained in the simulation of the CatOx process. At any given point in the simulation domain, the increase in NH_3 conversion due to the isobaric increase in temperature results from the increase in the NH_3 consumption rate. The decrease in NH_3 conversion due to the isothermal increase in pressure is an effect of the decrease in the residence time of the gases in the reactor.

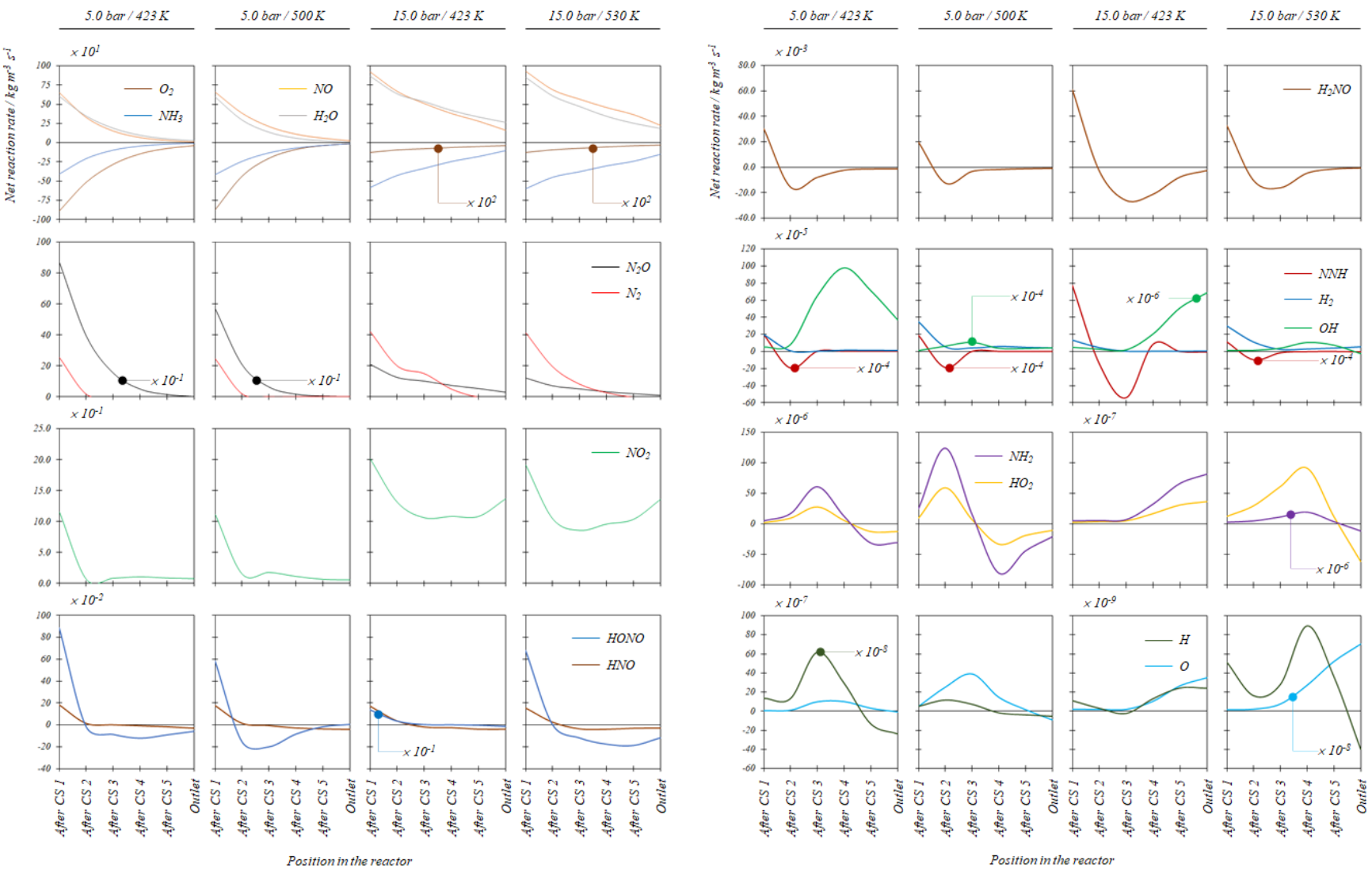

Figure 54. Results of the net reaction rate of the species in the simulation of the CatOxGP process in the planar channel flow reactor with six catalytic surfaces. Inlet conditions: 1.20 m s^{-1}, 10.0 v% NH_3, 90.0 v% dry air.

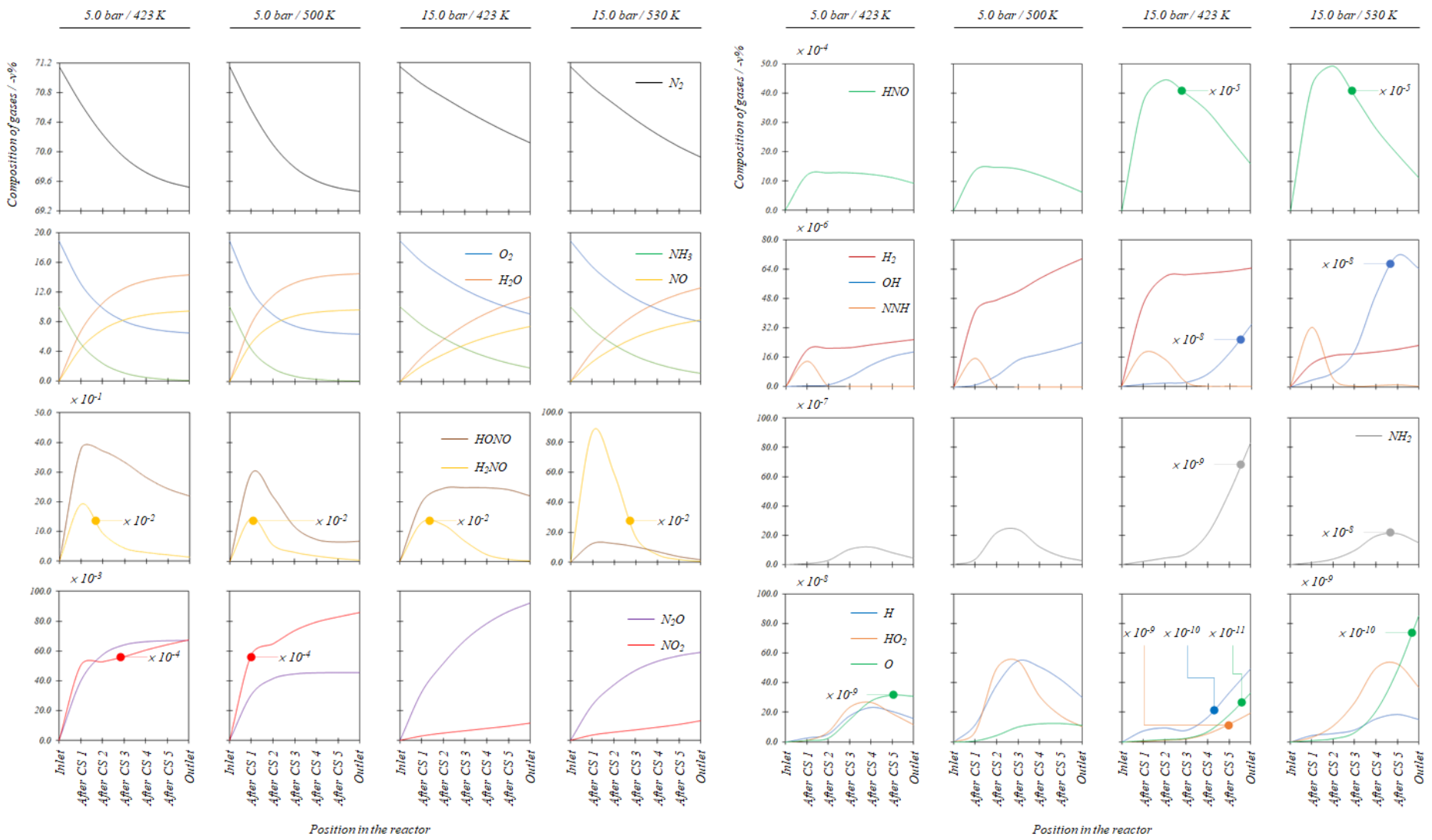

Figure 55. Results of the species composition in the simulation of the CatOxGP process in the planar channel flow reactor with six catalytic surfaces. Inlet conditions: 1.20 m s^{-1}, 10.0 v% NH_3, 90.0 v% dry air.

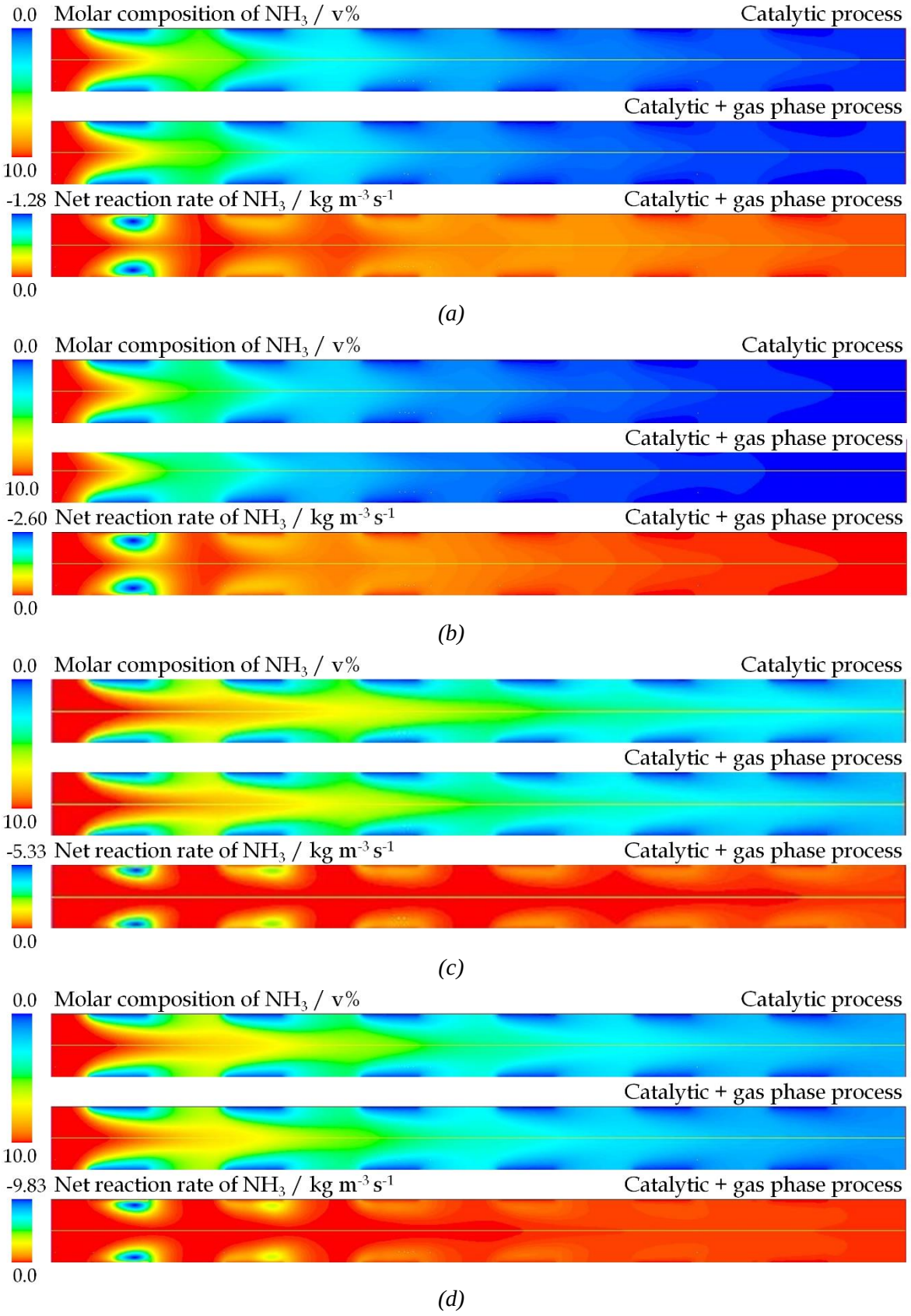

Figure 56. Results of the simulation of the CatOx and CatOxGP processes in a planar channel reactor with six catalytic surfaces. Contours of the composition and net reaction rate of NH_3. Inlet conditions: 1.20 m s^{-1}, 10.0 v% NH_3, 90.0 v% dry air.
(a) 423 K, 5.0 bar; (b) 500 K, 5.0 bar; (c) 423 K, 15.0 bar; (d) 530 K, 15.0 bar.

(a)

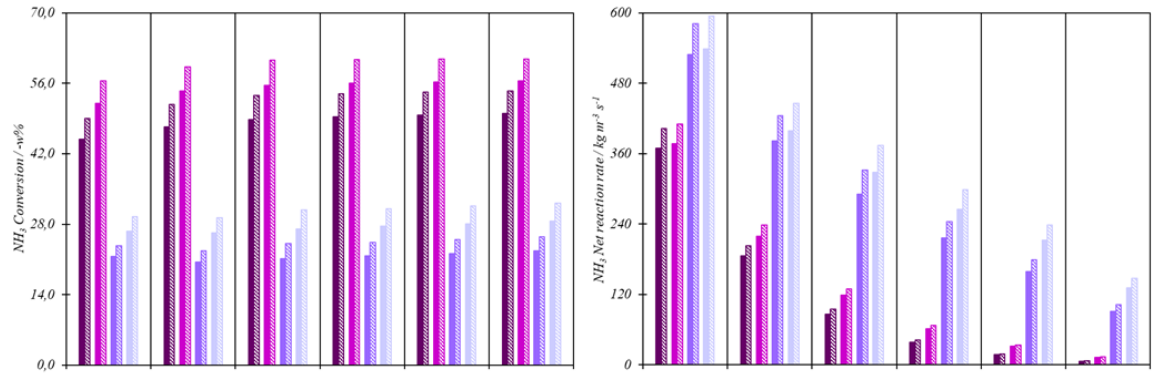

CatOx	CatOxGP	Pressure	Temperature	1st Cat. Surf.	2nd Cat. Surf.	3rd Cat. Surf.	4th Cat. Surf.	5th Cat. Surf.	6th Cat. Surf.
		bar	K	Difference due to gas phase process, %					
		5.0	423	+ 4.05	+ 4.44	+ 4.86	+ 4.52	+ 4.48	+ 4.38
		5.0	500	+ 4.56	+ 4.77	+ 5.04	+ 4.67	+ 4.54	+ 4.36
		15.0	423	+ 2.13	+ 2.29	+ 3.03	+ 2.71	+ 2.77	+ 2.83
		15.0	530	+ 2.79	+ 3.09	+ 3.79	+ 3.44	+ 3.50	+ 3.57

1st Cat. Surf.	2nd Cat. Surf.	3rd Cat. Surf.	4th Cat. Surf.	5th Cat. Surf.	6th Cat. Surf.
Difference due to gas phase process, %					
+ 9.0	+ 9.38	+ 9.98	+ 9.15	+ 9.01	+ 8.74
+ 8.78	+ 8.76	+ 9.06	+ 8.32	+ 8.07	+ 7.72
+ 9.82	+ 11.2	+14.3	+ 12.5	+ 12.5	+ 12.5
+ 10.5	+ 11.8	+ 14.0	+ 12.4	+ 12.4	+ 12.5

(b)

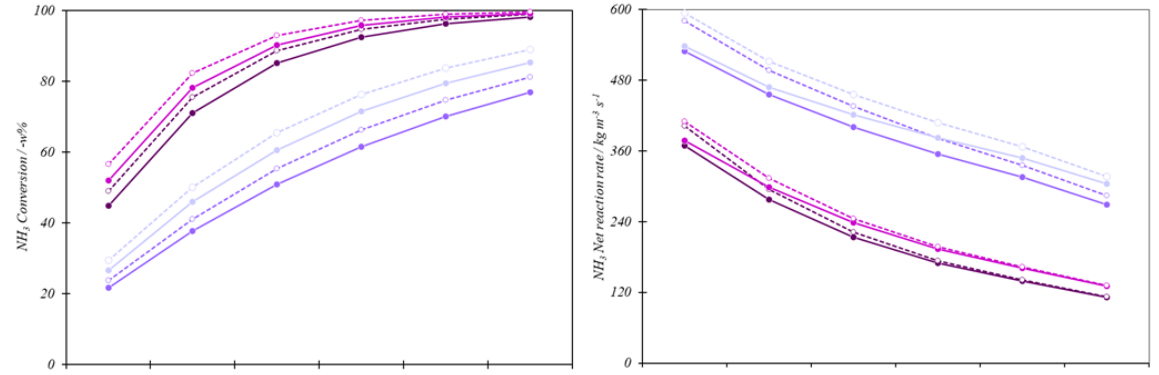

CatOx	CatOxGP	Pressure	Temperature	1st Cat. Surf.	2nd Cat. Surf.	3rd Cat. Surf.	4th Cat. Surf.	5th Cat. Surf.	6th Cat. Surf.
		bar	K	Difference due to gas phase process, %					
		5.0	423	+ 4.05	+ 4.40	+ 3.45	+ 2.26	+ 1.37	+ 0.719
		5.0	500	+ 4.56	+ 4.15	+ 2.74	+ 1.53	+ 0.792	+ 0.392
		15.0	423	+ 2.13	+ 3.44	+ 4.49	+ 4.73	+ 4.61	+ 4.28
		15.0	530	+ 2.79	+ 4.24	+ 4.98	+ 4.79	+ 4.27	+ 3.63

1st Cat. Surf.	2nd Cat. Surf.	3rd Cat. Surf.	4th Cat. Surf.	5th Cat. Surf.	6th Cat. Surf.
Difference due to gas phase process, %					
+ 9.0	+ 6.19	+ 4.05	+ 2.45	+ 1.43	+ 0.806
+ 8.78	+ 5.31	+ 3.03	+ 1.60	+ 0.808	+ 0.395
+ 9.82	+ 9.12	+ 8.83	+ 7.68	+ 6.58	+ 5.57
+ 10.5	+ 9.23	+ 8.22	+ 6.70	+ 5.38	+ 4.25

Figure 57. Simulation results in a planar channel flow reactor with six catalytic surfaces. NH_3 Conversion and Net reaction rate in each surface (a) and accumulated (b) throughout the reactor. Inlet conditions: 1.20 m s^{-1}, 10.0 v% NH_3, 90.0 v% dry air, variable inlet pressure and temperature.

8.4.2.2. NO contours

For all cases of pressure and temperature, the contours of NO composition of the CatOx and the CatOxGP processes do not show significant differences. In general, the highest NO composition occurs near the first catalytic surface and decreases throughout the reactor. For cases at 5.0 bar, the NO composition becomes stabilized after the fifth catalytic surface, while for cases at 15.0 bar, this stabilization in the NO composition does not occur even after the sixth catalytic surface. At a given pressure, the increase in the inlet temperature induces an increase in the NO composition along the reactor.

Regarding the contour of net reaction rate, NO is consumed throughout the reactor always close to the catalytic surfaces, but especially in the first one. The isobaric increment of temperature does not induce a qualitative change in this behaviour. However, the increase in pressure induces NO to react even up to near the second catalytic surface.

Figure 59 shows the results of the NO selectivity throughout the reactor for the simulations of the CatOx process and the CatOxGP process. Conditions of inlet temperature and pressure have been differentiated by means of the color code explained in the lower part of the figures. Figure 59 (a) presents the information referring to the NO selectivity calculated for each catalytic surface. Figure 59 (b) presents the information about accumulated value throughout the reactor.

The NO selectivity between the catalytic surfaces is defined according to the equation (93) for the local case and the equation (94) for the global case. The net reaction rate of NO between the wires is defined according to the equation (101) for the global case and the equation (100) for the local case. According to the Figure 51, in each catalytic surface of the planar channel flow reactor reactor $V^{CS_i} = 2.84 \times 10^{-8} m^3$.

For the NO selectivity as performance parameters (ϕ), the change due to the CatOxGP process is defined according to the equation (102). For the net reaction rate of NO the change due to the CatOxGP process is defined according to the equation (103).

Regardless of the inlet pressure and temperature, the results of the simulations of the CatOxGP process show that it decreases the NO selectivity throughout the reactor. From the point of view of local results, that is, considering the NO selectivity in each catalytic surface presented in Figure 59 (a), the results of the simulations of the CatOxGP processes decrease between 0.0515 % (15.0 bar, 423 K, fifth catalytic surface) and 8.32 % (15.0 bar, 530 K, first catalytic surface) with respect to the results for the CatOx processes.

In any case, the greatest difference in NO selectivity between the processes takes place in the first catalytic surfaces. In this region of the calculation domain, there are sufficient NO and NH_3 concentrations, therefore, the decrease in NO selectivity due to the CatOxGP process has to do with the selective non – catalytic reduction of NO in presence of NH_3. With a minor effect, the formation of the substances considered in the kinetic mechanism of the gas phase process decreases the NO selectivity as well.

In the simulation of the CatOx process, due to the high rate of catalytic NO generation on the first surface, the accumulated NO selectivity remains practically constant throughout the reactor as is shown by the Figure 59 (b). Under this simulation premise, the NO selectivity increases with the isobaric increase in temperature and decreases with the isothermal increase in pressure. At 5.0 bar and 423 K its value is close to 98.4 w% and it decreases to values close to 97.4 w% when the inlet conditions are 15.0 bar and 423 K.

Only in cases of simulation at 5.0 bar, the consideration of the CatOxGP process allows to achieve a NO selectivity close to that obtained in the simulation of the CatOx process. At 423 K, the NO selectivity in the simulation of the CatOxGP process becomes 97.9 w% in the sixth catalytic surface.

This value is 0.737 % higher than that obtained in the simulation of the CatOx process. At 500 K, the NO selectivity in the simulation of the CatOxGP process reaches the value of 98.7 w% in the sixth catalytic surface. This value is 0.380 % high than that obtained in the simulation of the CatOx process. In the cases of simulation at 15.0 bar, for the simulation of the CatOxGP process, the NO selectivity in the sixth catalytic surface does not exceed 95.0 w%.

For the CatOxGP process, the simulation results indicate that the NO selectivity increases between each catalytic surface. This is the consequence of the continuous decrement of the NH_3 concentration thorough the reactor, which favors its oxidation to NO instead of its reducing effect of NO. As explained, selective non – catalyticc reduction of NO requires a minimum NH_3 concentration, below which, the latter substance tends to oxidize to form NO instead of reducing it.

Figure 57 and 59 shows the results of the NH_3 and NO net reaction rates throughout the reactor for the simulations of the CatOx process and the CatOxGP process as well. The increase in NH_3 conversion, because of the CatOxGP process corresponds to the increase in the NO net reaction rate.

At 15.0 bar, this increase occurs on each catalytic surface and throughout the reactor. In this pressure condition, at 423 K, the NH_3 net reaction rate for the CatOx process decay from 529 kg m^{-3} s^{-1} in the first catalytic surface to an accumulated value of 269 kg m^{-3} s^{-1} in the sixth catalytic surface (values referring to NH_3 consumption). In these two surfaces, the NH_3 net reaction rate for the CatOxGP processes, is respectively 9.82 % and 5.57 % higher.

At 15.0 bar and 500 K, the NH_3 net reaction rate for the CatOx process decay from 538 kg m^{-3} s^{-1} in the first catalytic surface to an accumulated value of 304 kg m^{-3} s^{-1} in the sixth catalytic surface (values referring to NH_3 consumption). In these two surfaces, the NH_3 net reaction rate for the CatOxGP processes, is respectively 10.5 % and 4.25 % higher.

Indeed, due to the decrease in NH_3 concentration, or in other words, the difference in the NH_3 net reaction rate between the CatOx and CatOxGP processes decreases until reaching its minimum value on the sixth catalytic surface.

Also, on a given catalytic surface, the difference in the NH_3 reaction rates for the two processes is lower as lower been the pressure and the temperature of the reactor inlet, this is a consequence of the increase in the residence time of the gases. Therefore, at 5.0 bar and regardless of temperature, from the fourth catalytic surface the NH_3 net reaction rate is practically no longer affected, by the process carried out in the gas phase.

The effect of the increase in the NH_3 reaction rate due to the CatOxGP process induces the increase in the NO net reaction rate as shown in Figure 59. Since the NO selectivity in the CatOx process is so high, the change in the NO net reaction rate is not significant due to the CatOxGP process. However, as already presented in Figure 59, the gas phase process favors the decrease in NO selectivity, in turn decreasing its rate of formation, either due to the formation of substances present in the gas phase or due to the selective non – catalytic reduction of NO. As explained above, this effect on the overall process is greater the higher the temperature and pressure.

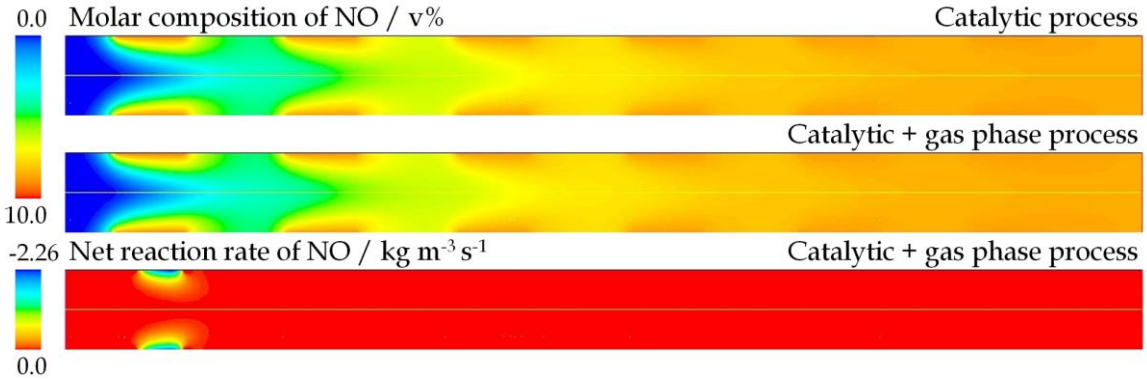

(a)

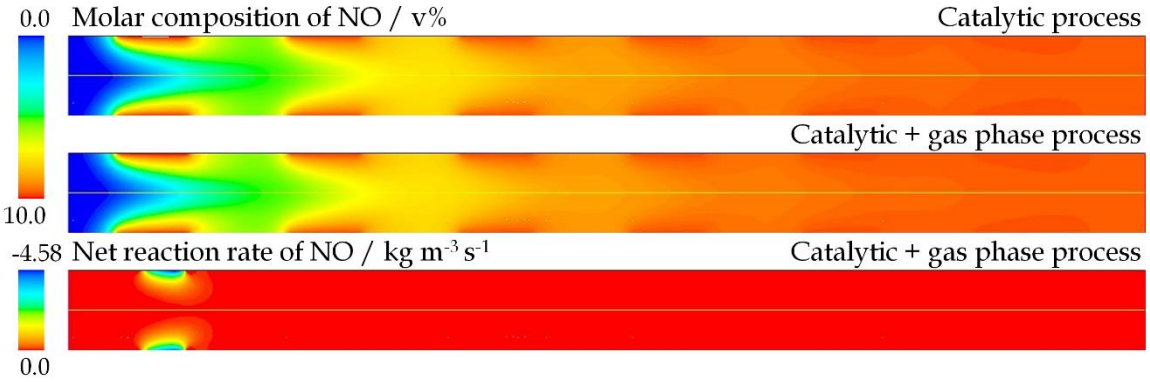

(b)

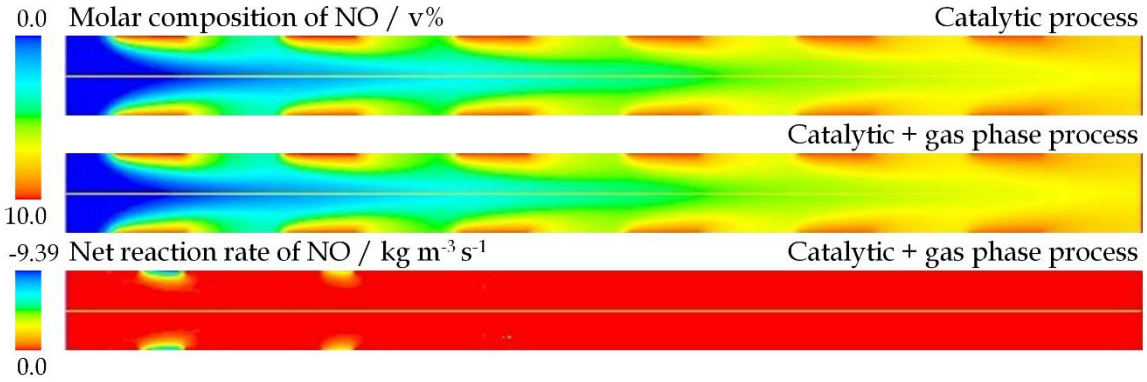

(c)

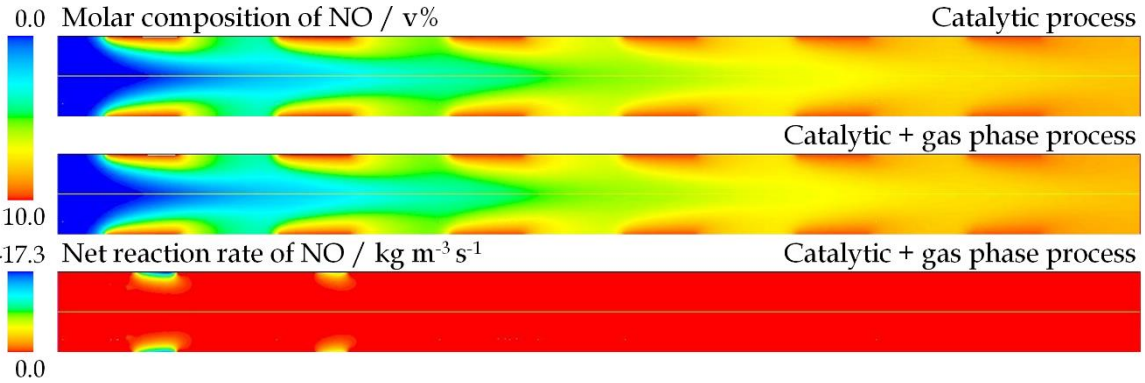

(d)

Figure 58. Results of the simulation of the CatOx and CatOxGP processes in a planar channel reactor with six catalytic surfaces. Contours of the composition and net reaction rate of NO. Inlet conditions: 1.20 m s^{-1}, 10.0 v% NH_3, 90.0 v% dry air.
(a) 423 K, 5.0 bar; (b) 500 K, 5.0 bar; (c) 423 K, 15.0 bar; (d) 530 K, 15.0 bar.

(a)

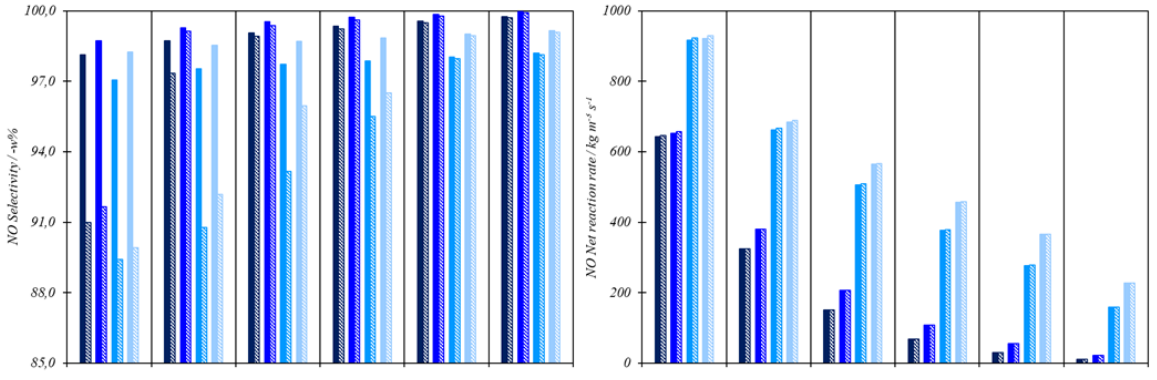

CatOx	CatOxGP	Pressure	Temperature	1st Cat. Surf.	2nd Cat. Surf.	3rd Cat. Surf.	4th Cat. Surf.	5th Cat. Surf.	6th Cat. Surf.
		bar	K	Difference due to gas phase process, %					
		5.0	423	− 7.15	− 1.39	− 0.152	− 0.118	− 0.0736	− 0.0564
		5.0	500	− 7.05	− 0.155	− 0.152	− 0.118	− 0.0736	− 0.0564
		15.0	423	− 7.64	− 6.76	− 4.54	− 2.36	− 0.0515	− 0.0813
		15.0	530	− 8.32	− 6.35	− 2.76	− 2.36	− 0.0515	− 0.0813

1st Cat. Surf.	2nd Cat. Surf.	3rd Cat. Surf.	4th Cat. Surf.	5th Cat. Surf.	6th Cat. Surf.
Difference due to gas phase process, %					
+ 0.652	+ 0.131	+ 0.0152	+ 0.0108	+ 0.00664	+ 0.00493
+ 0.631	+ 0.0137	+ 0.0139	+ 0.00988	+ 0.00596	+ 0.00437
+ 0.763	+ 0.768	+ 0.659	+ 0.298	+ 0.00649	+ 0.0102
+ 0.895	+ 0.769	+ 0.396	+ 0.30	+ 0.00654	+ 0.0103

(b)

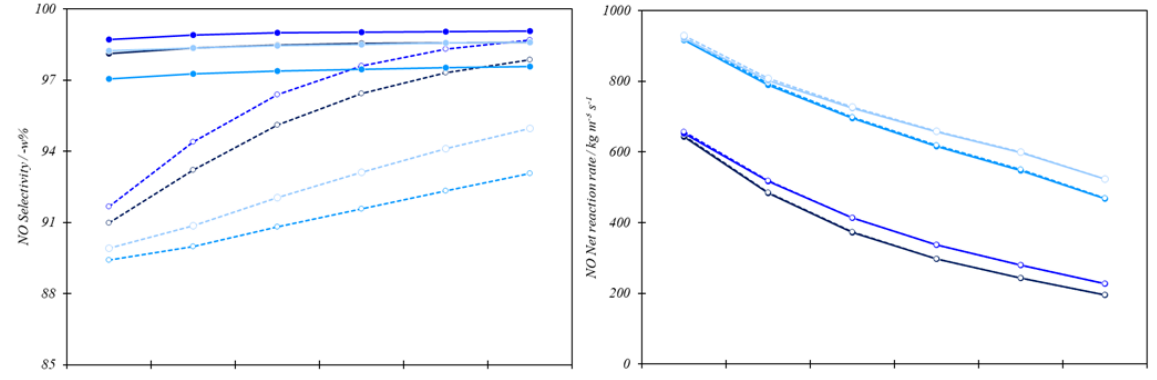

CatOx	CatOxGP	Pressure	Temperature	1st Cat. Surf.	2nd Cat. Surf.	3rd Cat. Surf.	4th Cat. Surf.	5th Cat. Surf.	6th Cat. Surf.
		bar	K	Difference due to gas phase process, %					
		5.0	423	− 7.15	− 5.14	− 3.36	− 2.11	− 1.27	− 0.737
		5.0	500	− 7.05	− 4.51	− 2.61	− 1.43	− 0.746	− 0.380
		15.0	423	− 7.64	− 7.27	− 6.57	− 5.88	− 5.19	− 4.52
		15.0	530	− 8.32	− 7.51	− 6.40	− 5.39	− 4.45	− 3.62

1st Cat. Surf.	2nd Cat. Surf.	3rd Cat. Surf.	4th Cat. Surf.	5th Cat. Surf.	6th Cat. Surf.
Difference due to gas phase process, %					
+ 0.652	+ 0.322	+ 0.138	+ 0.0521	+ 0.0183	+ 0.0060
+ 0.631	+ 0.244	+ 0.0803	+ 0.0231	+ 0.00611	+ 0.00152
+ 0.763	+ 0.674	+ 0.589	+ 0.459	+ 0.347	+ 0.256
+ 0.895	+ 0.713	+ 0.540	+ 0.370	+ 0.245	+ 0.158

Figure 59. Simulation results in a planar channel flow reactor with six catalytic surfaces. NO Selectivity and Net reaction rate in each surface (a) and accumulated (b) throughout the reactor. Inlet conditions: 1.20 m s^{-1}, 10.0 v% NH_3, 90.0 v% dry air, variable inlet pressure and temperature.

8.4.2.3. N_2 contours

For all cases of pressure and temperature, the qualitative comparison of the contours of N_2 composition shows important differences between the CatOx and CatOxGP processes. The contours of N_2 composition have greater values. Apart from the reactor inlet, the higher N_2 composition occurs near the first catalytic surface and decreases throughout the reactor.

The N_2 composition becomes stabilized first in the simulations of the CatOx process. When the CatOxGP process is considered, at 5.0 bar, the N_2 composition is stable after the fifth catalytic surface and at 15.0 bar, the N_2 composition does not stabilize even on the sixth catalytic surface. The isobaric increase in temperature does not have a significant effect on the N_2 composition.

For the contour of net reaction rate, N_2 is formed near the catalytic surfaces, but especially in the first one. The isobaric increase in temperature does not induce a qualitative change in this behaviour. However, the increase in pressure induces N_2 to react even to the second catalytic surface.

Figure 61 shows the results of the N_2 selectivity throughout the reactor for the simulations of the CatOx process and the CatOxGP process. Conditions of inlet temperature and pressure have been differentiated by means of the color code explained in the lower part of the figures. Figure 61 (a) presents the information referring to the N_2 selectivity calculated for each catalytic surface. Figure 61 (b) presents the information about accumulated value throughout the reactor.

Considering that different previous investigations, both theoretical and experimental, have shown that the N_2 selectivity of the CatOx process in various geometries is around 1.0 %, the effect of the CatOxGP process is remarkable. Up to the fourth surface, the effect of the gas phase process increases the N_2 selectivity. In the case of the first catalytic surface, the increase in N_2 selectivity at 15.0 bar and 530 K is 8.07 %. Regardless of pressure and temperature conditions, the highest N_2 selectivity occurs at the first catalytic surface. This result is consistent with the fact that in this region the presence of NO generated in the process simultaneously converges with the region of maximum possible NH_3 composition in the reactor.

The increase in N_2 selectivity due to the CatOxGP process is related to the increase in the N_2 net reaction rate, which is also shown in Figure 61. It is notable that in the cases of the CatOx process only the N_2 generation occurs in the first catalytic surface, while the CatOxGP process extends this generation to the second and fourth catalytic surfaces at 5.0 and 15.0 bar, respectively.

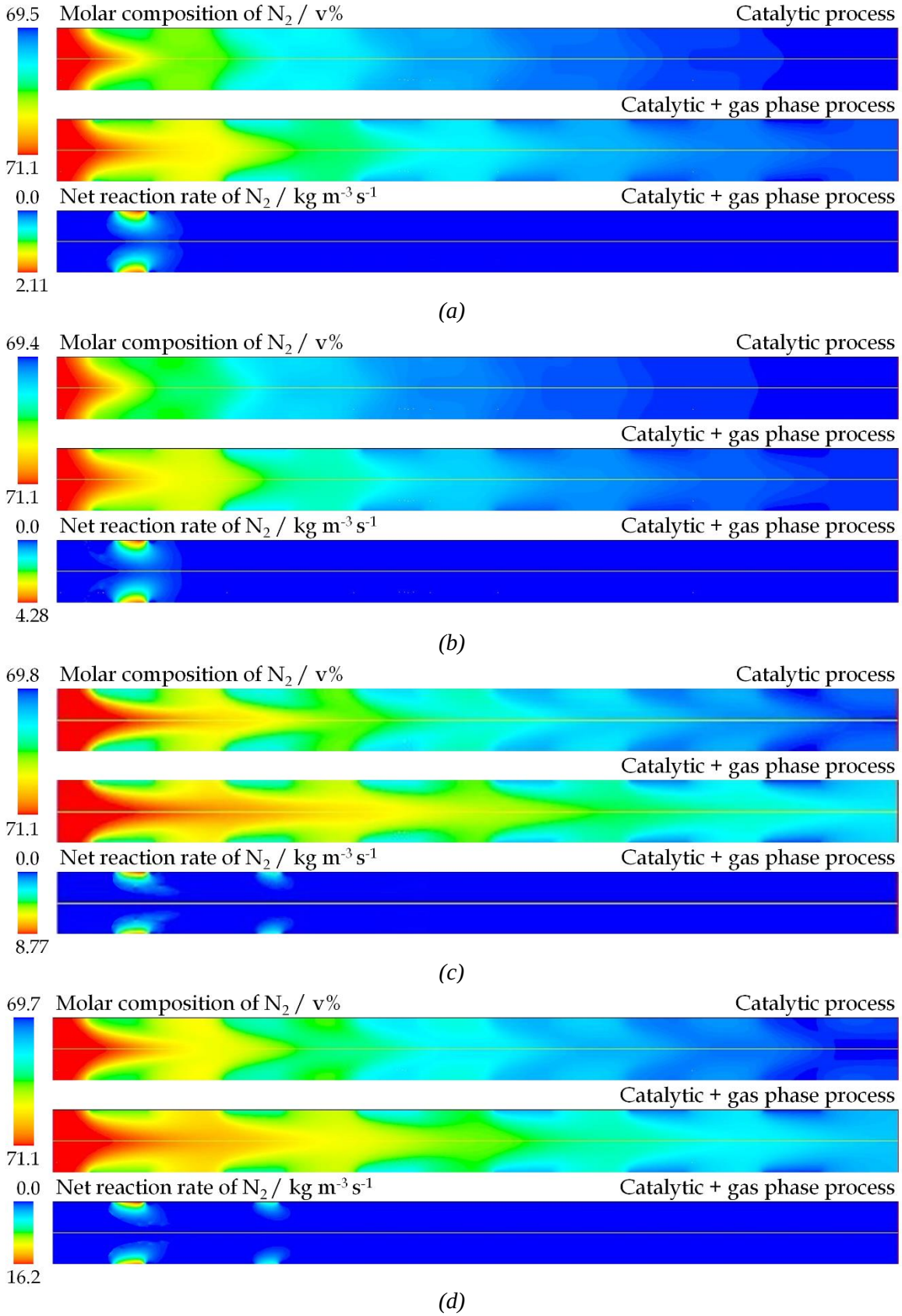

Figure 60. Results of the simulation of the CatOx and CatOxGP processes in a planar channel reactor with six catalytic surfaces. Contours of the composition and net reaction rate of N_2. Inlet conditions: 1.20 m s^{-1}, 10.0 v% NH_3, 90.0 v% dry air.
(a) 423 K, 5.0 bar; (b) 500 K, 5.0 bar; (c) 423 K, 15.0 bar; (d) 530 K, 15.0 bar.

(a)

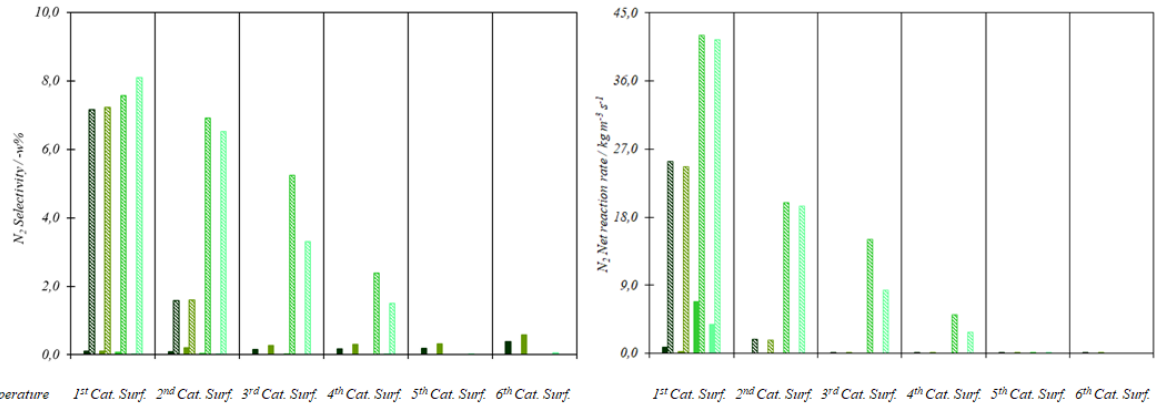

CatOx	CatOxGP	Pressure	Temperature	1st Cat. Surf.	2nd Cat. Surf.	3rd Cat. Surf.	4th Cat. Surf.	5th Cat. Surf.	6th Cat. Surf.
		bar	K	Difference due to gas phase process, %					
		5.0	423	+ 7.06	+ 1.49	- 0.148	- 0.171	- 0.186	- 0.392
		5.0	500	+ 7.13	+ 1.40	- 0.269	- 0.301	- 0.319	- 0.528
		15.0	423	+ 7.50	+ 6.88	+ 5.23	+ 2.39	0.0	0.0
		15.0	530	+ 8.07	+ 6.48	+ 3.30	+ 1.50	- 0.0108	- 0.0601

(b)

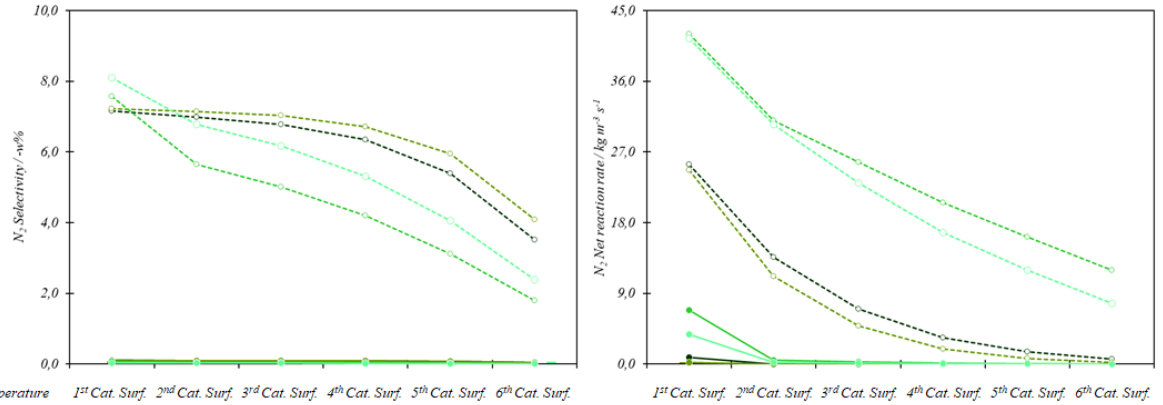

CatOx	CatOxGP	Pressure	Temperature	1st Cat. Surf.	2nd Cat. Surf.	3rd Cat. Surf.	4th Cat. Surf.	5th Cat. Surf.	6th Cat. Surf.
		bar	K	Difference due to gas phase process, %					
		5.0	423	+ 7.06	+ 6.89	+ 6.69	+ 6.26	+ 5.33	+ 3.46
		5.0	500	+ 7.13	+ 7.05	+ 6.93	+ 6.63	+ 5.87	+ 4.03
		15.0	423	+ 7.50	+ 5.60	+ 4.97	+ 4.15	+ 3.08	+ 1.78
		15.0	530	+ 8.07	+ 6.76	+ 6.15	+ 5.29	+ 4.05	+ 2.38

Figure 61. Simulation results in a planar channel flow reactor with six catalytic surfaces. N_2 Selectivity and Net reaction rate in each surface (a) and accumulated (b) throughout the reactor. Inlet conditions: 1.20 m s^{-1}, 10.0 v% NH_3, 90.0 v% dry air, variable inlet pressure and temperature.

8.4.2.4. N_2O contours

For all cases of pressure and temperature, the contours of N_2O composition for the CatOx and the CatOxGP processes do not show significant differences. In general, the higher N_2O composition occurs near the first catalytic surface and decreases throughout the reactor. At 15.0 bar there is N_2O concentration near all the catalytic surfaces. For cases at 5.0 bar, the N_2O composition stabilizes after the fourth catalytic surface, while for cases at 15.0 bar, this stabilization does not occur even after the sixth catalytic surface. The isobaric increase in temperature leads to a decrease in the N_2O composition throughout the reactor.

The contours of N_2O net reaction rate vary significantly with increasing pressure, temperature or both variables. At 5.0 bar and 423 K, there is N_2O generation especially near the first catalytic surface, it decreases in the following catalytic surfaces, until it stops on the sixth surface. From the third catalytic surface there is also N_2O generation in the fluid. At 5.0 bar, the increase in temperature favors the N_2O generation throughout the reactor. The isothermal increase in pressure generates the same effect. At 15.0 bar, the increase in temperature up to 530 K induces the N_2O reaction up to the sixth catalytic surface and along the reactor. Under these conditions both N_2O generation and consumption occur.

Figure 63 shows the results of the N_2O selectivity throughout the reactor for the simulations of the CatOx process and the CatOxGP process. Conditions of inlet temperature and pressure have been differentiated by means of the color code explained in the lower part of the figures. Figure 63 (a) presents the information referring to the N_2O selectivity calculated for each catalytic surface. Figure 63 (b) presents the information about accumulated value throughout the reactor.

Under all pressure and temperature conditions, on the first catalytic surface, the results of the simulations of the CatOxGP process show the effect on the decrease of N_2O selectivity throughout the reactor. This decrease is for all cases less than 0.25 %. The N_2O selectivity decreases with the isobaric increase in temperature and increases with the isothermal increase in pressure. This means that at a given pressure, the higher the temperature the values of N_2O selectivity will be more similar between the simulations of CatOx and CatOxGP processes. And at a given temperature, the increase in pressure will induce the values of N_2O selectivity to differ because of the chemical process in the gas phase.

Regardless of the pressure and temperature conditions, the local values of the N_2O selectivity show a generalized behaviour, according to which, between the second and the fifth catalytic surface, the difference between the results of the simulations for the CatOx and the CatOxGP process decreases, until finally, the N_2O selectivity in the sixth catalytic surface is greater for the CatOxGP process. For any case of pressure or temperature this difference is lower than 0.06 %, value reached at 15.0 bar and 530 K.

This local behaviour of N_2O selectivity induces that the accumulated N_2O selectivity in the CatOx and CatOxGP processes tends to be equal in the sixth catalytic surface. It does not occur is at 15.0 bar and 423 K. In any case, the cumulative N_2O selectivity is not lower than 1.0 %.

The tendency of the N_2O selectivity to decrease throughout the reactor is consistent with the increase in NO selectivity, which was previously presented in Figure 59. Furthermore, the characteristic that shows that under any conditions of the CatOxGP process, both the N_2O and NO selectivities are lower, evidences the formation of the substances of the gas phase mechanism and the effect of this homogeneous reactions on the global chemical process.

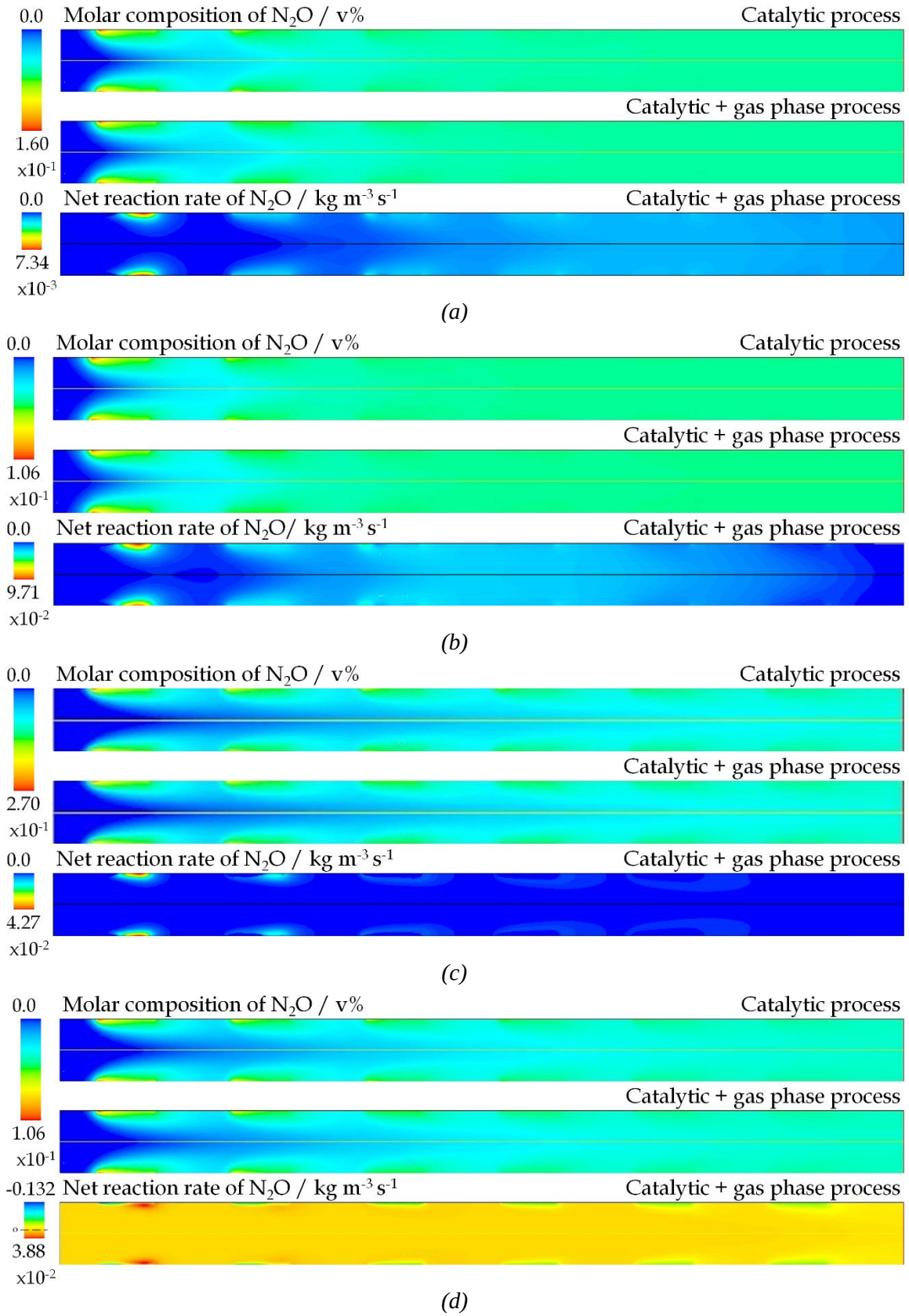

Figure 62. Results of the simulation of the CatOx and CatOxGP processes in a planar channel reactor with six catalytic surfaces. Contours of the composition and net reaction rate of N_2O. Inlet conditions: 1.20 m s^{-1}, 10.0 v% NH_3, 90.0 v% dry air.
(a) 423 K, 5.0 bar; (b) 500 K, 5.0 bar; (c) 423 K, 15.0 bar; (d) 530 K, 15.0 bar.

(a)

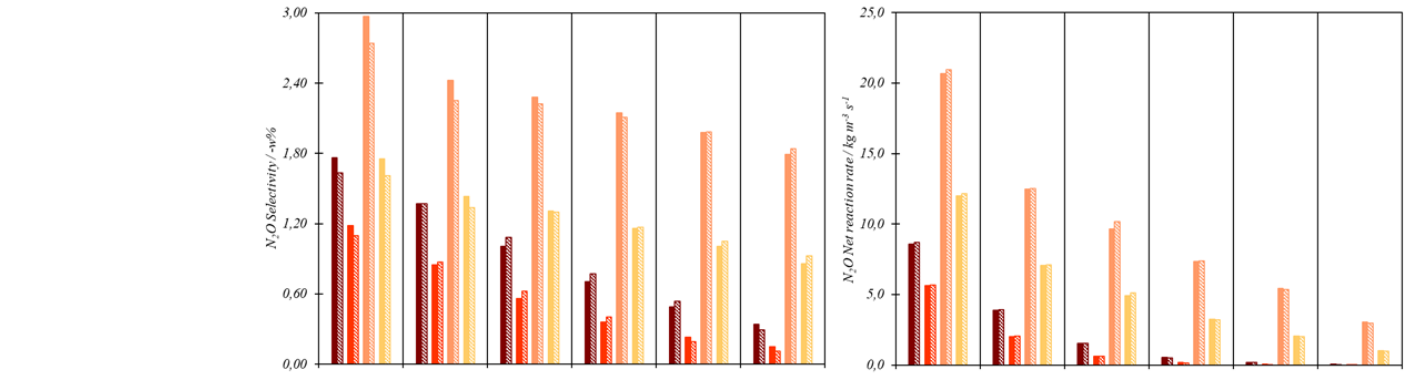

CatOx	CatOxGP	Pressure	Temperature	1st Cat. Surf.	2nd Cat. Surf.	3rd Cat. Surf.	4th Cat. Surf.	5th Cat. Surf.	6th Cat. Surf.
		bar	K	Difference due to gas phase process, %					
		5.0	423	- 0.130	- 0.000294	+ 0.0727	+ 0.0692	+ 0.0472	+ 0.0472
		5.0	500	- 0.0868	+ 0.0244	+ 0.0631	+ 0.0407	+ 0.0407	+ 0.0407
		15.0	423	- 0.227	- 0.172	- 0.0547	- 0.040	+ 0.00459	+ 0.0490
		15.0	530	- 0.146	- 0.0950	- 0.00743	+ 0.0112	+ 0.0424	+ 0.0634

1st Cat. Surf.	2nd Cat. Surf.	3rd Cat. Surf.	4th Cat. Surf.	5th Cat. Surf.	6th Cat. Surf.
Difference due to gas phase process, %					
+ 0.936	+ 1.32	+ 0.0167	- 7.95	- 16.4	- 30.6
+ 0.794	+ 1.27	- 1.72	- 13.4	- 30.5	- 65.6
+ 1.39	+ 0.522	+ 5.42	+ 0.308	- 1.12	- 2.24
+ 1.27	+ 0.440	+ 4.47	- 0.819	- 2.50	- 4.56

(b)

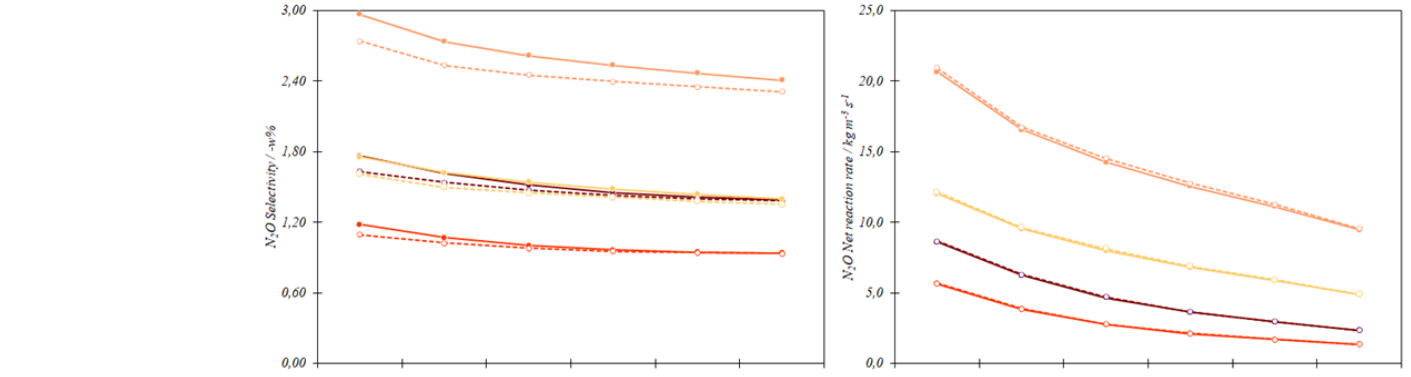

CatOx	CatOxGP	Pressure	Temperature	1st Cat. Surf.	2nd Cat. Surf.	3rd Cat. Surf.	4th Cat. Surf.	5th Cat. Surf.	6th Cat. Surf.
		bar	K	Difference due to gas phase process, %					
		5.0	423	- 0.130	- 0.0782	- 0.0453	- 0.0262	- 0.0147	- 0.00803
		5.0	500	- 0.0868	- 0.0447	- 0.0225	- 0.0112	- 0.00537	- 0.00254
		15.0	423	- 0.227	- 0.202	- 0.163	- 0.139	- 0.118	- 0.0985
		15.0	530	- 0.146	- 0.123	- 0.0934	- 0.0740	- 0.0582	- 0.0452

1st Cat. Surf.	2nd Cat. Surf.	3rd Cat. Surf.	4th Cat. Surf.	5th Cat. Surf.	6th Cat. Surf.
Difference due to gas phase process, %					
+ 0.936	+ 1.06	+ 0.942	+ 0.60	+ 0.372	+ 0.226
+ 0.794	+ 0.920	+ 0.721	+ 0.422	+ 0.236	+ 0.123
+ 1.39	+ 1.06	+ 2.05	+ 1.79	+ 1.51	+ 1.26
+ 1.27	+ 0.961	+ 1.68	+ 1.38	+ 1.11	+ 0.867

Figure 63. Simulation results in a planar channel flow reactor with six catalytic surfaces. N_2O Selectivity and Net reaction rate in each surface (a) and accumulated (b) throughout the reactor. Inlet conditions: 1.20 m s^{-1}, 10.0 v% NH_3, 90.0 v% dry air, variable inlet pressure and temperature.

The experimental verification of the behaviour presented in Figure 63, it is the effect of the CatOxGP process on the decrease in N_2O selectivity has interest since the decrease in the N_2O generation is a desirable characteristic of the process not only from the point of view of the efficiency in the conversion of NH_3 to NO, but from the environmental point of view for the potential decrease in the generation of greenhouse gases.

The behaviour presented above for N_2O selectivity, by means of which this variable decrease with the isobaric increase in temperature and increases with the isothermal increase in pressure, also occurs in the case of the N_2O net reaction rate. Under all simulation conditions, the effect of the CatOxGP process induces an increase in the N_2O net reaction rate throughout the reactor. This behaviour is consistent with the decrease in the N_2O selectivity since, as Figure 61 (a) showed, the gas phase process increases the N_2 selectivity. However, the maximum increase in the N_2O net reaction rate is 7.95 %, which takes place on the fourth catalytic surface at 5.0 bar and 423 K. This value does not seem considerable, even more considering that the kinetic mechanism of the CatOx process does not adequately describe the formation of N_2O.

8.4.2.5. Contours of the species associated with the mechanism in the gas phase

The Appendix 11 presents the contours of concentration and net reaction rate of different species and radical associated with the AA – Mech [Kil 1999] [Cod 2001].

According to the composition contours, in the case of species such H_2, O – atom, NH_2 and OH, the isobaric increment in temperature increases the composition of these species. In the case of the H – atom, HNO, NO_2, H_2NO and HONO, the composition of these species decreases due to the increase in temperature. In the case of H_2NO, under all simulation conditions, there is no presence of this substance in the reactor discharge. This same absence in the composition occurs for OH, H – atom and NH_2 under the conditions of higher pressure and temperature. In the case of the isothermal increase in pressure, all the species, except HNO, NO_2 and H_2NO, show a decrease in their composition.

The complexity of the chemical interactions described by the gas phase mechanism, make not possible the grouping of species to describe the qualitative characteristics of the contours of net reaction rate. Therefore, it is necessary to carry out an analysis that varies not only with the species considered but with the pressure and temperature conditions.

- **H_2**

The H_2 generation occurs primarily on the first catalytic surface. With the increase in pressure to 15.0 bar, it also takes place significantly on the second catalytic surface. However, on all catalytic surfaces there is some level of H_2 generation, except on the sixth surface, at 15.0 bar and 530 K, where the H_2 net reaction rate is null. At 15.0 bar, H_2 generation occurs exclusively near the catalytic surfaces, while at 5.0 bar this process also occurs within the fluid. At 423 K and 500 K, from the surroundings of the second and the first catalytic surfaces, there is H_2 generation within the fluid.

- **O – atom**

The reaction of O – atom takes place, both in terms of generation and consumption, mainly on the first and second catalytic surfaces. In the first catalytic surface, the O – atom generated at the beginning is subsequently consumed near the remaining area of that surface. From the second catalytic surface, the reactive process of the O – atom consists of its generation and its subsequent consumption to the extent that the fluid moves away from the surface. In the fluid, the reactive process tends to consume, however, the O – atom net reaction rate in this region is practically null. With the isobaric

increase in temperature up to 500 K, from the third catalytic surface, the O – atom stops reacting within the fluid. With the increase in pressure up to 15.0 bar, although the characteristics of the reactive process of the O – atom are like those already described the zone in the gas phase where the O – atom reaction occurs is much smaller.

- **H – atom**

At 5.0 bar, the reaction of H – atom consists mainly of its generation on the first catalytic surface. From the second catalytic surface, there is no reactive process of H – atom. The increase in pressure to 15.0 bar extends the H – atom generation to the second catalytic surface and its subsequent consumption. This feature does not occur at 5.0 bar. Regardless of pressure and temperature conditions, no reactive process for H – atom occurs throughout the fluid.

- **HNO**

At 5.0 bar and 423 K, there is both HNO consumption and generation. In this case, after the first catalytic surface, the entire process consists of the HNO consumption. The isobaric increase of temperature to 500 K or the pressure increment to 15.0 bar lead to the HNO generation, near the first and the second catalytic surfaces. With the increase in temperature, pressure, or the simultaneous increase of both variables, starting from the third catalytic surface, the HNO stops reacting.

- **NO_2**

Regardless of pressure and temperature, the reactive process of NO_2 consists in its generation. At 5.0 bar the NO_2 generation occurs mainly on the first catalytic surface. Increasing the pressure to 15.0 bar extends the NO_2 generation to the second catalytic surface and decreases it close to subsequent catalytic surfaces. At 5.0 bar and 423 K, NO_2 generation occurs up to the fourth catalytic surface. At 423 K, within the fluid, the NO_2 generation takes place from the third catalytic surface. The isobaric increase in temperature causes that the NO_2 generation in the fluid takes place from the second catalytic surface. The NO_2 formation at considerable amounts have been explained for Klippenstein [Klip 2011] for rich O_2 mistures like those who taka place in this process.

- **NH_2**

At 5.0 bar, the contours of net reaction rate have the same characteristics regardless of temperature. The generation of this substance occurs near the first catalytic surface, near the second and third catalytic surfaces the level of generation decreases and from the fourth catalytic surface, as well as on the axial axis of the reactor, the NH_2 generation is null. With increasing pressure, the characteristics with respect to generation near the first and second catalytic surfaces remain and additionally there is a certain level of generation throughout the fluid.

- **H_2NO**

Regardless of pressure and temperature, the reactive process of H_2NO consists in its generation in the fluid and its consumption near the catalytic surfaces. This process occurs fundamentally up to the second catalytic surface. With the isothermal increase in pressure, the H_2NO net reaction rate decreases, especially from the second catalytic surface. However, at 5.0 bar the reactive effect occurs even up to

near the fourth catalytic surface, while at 15.0 bar this phenomenon occurs significantly up to the third catalytic surface. Up to these same surfaces and under the same pressure conditions, H_2NO generation occurs in the gas phase.

- **HONO**

At 5.0 bar, the contours of net reaction rate have the same characteristics regardless of temperature. The generation and consume of this substance occurs near the first catalytic surface, until the fifth catalytic surface there is a certain level of generation lower than the generation level in the fluid. It is notable that with increasing temperature, the generation level near the last catalytic surfaces is much closer to the generation level within the fluid. With increasing pressure, the HONO generation has the same qualitative characteristics.

- **OH**

At all studied pressure and temperature levels, the qualitative characteristics of OH generation remain unchanged. In general, the generation of the species occurs near the first catalytic surface and, in the immediately nearby region, the consumption rate reaches its highest value. Once the first catalytic surface has been passed, throughout the fluid and near the other catalytic surfaces, the consumption of the species occurs at a lower level.

8.5. Comparison of simulation results between the planar channel reactor and the square mesh reactor at 5.0 bar and 423 K

The following figures present the comparison between the contours of composition and net reaction rate for the simulations carried out with the channel and square mesh reactors, under the considerations of the CatOx and CatOxGP processes, at 5.0 bar and 423 K:

- Figure 64. Comparison for the contours of NH_3.
- Figure 65. Comparison for the contours of NO.
- Figure 66. Comparison for the contours of N_2O.
- Figure 67. Comparison for the contours of N_2.

In the cases of contour of concentration of NH_3, NO and N_2O, considering the CatOx and CatOxGP processes there is not significant differences between the results. Furthermore, in the cases of NH_3 and NO, the concentration profiles for the two types of reactors show that, with or without the effect of the gas phase process, the concentration of these species becomes practically null after the fifth catalytic surface. In the case of N_2O, the same behaviour occurs from the fourth catalytic surface. In the case of N_2, due to the low changes in its concentration, there are no significant differences when comparing the N_2 composition contours.

Comparison of the contours of NH_3 net reaction rate presents an important advantage from the point of view of the shape of the reactor. This is, the largest values of NH_3 net reaction rate, tending to the consumption of the substance in the gas phase, in the case of the square mesh reactor, only takes place in the posterior zone of the first catalytic surface. This behaviour is different from what occurs in the case of the channel reactor, in which the greatest consumption of NH_3 in the gas phase takes place practically throughout the entire region near the first catalytic surface.

Regardless of the reactor geometry, the NH_3 consumption in the gas phase takes place in the process region where the highest NO concentration exists. Such a characteristic remains on subsequent catalytic surfaces, in which the two substances coexist. In fact, from the third catalytic surface of the square mesh reactor, there is some level of NH_3 consumption in the area before the catalytic surface.

Since the gas phase reaction of NO takes place fundamentally in the presence of NH_3, the analysis presented above for NH_3 is also applicable in the comparison of the contours of NO net reaction rate. However, the contours of NO net reaction rate have a fundamental characteristic that is worth highlighting. In the case of the channel reactor, the contour of NH_3 net reaction rate presents the consumption of this substance in areas of the fluid close not only to the first one but to the following catalytic surfaces. The contour of NO net reaction rate shows no reaction from the second catalytic surface. This may indicate that the reaction between NO and NH_3 occurs fundamentally on the first catalytic surface. On subsequent catalytic surfaces, the NH_3 dehydrogenation takes place for the formation of other substances considered in the kinetic mechanism of the gas phase process. This behaviour also occurs in the case of the square mesh reactor, starting from the third catalytic surface.

Figure 68 presents the countours of the beta ratio for values between 0.0 and 1.0 in the simulation cases of the CatOx process. These contours show that in the zone where the beta ratio takes these values, the greatest net reaction rate in the gas phase occurs for the species involved in the selective non – catalytic reduction of NO by NH_3.

From the point of view of reactor shape, the comparison of the contours of N_2O net reaction rate presents an important advantage. The highest value of N_2O net reaction rate, in the gas phase, in the case of the square mesh reactor only occurs in the posterior zone of the first catalytic surface. Unlike what happens in the case of the channel reactor, in which the largest N_2O generation in the gas phase takes place practically throughout the entire region near the first catalytic surface.

Regardless of the geometry of the reactor, the N_2O generation in the gas phase takes place in the region of the process where NH_3 and NO coexist, or where there is only NO concentration. The same behaviour occurs on the following catalytic surfaces. Indeed, in the square mesh reactor, from the third catalytic surface, in the zone before the surfaces, some level of N_2O generation takes place.

Comparison of the contours of the N_2 net reaction rate shows that the N_2 generation takes place in the areas where NH_3 and NO react. These zones are the one after the first catalytic surface in the case of both reactors and the one after the second catalytic surface in the case of the square mesh reactor. As previously presented, in the case of the channel reactor, the absence of NO consumption on the second catalytic surface induces the absence of N_2 generation on the same surface and confirms the NH_3 dehydrogenation to other substances considered in the kinetic mechanism of the gas phase and in this area of the simulation domain.

In this comparison, the chemical effects of the process in the gas phase on the overall process are not reflected in the temperature behaviour presented in Figure 69. This is because from the point of view of the thermal behaviour, the CatOx process governs widely the thermodynamics of the reactor.

Figures between 110 and 113 show different results throughout the reactor for the simulations of the cases with the CatOx process and the CatOxGP process. Type of reactors have been differentiated by means of the color code explained in the figure. It presents simultaneously the information referring to the parameters calculated for each catalytic surface and the accumulated value throughout the reactor. Those figures show the following parameters:

- Figure 110. NH_3 conversion and Net reaction rate.
- Figure 111. NO selectivity and Net reaction rate.
- Figure 112. N_2O selectivity and net reaction rate.
- Figure 113. N_2 selectivity and net reaction rate.

The comparison of the results for the simulations of the two types of reactors, in terms of the local or accumulated values of NH_3 conversion and NO selectivity, does not present a difference greater than 10.8 % and 0.50 % respectively. In the case of NH_3 conversion, the maximum difference occurs on the first catalytic surface. In the case of NO selectivity, the maximum difference occurs in the fourth catalytic surface. Therefore, the simulation results of the CatOxGP process obtained for the two types of reactors are comparable.

The reactive process in the gas phase does not have a representative effect on the NH_3 conversion. For this parameter, close to any of the catalytic surfaces, the effect of the gas phase on the overall process is greater in the case of the simulation of the channel reactor.

The effect of the CatOxGP process on NO selectivity is significantly higher in the case of the simulation of the channel reactor, especially on the first catalytic surface. Also, in the case of the square mesh reactor, the maximum difference in NO selectivity, by comparison between the simulation results of the CatOx and CatOxGP processes, occurs on the first catalytic surface.

In the results of the simulation of the square mesh reactor, the maximum values of the net reaction rate of NH_3, NO and N_2O are higher than the maximum values in the contours of the channel reactor. However, since the NH_3 conversion, and the N_2 and N_2O selectivities, are independent of the type of reactor, and that the volume of the gas phase is lower in the case of the channel reactor (56.9 mm^3 vs. 82.1 mm^3), it is logical that the net reaction rate of the three species is greater in the channel reactor. For this reason, in Figures 110 and 111, the local NH_3 and NO net reaction rates at the first catalytic surface of the channel reactor are higher.

The fact that most of the gas phase reaction of NO occurs on the first catalytic surface of the channel reactor induces higher values of the local NO net reaction rate in the square mesh reactor. In the case of the channel reactor, the highest contribution to the NH_3 reaction in the gas phase occurs up to the second catalytic surface. Therefore, starting from the third catalytic surface, the local values of the NH_3 net reaction rate are higher in the case of the square mesh reactor.

The accumulated NH_3 and NO net reaction rates are higher in the case of the channel reactor. The contribution of the gas phase process to the increase in the values of these reaction rates is also greater for this type of reactor.

The effect of the CatOxGP process on N_2O selectivity is especially higher in the case of the simulation of the channel reactor, particularly on the sixth catalytic surface where the selectivity decreases by 13.9 %. In the case of the square mesh reactor, this decrease in the N_2O selectivity presents its maximum value of 1.32 % in the fourth catalytic surface.

In the case of the square mesh reactor, the small difference in N_2O selectivity is a consequence of the low difference that the net reaction rate also presents when the simulation of this type of reactor considers the CatOxGP process.

The effect of the CatOxGP process and the geometry of the reactor is notable in the cases of selectivity and the N_2 net reaction rate. The N_2 selectivity not only increases by 84.8 % in the first catalytic surface of the channel reactor, but also takes nonzero values for the following surfaces. This corresponds to the increase in the N_2 net reaction rate on the same catalytic surface. In the case of the square mesh reactor, the CatOxGP process increases the N_2 net rate of reaction rate up to the third catalytic surface.

The comparative behaviour of the process variables presented between Figures 110 and 113 for the two types of reactors shows the importance of geometry and flow profile in the effect of the gas phase process on the global process of the catalytic oxidation of NH_3. Indeed, Figure 114 presents the comparison between the contours of the pathlines of the velocity magnitude. This figure shows that in the case of the channel flow reactor, in which the net reaction rate in the gas phase has already been shown to extend throughout the reactor, the velocity of the gases near the catalytic surfaces is greater than the which is observed in the case of the square mesh reactor.

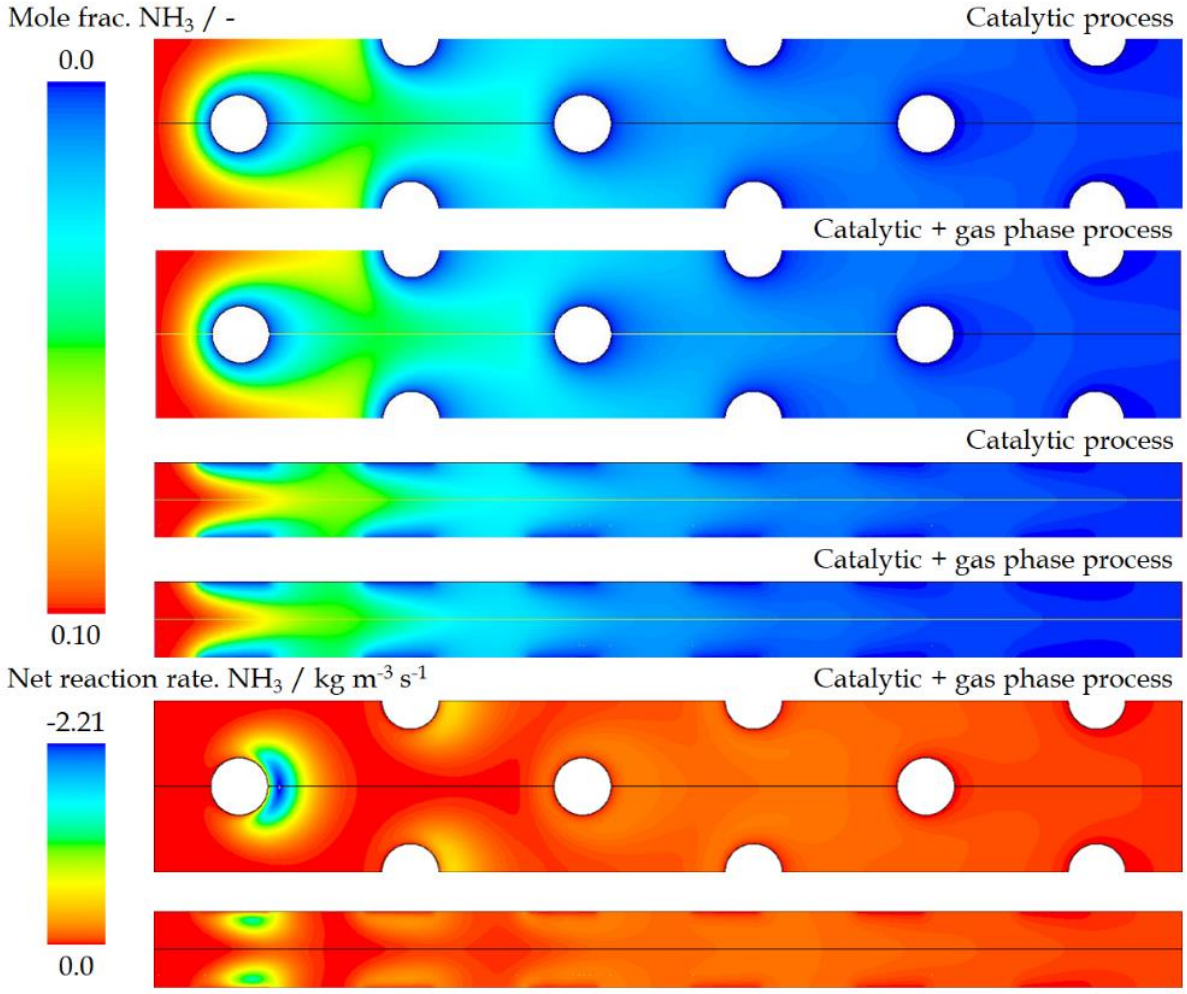

Figure 64. Comparison between contours of NH_3 composition and net reaction rate in the simulations of the planar channel flow reactor and square mesh reactor for CatOx and CatOxGP processes.
Inlet conditions: 5.0 bar, 423 K, 10.0 v% NH_3, 90.0 v% dry air,
0.75 m s^{-1} (square mesh reactor),
1.20 m s^{-1} (planar channel flowreactor).

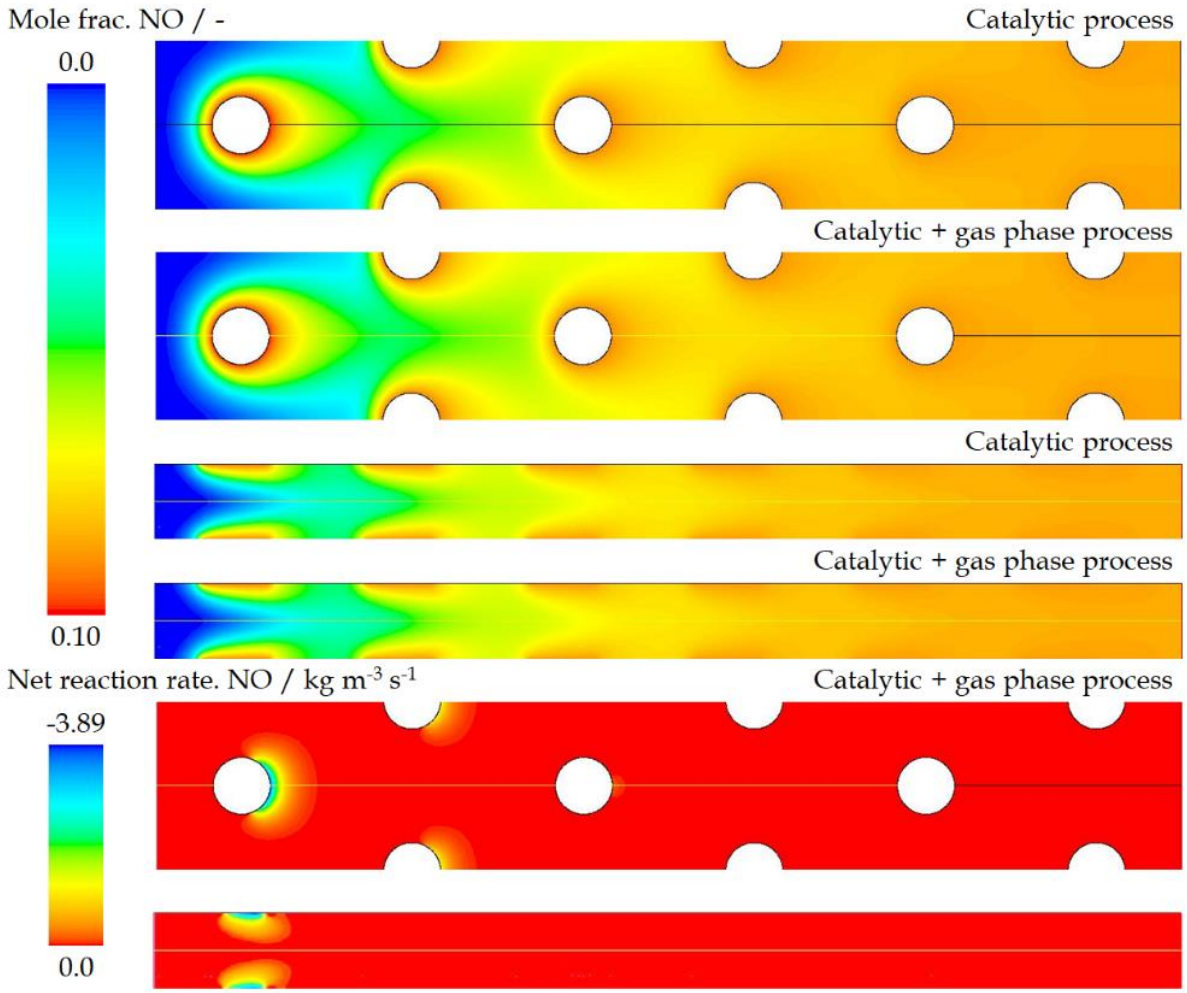

Figure 65. Comparison between contours of NO composition and net reaction rate in the simulations of the planar channel flow reactor and square mesh reactor for CatOx and CatOxGP processes.
Inlet conditions: 5.0 bar, 423 K, 10.0 v% NH_3, 90.0 v% dry air,
0.75 m s^{-1} (square mesh reactor),
1.20 m s^{-1} (planar channel flow reactor).

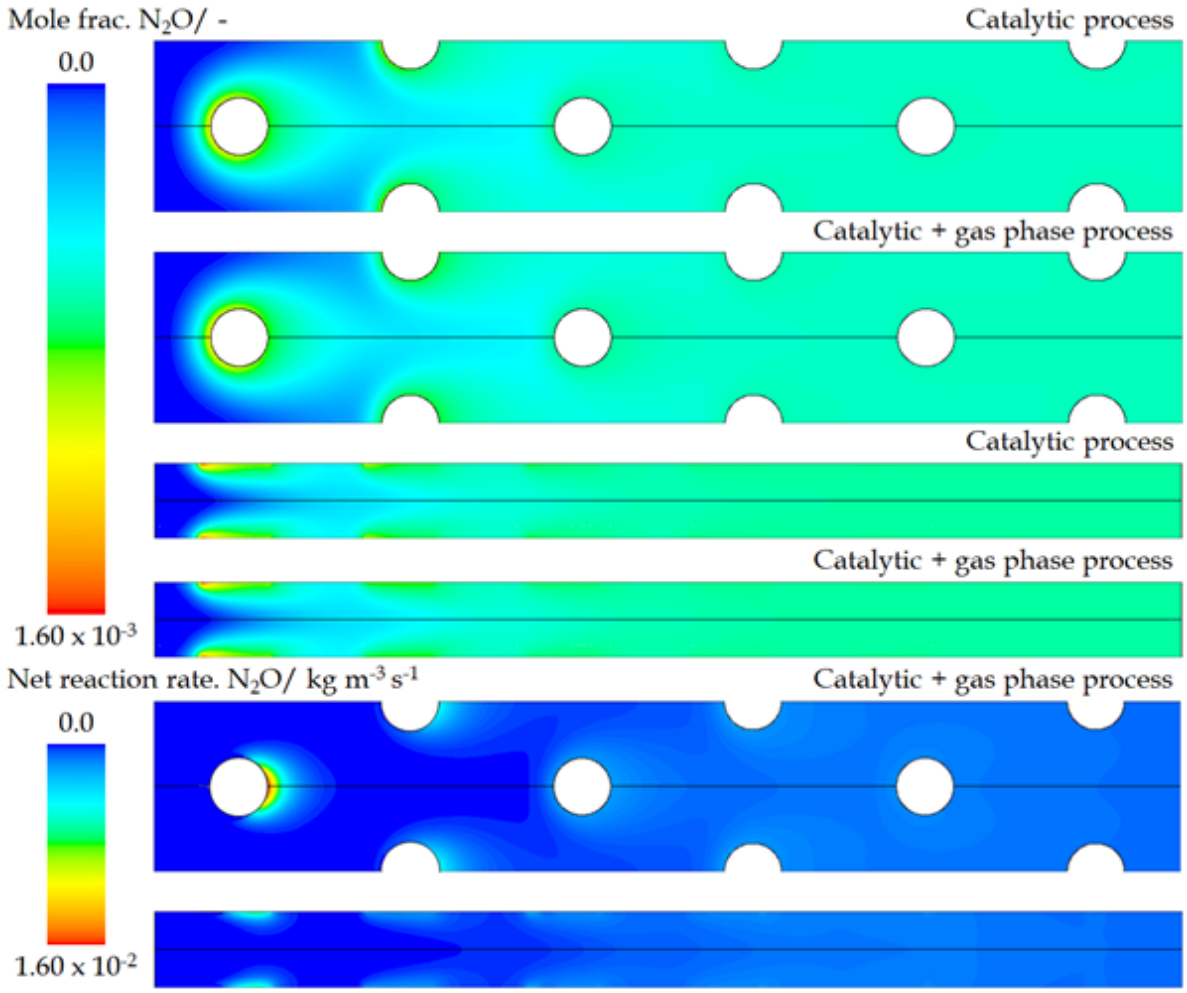

Figure 66. Comparison between contours of N_2O composition and net reaction rate in the simulations of the planar channel flow reactor and square mesh reactor for CatOx and CatOxGP processes.
Inlet conditions: 5.0 bar, 423 K, 10.0 v% NH_3, 90.0 v% dry air,
0.75 m s^{-1} (square mesh reactor),
1.20 m s^{-1} (planar channel flow reactor).

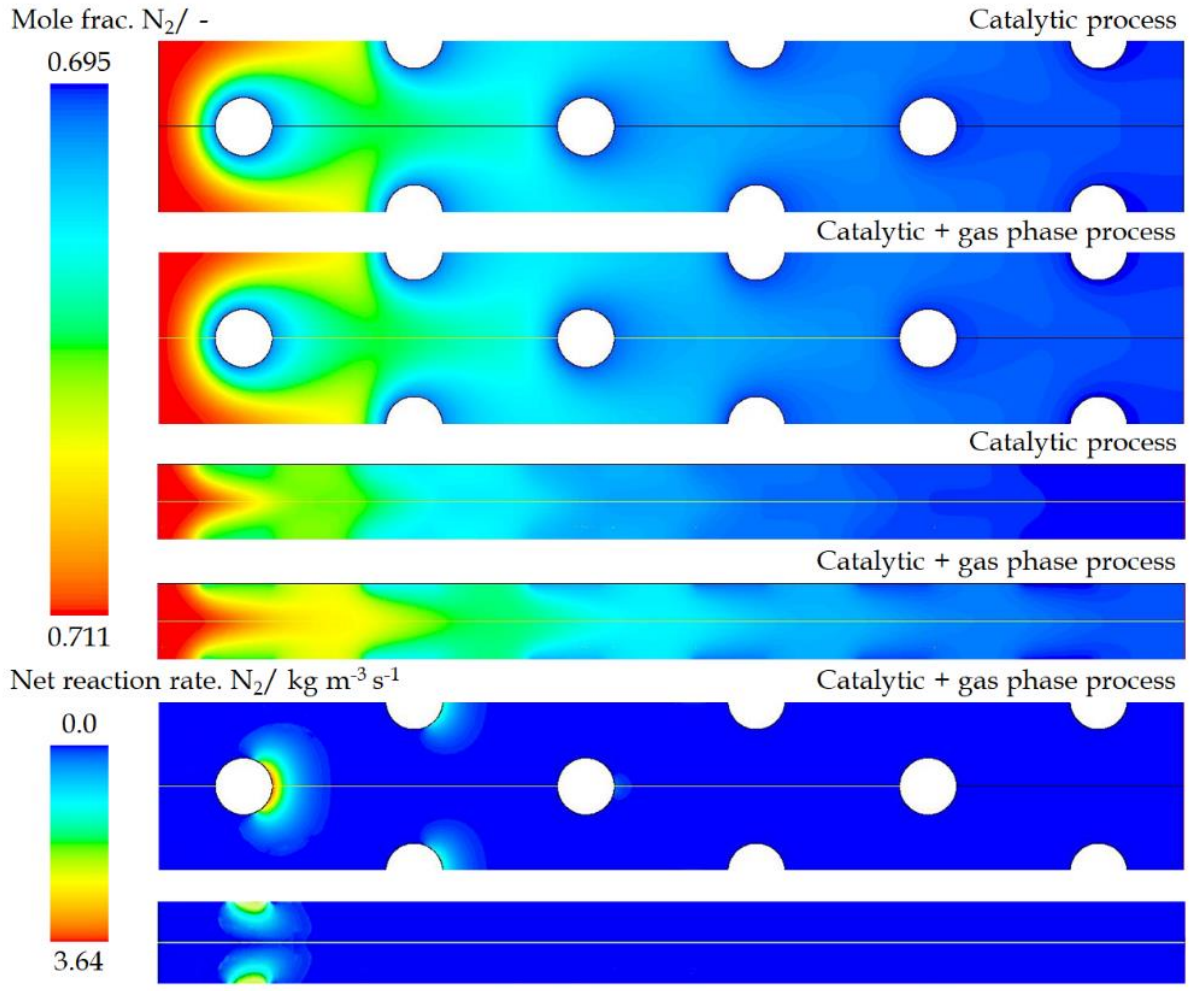

Figure 67. Comparison between contours of N_2 composition and net reaction rate in the simulations of the planar channel flow reactor and square mesh reactor for CatOx and CatOxGP processes.
Inlet conditions: 5.0 bar, 423 K, 10.0 v% NH_3, 90.0 v% dry air,
0.75 m s^{-1} (square mesh reactor),
1.20 m s^{-1} (planar channel flow reactor).

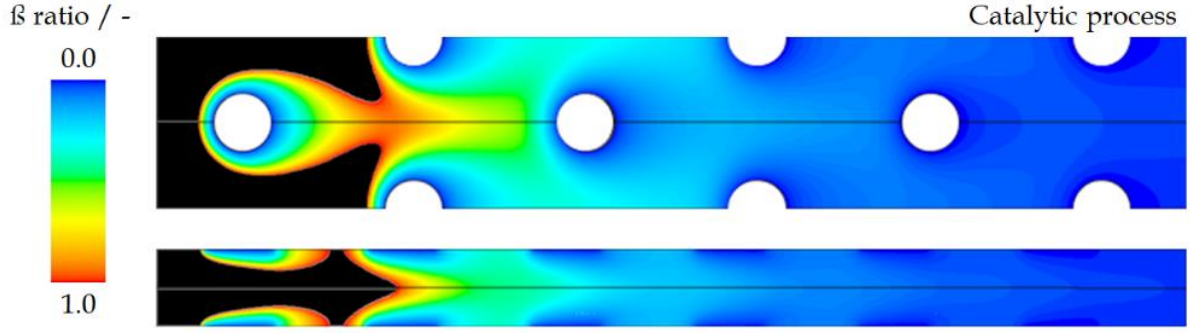

Figure 68. Comparison between contours of Beta ratio in the simulations of the planar channel flow reactor and square mesh reactor for CatOx.
Inlet conditions: 5.0 bar, 423 K, 10.0 v% NH_3, 90.0 v% dry air,
0.75 m s^{-1} (square mesh reactor),
1.20 m s^{-1} (planar channel flow reactor).

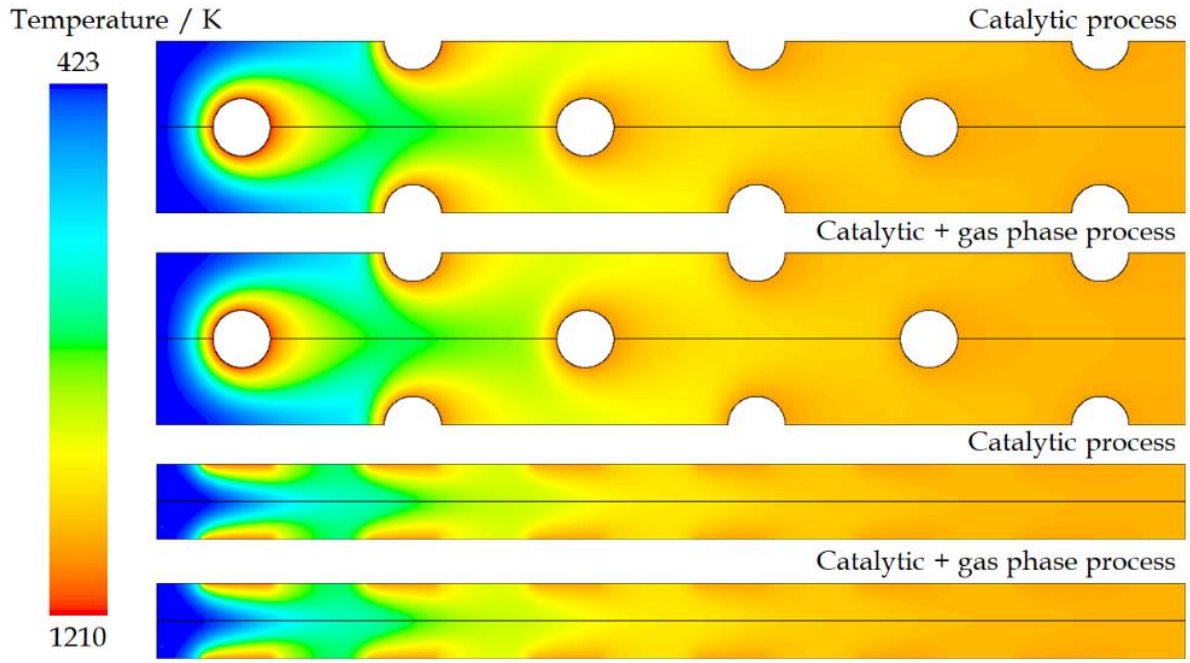

Figure 69. Comparison between contours of temperature in the simulations of the planar channel flow reactor and square mesh reactor for CatOx and CatOxGP processes.
Inlet conditions: 5.0 bar, 423 K, 10.0 v% NH_3, 90.0 v% dry air,
0.75 m s^{-1} (square mesh reactor),
1.20 m s^{-1} (planar channel flow reactor).

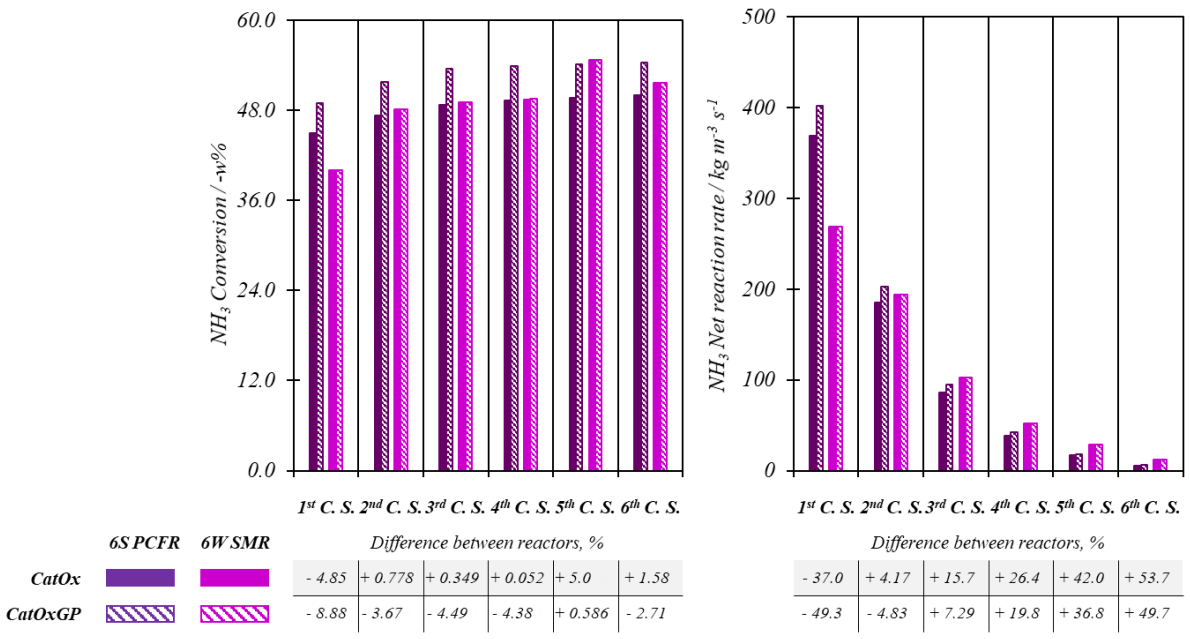

(a)

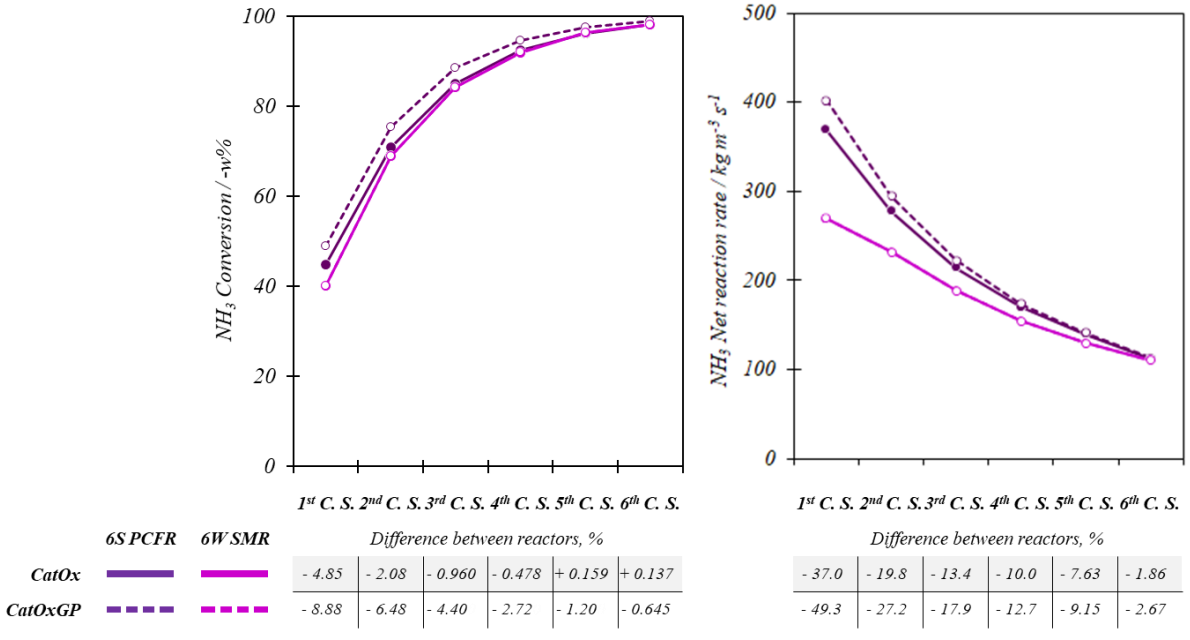

(b)

Figure 110. Comparison of simulation results in a planar channel reactor and square mesh reactor in each surface and accumulated throughout the reactor. NH_3 Conversion and Net reaction rate in each surface (a) and accumulated (b) throughout the reactor.
Inlet conditions: 5.0 bar, 423 K, 10.0 v% NH_3, 90.0 v% dry air,
0.75 m s^{-1} (square mesh reactor),
1.20 m s^{-1} (planar channel flow reactor).

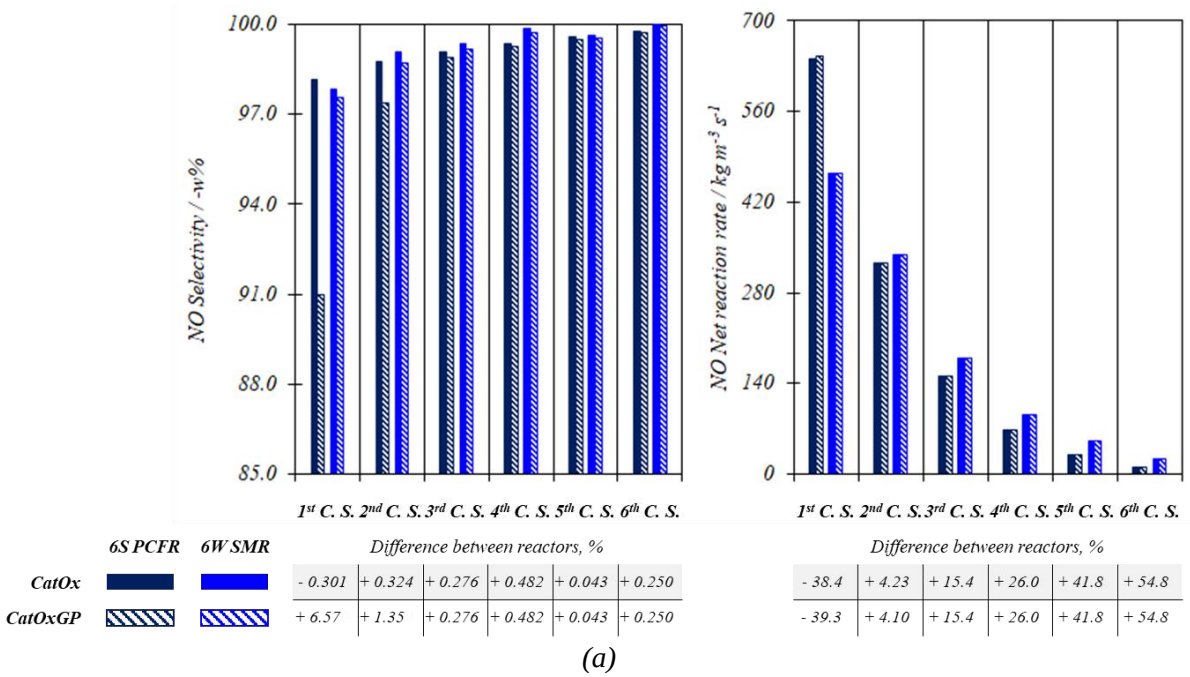

(a)

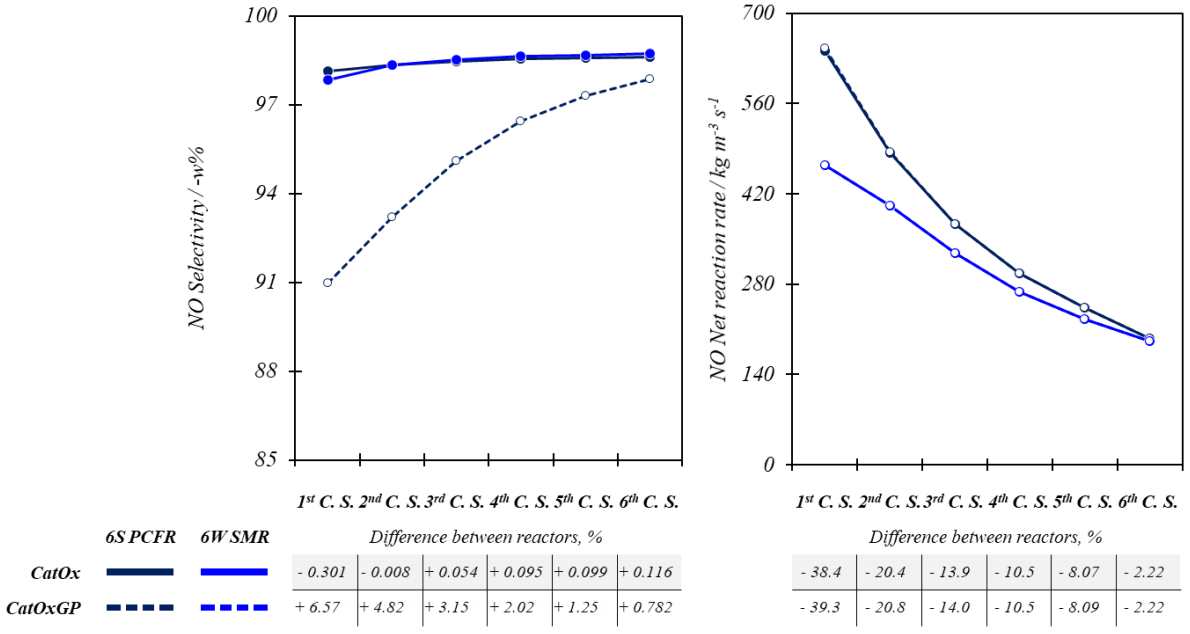

(b)

Figure 111. Comparison of simulation results in a planar channel reactor and square mesh reactor in each surface and accumulated throughout the reactor. NO Selectivity and Net reaction rate in each surface (a) and accumulated (b) throughout the reactor.
Inlet conditions: 5.0 bar, 423 K, 10.0 v% NH_3, 90.0 v% dry air,
0.75 m s^{-1} (square mesh reactor),
1.20 m s^{-1} (planar channel flow reactor).

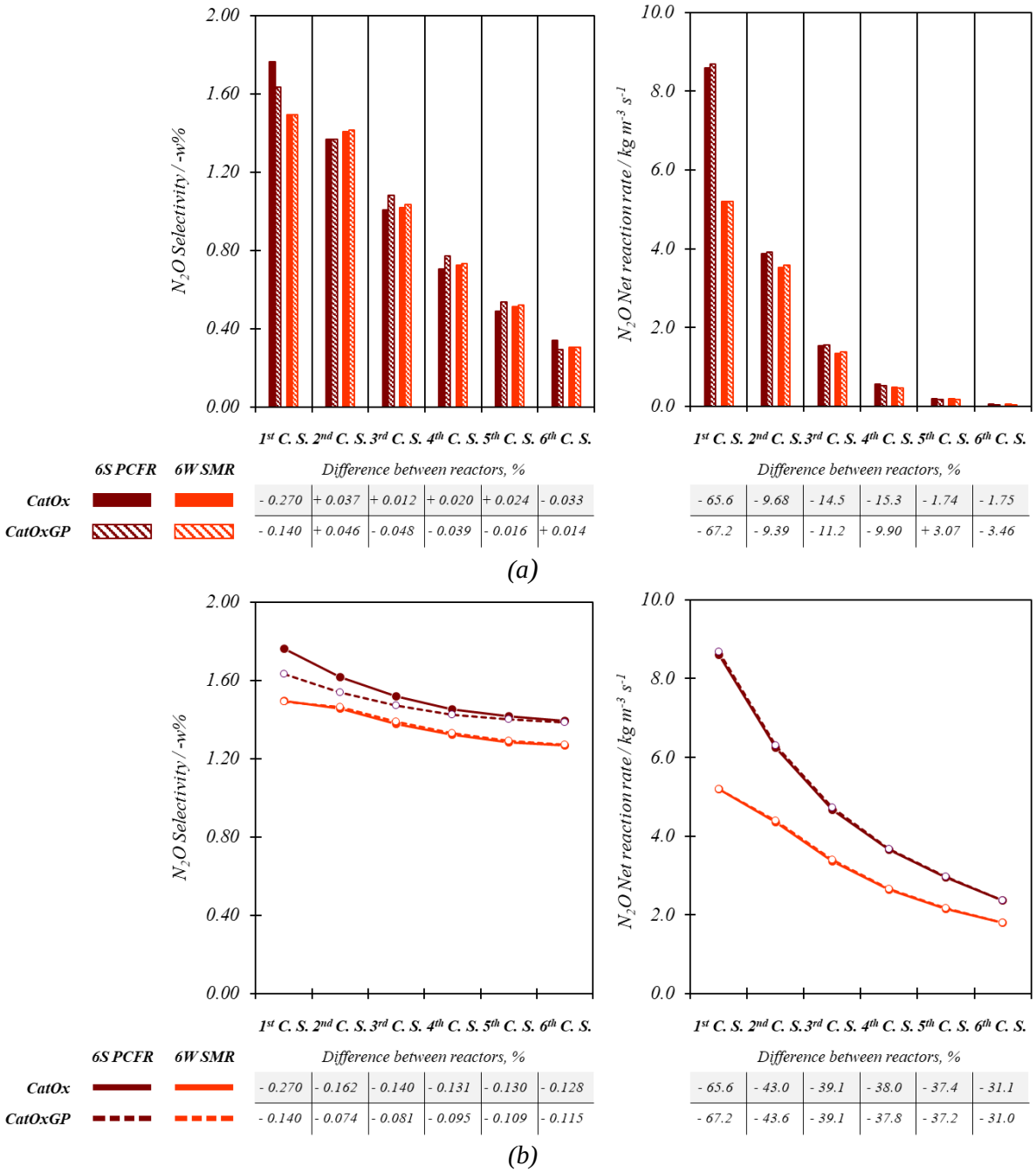

Figure 112. Comparison of simulation results in a planar channel reactor and square mesh reactor in each surface and accumulated throughout the reactor. N_2O Selectivity and Net reaction rate in each surface (a) and accumulated (b) throughout the reactor.
Inlet conditions: 5.0 bar, 423 K, 10.0 v% NH_3, 90.0 v% dry air,
0.75 m s^{-1} (square mesh reactor),
1.20 m s^{-1} (planar channel flow reactor).

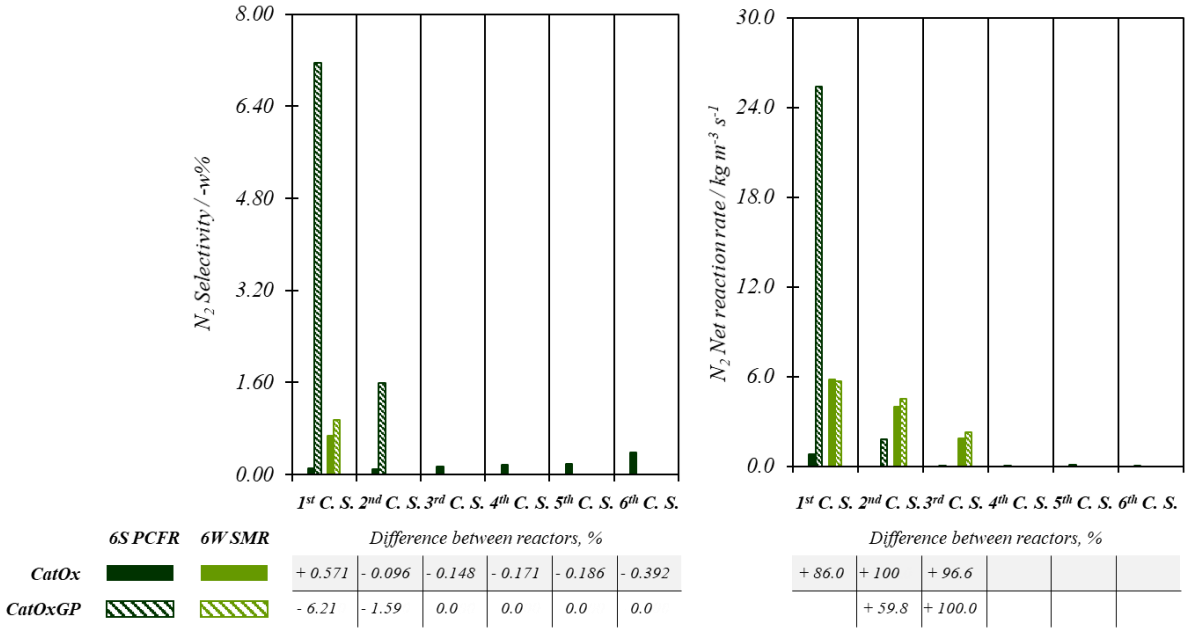

(a)

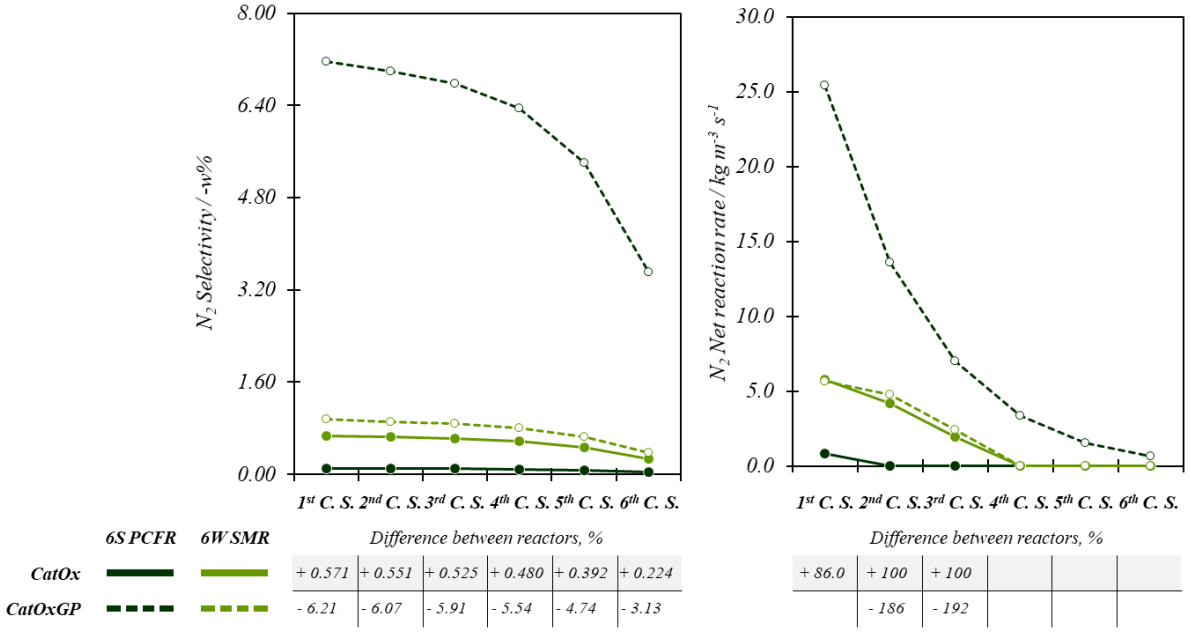

(b)

Figure 113. Comparison of simulation results in a planar channel reactor and square mesh reactor in each surface and accumulated throughout the reactor. N_2 Selectivity and Net reaction rate in each surface (a) and accumulated (b) throughout the reactor.
Inlet conditions: 5.0 bar, 423 K, 10.0 v% NH_3, 90.0 v% dry air,
0.75 m s^{-1} (square mesh reactor),
1.20 m s^{-1} (planar channel flow reactor).

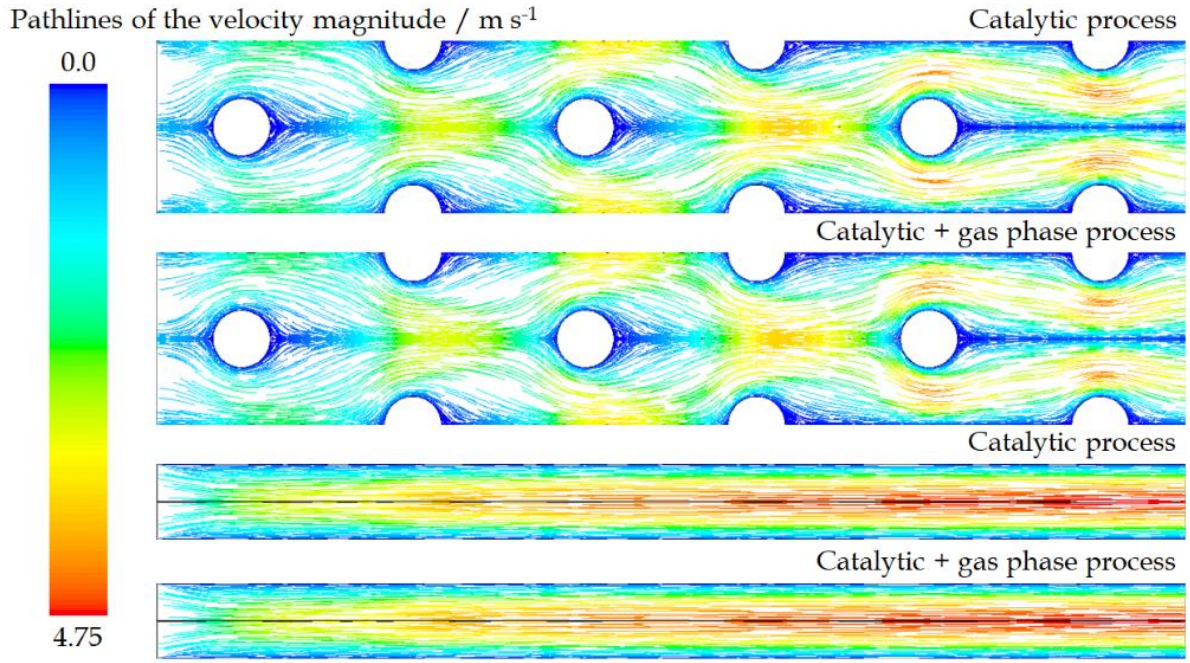

Figure 114. Comparison between the contours of the path lines of velocity magnitude in the simulations of the planar channel flow reactor and square mesh reactor for CatOx and CatOxGP processes.
Inlet conditions: 5.0 bar, 423 K, 10.0 v% NH_3, 90.0 v% dry air,
0.75 m s^{-1} (square mesh reactor),
1.20 m s^{-1} (planar channel flow reactor).

9. Summary and concluding remarks

For the simulation of the reactive process in the gas phase that could take place during the catalytic oxidation of NH_3 over platinum, the mechanism proposed by the Group of Inorganic Chemistry of the Abo Akademi in Findland [Kil 1999] [Cod 2001] was used. This mechanism had been previously reported as a plausible mechanism for the simulation of this process [Tra 2007]. In this mechanism, the group of reactions associated with nitrogen chemistry consider 145 elementary steps and involve 25 chemical species. The comparison between this mechanism and the mechanism proposed by Glarborg [Gla 2018] showed that, despite their differences, both mechanisms present similar responses regarding the description of the gas phase process. Indeed, at 1.0 atm and temperatures close to those expected in the catalytic oxidation of NH_3 (between 1000 and 1200 K), the AA – Mech [Kil 1999] [Cod 2001] simulates better some results previously obtained by experimentation [Vil 2004].

The strategies of rate production analysis [Tur 2014], the degree of rate control [Steg 2009] and sensitivity analysis [Gla 1986] were useful not only to obtaining a reduced mechanism for the simulation of the chemical process in the gas phase, seeking to reduce the computational cost, but also for the analysis of the chemical path that is carried out in this phase.

For the use of CFD tools, the process conditions were taken from those reported in conditions of industrial operation. With this, the study range for the effect of the chemistry in the gas phase on the global process was broadened. The meshing of the computational domains was chosen after the application of the analysis of the spatial convergence of the mesh explained by Slater [Sla 2012]. This methodology was applied to the geometries proposed for the three types of reactors considered in this study.

In the model of the first catalytic surfaces, in each type of reactors and depending on the operating conditions, the conclusion reported by Gardiner [Gar 2000] is confirmed. That is, NO is a suitable oxidant for NH_3; or what is the same, NH_3 acts as a reducing agent for NO as occurs when these species interact in the regions of the gas phase in which their highest concentration occurs simultaneously. It that way the simplification taked into account in this investigation and reflected in the Figure 115 allows to define the extend of the chemistry en the gas phase on the catalytic NH_3 oxidation over platinum.

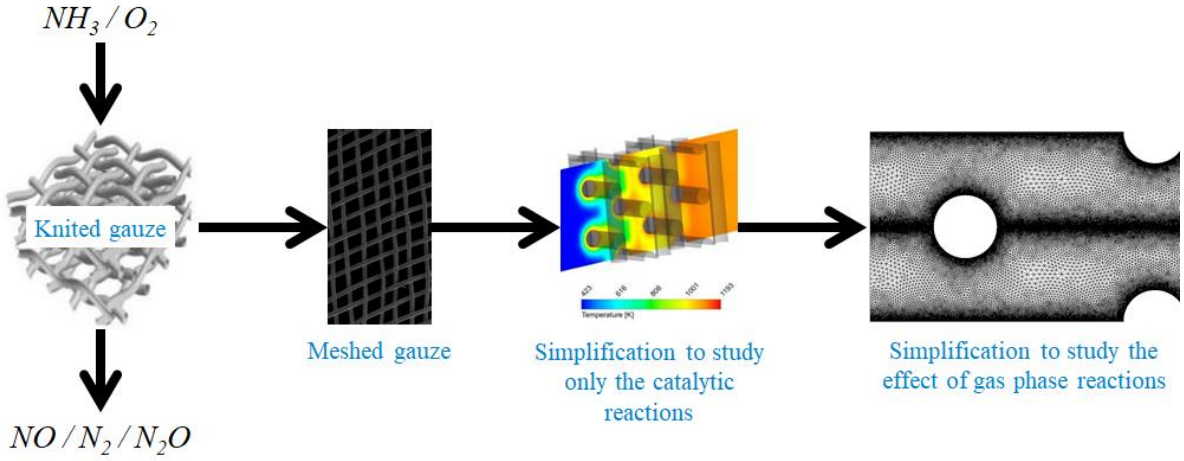

Figure 115. Simplification of the computational domain to conduct the study of the effect of gas phase reactions on the NH_3 oxidation [Hey 2018] [Wis 2020].

This investigation reflects that:

For the single catalytic wire reactor:

The simulation results, under the following initial conditions: 0.75 m s^{-1}, 423 K, 5.0 bar, 10.0 v% NH_3, 90.0 v% dry air; locate the zone for the gas phase reaction on the back face of the catalytic wire. In this zone the NH_3 consumption, the formation of radicals, the NO consumption, and the formation of N_2, N_2O and NO_2 occur simultaneously. In this area, the higher temperature of the process also favors the process in the gas phase. Compared with the CatOx process, the effect of the CatOxGP process decreases the NO selectivity by 0.50 % and increases the N_2 and N_2O selectivities by 0.471 % and 0.010 % respectively.

For the stagnation point reactor:

The simulation results, under the following initial conditions: 3.0 kg m^{-2} s^{-1}, 423 K, 5.0 bar, 10.0 v% NH_3, 90.0 v% dry air; locate the zone for the gas phase reaction near to the catalytic surface (the stagnation surface). In this zone the NH_3 consumption, the formation of radicals and N_2, the consumption of NO and N_2O occur simultaneously. In this area, the higher temperature of the process also favors the process in the gas phase. Compared with the CatOx process, the effect of the CatOxGP process decreases the NO and N_2O selectivities by 0.069 % and 0.259 % respectively and increases the N_2 selectivity by 0.189 %.

For the planar channel flow reactor with one catalytic surface:

The simulation results, under the following initial conditions: 1.20 m s^{-1}, 423 K, 5.0 bar, 11.0 v% NH_3, 89.0 v% dry air; locate the zone for the gas phase reaction near to the catalytic surfaces. In this zone the NH_3 consumption, the formation of radicals and N_2, the consumption of NO and N_2O occur simultaneously. In this area, the higher temperature of the process also favors the process in the gas phase. Compared with the CatOx process, the effect of the CatOxGP process decreases the NO selectivity by 6.61 % and increases the N_2 selectivity and N_2O selectivity by 2.57 % and 0.10 % respectively. With increasing pressure up to 15.0 bar, the process simulation up to the second catalytic surface, shows that the effect of the gas phase process on the decrement of the NO selectivity and on the increament of the N_2 selectivity remains even util the second catalytic surface.

The simulation results for **the model of the planar channel flow reactor with six catalytic surfaces**, under the following initial conditions: 1.20 m s^{-1}, 10.0 v% NH_3, 90.0 v% dry air and different pressure and temperature conditions; locate the zone for the gas phase reaction near to the first catalytic surface. In this zone, where the presence of NO and NH_3 coincide, as well as the highest temperature level of the simulation, the process in the gas phase at 15.0 bar and 530 K induces a decrease in the NO and N_2O selectivities close to 8.0 % and 0.15 % respectively with respect to the calculated in the CatOx process. In the same case, the N_2 selectivity goes from null to close to 8.0 %. These effects are consistent with the formation and consumption of the species in the gas phase due to the selective non – catalytic reduction of NO with NH_3. In agreement with Klippenstein [Klip 2011] the results in the planar channel reactor show that the N_2O formation is important at high pressures and moderate temperatures. It means that in terms of process operation, when the process is conducted at high pressures, it is recommendable as well to allow simultaneously high temperatures.

The Figure 116 sumarises the quantative results of this investigation.

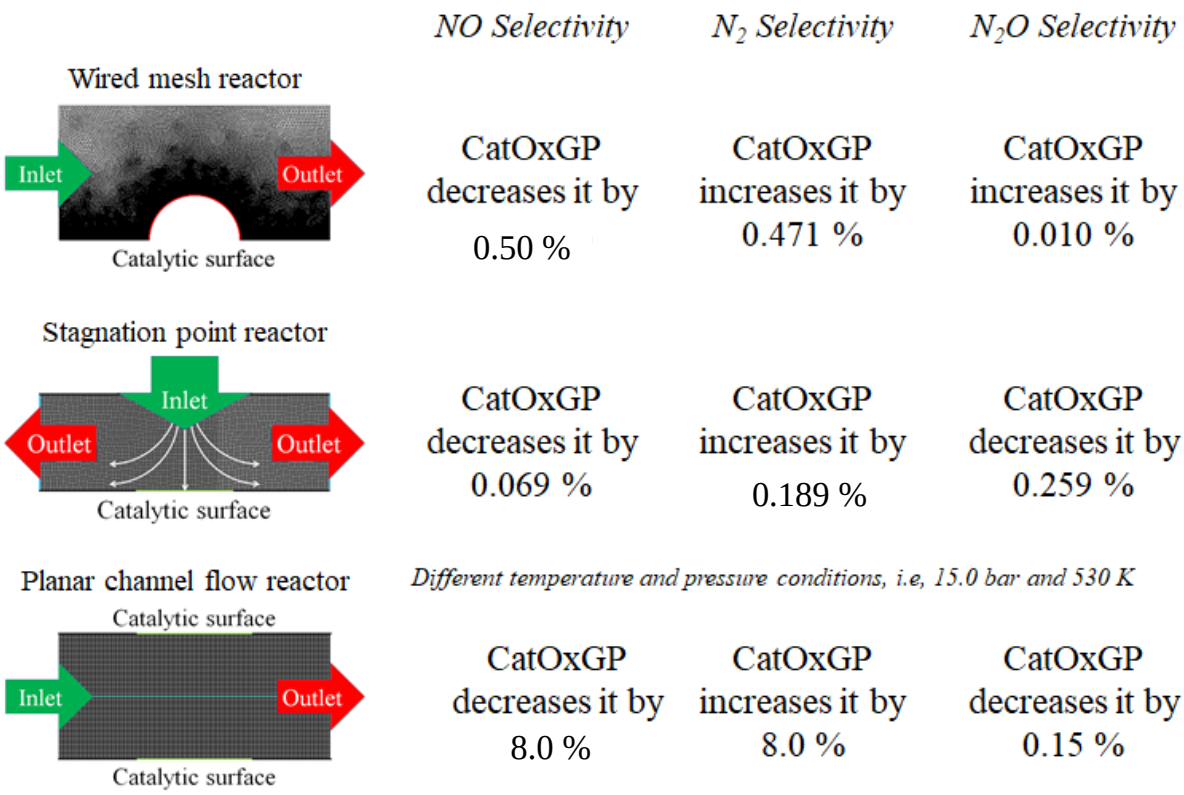

Figure 116. Summary of thequantitative results of this investigation

Based on the methodology and results presented in this document, it defends the following theses:

1. It is understood then, that within the framework of the chemical kinetics mechanism in the gas phase used in this work and under the considered operating conditions, the catalytic oxidation of NH_3 undergoes the effect of the gas phase process if the pressure of the reactive medium increases. This effect induces an increase in NH_3 consumption (either by direct oxidation with O_2 or by acting as a reducing agent for NO), a decrease in selectivity to NO (attributable to selective non – catalytic reduction), an increase in selectivity to N_2 and less markedly to N_2O (induced by both possible processes in the gas phase). As was presented in the state of knowledge (Section 3), The homogeneous reactions are dominant over higher temperatures, at those conditions the higher amount of energy, which is available in the system, promotes the process in the gas phase.

2. This analysis leads to the main conclusion, which is that in the catalytic oxidation of NH_3, part of the Ostwald process, it is important to preserve the lowest possible temperature and pressure to avoid the effect of the gas phase reactions. This effect conducts primarly to the reducción of NO to N_2 througt its reaction with NH_3.

3. Regardless of the type of reactor, since the effect is observed markedly near the first catalytic surface, in which NH_3 and NO coexist, it is to be expected that the fundamental chemical pathway observed in the gas phase corresponds to the selective non − catalytic reduction of NO with NH_3. The simulation results shows as well that the effect also depends on the geometry of the catalytic surface.

Uncertanity in the results:

Undoubtedly, the greatest sources of uncertainty in the results presented in this work are related to the small changes in the concentration of the fundamental species because of the gas phase process. This uncertainty, of course, is associated with the reactive mechanism and the information on the physical − chemical properties that describe the gas phase, and the adjustment of numerical and configuration parameters of the simulation tools used. In fact, previous investigations have indicated that remaining uncertainties in the application of the gas phase chemical models lies in the difficulty to scrutinize unambiguously the rate constants due to experimental uncertainties [Bra 2016].

Proposals of future work:

From the results obtained during this investigation, it is of interest to make an experimental verification of the results especially at high pressures (> 10.0 bar). At low pressures (~5.0 bar) the validation of the presented results using other (better detailed) mechanisms could be an interesting topic to discard completely the importance of the effect of the gas phase process in the catalytic oxidation of NH_3. However, the use of catalytic mechanisms, in which the formation and transport of species such as OH, H_2, H, HNO, O, among others, is considered (which in this study have only been considered in the gas phase) would allow to elucidate the reasons for the formation of N_2 and N_2O in the catalytic process. One advantage in the study of those radical species lies in the fact, that from the point of view of physicochemical behaviour, the NH_3 combustion is relatively simple compared with hydrocarbon flames, therefore all major intermediates (OH, NH_2, NH) can be measured with spectroscopic methods, which have been applied in studies of H / N / O mixtures, where NH_3 is a major component, at differente pressures [Bra 2016].

Since the effect of the gas phase process on the catalytic oxidation of NH_3 increases with increasing pressure, and that this parameter modifies the conditions of the gas flow inside the reactors, it is of interest to lead out studies of the effect of homogeneous processes for different pressures and with different catalyst geometries, in which the chemical behaviour of the species is followed in different flow lines and at different residence times.

Any research effort made in this matter, linking the use of mechanisms and physicochemical processes in the gas phase, or considering the formation of more diverse radicals on the surface of the catalyst, will require more and better computational resources. Therefore, the need to review and optimize the calculation processes remains, which tend to decrease the computational cost, without sacrificing the validity of the results.

10. References

[All 1994] M. T. Allen, R. A. Yetter, F. L. Dryer. **The decomposition of nitrous oxide at elevated pressures.** *Spring western states section meeting of the Combustion Institute,* **Paper No. 94 – 012**.

[All 1995] M. T. Allen, R. A. Yetter, F. L. Dryer. **The decomposition of nitrous oxide at 1.5 ≤ P ≤ 10.5 atm and 1103 ≤ T ≤ 1173 K.** *International Journal of Chemical Kinetics,* **27** (1995) 883 – 909.

[Amo 2017] P. Amodio, Y. Blinkov, V. Gerdt, R. La Scalaa. **Algebraic construction and numerical behaviour of a new – consistent difference scheme for the 2D Navier – Stokes equations.** *Applied Mathematics and Computation*, **314** (2017) 408 – 421.

[Bae 2005] M. Baerns, R. Imbihl, V. A. Kondratenko, R. Kraehnert, W. K. Offermans, R. A. van Santen, A. Scheibe. **Bridging the pressure and material gap in the catalytic ammonia oxidation: structural and catalytic properties of different platinum catalysts.** *Journal of Catalysis*, **232** (2005) 226 – 238.

[Bir 2018] R. B. Bird, W. E. Steward, E. N. Lightfoot. **Transport Phenomena**. Jhon Wiley & Sons (Asia) New Delhi. Second Edition, 2018, xii – 895 p.

[Bor 2018] D. Born, internal communication. Umicore AG & Co. KG, 2018

[Boy 2005] J. E. Boyer. **Combustion characteristics and flame structure of nitromethane liquid monopropellant**. *Thesis. The Pennsylvania State University, The Graduate School College of Engineering,* December 2005.

[Bra 2016] C. Brackmann, V. A. Alekseev, B. Zhou, E. Nordström, P – E. Bengtsson, Z. Li, M. aldén, A. A. Konnov. **Structure of premixed ammonia + air flames at atmospheric pressure: laser diagnostics and kinetic modeling.** *Combustion and Flame,* **163** (2016) 370 – 381.

[Bri 1951] H. C. Brinkman. **Heat effects in capillary flow I.** *Appl. Sci. Research,* **2** (1951) 120 – 124.

[Bur 1999] R. Burch, E. M. Crabb. **Homogeneous and heterogeneous contributions to the catalytic oxidative dehydrogenation of ethane.** *Appl. Catl. A,* **97 1** (8 April 1999) 49 – 65.

[Bus 1975] J. A. Busby. **The activation and deactivation of platinum / rhodium catalysts for ammonia oxidation**. *Thesis. University of London,* November 1975.

[Cat 1989] J. A. Caton, D. L. Siebers. **Comparison of nitric oxide removal by cyanuric acid and by ammonia**. *Combustion Science and Technology,* **65: 4 – 6** (1989) 277 – 293.

[CEW 202] Chemical Engineering World. **Nitric Acid Manufacturing Process**, *https://chemicalengineeringworld.com/*. Visited on 23.07.2021

[Che 2016] J. Chen, W. Song, X. Gao, D. Xu. **Hetero – / homogeneous combustion and flame stability of fuel – lean propane – air mixtures over platinum in catalytic microcombustors.** *Appl. Them. Eng.*, **100** (2016) 932 – 943.

[Chem 2015] **ANSYS Chemkin Theory Manual 17.0** (15151), Reaction Design: San Diego, 2015.

[Clo 2000] L. D. Cloutman. **A selected library of transport coeffients for combustion and plasma physics applications.** *Lawrence Livermore National Laboratory report UCRL – ID – 139893,* August 2000

[Cre 2000] M. A. Cremer, C. J. Montgomery, D. H. Wang, M. P. Heap, J. – Y. Chen. **Development and implementation of reduced chemistry for computional fluid dynamics modeling of selective non – catalytic reduction.** *Proceedings of the Combustion Institute,* **28 2** (2000) 2427 – 2434.

[Cod 2001] E. G. Coda Zabetta, P. T. Kilpinen. **Gas – Phase conversion of NH_3 to N_2 in gasification. Part II: testing the kinetic model.** *IFRF Comb. Journal,* 200104, March 2001. ISSN 1562 – 479X.

[Com 2020] COMSOL AB. **CFD Module User's Guide, COMSOL Multiphysics® v. 5.6.** COMSOL AB, Stockholm, Sweden. 2020, 862 p.

[Dat 2014] G. K. P. Dathar, Y. – T. Tsai, K. Gierszal, Y. Xu, C. Liang, A. J. Rondinone, S. H. Overbury, V. Schwartz. **Identifying active functionalities on few – layered graphene catalysts for oxidative dehydrogenation of isobutane.** *ChemSusChem.,* **7** (2014) 483 – 491.

[Dav 2000] M. B. Davis, M. D. Pawson, G. Veser, L. D. Schmidt. **Methane oxidation over noble metal gauzes: an LIF study.** *Combust. Flame,* 123 (2000) 159 – 174.

[Deu 1998 – 01] O. Deutschmann, L. D.Schmidt. **Two dimensional modeling of partial oxidation of methane on rhodium in a short contact time reactor.** *Proc. Combust. Inst.,* **27 2** (1998) 2283 – 2291.

[Deu 1998 – 02] O. Deutschmann, L. D.Schmidt. **Modeling the partial oxidation of methane in a short contact time reactor.** *AIChE J.,* **44 11** (1999) 2465 – 2477.

[Dia 1995] E. W. Diau, M. J. Halbgewachs, A. R. Smith, M. C. Lin. **Thermal reduction of NO by H_2: kinetic measurement and computer modeling of the HNO + NO reaction.** *Int. J. Chem. Kinet.,* **27** (1995) 867 – 881.

[Duy 2012] C. Duynslägher, F. Contino, J. Vandooren, H. Jeanmart. **Modeling of ammonia combustion at low pressure.** *Combustion and flame,* **159** (2012) 2799 – 2805.

[Flu 16 – 01] ANSYS ® Academic Fluent, Relase 16.

[Flu 16 – 02] ANSYS ® Academic Meshing, Relase 16.

[Flu 2012 – 01] ANSYS ® Academic Fluent, Relase 14.5, Help System, ANSYS FLUENT Users's Guide, October 2012. ANSYS, Inc.

[Flu 2012 – 02] ANSYS ® Academic Fluent, Relase 14.5, Help System, ANSYS FLUENT Theory Guide, October 2012. ANSYS, Inc.

[Fuj 1981] N. Fujji, H. Miyama, M. Koshi, T. Asaba. **Kinetics of ammonia oxidation in shock waves**. *The Combustion Institute, Eighteenth symposium (international) on combustion*, (1981) 873 – 883.

[Gar 2000] W. C. Gardiner, Jr. **Gas – phase combustion chemistry.** Springer science+business media New York 2000. Capitel 2: A. M. Dean, J. W. Bozzelli. **Combustion Chemistry of Nitrogen.**

[Geu 1999] J. W. Geus, J. C. van Giezen. **Monoliths in catalytic oxidation.** *Catalysis Today,* **47** (1999) 169 – 180.

[Gil 1983] R. G. Gilbert, K. Luther, J. Troe. **Theory of Thermal Unimolecular Reactions in the Fall-off Range. II. Weak Collision Rate Constants.** *Berg. Bunsenges. Phys. Chem.,* 87 (1983) 169 – 177.

[Gla 1986] P. Glarborg, J. A. Miller, R. J. Kee. **Kinetic modeling and sensitivity analysis of nitrogen oxide formation in well – stirred reactors.** *Combustion and Flame,* **65** (1986) 177 – 202.

[Gla 2018] P. Glarborg, J. A. Miller, B. Ruscic, S. J. Klippenstein. **Modeling nitrogen chemistry in combustion.** *Progress in Energy and Combustion Science,* **00** (2018) 1 – 38.

[Gni 2009] I. Gniot, P. Kirszensztejn, M. Kozlowski. **Oxidative dehydrogenation of isobutane using modified activated carbons as catalysts.** *Appl. Catal. A Gen.,* **362** (2009) 67 – 74.

[Gon 2006] J. Gong, R. A. Ojifinni, T. S. Kim, J. M. White, C. B. Mullins. **Selective catalytic oxidation of ammonia to nitrogen on atomic oxygen precovered Au (111).** *J. AM. CHEM. SOC.,* **128** (2006) 9012 – 9013.

[Gon 2017] J. D. Gonzalez, M. Warner, B. S. Haynes, A. Montoya. **N_2O formation and dissociation during ammonia combustion: a combined DFT and experimental study.** *Proceedings of the Combustion Institute*, **36 1** (2017) 637 – 644.

[Goo 2017] D. G. Goodwin, H. K. Moffat, R. L. Speth. **Cantera: an object – oriented software toolkit for chemical kinetics, thermodynamics, and transport processes.** http://www.cantera.org, 2017. Version 2.3.0. DOI:10.5281/zenodo.170284.

[Gri 30] G. P. Smith, D. M. Golden, M. Frenklach, N. W. Moriarty, B. Eiteneer, M. Goldenberg, C. T. Bowman, R. K. Hanson, S. Song, W. C. Gardiner, Jr., V. V. Lissianski, Z. Qin. **GRI – Mech 3.0, The Gas Research Institute.** http://www.me.berkeley.edu/gri_mech/

[Hey 2018] T. Heydt. **Untersuchung der Pt-katalysierten NH_3 – Oxidation unter operando Bedingungen und CFD-Simulation.** *Thesis. Technische Universität Darmstadt, Facbereich Chemie,* July 2018.

[Hin 2016] S. Hinokuma, S. Matsuki, Y. Kawabata, H. Shimanoe, S. Kiritoshi, M. Machida. **Copper oxides supported on aluminum oxide borates for catalytic ammonia combustion.** *J. Phys. Chem. C,* **120, 43** (2016) 24734 – 24742.

[Hin 2018] S. Hinokuma, S. Kiritoshi, Y. Kawabata, K. Araki, S. Matsuki, T. Sato, M. Machida. **Catalytic ammonia combustion properties and operando characterization of copper oxides supported on aluminum silicates and silicon oxides.** *Journal of Catalysis,* **361** (2018) 267 – 277.

[IHS 2020] IHS Markit. **Nitric Acid – Chemical Economics Handbook.** [Online]. Available: https://ihsmarkit.com/products/nitric−acid−chemical−economics−handbook.html [Accessed: 20.07.20]

[Imb 2007] R. Imbihl, A. Scheibe, Y. F. Zeng, S. Günther, R. Kraehnert, V. A. Kondratenko, M. Baerns, W. K. Offermans, A. P. J. Jansen, R. A. van Santen. **Catalytic ammonia oxidation on platinum: mechanism and catalyst restructuring at high and low pressure.** *Phys. Chem. Chem. Phys.,* **9** (2007) 3522 – 3540.

[Kas 1995] F. Kasuya, P. Glarborg, K. Dam – Johansen. **The thermal $DeNO_X$ process: influence of partial pressures and temperature.** *Chem Eng Sci,* **50** (1995) 1455 – 66.

[Kee 2003] R. J. Kee, M. E. coltrin, P. Glarborg. **Chemically reacting flow: Theory and practice**. Wiley Interscience, Hoboken, New Jersey.2003.

[Kil 1999] P. T. Kilpinen, J. K. Leppälahti, E. G. Coda Zabetta, M.M. Hupa. **Gas – Phase conversion of NH_3 to N_2 in gasification. Part I: a kinetic modeling study on the potential of the method.** *IFRF Comb. Journal,* 199901, September 1999. ISSN 1562 – 479X.

[Kli 2017] M. Klingenberger, O. Hirscha, M. Votsmeier. **Efficient interpolation of precomputed kinetic data employing reduced multivariate Hermite Splines.** *Computers and Chemical Engineering*, **98** (2017) 21 – 30.

[Klip 2011] S. J. Klippenstein, L. B. Harding, L. B. Harding, P. Glarborg, J. A. Miller. **The role of NNH in NO formation and control.** *Combustion and Flame*, **158 4** (2011) 774 – 789.

[Klip 2013] S. J. Klippenstein, L. B. Harding, P. Glarborg, Y. Gao, H. Hu, P. Marshall. **Rate constant and branching fraction fort he NH_2 + NO_2 reaction.** *J. Phys. Chem. A*, **117** (2013) 9011 – 9022.

[Kra 2008] R. Krähnert, M. Bärns. **Kinetics of ammonia oxidation over Pt foil studied in micro – structured quartz – reactor.** *Chemical Engineering Journal*, **137** (2008) 361 – 375.

[Li 2010] J. – H. Li, C. – C. Wang, C. – J. Huang, Y. – F. Sun, W. – Z. Weng, H. – L. Wan. **Mesoporous nickel oxides as effective catalysts for oxidative dehydrogenation of propane to propene.** *Appl. Catal. A Gen.*, **382** (2010) 99 – 105.

[Li 2017] Q. Li, J. Wang, L. Meng, J. Li, Z. Guo. **CFD Study on stability limits of hydrogen/air premixed flames in planar microcombustors with catalytic walls.** *Applied Thermal Engineering*, **121** (2017) 325 – 335.

[Lin 1994] R. P. Lindstedt, F. C. Lockwood, M. A. Selim. **Detailed kinetic modeling of chemistry and temperature effects on ammonia oxidation.** *Combustion Science and Technology*, **99: 4 – 6** (1994) 253 – 276.

[Lød 1999] R. Lødeng, O. A. Lindvåg, S. Kvisle, H. Reier – Nielsend, A. Holmen. **Short contact time oxidative dehydrogenation of C_2 and C_3 alkanes over noble metal gauze catalysts.** *Appl. Catal. A*, **187** (1999) 25 – 31.

[Lyo 1975] R. K. Lyon. **Method for the reduction of the concentration of NO in combustion effluents using ammonia.** *U. S. Patent* **3900554** (1975).

[Mac 1967] D. I. Maclean, H. GG. Wagner. **The structure of the reaction zones of ammonia – oxygen and hydrazine – decomposition flames.** *Symposium (International) on Combustion*, 11 1 (1967) 871 – 878.

[Mar 1989] G. A. Martin, A. Bates, V. Ducarme, C. Mirodatos. **Oxidative Conversion of Methane and C2 Hydrocarbons on Oxides: Homogeneous versus Heterogeneous Processes.** *Appl. Catal.*, **47 2** (15 February 1989) 287 – 297.

[Mat 2015] O. Mathieu, E. L. Petersen. **Experimental and modeling study on the high – temperature oxidation of ammonia and related NO_X chemistry.** *Combustion and Flame*, **162** (2015) 554 – 570.

[Mill 1983] J. A. Miller, M. D. Smooke, R. M. Green, R. J. Kee. **Kinetic modeling of the oxidation of ammonia in flames.** *Combustion Science and Technology*, **34: 1 – 6** (1983) 149 – 176.

[Mill 1989] J. A. Miller, C. T. Bowman. **Mechanism and modeling of nitrogen chemistry in combustion**. *Prog. Energy Combust. Sci.*, **15** (1989) 287 – 338.

[Mor 1989] E. Morales, J. H. Lunsford. **Oxidative dehydrogenation of ethane over a lithium promoted magnesium oxide catalyst.** *J. Catal.*, **118 1** (July 1989) 255 – 265.

[Ost 1902] W. Ostwald. **Improvements in the manufacture of nitric acid and nitrogen oxides.** *GB190200698A.* 20.03.1902

[Pat 2020] B. S. Patil, N. Cherkasov, N. V. Srinath, J. Lang, A. O. Ibhadon, Q. Wang, Volker **Hessel. The role of heterogeneous catalysts in the plasma – catalytic ammonia synthesis.** https://doi.org/10.1016/j.cattod.2020.06.074.

[Raf 2012] M. Rafti, J. L. Vicente, A. Albesa, A. Scheibe, R. Imbihl. **Modelling ammonia oxidation over a Pt (533) surface.** *Surface Science*, **606, 1** (2012) 12 – 20.

[Rai 2002] S. Raimondeu, D. Norton, D. g. Vlachos, R. I. Masel. **Modeling of high temperature microburners.** *Proc. Combust. Inst.*, **29** (2002) 901 – 907.

[Ram 2019] A. Ramirez, J. L. Hueso, M. Abian, M. U. Alzueta, R. Mallada, J. Santamaria. **Escaping undesired gas phase chemistry: Microwave – driven selectivity enhancement in heterogeneous catalytic reactors.** *Sci. Adv.*, **5** (2019) eaau9000.

[Reb 2002] E. V. Rebrov, M. H. J. M. de Croon, J. C. Schouten. **Development of the kinetic model of the platinum catalyzed ammonia oxidation in a microreactor.** *Chemical Engineering Journal,* **90, 1** (2002) 61 – 76.

[Res 2020] A. Resta, U. Hejral, S. Blomberg, S. Albertin, A. Vlad, Y. Garreau, C. Chatelier, F. Venturini, P. Ferrer – Escorihuela, G. Held, D. Grinter, E. Lundgren, A. Coati. **Ammonia oxidation over a $Pt_{25}Rh_{75}$ (001) model catalyst surface: an operando study.** *J. Phys. Chem. C*, Just Accepted Manuscript. DOI: 10.1021/acs.jpcc.0c07128, Publication Date (Web): 16 Sep 2020.

[Rud 1996] Y. Rudich, R. K. Talukdar, A. R. Ravishankara, R. W. Fox. **Reactive uptake of NO_3 on pure water and ionic solutions.** *Journal of Geophysical Research,* **101, D15** (1996) 21023 – 21031.

[Sad 2000] V.A. Sadykov, L.A. Isupova, I.A. Zolotarskii, L.N. Bobrova, A.S. Noskov, V.N. Parmon, E.A. Brushtein, T.V. Telyatnikova, V.I. Chernyshev, V.V. Lunin. **Oxide catalysts for ammonia oxidation in nitric acid production: properties and perspectives.** *Applied Catalysis A: General*, **204** (2000) 59 – 87.

[Seg 2002] N. Segond, Y. Matsumura, K. Yamamoto. **Determination of ammonia oxidation rate in sub− and supercritical water.** *Ind. Eng. Chem. Res.*, **41** (2002) 6020 – 6027.

[Shr 2018] K. P. Shrestha, L. Seidel, T. Zeuch, F. Mauss. **A detailed kinetic mechanism for the oxidation of ammonia including the formation and reduction of nitrogen oxides.** *Energy Fuels*, 07 Jul 2018, DOI: 10.1021/acs.energyfuels.8b01056.

[Sla 2012] J.W. Slater. **Computational fluid dynamics (CFD) verification and validation website of the NPARC Alliance**. Last Updated: Thursday, 23.02.12. https://www.grc.nasa.gov/www/wind/valid/homepage.html.

[Son 2016] Y. Song, H. Hashemi, J. M. Christensen, C. Zou, P. Marshall, P. Glarborg. **Ammonia oxidation at high pressure and intermediate temperatures.** *Fuel*, **181** (2016) 358 – 365.

[Stef 2009] G. D. Stefanidis, D. G. Vlachos. **Controling homogeneous chemistry in homogeneous heterogeneous reactors: application to propane combustion.** *Ind. Eng. Chem. Res.*, **48** (2009) 5962 – 5968.

[Steg 2009] C. Stegelmann, A. Andreasen, C. T. Campbell. **Degree of rate control: how much the energies of intermediates and transition states control rates.** *J. Am. Chem. Soc.*, **131 23** (2009) 8077 – 8082.

[Tak 1967] T. Takeyama, H. Miyama. **A shock – tube study of the ammonia – oxygen reaction**. 1967

[Tay 2007] M. Tayyeb Javed, N. Irfan, B. M. Gibbs. **Control of combustion generated nitrogen oxides by selective non – catalytic reduction.** *Journal of Environmental Management*, **83** (2007) 251 – 289.

[Tra 2007] X. Traversac. **Experimental and microkinetic modeling study of ammonia oxidation over platinum.** *Thesis, University of Sydney*, 2007. 218 p.

[Tur 2014] T. Turanyi, A. S. Tomlin. **Analysis of kinetic reaction mechanisms.** Springer – Verlag Berlin Heidelberg. First Edition, 2014, IX – 363 p.

[Ull 2012] F. Ullmann, W. Gerhartz, Y. S. Yamamoto, F. T. Campbell, R. Pfefferkorn, J. F. Rounsaville, F. Ullmann. **Ullmann's Encyclopedia of Industrial Chemistry.** Wiley – VCH Verlag GmbH & Co. Weinhem. 2012.

[Ves 2000] G. Veser, J. Frauhammer. **Modelling steady state and ignition during catalytic methane oxidation in a monolith reactor.** *J. Chem. Eng. Sci.*, **55 12** (June 2000) 2271 – 2286.

[Vil 2004] E. Vilas, P. Glarborg. **The selective non – catalytic reduction of NO with ammonia at high oxygen concentration.** Tech. Rep. *DTU Chemical Engineering*, 2004.

[Wal 1927] W. H. Walker, W. K. Lewis, W. H. McAdams. **Principles of Chemical Engineering.** McGraw−Hill book Company, Incorporated, 1927. 770p.

[Wis 2020] A. Wiser. **Investigation of the industrial NH_3 oxidation by CFD simulations including detailed surface kinetics.** *Thesis. Technische Universität Darmstadt, Facbereich Chemie*, August 2020.

[Zel 1946] Y. B. Zel'dovich. **The Oxidation of Nitrogen in Combustion Explosions**. *Acta Physicochimica U.S.S.R.*, **21** (1946) 577 – 628.

[Zer 2000] D. K. Zerkle, M. D. Allendorf, M. Wolf, O. Deutschmann. **Understanding homogeneous and heterogeneous contributions to the platinum – catalyzed partial oxidation of ethane in a short contact time reactor.** *Journal of Catalysis*, **196** (2000) 18 – 39.

[Zhe 2007] V. I. Zheivot, T. A. Nikoro, V. N. Krivoruchko, L. I. Panina, L. G. Pinaeva, L. A. Isupova. **Potentials of gas chromatography in the determination of reaction products in the catalytic oxidation of ammonia to nitrogen(ii) oxide.** *Journal of Analytical Chemistry*, **62** (2007) 1170 – 1175.

[Zho 2009] J. Zhou, W. Yang, W. Yang, J. Liu, Z. Wang, K. Cen. **Combustion of hydrogen – air in catalytic micro combustors made of different material.** *Int. J. Hydrogen Energy*, **34** (2009) 3535 – 3545.

Appendix 1
Abo Akademi mechanism

	Reactions	A	b	E_A
		mol, cm, s, K	dimensionless	cal mol^{-1}
R001	2 H + H2 ↔ H2 + H2	9.20×10^{16}	−0.600	0.00
R002	2 H + H2O ↔ H2 + H2O	6.00×10^{19}	−1.250	0.00
R003	2 H + M ↔ H2 + M	1.00×10^{18}	−1.000	0.00
	Third body effect enhanced by: H2O : 0.000			
	H2 : 0.000			
R004	H + H2O2 ↔ H2 + HO2	1.70×10^{12}	0.000	3755.00
R005	H + HNO ↔ H2 + NO	4.40×10^{11}	0.720	650.00
R006	H + HO2 ↔ H2 + O2	4.30×10^{13}	0.000	1411.00
R007	H + HO2 ↔ OH + OH	1.70×10^{14}	0.000	875.00
R008	H + O + M ↔ OH + M	6.20×10^{16}	−0.600	0.00
	Third body effect enhanced by: N2 : 1.500			
R009	H + O2 + M ↔ HO2 + M	2.10×10^{18}	−1.000	0.00
	Third body effect enhanced by: N2 : 0.000			
	H2O : 10.000			
	O2 : 1.500			
R010	H + OH + M ↔ H2O + M	8.40×10^{21}	−2.000	0.00
	Third body effect enhanced by: N2 : 2.600			
	H2O : 16.500			
R011	H + NH ↔ H2 + N	3.00×10^{13}	0.000	0.00
R012	H + NH2 ↔ H2 + NH	4.00×10^{13}	0.000	3650.00
R013	H + NH3 ↔ H2 + NH2	6.40×10^{5}	2.390	10171.00
R014	H + NNH ↔ H2 + N2	1.00×10^{14}	0.000	0.00
R015	H + NO2 ↔ NO + OH	8.40×10^{13}	0.000	0.00
R016	H2 + OH ↔ H + H2O	2.10×10^{8}	1.520	3450.00
R017	H2O2 + OH ↔ H2O + HO2	7.80×10^{12}	0.000	1330.00
R018	H2O2 + OH ↔ H2O + HO2	5.80×10^{14}	0.000	9560.00
R019	HNO + OH ↔ H2O + NO	3.60×10^{13}	0.000	0.00
R020	HO2 + HO2 ↔ H2O2 + O2	1.30×10^{11}	0.000	−1630.00
R021	HO2 + HO2 ↔ H2O2 + O2	4.20×10^{14}	0.000	11980.00
R022	HO2 + NO ↔ NO2 + OH	2.10×10^{12}	0.000	−480.00
R023	HO2 + O ↔ O2 + OH	3.30×10^{13}	0.000	0.00
R024	HO2 + OH ↔ H2O + O2	2.90×10^{13}	0.000	−497.00
R025	N2O + M ↔ O + N2 + M	4.00×10^{14}	0.000	56100.00
	Third body effect enhanced by: N2 : 1.700			
	H2O : 12.000			
	O2 : 1.400			
R026	2 O + M ↔ O2 + M	1.90×10^{13}	0.000	−1788.00
	Third body effect enhanced by: N2 : 1.500			
R027	N + NH ↔ H + N2	3.00×10^{13}	0.000	0.00
R028	N + NO ↔ N2 + O	3.30×10^{12}	0.300	0.00
R029	N + O2 ↔ NO + O	6.40×10^{9}	1.000	6280.00
R030	N + OH ↔ H + NO	3.80×10^{13}	0.000	0.00
R031	N2O + O ↔ N2 + O2	1.40×10^{12}	0.000	10800.00
R032	N2O + O ↔ NO + NO	2.90×10^{13}	0.000	23150.00
R033	N2O + OH ↔ HO2 + N2	2.00×10^{12}	0.000	40000.00
R034	NH + NO ↔ H + N2O	2.90×10^{14}	−0.400	0.00
	Declared duplicate reaction…			
R035	NH + NO ↔ H + N2O	-2.20×10^{13}	−0.230	0.00
	Declared duplicate reaction…			
R036	NH + O ↔ H + NO	9.20×10^{13}	0.000	0.00
R037	NH + O2 ↔ HNO + O	4.60×10^{5}	2.000	6500.00
R038	NH + O2 ↔ NO + OH	1.30×10^{6}	1.500	100.00
R039	NH + OH ↔ H + HNO	2.00×10^{13}	0.000	0.00
R040	NH + OH ↔ H2O + N	5.00×10^{11}	0.500	2000.00
R041	NH2 + O ↔ H + HNO	6.60×10^{14}	−0.500	0.00
R042	NH2 + O ↔ NH + OH	6.80×10^{12}	0.000	0.00
R043	NH2 + OH ↔ H2O + NH	4.00×10^{6}	2.000	1000.00
R044	NH3 + O ↔ NH2 + OH	9.40×10^{6}	1.940	6460.00
R045	NH3 + OH ↔ H2O + NH2	2.00×10^{6}	2.040	566.00
R046	NNH + OH ↔ H2O + N2	5.00×10^{13}	0.000	0.00

R047	NNH ↔ H + N2	1.00×10^{7}	0.000	0.00
R048	2 OH ↔ H2O + O	4.30×10^{3}	2.700	−2486.00
R049	2 HNO ↔ H2O + N2O	4.00×10^{12}	0.000	5000.00
R050	HNO + M ↔ H + NO + M	1.50×10^{16}	0.000	48680.00

Third body effect enhanced by: N2 : 2.000
H2O : 10.000
O2 : 2.000
H2 : 2.000

R051	HNO + NH2 ↔ NH3 + NO	2.00×10^{13}	0.000	1000.00
R052	HNO + NO ↔ N2O + OH	2.00×10^{12}	0.000	26000.00
R053	N2H2 + M ↔ H + NNH + M	5.00×10^{16}	0.000	50000.00

Third body effect enhanced by: N2 : 2.000
H2O : 15.000
O2 : 2.000
H2 : 2.000

R054	N + NH2 ↔ H + H + N2	7.00×10^{13}	0.000	0.00
R055	N2H2 + NH ↔ NH2 + NNH	1.00×10^{13}	0.000	1000.00
R056	N2H2 + NH2 ↔ NH3 + NNH	1.00×10^{13}	0.000	1000.00
R057	N2H2 + NO ↔ N2O + NH2	3.00×10^{12}	0.000	0.00
R058	N2H2 + O ↔ NH2 + NO	1.00×10^{13}	0.000	1000.00
R059	N2H2 + O ↔ NNH + OH	2.00×10^{13}	0.000	1000.00
R060	N2H2 + OH ↔ H2O + NNH	1.00×10^{13}	0.000	1000.00
R061	2 NH ↔ H + H + N2	2.50×10^{13}	0.000	0.00
R062	NH + NH2 ↔ H + N2H2	5.00×10^{13}	0.000	0.00
R063	NH + NNH ↔ N2 + NH2	5.00×10^{13}	0.000	0.00
R064	2 NH2 ↔ H2 + N2H2	8.50×10^{11}	0.000	0.00
R065	H2O2 + M ↔ OH + OH + M	1.30×10^{17}	0.000	45500.00

Third body effect enhanced by: N2 : 1.500
H2O : 10.000
O2 : 1.500

R066	H2 + O ↔ H + OH	5.10×10^{4}	2.670	6290.00
R067	H + N2O ↔ N2 + OH	3.30×10^{10}	0.000	4729.00
R068	H + N2O ↔ N2 + OH	4.40×10^{14}	0.000	19254.00
R069	H + N2H2 ↔ H2 + NNH	5.00×10^{13}	0.000	1000.00
R070	NH2 + NNH ↔ N2 + NH3	5.00×10^{13}	0.000	0.00
R071	NH2 + NO ↔ H2O + N2	1.30×10^{16}	−1.250	0.00
R072	NH2 + NO ↔ H2O + N2	-8.90×10^{12}	−0.350	0.00
R073	NH2 + NO ↔ NNH + OH	8.90×10^{12}	−0.350	0.00
R074	NNH + NO ↔ HNO + N2	5.00×10^{13}	0.000	0.00
R075	NNH + O ↔ H + N2O	1.00×10^{14}	0.000	0.00
R076	O + OH ↔ H + O2	2.00×10^{14}	−0.400	0.00
R077	H + H2O2 ↔ H2O + OH	1.00×10^{13}	0.000	3576.00
R078	H + HO2 ↔ H2O + O	3.00×10^{13}	0.000	1721.00
R079	H + N2 + O2 ↔ HO2 + N2	6.70×10^{19}	−1.420	0.00
R080	H2O2 + O ↔ HO2 + OH	6.60×10^{11}	0.000	3974.00
R081	HNO + O ↔ NO + OH	1.00×10^{13}	0.000	0.00
R082	HNO + O2 ↔ HO2 + NO	1.00×10^{13}	0.000	25000.00
R083	O + NO + M ↔ NO2 + M	7.50×10^{19}	−1.410	0.00

Third body effect enhanced by: N2 : 1.700
H2O : 10.000
O2 : 1.500

R084	NH + NO ↔ N2 + OH	2.20×10^{13}	−0.230	0.00
R085	NNH + O ↔ NH + NO	5.00×10^{13}	0.000	0.00
R086	NNH + O2 ↔ HO2 + N2	2.00×10^{14}	0.000	0.00
R087	NO2 + O ↔ NO + O2	3.90×10^{12}	0.000	−238.0
R088	H + H2NO ↔ H2 + HNO	3.00×10^{7}	2.000	2000.00
R089	H + H2NO NH2 + OH	5.00×10^{13}	0.000	0.00
R090	H + HNNO ↔ H2 + N2O	2.00×10^{13}	0.000	0.00
R091	H + HNNO ↔ NNH + OH	1.00×10^{13}	0.000	0.00
R092	H + HONO ↔ H2 + NO2	1.20×10^{13}	0.000	7350.00
R093	H + N2H3 ↔ NH2 + NH2	1.60×10^{12}	0.000	0.00
R094	H + N2H4 ↔ H2 + N2H3	1.30×10^{13}	0.000	2500.00
R095	H + NO3 ↔ NO2 + OH	6.00×10^{13}	0.000	0.00
R096	H2NO + M ↔ H + HNO + M	2.50×10^{16}	0.000	50000.00
R097	H2NO + NH2 ↔ HNO + NH3	3.00×10^{12}	0.000	1000.00

R098		H2NO	+	NO	↔	HNO	+	HNO				2.00×10^{7}	2.000	13000.00
R099		H2NO	+	NO2	↔	HNO	+	HONO				6.00×10^{11}	0.000	2000.00
R100		H2NO	+	O	↔	HNO	+	OH				3.00×10^{7}	2.000	2000.00
R101		H2NO	+	O	↔	NH2	+	O2				2.00×10^{14}	0.000	0.00
R102		H2NO	+	OH	↔	H2O	+	HNO				2.00×10^{7}	2.000	1000.00
R103		HNNO	+	M	↔	H	+	N2O	+	M		2.20×10^{15}	0.000	21600.00
R104		HNNO	+	M	↔	OH	+	N2	+	M		1.00×10^{15}	0.000	25600.00
R105		HNNO	+	NO	↔	HNO	+	N2O				1.00×10^{12}	0.000	0.00
R106		HNNO	+	NO	↔	NNH	+	NO2				3.20×10^{12}	0.000	270.00
R107		HNNO	+	NO2	↔	HONO	+	N2O				1.00×10^{12}	0.000	0.00
R108		HNNO	+	NO2	↔	NNH	+	NO3				1.00×10^{13}	0.000	0.00
R109		HNNO	+	O	↔	N2O	+	OH				2.00×10^{13}	0.000	0.00
R110		HNNO	+	O	↔	NNH	+	O2				1.00×10^{13}	0.000	0.00
R111		HNNO	+	OH	↔	H2O	+	N2O				2.00×10^{13}	0.000	0.00
R112		HNNO	+	OH	↔	HO2	+	NNH				1.00×10^{13}	0.000	0.00
R113		HNO	+	NO2	↔	HONO	+	NO				6.00×10^{11}	0.000	2000.00
R114		HO2	+	NH2	↔	H2NO	+	OH				5.00×10^{13}	0.000	0.00
R115		HO2	+	NH2	↔	NH3	+	O2				1.00×10^{13}	0.000	0.00
R116		HO2	+	NH3	↔	H2O2	+	NH2				3.00×10^{11}	0.000	22000.00
R117		HO2	+	NO3	↔	NO2	+	O2	+	OH		1.50×10^{12}	0.000	0.00
R118		HONO	+	HONO	↔	H2O	+	NO	+	NO2		2.30×10^{12}	0.000	8400.00
R119		HONO	+	NH	↔	NH2	+	NO2				1.00×10^{13}	0.000	0.00
R120		HONO	+	NH2	↔	NH3	+	NO2				5.00×10^{12}	0.000	0.00
R121		HONO	+	O	↔	NO2	+	OH				1.20×10^{13}	0.000	6000.00
R122		HONO	+	OH	↔	H2O	+	NO2				4.00×10^{12}	0.000	0.00
R123		N2H3	+	M	↔	H	+	N2H2	+	M		3.50×10^{16}	0.000	46000.00
R124		2 NH2	+	M	↔	N2H4	+	M				1.50×10^{13}	0.000	0.00
				Third body effect enhanced by:				N2	:	2.500				
								H2O	:	5.000				
								NH3	:	10.000				
				Low pressure limit parameters				A_0	=	1.00×10^{21}				
								b_0	=	0.000				
								E_{A0}	=	0.000				
R125		NH3	+	M	↔	H	+	NH2	+	M		2.20×10^{16}	0.000	93470.00
R126	NO	+ OH	+	M	↔	HONO	+	M				5.00×10^{23}	−2.510	−68.00
				Third body effect enhanced by:				N2	:	1.000				
								H2O	:	5.000				
R127	NO2	+ O	+	M	↔	NO3	+	M				1.30×10^{13}	0.000	0.00
				Third body effect enhanced by:				N2	:	1.500				
								H2O	:	18.600				
								O2	:	1.500				
				Low pressure limit parameters				A_0	=	1.00×10^{31}				
								b_0	=	-4.08×10^{3}				
								E_{A0}	=	2.47×10^{6}				
R128		N2H3	+	NH	↔	N2H2	+	NH2				2.00×10^{13}	0.000	0.00
R129		N2H3	+	O	↔	HNO	+	NH2				1.00×10^{13}	0.000	0.00
R130		N2H3	+	O	↔	N2H2	+	OH				5.00×10^{12}	0.000	5000.00
R131		N2H3	+	OH	↔	H2O	+	N2H2				1.00×10^{13}	0.000	1000.00
R132		N2H3	+	OH	↔	HNO	+	NH3				1.00×10^{12}	0.000	15000.00
R133		N2H4	+	NH2	↔	N2H3	+	NH3				3.90×10^{12}	0.000	1500.00
R134		N2H4	+	O	↔	H2O	+	N2H2				8.50×10^{13}	0.000	1200.00
R135		N2H4	+	OH	↔	H2O	+	N2H3				4.00×10^{13}	0.000	0.00
R136		NH	+	NO2	↔	N2O	+	OH				1.00×10^{13}	0.000	0.00
R137		NH2	+	NH2	↔	NH	+	NH3				5.00×10^{13}	0.000	10000.00
R138		NH2	+	NO2	↔	H2NO	+	NO				3.50×10^{12}	0.000	0.00
R139		NH2	+	NO2	↔	H2O	+	N2O				3.20×10^{18}	−2.200	0.00
R140		NNH	+	O2	↔	H	+	N2	+	O2		5.00×10^{13}	0.000	0.00
R141		NO2	+	NO2	↔	NO	+	NO	+	O2		1.60×10^{12}	0.000	26123.00
R142		NO2	+	NO2	↔	NO	+	NO3				9.60×10^{9}	0.730	20900.00
R143		NO2	+	NO3	↔	NO	+	NO2	+	O2		5.00×10^{10}	0.000	2940.00
R144		NO3	+	O	↔	NO2	+	O2				1.00×10^{13}	0.000	0.00
R145		NO3	+	OH	↔	HO2	+	NO2				1.40×10^{13}	0.000	0.00

Appendix 2

Degree of rate control and Sensitivity analysis

Bars: Filled (■) Degree of rate control / Empty (□) Sensitivity analysis

■□ NH_3 / ■□ NO / ■□ N_2 / ■□ N_2O

(10.2 NH_3 / 17.2 O_2 / − N_2) v% → 80% ξ → (2.01 NH_3 / 8.02 NO / 12.0 H_2O / 6.86 O_2 / − N_2) v% / 5.0 bar / 2.8 ms (τ)

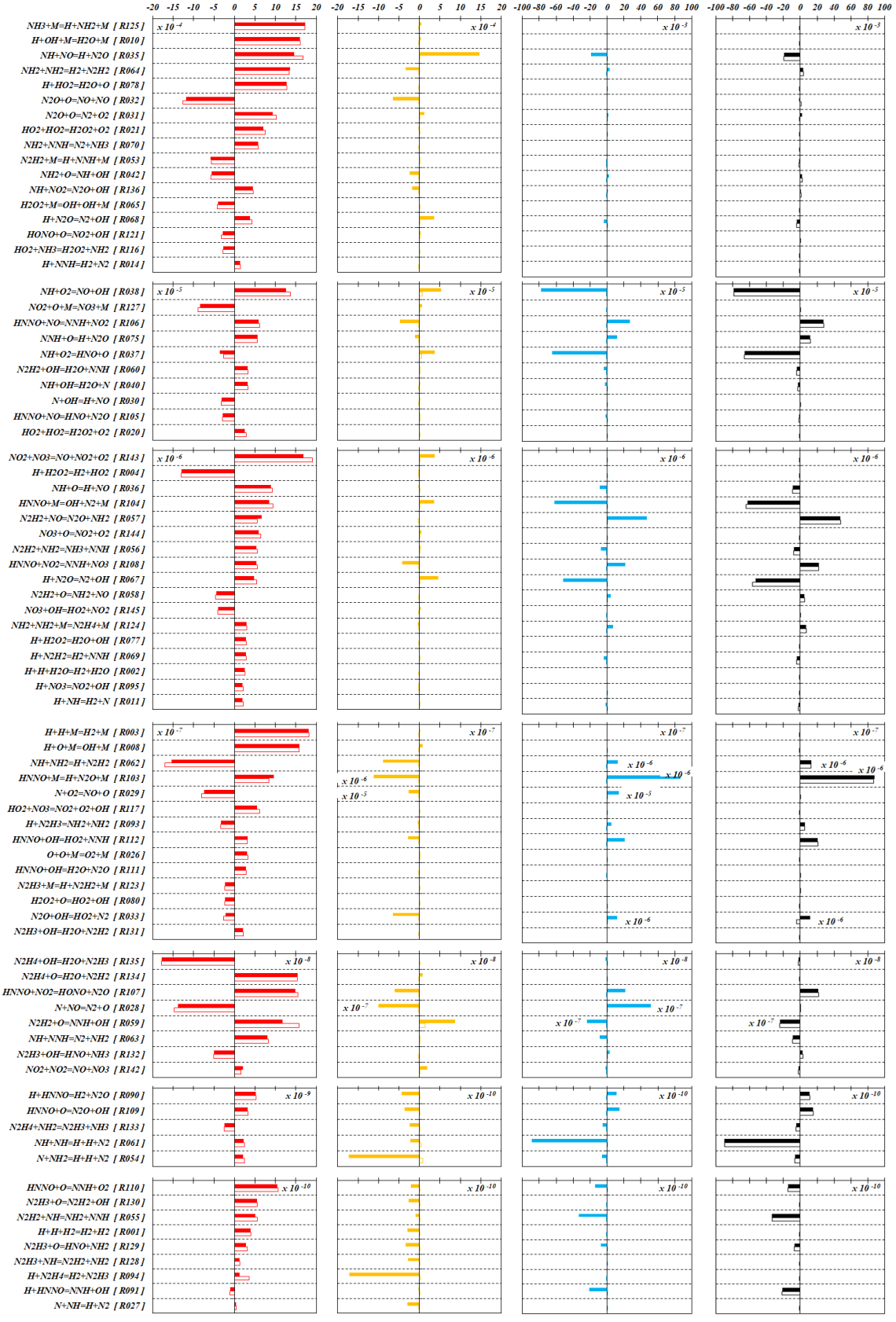

Appendix 3
Reduced mechanism

	Reactions	A	b	E_A
		mol, cm, s, K	*dimensionless*	*cal mol^{-1}*
R001	H + O2 + M → HO2 + M	2.10×10^{18}	−1.000	0.00
	Third body effect enhanced by: N2 : 0.000; H2O : 10.000; O2 : 1.500			
R002	H + NH3 → H2 + NH2	6.40×10^{5}	2.390	10171.00
R003	H + NO2 → NO + OH	8.40×10^{13}	0.000	0.00
R004	H2 + OH ↔ H + H2O	2.10×10^{8}	1.520	3450.00
R005	HNO + OH → H2O + NO	3.60×10^{13}	0.000	0.00
R006	HO2 + NO → NO2 + OH	2.10×10^{12}	0.000	−480.00
R007	HO2 + OH → H2O + O2	2.90×10^{13}	0.000	−497.00
R008	N2O + M → O + N2 + M	4.00×10^{14}	0.000	56100.00
	Third body effect enhanced by: N2 : 1.700; H2O : 12.000; O2 : 1.400			
R009	NH3 + O → NH2 + OH	9.40×10^{6}	1.940	6460.00
R010	NH3 + OH → H2O + NH2	2.00×10^{6}	2.040	566.00
R011	2 OH ← H2O + O	4.30×10^{3}	2.700	−2486.00
R012	HNO + M → H + NO + M	1.50×10^{16}	0.000	48680.00
	Third body effect enhanced by: N2 : 2.000; H2O : 10.000; O2 : 2.000; H2 : 2.000			
R013	HNO + NH2 → NH3 + NO	2.00×10^{13}	0.000	1000.00
R014	HNO + NO → N2O + OH	2.00×10^{12}	0.000	26000.00
R015	NH2 + NO → H2O + N2	1.30×10^{16}	−1.250	0.00
R016	NH2 + NO ← H2O + N2	-8.90×10^{12}	−0.350	0.00
R017	NH2 + NO → NNH + OH	8.90×10^{12}	−0.350	0.00
R018	NNH + NO → HNO + N2	5.00×10^{13}	0.000	0.00
R019	O + OH ← H + O2	2.00×10^{14}	−0.400	0.00
R020	HNO + O2 → HO2 + NO	1.00×10^{13}	0.000	25000.00
R021	O + NO + M ↔ NO2 + M	7.50×10^{19}	−1.410	0.00
	Third body effect enhanced by: N2 : 1.700; H2O : 10.000; O2 : 1.500			
R022	NNH + O2 → HO2 + N2	2.00×10^{14}	0.000	0.00
R023	NO2 + O ↔ NO + O2	3.90×10^{12}	0.000	−238.0
R024	H2NO + NO → HNO + HNO	2.00×10^{7}	2.000	13000.00
R025	H2NO + OH → H2O + HNO	2.00×10^{7}	2.000	1000.00
R026	HNO + NO2 → HONO + NO	6.00×10^{11}	0.000	2000.00
R027	HO2 + NH2 → NH3 + O2	1.00×10^{13}	0.000	0.00
R028	HONO + NH2 ← NH3 + NO2	5.00×10^{12}	0.000	0.00
R029	HONO + OH ← H2O + NO2	4.00×10^{12}	0.000	0.00
R030	NO + OH + M → HONO + M	5.00×10^{23}	2.510	−68.00
	Third body effect enhanced by: N2 : 1.000; H2O : 5.000			
R031	NH2 + NO2 ↔ H2NO + NO	3.50×10^{12}	0.000	0.00
R032	NH2 + NO2 → H2O + N2O	3.20×10^{18}	−2.200	0.00
R033	NNH + O2 → H + N2 + O2	5.00×10^{13}	0.000	0.00
R034	NO2 + NO2 ↔ NO + NO + O2	1.60×10^{12}	0.000	26123.00

Appendix 4
Constants for calculation of thermodynamic properties

Species	a_{1j}	a_{2j}	a_{3j}	a_{4j}	a_{5j}	a_{6j}	a_{7j}
H	2.0622×10^{4}	-3.9295×10^{-12}	-7.7903×10^{-14}	1.0917×10^{-16}	-2.7294×10^{-20}	2.1013×10^{8}	-3.7066×10^{3}
	2.0622×10^{4}	-3.1990×10^{-9}	4.0411×10^{-12}	-2.2149×10^{-15}	4.3670×10^{-19}	2.1013×10^{8}	-3.7066×10^{3}
H_2	1.4521×10^{4}	-2.4771×10^{0}	4.5400×10^{-3}	-1.8853×10^{-6}	2.7157×10^{-10}	-4.1208×10^{6}	-1.7096×10^{4}
	1.2499×10^{4}	1.3335×10^{1}	-3.2130×10^{-2}	3.2961×10^{-5}	-1.1694×10^{-8}	-4.0996×10^{6}	-9.2285×10^{3}
H_2NO	1.4393×10^{3}	9.5079×10^{-1}	-7.7434×10^{-4}	5.2035×10^{-7}	-1.3568×10^{-10}	1.4365×10^{6}	-1.5023×10^{4}
	1.4731×10^{3}	5.9689×10^{-1}	-4.6073×10^{-5}	-2.8652×10^{-8}	4.8289×10^{-12}	1.4461×10^{6}	-1.5977×10^{3}
H_2O	1.5752×10^{3}	4.9831×10^{-1}	4.6654×10^{-4}	-3.0001×10^{-7}	5.0661×10^{-11}	-1.3888×10^{7}	1.3941×10^{3}
	1.8676×10^{3}	-4.6554×10^{-1}	1.8848×10^{-3}	-1.4208×10^{-6}	4.2464×10^{-10}	-1.3966×10^{7}	-9.1355×10^{1}
HNO	7.9870×10^{2}	9.3681×10^{-1}	-2.1058×10^{-4}	1.5410×10^{-8}	-5.1837×10^{-14}	3.1002×10^{6}	2.3073×10^{3}
	1.2154×10^{3}	-1.5200×10^{0}	4.9524×10^{-3}	-4.5942×10^{-6}	1.4867×10^{-9}	3.0960×10^{6}	4.6911×10^{2}
HO_2	9.1008×10^{2}	8.1997×10^{-1}	-3.8410×10^{-4}	1.0985×10^{-7}	-1.3009×10^{-11}	5.8776×10^{4}	1.4891×10^{3}
	8.6069×10^{2}	3.6628×10^{-1}	1.4658×10^{-3}	-2.0953×10^{-6}	8.4525×10^{-10}	9.8000×10^{4}	1.8795×10^{3}
HONO	2.5651×10^{2}	2.9265×10^{0}	-2.7025×10^{-3}	1.1894×10^{-6}	-1.9816×10^{-10}	-1.8154×10^{6}	3.1136×10^{3}
	5.0216×10^{2}	2.0711×10^{0}	-1.6208×10^{-3}	5.6012×10^{-7}	-4.2099×10^{-11}	-1.8673×10^{6}	1.9020×10^{3}
N_2	8.3897×10^{2}	4.8801×10^{-1}	-1.8442×10^{-4}	2.5595×10^{-8}	1.4800×10^{-13}	-2.6145×10^{5}	1.9423×10^{3}
	1.1082×10^{3}	-4.0743×10^{-1}	7.0618×10^{-4}	-1.4669×10^{-7}	-9.1962×10^{-11}	-3.1835×10^{5}	6.1308×10^{2}
N_2O	9.1113×10^{2}	4.9627×10^{-1}	-1.8107×10^{-4}	3.0227×10^{-8}	-1.8466×10^{-12}	1.5251×10^{6}	-4.1593×10^{2}
	4.2640×10^{2}	2.1356×10^{0}	-2.5827×10^{-3}	1.8290×10^{-6}	-5.5364×10^{-10}	1.6514×10^{6}	2.0323×10^{3}
NH_2	1.4710×10^{3}	1.6643×10^{0}	-4.8463×10^{-4}	7.1108×10^{-8}	-4.1102×10^{-12}	1.1506×10^{7}	3.3836×10^{3}
	2.1816×10^{3}	-1.0929×10^{0}	3.6879×10^{-3}	-2.9119×10^{-6}	8.5315×10^{-10}	1.1357×10^{7}	-7.3605×10^{1}
NH_3	1.4847×10^{3}	2.1512×10^{0}	-1.6894×10^{-4}	-1.9257×10^{-7}	4.4138×10^{-11}	-3.2452×10^{6}	2.1985×10^{3}
	1.9353×10^{3}	-1.0961×10^{0}	7.5356×10^{-3}	-7.8181×10^{-6}	2.7619×10^{-9}	-3.2775×10^{6}	3.4345×10^{2}
NNH	1.0792×10^{3}	8.2840×10^{-1}	-2.9843×10^{-4}	4.8253×10^{-8}	-2.8913×10^{-12}	8.2083×10^{6}	1.2808×10^{3}
	1.2447×10^{3}	-1.3894×10^{0}	5.7469×10^{-3}	-6.2245×10^{-6}	2.2768×10^{-9}	8.2488×10^{6}	8.5317×10^{2}
NO	8.4895×10^{2}	4.5547×10^{-1}	-2.1725×10^{-4}	5.1082×10^{-8}	-4.8027×10^{-12}	2.7666×10^{6}	2.0553×10^{3}
	1.0886×10^{3}	-7.6849×10^{-1}	1.8762×10^{-3}	-1.4407×10^{-6}	3.7784×10^{-10}	2.7375×10^{6}	9.7897×10^{2}
NO_2	8.8281×10^{2}	3.9261×10^{-1}	-1.4966×10^{-4}	2.8460×10^{-8}	-1.8996×10^{-12}	4.1866×10^{5}	-2.1221×10^{1}
	7.1280×10^{2}	-2.8653×10^{-1}	3.0105×10^{-3}	-3.7005×10^{-6}	1.4160×10^{-9}	5.2350×10^{5}	1.1408×10^{3}
O	1.3711×10^{3}	-1.4935×10^{-1}	1.3055×10^{-4}	-5.3519×10^{-8}	8.4365×10^{-12}	1.5175×10^{7}	2.3010×10^{3}
	1.5099×10^{3}	-7.5666×10^{-1}	1.1192×10^{-3}	-7.5924×10^{-7}	1.9404×10^{-10}	1.5150×10^{7}	1.6441×10^{3}
O_2	7.9001×10^{2}	5.7283×10^{-1}	-3.9830×10^{-4}	1.4633×10^{-7}	-2.0718×10^{-11}	-2.6648×10^{5}	1.7373×10^{3}
	9.5953×10^{2}	-6.4334×10^{-1}	2.2727×10^{-3}	-2.2540×10^{-6}	7.5530×10^{-10}	-2.7335×10^{5}	1.0531×10^{3}
OH	1.7103×10^{3}	-2.8469×10^{-1}	6.1922×10^{-4}	-2.8414×10^{-7}	4.3571×10^{-11}	1.8315×10^{6}	1.1633×10^{3}
	1.8958×10^{3}	-7.6286×10^{-1}	1.2072×10^{-3}	-7.7714×10^{-7}	2.4121×10^{-10}	1.7728×10^{6}	1.8076×10^{2}

Constants for temperatures between 1000 and 2000 K

Constants for temperatures between 300 and 1000 K

Appendix 5
Constants for calculation of transport properties

Species	Enthalpy at standar state (1.0 bar)	Entropy at standar state (1.0 bar)	L – J characteristic length	L – J *energy*
	J kmol^{-1}	***J kmol^{-1} K^{-1}***	***angstrom***	***K***
H	2.1799×10^{8}	1.1460×10^{5}	2.050	145
H_2	0.0	1.3058×10^{5}	2.920	38.0
H_2NO	6.6191×10^{7}	2.3301×10^{5}	3.492	116.7
H_2O	-2.4184×10^{8}	1.8874×10^{5}	2.605	572.4
HNO	9.9579×10^{7}	2.2062×10^{5}	3.492	116.7
HO_2	1.0460×10^{7}	2.2899×10^{5}	3.458	107.4
HONO	-7.6735×10^{7}	2.4932×10^{5}	3.600	572.4
N_2	0.0	1.9150×10^{5}	3.621	97.5
N_2O	8.2048×10^{7}	2.1987×10^{5}	3.828	232.4
NH_2	1.9037×10^{8}	1.9460×10^{5}	2.650	80.0
NH_3	-4.5898×10^{7}	1.9267×10^{5}	2.920	481
NNH	2.4506×10^{8}	2.2439×10^{5}	3.798	71.4
NO	9.0291×10^{7}	2.1066×10^{5}	3.621	97.5
NO_2	3.3095×10^{7}	2.3991×10^{5}	3.500	200
O	2.4916×10^{8}	1.6096×10^{5}	2.750	80.0
O_2	0.0	2.0506×10^{5}	3.458	107.4
OH	3.8995×10^{7}	1.8359×10^{5}	2.750	80.0

Appendix 6

Values of the parameter relationships for the fundamental reactions of the AA – Mech

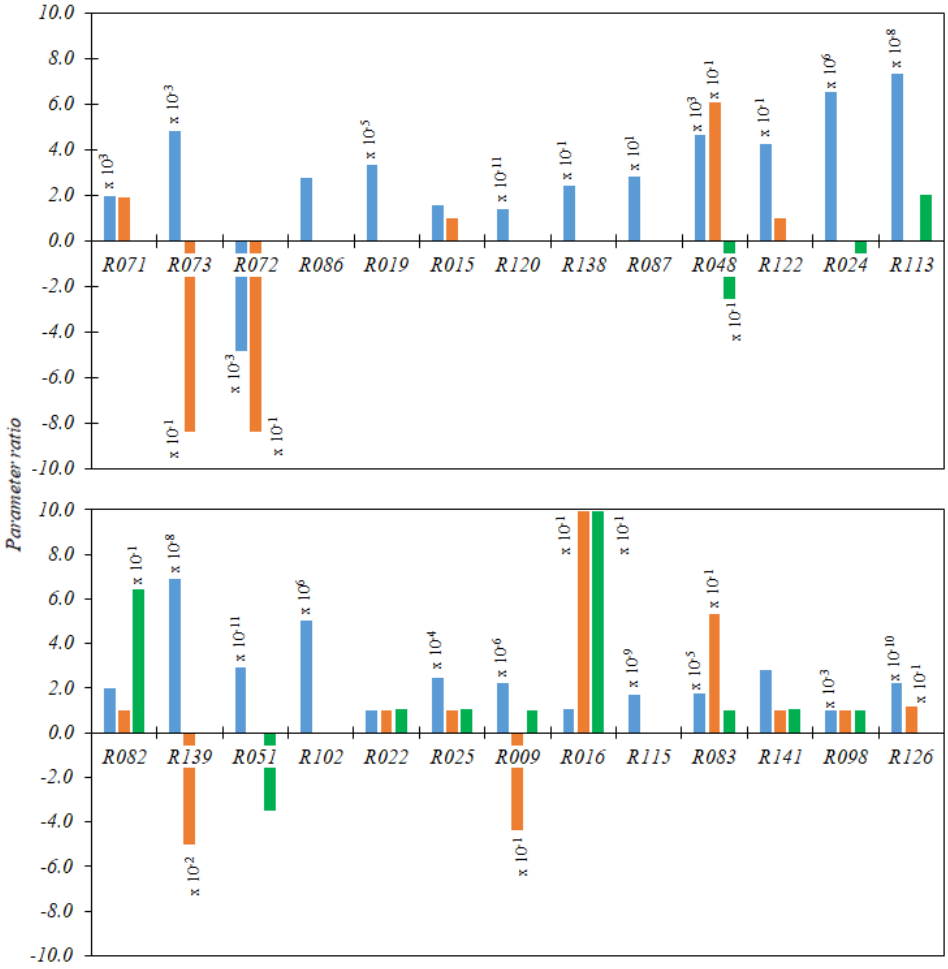

Ratio between:

Preexponential factors (A)

Temperture exponents (b)

Activation energies (E_A)

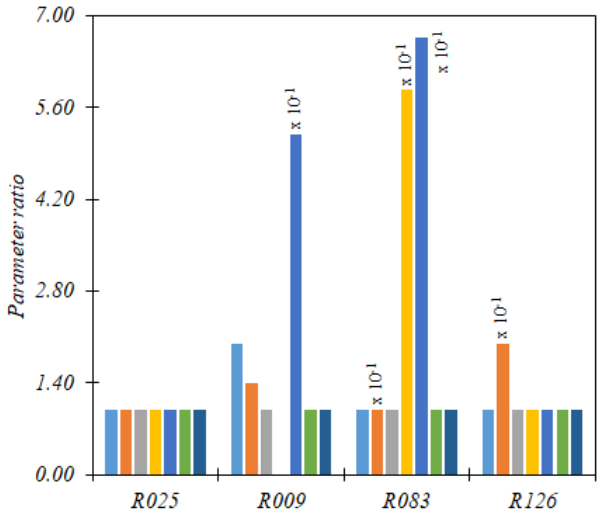

Ratio between third body effect parameter for

H_2 H_2O H_2O_2 N_2

O_2 Ar NH_3

Appendix 7

Values of the parameter relationships for the remaining comparable reactions

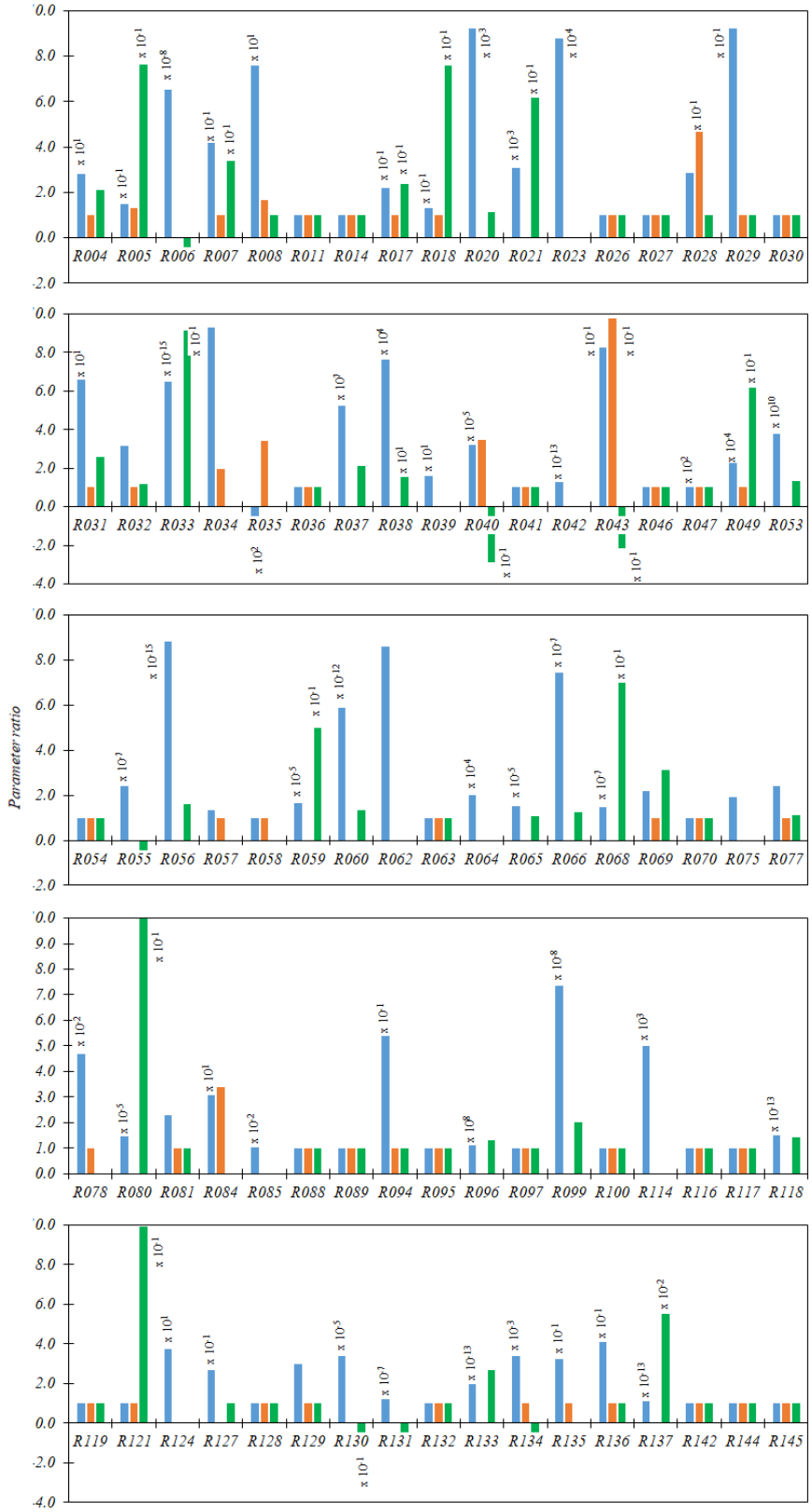

Ratio between:

	Preexponential factors	(A)
	Temperture exponents	(b)
	Activation energies	(E_A)

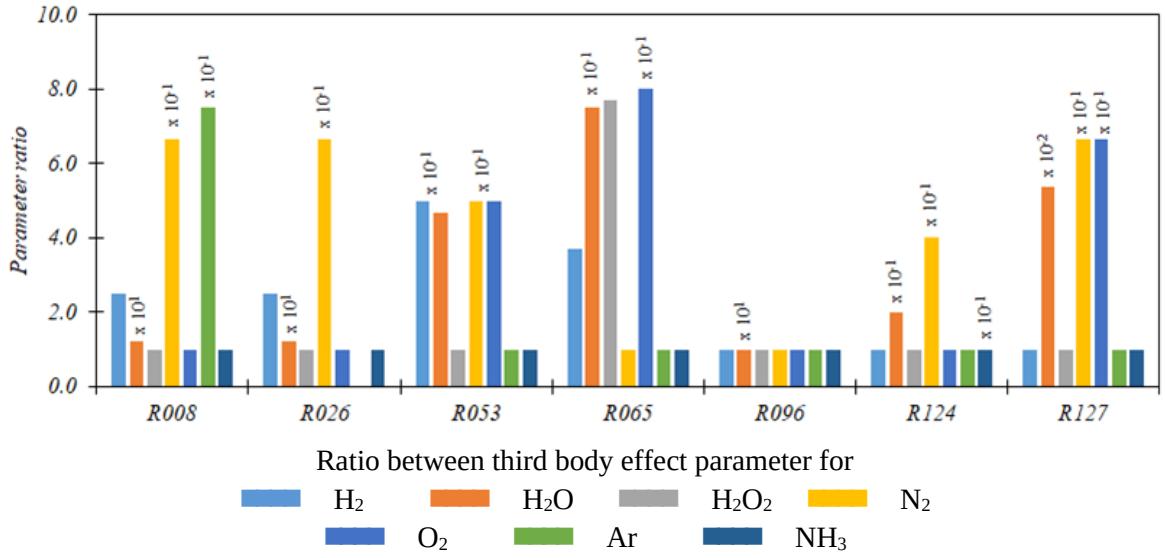

Ratio between third body effect parameter for

H_2 H_2O H_2O_2 N_2 O_2 Ar NH_3

Appendix 8

Further results of the simulation of the CatOx and CatOxGP processes in the first wire of the square mesh reactor

Inlet conditions: 423 K, 5.0 bar, 10.0 v% NH_3, 90.0 % dry, inlet velocity of 0.75 m s^{-1}

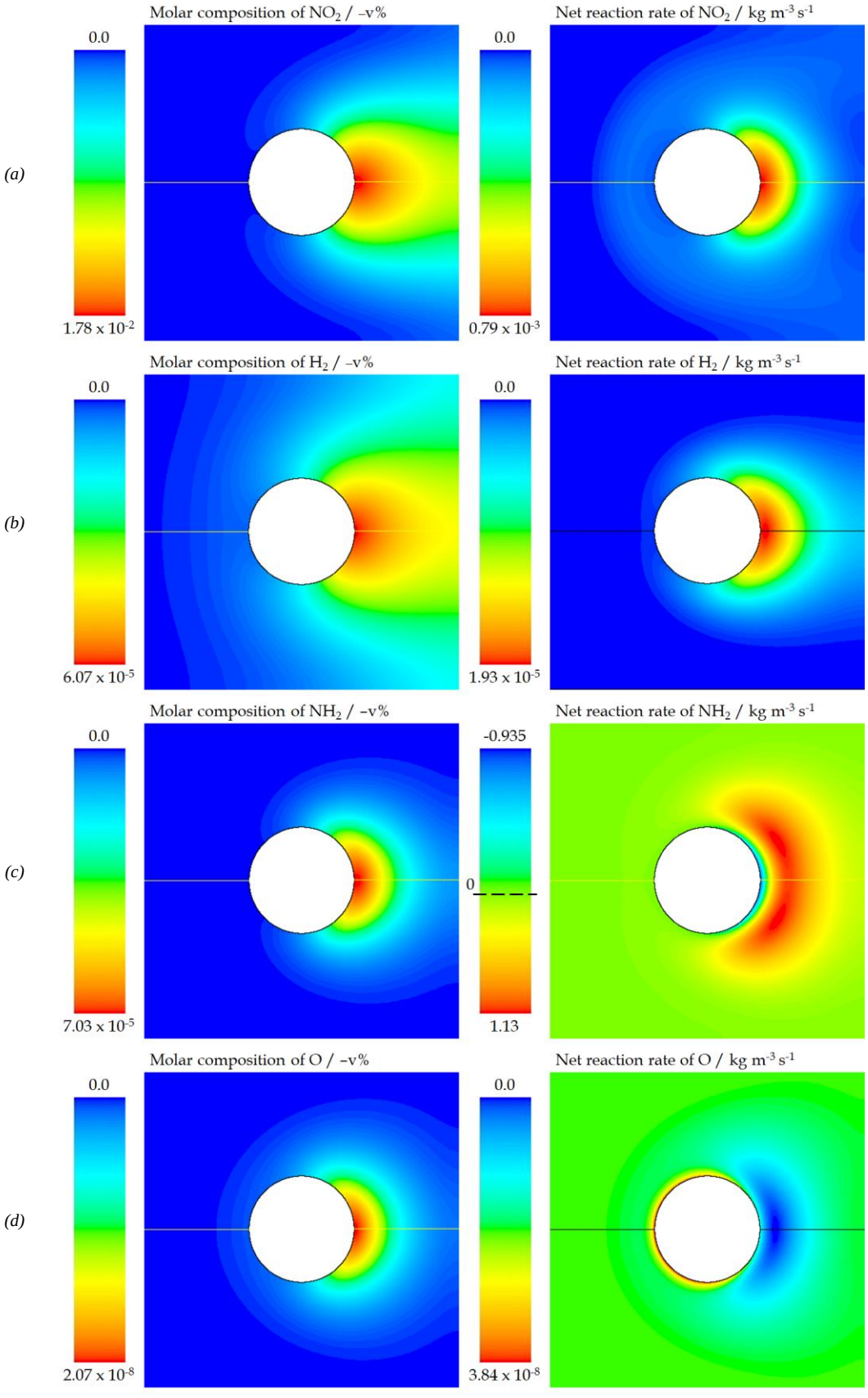

Appendix 9

Further results of the simulation of the CatOx and CatOxGP processes in a stagnation point reactor

Inlet conditions: 423 K, 5.0 bar, 10.0 v% NH_3, 90.0 % dry, 3.0 kg m^{-2} s^{-1}

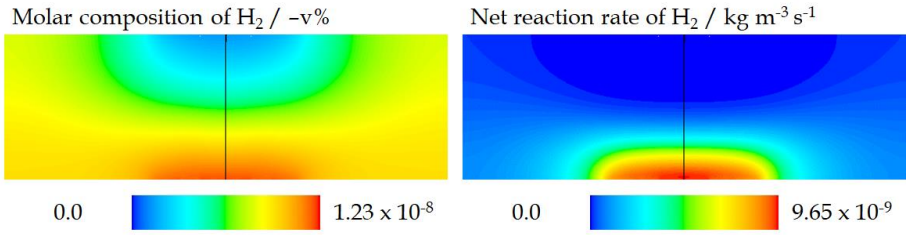

(a)

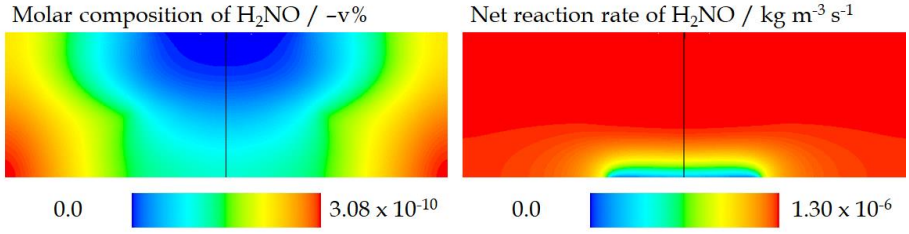

(b)

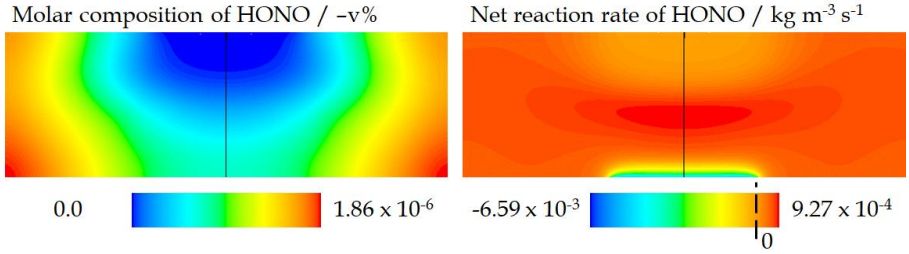

(c)

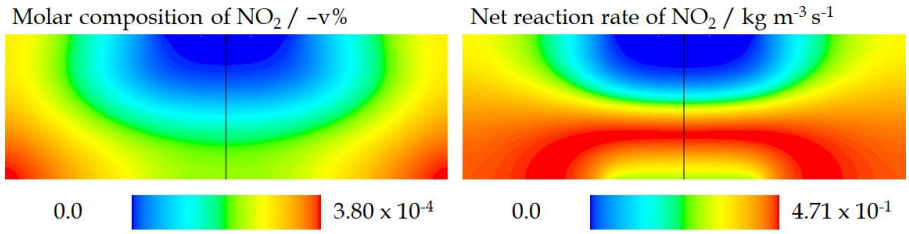

(d)

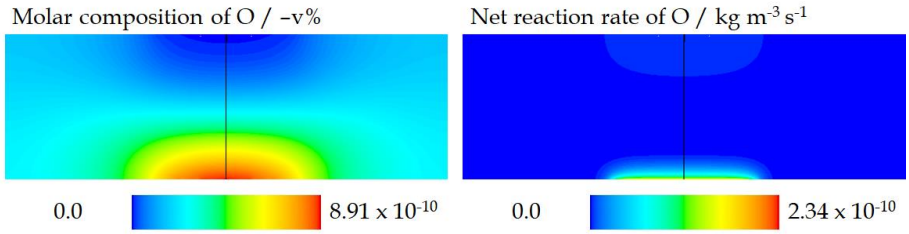

(e)

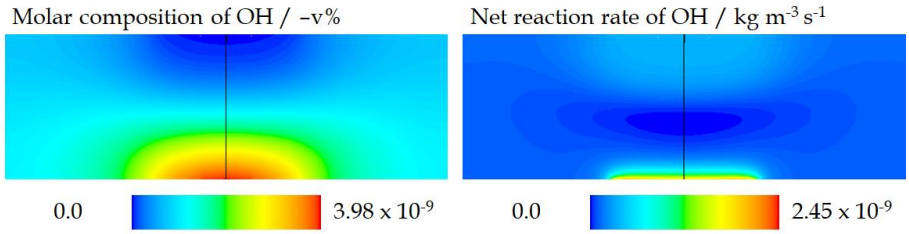

(f)

Appendix 10

Further results of the simulation of the CatOx and CatOxGP processes in a planar channel reactor

Inlet conditions: 423 K, 5.0 bar, 11.0 v% NH_3, 90.0 % dry, 1.20 m s^{-1}

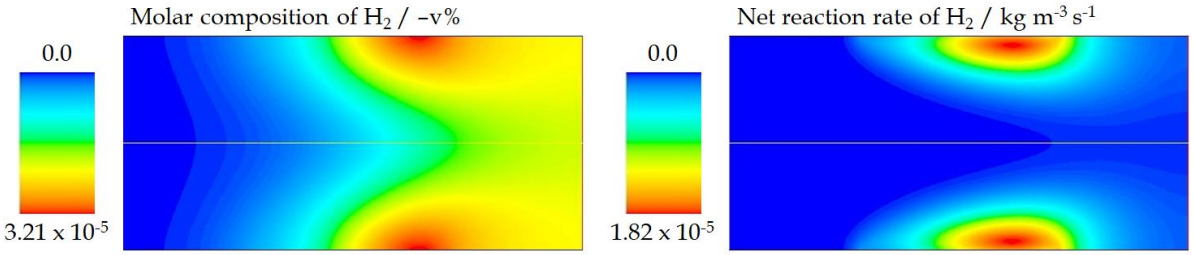

(a)

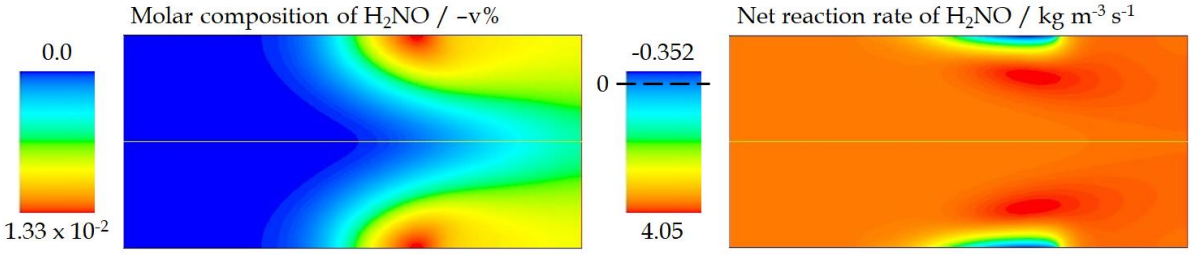

(b)

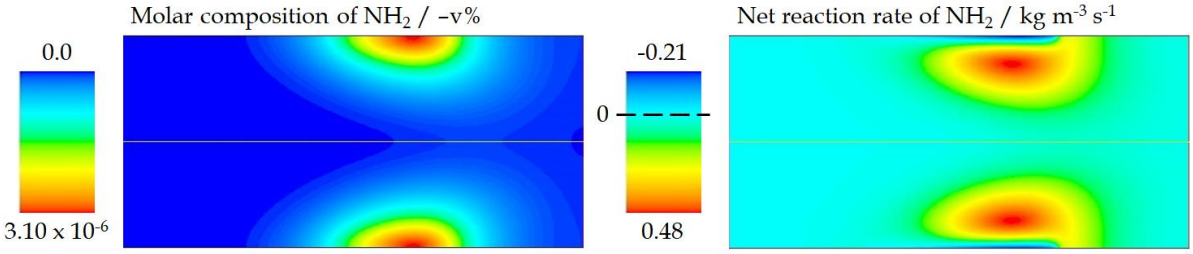

(c)

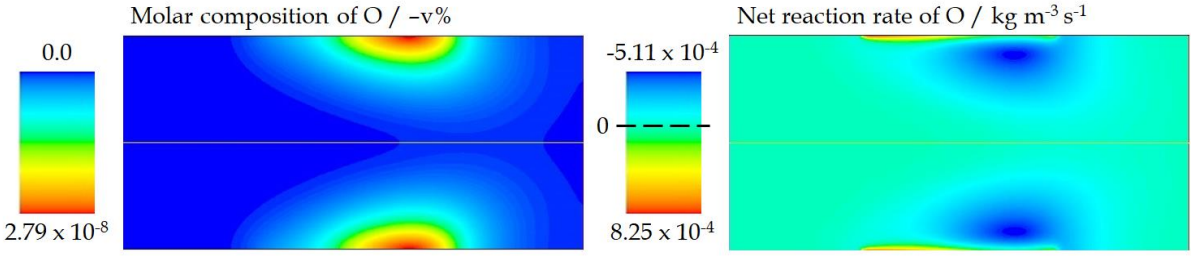

(d)

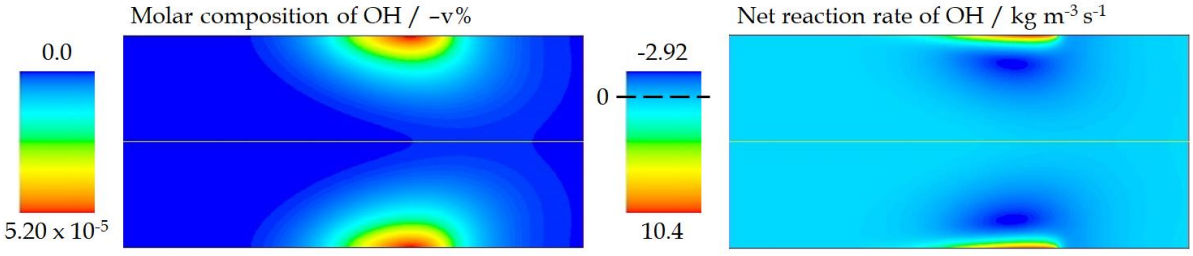

(e)

Appendix 11
Further results of the simulation of the CatOx and CatOxGP processes in a planar channel reactor with six catalytic surfaces
Inlet conditions: 1.20 m s^{-1}, 10.0 v% NH_3, 90.0 v% dry air.
(a) 423 K, 5.0 bar; (b) 500 K, 5.0 bar; (c) 423 K, 15.0 bar; (d) 530 K, 15.0 bar.

O – atom Contours

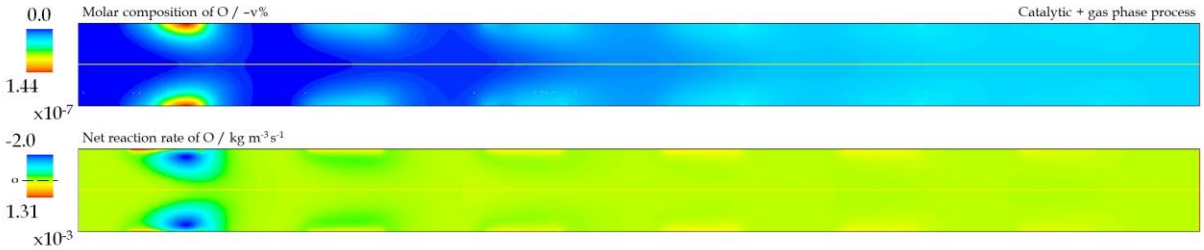

(a)

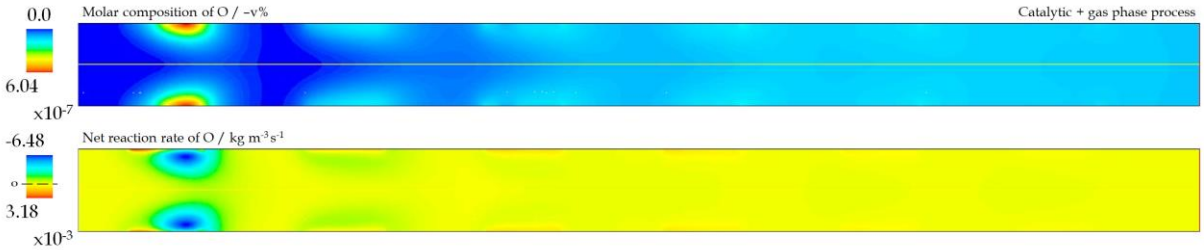

(b)

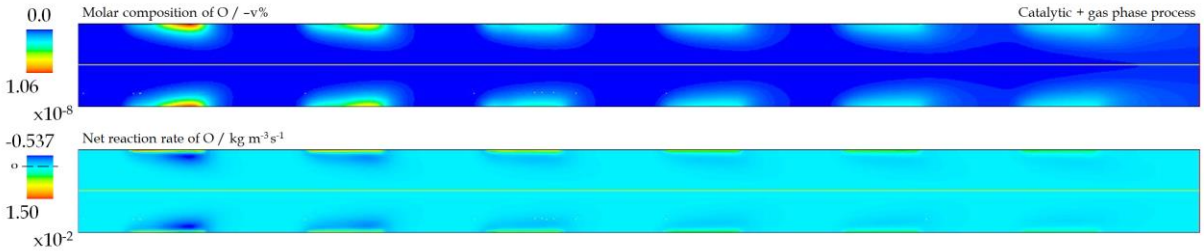

(c)

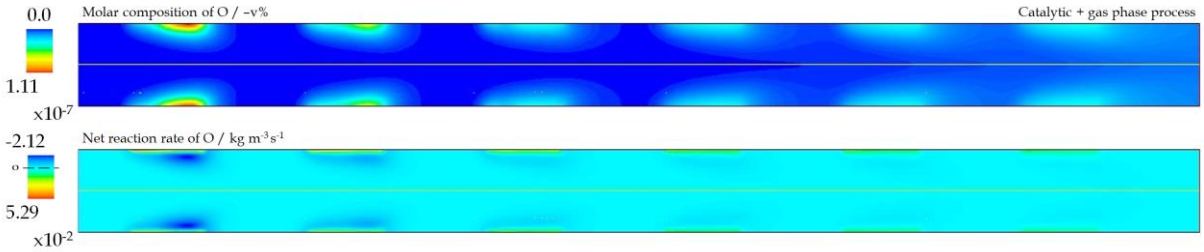

(d)

H – atom Contours

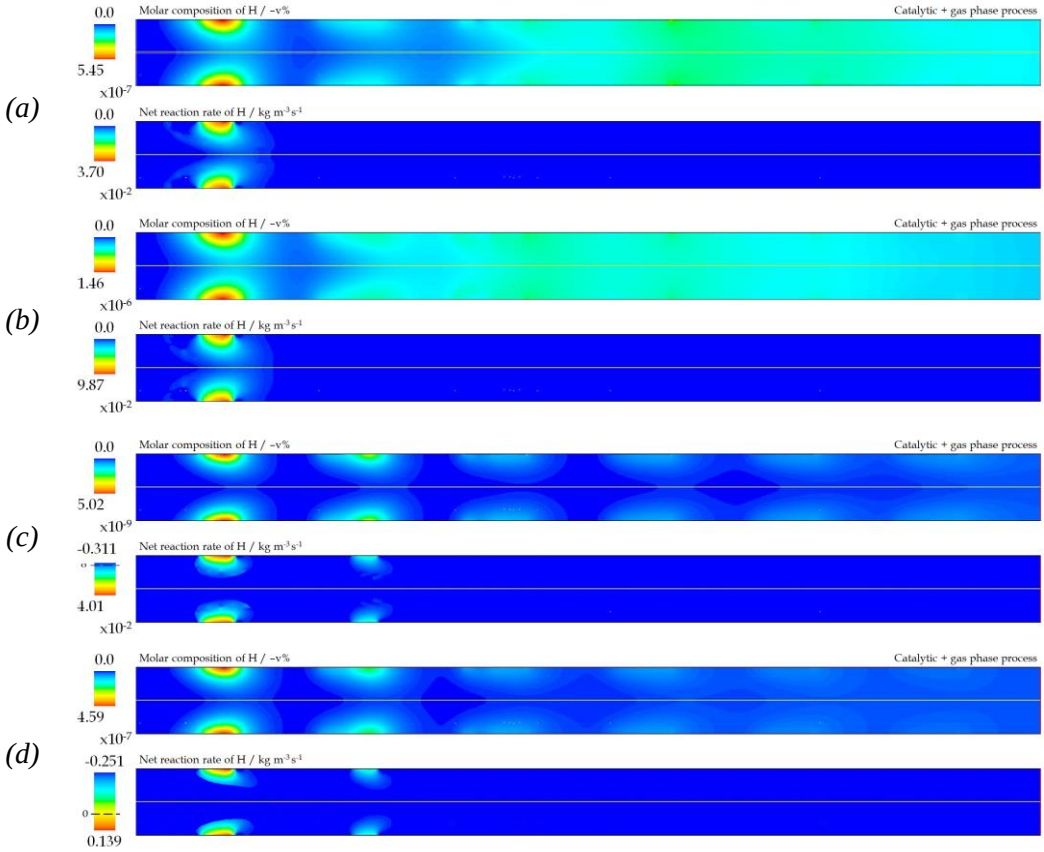

HNO Contours

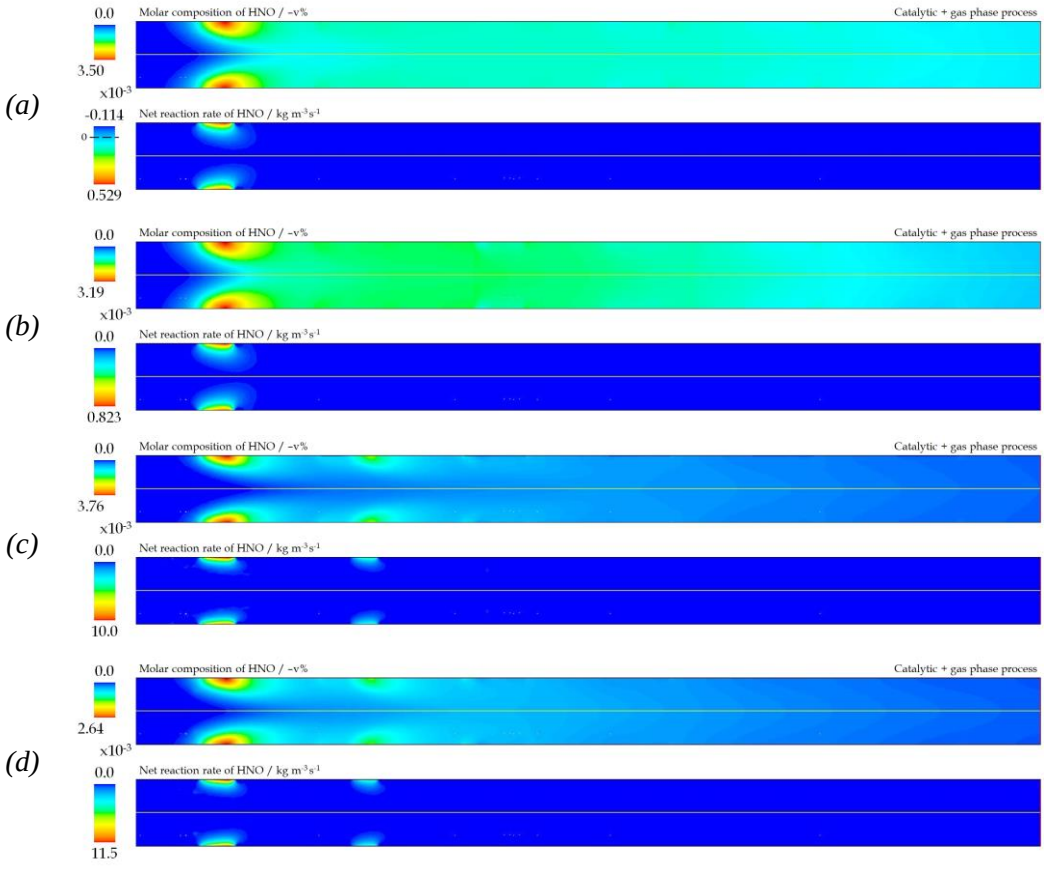

NH_2 Contours

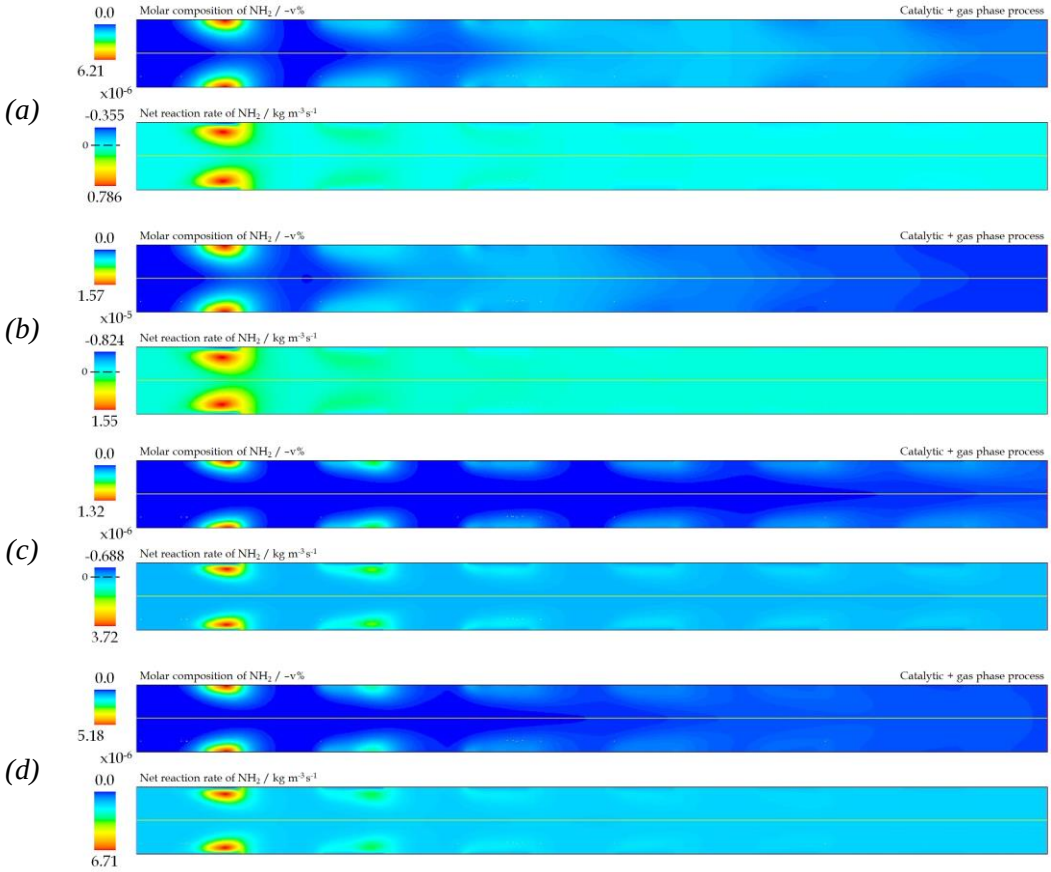

H_2NO Contours

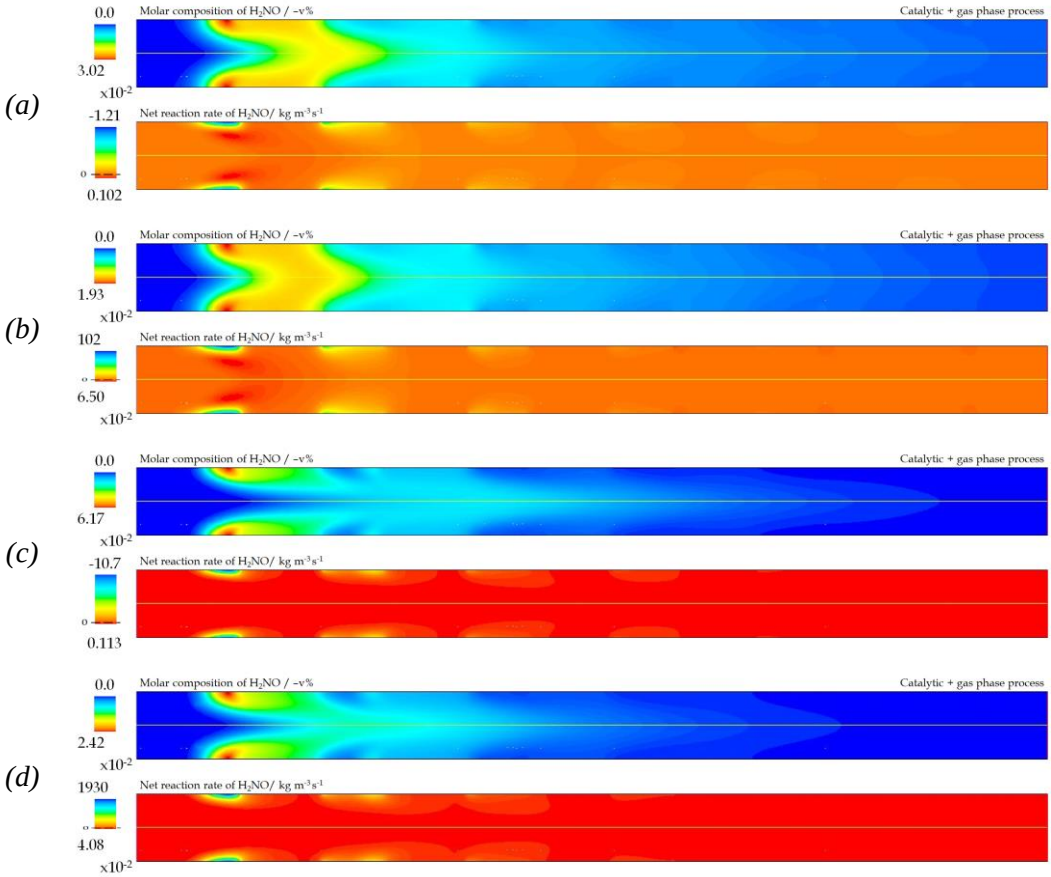

HONO Contours

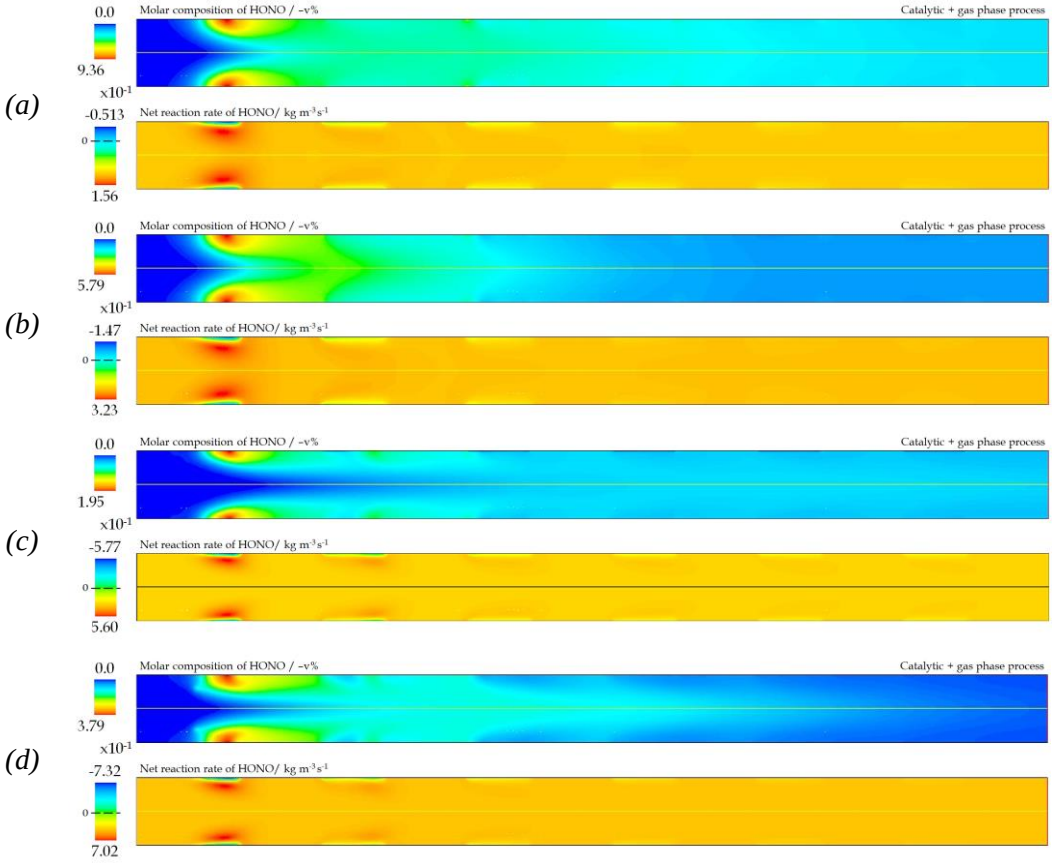

OH Contours